

वार्षिक प्रतिवेदन
Annual Report

2013-2014

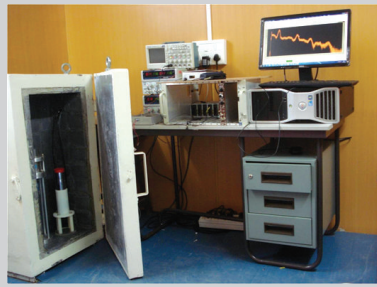
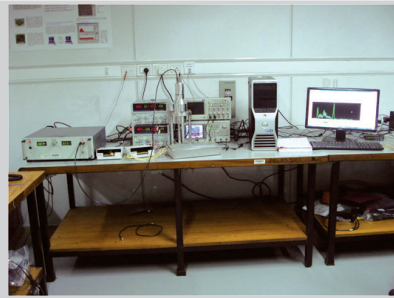
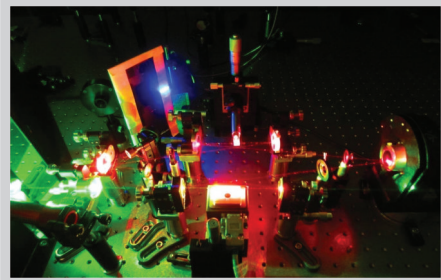


भौतिक अनुसंधान प्रयोगशाला, अहमदाबाद
Physical Research Laboratory, Ahmedabad



NICS (gold cell unit) on the 1.2m telescope at Aro.

पी.आर.एल. में सुविधाएं Facilities at PRL



वार्षिक प्रतिवेदन
Annual Report
2013 - 2014



भौतिक अनुसंधान प्रयोगशाला, अहमदाबाद
Physical Research Laboratory, Ahmedabad

Front Cover: PRL main Campus, Navrangpura & PRL Thaltej Campus, Ahmedabad.

Inside front cover: Some Experimental Facilities at PRL.

Inside back cover: Events at PRL.

Back cover:

Top left Panel: Near Infrared Camera (Golden colored unit) on the 1.2 m telescope, Mt. Abu.

Centre right panel: Supernova 2014J in M82 JHK color composite, observed at Mt. Abu observatory.

Bottom right Panel: Inside view of 1.2 m telescope, Mt. Abu.

Compiled & Layout by:
Office of the Dean, PRL.

Published by:
Physical Research Laboratory, Ahmedabad.

Printed by:
Creative Printers Private Limited, Ahmedabad.

Council of Management

Chairman

Professor U.R. Rao
Antariksh Bhavan, New BEL Road
Bengaluru-560231

Chairman, PRL Council of Management

Members

Dr. K. Radhakrishnan
Secretary, Department of Space, Govt. of India
Antariksh Bhavan, Bengaluru-560231

Chairman, ISRO

Shri S. Srinivasan, IAS
Department of Space, Govt. of India
Antariksh Bhavan, Bengaluru-560231

Additional Secretary & FA
(Upto 19.01.2014)

Shri A. Vijay Anand, IRS
Department of Space, Govt. of India
Antariksh Bhavan, Bengaluru-560231

Additional Secretary & FA
(From 20.01.2014)

Shri Sanjay S. Lalbhai
Ahmedabad Education Society
Ahmedabad

Nominee, Ahmedabad Education Society

Shri Kartikeya V. Sarabhai
Chidambaram,
Usmanpura, Ahmedabad

Nominee, Karmakshetra Educational
Foundation

The Principal Secretary,
Department of Education,
(Higher & Technical Education)
Government of Gujarat, Gandhinagar

Nominee, Government of Gujarat

Professor J.N.Goswami,
Director,
Physical Research Laboratory, Ahmedabad

Ex-Officio

Member - Secretary

Shri Y.M.Trivedi,
Registrar
Physical Research Laboratory, Ahmedabad

Ex-Officio

Contents

| | |
|---|-----|
| Director's Foreword | 1 |
| Science Highlights | 3 |
| Awards and Honours | 7 |
| Human Resource Development | 10 |
| Theses Submitted | 11 |
| Colloquia/Public Lectures by Visitors | 12 |
| Conference/Symposia/Workshops held by PRL | 14 |
| Invited Talks at Conference / Symposia / Workshops | 15 |
| Lectures at Universities / Institutions | 22 |
| Science | |
| <i>Astronomy and Astrophysics</i> | 25 |
| <i>Solar Physics</i> | 34 |
| <i>Planetary Sciences and PLANEX Program</i> | 47 |
| <i>Space, Atmospheric, Molecular and Laser Physics</i> | 61 |
| <i>Geosciences</i> | 78 |
| <i>Theoretical and Computational Physics</i> | 93 |
| Publications | |
| <i>Publications in Journals</i> | 102 |
| <i>Publications in Proceedings of Conference/Symposia/Workshops</i> | 110 |
| <i>Books Edited/Review Articles/Technical Notes</i> | 113 |
| Promotion of Basic Sciences and Official Language | 114 |
| Facilities and Services | 117 |
| Honorary Fellows | 121 |
| Honorary Faculties | 122 |
| Academic Faculty | 123 |
| Technical Faculty | 127 |
| Audited Statement of Accounts | 128 |

Director's Foreword

Scientific activities at PRL are advancing at a good pace with some of the new research initiatives, taken up during the last plan period, yielding significant results. The laboratory is also gearing up to enhance the scope of the current research activities and pursue new research avenues during the current five year plan period. Generous support received from the Department of Space has enabled PRL to initiate scientific programmes in frontier areas of research, that include, search of exo-planets, laboratory studies of interstellar grains, laboratory synthesis of astro-molecules and experimental studies in the field of quantum optics. Significant progress has also been made in the areas of planetary sciences and exploration and PRL is developing several payloads for the upcoming Chandrayaan-2 and proposed Aditya missions.

Several new facilities, that include a high end computing system, an Accelerator Mass Spectrometer and a Ground-based Radar will be operational within the next couple of years and provide new impetus for research in the fields of Computational Sciences, Atmospheric & Space Sciences, Geosciences and Planetary Sciences. Plans for establishing a 2.5 meter telescope facility at Mt. Abu is nearing completion. This facility, expected to be realized within a time frame of four years, will significantly enhance the capabilities of the Astronomy and Astrophysics division. A major infrastructure facility for housing the newly acquired laboratory instruments has been built in the Thaltej campus of PRL. Currently spadework has started to house the quantum optics laboratory, the Accelerator Mass Spectrometer and the Planetary Science Data Center in this new facility.

Research carried out at PRL during the year led to several very significant results. The new near infrared Camera cum Spectrograph provided excellent data for the outburst

of the Type Ia supernova SN2014J on 21 January, 2014, and PRL was one of the primary participants in the global effort to monitor this event. Analysis of the solar data led to identification of dark solar filament as progenitor of an ensuing coronal mass ejection event. Installation and test-runs with the Multi-Application-Solar-Telescope were conducted successfully and routine operations are expected by late 2014. Laboratory models of several PRL payloads for the Orbiter, Rover and Lander on the proposed Chandrayaan-2 mission have been completed. A major study of aerosols over the Indo-Gangetic plain suggests that a mix of dust and black carbon are the dominant aerosol over this region. Analysis of the isotopic composition of water vapour over the Bay of Bengal showed that it is controlled by atmospheric temperature rather than sea surface temperature. Oxygen isotopic studies of Stalagmite from a cave provided evidence for an abrupt change in monsoon intensity during the last glacial transition. Analysis of Chandrayaan-1 and other lunar mission data suggest variations in mineral chemistry of mare basalts that erupted during late stage of lunar volcanism. Analytical studies suggest that the atmospheric neutrino experiment proposed to be pursued at the upcoming India based Neutrino Observatory, together with the long baseline experiments T2K and NOVA, can play a significant role in discovering CP violation for certain parameter spaces.

In the Academic front, the strength of core faculty has reached nearly seventy five. They are engaged in scientific and technical activities together with twenty five supporting Technical Faculty and more than twenty five junior scientists, engineers and technicians. Nearly a hundred research scholars and post-doctoral fellows along with a significant number of project associates are currently associated with PRL.

The eighth UN CSSTEAP course on Space Sciences for the Asia-Pacific region conducted by PRL started on 01 August, 2012 with fourteen participants from seven countries and was completed with a convocation ceremony held on 29 April, 2013. Several university faculty members visited PRL for extended periods for collaborative studies as a part of our continuing effort to provide opportunity for academic interactions to interested faculty members from universities. PRL continues its academic association with Gujarat University, Ahmedabad, M. S. University of Baroda, Vadodara, M.L.S University, Udaipur, S. P. University, V. V. Nagar, Indian Institute of Technology, Gandhinagar, Pondicherry University, Pondicherry and Nirma University, Ahmedabad.

The laboratory continues to maintain a high level of academic excellence with more than two hundred scientific publications, with a large fraction in high impact journals, in addition to one monograph and seven invited review articles. Ten research scholars have submitted their thesis during the year. Collectively, PRL Faculty members received invitations to give more than two hundred lectures at Conferences, Symposia and Workshops and also at Universities and Academic Institutions. PRL also invited close to twenty faculty members from both within the country and abroad for scientific interactions. An international meet on "From Mantle to the Moon" was held in February 2014 in remembrance of Prof. Devendra Lal, past Director of PRL, who breathed his last in late 2012. Several other meetings and workshops in the area of planetary and atmospheric sciences were also held during the year.

Honours and acclamation received by faculty members from different national and international academic forum reflects the mature state of scientific research done at PRL. The recognitions include J. C. Bose Fellowship of Science & Engineering Research Board (SERB), Honorary Fellow of Royal Astronomical Society, SERB Women Excellence Award, Vasvik Award, Fellowship of Science Academies, Space Science Award of the Astronautical Society of India, Indira Gandhi Prize for popularization of Science, National Geoscience Award and Award from Rumanian Academy. PRL faculty members serve as Council Member of National and International Science Academies as well as in Council and Advisory Committees of several academic institutions as well as government departments such as SERB, CSIR and MOES. Several PRL research scholars received awards for their presentation in scientific meets that include the URSI Young Scientist award and the Zirin Studentship Award of the American Astronomical Society.

PRL continues to expand its HRD activities by inducting more number of college and university students from all over India for its summer programme and also through its association with similar programme conducted jointly by the three Science

Academies in India. Nearly forty graduate students, several undergraduate students as well as an equal number of engineering students have participated this year in the PRL summer student programme. PRL is entrusted to conduct the PLANEX and RESPOND programmes of the Department of Space and currently more than forty research groups at various universities and research institutions across the country are receiving funds and advice to carry out scientific investigations in the fields of Astronomy, Planetary and Space Sciences. Several interactive meetings of interested faculty members and scientists from universities and research institutes with technical personnel involved in Indian planetary missions were also held during the year.

"Science Day" celebration at PRL has now become a major event for the state of Gujarat with participation of selected students from across the state. PRL offers scholarships and incentives to students based on their performance in various science related activities conducted on that day. Starting last year, special events are also arranged for the accompanying teachers.

Continuous efforts are on to ensure use of Hindi in administrative matters and official communications. The Hindi version of PRL web site is getting ready and will be operational by mid-2014. The Town Official Language Committee has recognized the various initiatives taken by PRL and the work done in implementation of Hindi in various domains.

Thanks to generous support from the Department of Space (DOS), implementation of the 12th Five year plan is proceeding well with several new facilities already in place and a few others expected to be at PRL soon. Collective efforts and coordination between academic and administrative personnel have ensured timely acquisition and the onus is now on Team PRL to deliver high quality science. The untiring effort put in by all members of the PRL family ensured that we have been able to do reasonable justice to the faith reposed on us by DOS and we need to give our best to achieve the next higher level of excellence.

I am grateful to all the members of the PRL Council for their encouragement, invaluable advice and whole hearted support for all the scientific activities pursued at PRL. In particular, I am indebted to Chairman, PRL Council, Prof. U. R. Rao, for his sage advice and unstinted support and grateful to Chairman, ISRO, for his advice and encouragement that resulted in a year of steady growth and progress at PRL.

J.N. Goswami

Director

SCIENCE HIGHLIGHTS

Astronomy and Astrophysics

- Near-infrared spectro-photometric observations of two novae V476 Scuti and KT Eridani were carried out from Mt Abu. V476 Scuti showed the formation of an optically thin dust shell, a phenomenon which is not commonly observed in novae. By fitting black body curves to the spectral energy distributions (SEDs) the evolution of the dust shell temperature was studied. The spectra of KT Eri showed it to be a nova of the He/N class with strong emission lines of He I, H I and O I whose profiles showed broad wings with a relatively narrow central component, indicative of a bipolar flow. Estimates were made of the distance to the nova, its height above the galactic plane and the ejecta mass.
- Near-infrared observations were made of the Be star X Persei during an unprecedented state of IR brightness. Interestingly, the equivalent widths and line fluxes of the prominent Hydrogen and Helium lines were found to anti-correlate with the strength of the adjacent continuum. Such an anti-correlation effect is not normally expected and has not been observed earlier in the infrared for any Be star. This observed behavior is suggested to originate due to a radiatively warped, precessing circumstellar disk.
- Successful commissioning was carried out of the spectroscopic segment of the new Near-IR Camera/Spectrograph (NICS) which, apart from imaging capabilities in the NIR, is designed to obtain spectra in the 0.85 to 2.5 micron region at a resolution of 1000. Immediately after deployment, the instrument has given invaluable data on 2 major astronomical events viz. (i) the outburst of the Type Ia supernova SN2014J on 21 January 2014 and (ii) the third recorded eruption of recurrent nova V745 Sco on 6 February 2014.
- The optical light-curve of the blazar S5 0716+714 was analyzed to study duty cycle of variability and long-term trend of variation. The results show the source to be highly variable with 84% duty cycle and a slow decrease in average brightness during 2005-2012, while the viewing angle, with respect to jet, was seen to increase by more than 4 degrees in December 2012. The most likely reason for this change in brightness appears to be due to the precession of the jet with a time scale of 10-12 years resulting in a change in viewing angle which in turn is expected to lead to changes in brightness.
- Detection of cyclotron resonance scattering feature in the spectrum of accretion powered X-ray pulsar provides direct measurement of the strength of the pulsar magnetic field. For the first time, the cyclotron resonance scattering feature was detected at 44 keV in the broad-band spectrum of high mass X-ray binary pulsar 4U 1909+07. After performing several tests on the spectral data, the absorption-like feature at 44 keV was confirmed as the cyclotron resonance scattering feature of the pulsar. At this energy, the surface magnetic field of the pulsar was estimated to be 3.8×10^{12} G. This is possibly the 20th accretion powered X-ray pulsar in which the cyclotron feature

has been detected. Apart from the detection of the cyclotron features, a weak iron fluorescence emission line at 6.4 keV was also detected in the spectrum.

- The detection of quasi-periodic oscillation (QPO) features and measurement of the QPO frequency allow estimation of the inner radius of the accretion disk at which the QPOs are generally believed to originate. The accretion powered pulsars generally show QPOs over a narrow range of frequency, from about 20 mHz to 200 mHz, with some exceptions. A variable QPO at ~ 41 mHz was detected in the transient high-mass Be/X-ray binary pulsar 4U 0115+634 at several epochs during outbursts in 1999 March-April, 2004 September-October and 2008 March-April. The frequency of the newly detected QPO was found to vary in 27-46 mHz range. The ~ 41 mHz QPO and its first harmonic were detected for the first time in this pulsar. There are three epochs where multiple QPOs, rarely seen in X-ray pulsars, were also detected in the power-density spectrum of 4U 0115+634.

Solar Physics

- A study of the flare associated changes seen in the solar active region NOAA 11719 during an M-class flare revealed that a dark filament was the progenitor of an ensuing CME.
- By employing nearly simultaneous observations from HMI and AIA instrument onboard SDO spacecraft and the H-alpha observations from the ground based network of solar telescopes, GONG, it was found that the power spectrum of the photospheric velocity oscillations show significant flare-induced enhancement in a localized region located far away from the sites of the flare-ribbons.
- The arrival time estimation of CMEs using remote sensing observations from Heliospheric Imagers, was shown to be more accurate than the estimation based solely on observations near the Sun.
- Tracking the CMEs continuously in the heliosphere, strong evidence of interaction and collision was found between CMEs of February 14 and 15 around 8 R_s and 28 R_s , respectively while CME of February 14 caught the CME of February 13 between 138-187 R_s .
- The existence of a particular type of topological structure containing the null point of the 3D magnetic field of AR11166 was pin-pointed as the cause of an X1.5 flare.
- Evolution of net current in the solar active region NOAA 11158 was seen to be correlated with the length of strongly sheared PIL and could possibly explain the evolution of activity in the active region.
- Contraction and disruption of coronal magnetic fields during the failed eruption of a filament and associated M6.2 flare provide evidence for the breakout model of solar eruptions as the triggering mechanism for the onset of fast rise of the filament.
- The formation of magnetic islands through magnetic reconnection was numerically demonstrated using the Implicit Large Eddy simulation (ILES) mode of the EULAG-MHD code, which is a magnetohydrodynamic extension of the standard EULAG code.
- It was demonstrated numerically that current sheets form because of contortion of the flux surfaces in such a way as to bring portions of the same flux surface having oppositely directed field lines close to each other and thereby increasing the gradient of magnetic field.
- Development of a narrow band imager as one of the back-end instruments for the newly installed Multi Application Solar Telescope was completed.

Planetary Sciences and PLANEX Program

- A large meteorite shower occurred in Katol, Nagpur district, Maharashtra on 22nd May, 2012. Mineral chemistry, petrography and oxygen isotopic composition suggests Katol meteorite to be a highly equilibrated L6-7 and shocked ordinary chondrite. A unique feature of Katol is the occurrence of an unusually large nodule that mostly comprised of immiscible troilite-metal melt and intensely fractured silicates without any silicate-melt phase. High-pressure phases like impact-produced glass and ringwoodite are observed only in this nodule. The large pre-atmospheric size of Katol has been confirmed by cosmic ray produced radioactive (^{60}Co) and stable (noble gas) isotopes. Activity of ^{60}Co , larger in comparison to Kendrapada meteorite (pre-atmospheric radius of 50-150 cm) and clear presence of ^{36}Ar , ^{82}Kr and ^{128}Xe produced by (n,γ) reactions on ^{35}Cl , ^{81}Br and ^{127}I , produced inside large meteoroids, indicates that the pre-atmospheric radius of Katol is ≥ 100 cm.
- Sutter's Mill is a CM carbonaceous chondrite breccia which fell in April 2012. Nitrogen and noble gases have been studied to determine cosmic ray exposure age and to decipher the trapped gas components of local and interstellar origin. He and Ne are dominated by trapped components whereas no clear signal of cosmogenic ^3He is apparent. $^{21}\text{Ne}_c$ determinations suggests an exposure age of $\sim 5,500$ years. This extremely young exposure age suggests that the object broke only after reaching the inner solar system. Xe isotopes from interstellar diamonds and SiC are clearly seen in the chemically separated acid resistant residue.
- A comparative assessment of the mineralogy of young basalts (~ 1.2 Ga to ~ 2.8 Ga) from the western nearside, Moscoviense basin, and the Orientale basin of the Moon has been made using Level 2 Moon Mineralogy Mapper (M^3) data from the Chandrayaan-1 mission. Most of the young basalts of Oceanus Procellarum are characterized by abundant olivines suggesting a complex volcanic history, whereas Fe-rich glasses and clinopyroxenes are observed in the Moscoviense unit. Orientale basin basalts are typically devoid of olivine, and are rich in high-Ca pyroxene, implying that mineralogy of Mare basalts erupting during late stage volcanism varied across the lunar surface.

- Morphologic characteristics of ice-rich landforms in the Martian mid-latitudes record evidence for significant degradation of the landscape in response to spin-axis/orbital parameter driven shifts in the Late Amazonian climate. Detailed investigations of Moreux crater have documented piedmont lobes/lobate debris aprons/linear valley fills (500-100 Ma), viscous flow features (100-5 Ma) and gullies/thermal contraction crack polygons (5-0.4 Ma) in this region. It is inferred that central peak of Moreux probably acted as the locus for accumulation of ice/snow and the diversity of glacial/periglacial features within the crater was possibly controlled by differences in the amount of accumulated ice or snow and the rate at which the terrain responded to the shifts in climate during the periods of higher obliquity.
- The Moon Electrostatic Potential and Dust Analyzer (MESDA) and Chandra's Surface Thermal Experiment (CHaSTE) have been proposed and shortlisted for Chandrayaan-2 lander, scheduled for launch in early 2017. CHaSTE, being developed in collaboration with Space Physics Laboratory, aims at determination of the thermal conductivity and thermal diffusivity of the upper 10 cm of lunar regolith at the landing site. The MESDA payload includes a Lunar Surface Potential Detector (LSPD) and Lunar Dust Detector (LDD) for measurement of lunar electrostatic surface potential at ~50 mm from the lunar surface, and detection of charged dust particles at a similar altitude using an Inter Digitated Transducer (IDT) dust sensor, for the first time. Laboratory prototypes have been developed for both CHaSTE and LSPD payloads.

Space, Atmospheric, Molecular and Laser Physics

- It has been demonstrated that black carbon, and dust mixed with black carbon dominate the absorbing aerosol abundance over the Indo-Gangetic Plain. This characterization of the type of absorbing aerosols over a region is important as the absorbing aerosols strongly influence Earth-atmosphere radiation balance.
- Experimental evidence has been obtained for setting up of a meridional circulation cell in winds from high to low latitudes during stratospheric sudden warming (SSW) events. This result has been enabled by multi-wavelength dayglow measurements from Hyderabad, which consistently showed an enhancement in the oxygen emission intensities specifically during the SSW events of the past four years. This intensity enhancement has been interpreted to be due to the transport of atomic oxygen from high latitudes. Independent satellite-based observations of winds and temperatures over high-latitudes do support this proposition.
- Investigations on the ionospheric layer movement over the magnetic equator during midnights of solar minimum has been found to be associated with semi-diurnal tidal influence in reversing the polarity of the electric field to eastwards which is otherwise westwards during magnetically quiet times.

Geosciences Division

- A new data set of high resolution oxygen isotope variations in a stalagmite from the Belum cave, Andhra Pradesh was generated. This has provided evidence for abrupt changes in monsoon intensity during the least glacial transition, which was earlier known only during the Holocene transition from marine records.
- We continued measurements of the isotopic composition of water vapour over the Bay of Bengal for another season (winter). This reconfirms our earlier finding that it is controlled by atmospheric temperature rather than sea surface temperature. The amount effect in Kerala rainfall has been found to be mainly caused by large scale convective activity rather than by Rayleigh isotopic distillation.
- Molybdenum isotope studies in the northern Bay of Bengal water column display significant source of lighter Mo. Sub-oxic condition prevailing in the water column of the shelf region of the northern Bay of Bengal dissolves Fe-Mn oxy-hydroxide coating resulting in supply of lighter $\delta^{98}\text{Mo}$ to the water column. This study suggests that shelf region could be a major contributor and represents the missing source of lighter Mo in global ocean.
- Chemical extraction and measurement of Si isotope in the seawater were established. Results on Si isotopes in the Bay of Bengal display large fractionation due to utilization of lighter isotopes by diatoms in photic zone and further its demineralization at deeper depth. The fractionation of Si isotope in water column of the Bay of Bengal is explained by steady state model.
- As part of the IWIN National Programme, two major research issues have been investigated using stable oxygen and hydrogen isotopic characteristics of water. These are: (1) surface water dynamics of the Arabian Sea and (2) Groundwater recharge characteristics in Gujarat.

Theoretical and Computational Physics

- Accurate calculation of the electric dipole moment of ^{129}Xe due to parity and time reversal violation has been reported which in combination with its experimental result, when it becomes available, could yield the best limits for many fundamental parameters that are predicted by the leptoquark and supersymmetric models.
- Generation and decay of topological defects, vortex-antivortex pairs, in superfluid flow with thermal fluctuations were studied. The studies were carried out using stochastic Gross-Pitaevskii equations.
- We have studied the synergistic aspects of the long baseline accelerator experiments T2K and NOVA and the atmospheric neutrino experiment as is being pursued by the India-Based Neutrino Observatory (INO). We have shown that INO can play a significant role in discovering CP violation for certain parameter values. We also studied the synergistic effects between

the future long baseline neutrino project LBNO in Europe and INO.

- Considering various baselines for LBNO, we showed that inclusion of information from INO would help LBNO to reach the same sensitivity with a lower exposure thereby reducing its cost of operation.
- We studied the implications for neutrinoless double beta decay in the context of the results from GERDA, KAMLAND-ZEN and EXO experiments and the recent PLANCK results on sum of neutrino masses. In particular we showed that notwithstanding the uncertainties from Nuclear matrix elements the recent results on neutrinoless double beta decay strongly disfavour the earlier positive claim on observance of this rare process. The saturation of the present bounds require neutrinos to be quasi-degenerate which is strongly disfavoured by the Planck data. We showed that if one considers TeV scale Left-Right symmetric models then the saturation of present bounds on neutrino less double beta decay half-life can be achieved even for hierarchical neutrinos. These considerations enable one to put a model dependent lower limit on absolute neutrino mass.
- Recent discovery of 125 GeV SM like Higgs boson with no hints of new physics yet at the LHC throws a critical challenge to most beyond standard models. Stability of EW vacuum taking input from Higgs, Top masses as well as strong coupling constant can throw light on scale of new physics and also can constrain its parameters.
- Models based on seesaw mechanism provide an widely accepted explanation for a small but non-zero neutrino mass which unambiguously established in the experiments however absent in the standard model. TeV scale neutrino mass models are testable at high energy collider like Large Hadron Collider (LHC). Parameters can be constrained indirectly by studying different signals supported by the model.
- It is well known that mean-field theories fail to reproduce the experimentally known critical exponents. The traditional argument which explain this failure of mean-field theories near a critical point is the Ginzburg criterion. We argue, contrary to the above mentioned traditional view, that diverging fluctuations in real physical systems near a critical point are genuine consequence of the breakdown of the property of statistical independence, and are faithfully reproduced by the mean-field theory. To address the question of why mean-field theories fail to reproduce the known values of critical indices we argue, using the essential ideas of the Wilsonian re-normalization group, that mean-field theories fail to capture the long length scale averages of an order parameter near a critical point.
- We report the results of a theoretical investigation on charge dynamics in cuprates using the phenomenological theory of Yang, Rice, and Zhang (YRZ). We find that YRZ model only qualitatively explain the experiments. The quantitative discrepancy in magnitudes of the conductivity is attributed to the neglected electron-Boson scattering.

Awards and honours

Faculty Members

U. R. Rao

1. D.Sc. (Hon. Causa) from Bangalore University.
2. D.Sc. (Hon. Causa) Indian Institute of Technology-Bhubaneswar.

J. N. Goswami

3. Chairman, Commission-1 (Space Sciences), International Academy of Astronautics.
4. Laurel for Team Achievement Award (Chandrayaan-1 mission), International Academy of Astronautics.

R. Sridharan

5. Adjudged as one of the top ten reviewers in the year 2013, in *Advances in Space Research*, a peer reviewed journal of Elsevier publications.

A. K. Singhvi

6. Elected as President, Gujarat Science Academy, 2014-2016.
7. VASVIK Award-2009, Applied Sciences, Awarded in 2013.
8. Chair, Sectional Committee on Earth Sciences, Indian Academy of Sciences (IAS).
9. Member, Sectional Committee on Earth Sciences, Indian National Science Academy (INSA).

U. Sarkar

10. Awarded J. C. Bose National Fellowship, DST, Govt. of India, 2013.

R. Ramesh

11. Distinguished Guest Professor, Indian Institute of Technology, Mumbai.
12. Visiting Professor, University of Hyderabad.
13. Member, Research Advisory Council, National Geophysical Research Institute, Hyderabad.
14. Honorary Member, Science Faculty, University of Delhi.
15. Member, Board of Studies for Earth System Studies, Sardar Patel University, Vallabh Vidyanagar.
16. Member, Council, Indian National Science Academy.

V.K.B. Kota

17. Member, Editorial Board, *Journal of Nuclear Physics, Material Sciences, Radiation and Applications*, Elsevier.

M. M. Sarin

18. Awarded J. C. Bose National Fellowship, DST, Govt. of India, 2013.
19. Vice-Chairman, UN/GESAMP (United Nations Group of Experts on Scientific Aspects of Marine Environment Protection).
20. Member, Scientific Advisory Committee, Space Physics Laboratory, Thiruvananthapuram.

N.M. Ashok

21. Astronautical Society of India award for the year 2011 in the area of Space Science and Applications.

Rajmal Jain

22. Honorary Fellowship of the Royal Astronomical Society, 2014.

Hari Om Vats

23. The Indira Gandhi Prize for Popularization of Science (2014), Indian National Science Academy New Delhi.

S. A. Haider

24. Fellow, National Academy of Sciences (NASI), 2013.
25. Council Member, AOGS. Elected for the period of 2013-2014.
26. Editor, Geoscience Letters, a Springer open journal.

D. Pallamraju

27. Main Convener, "General session on the Ionosphere and Atmosphere", 10th annual Asia Oceania Geosciences Society (AOGS) Meeting, Brisbane, Australia, June, 2013.
28. Secretary, for Solar Terrestrial Section (AOGS). Elected for the period 2014-2018.
29. Guest Editor, JASTP Special Issue on CAWSES-India Phase II program.
30. Member, International Organizing Committee, of the 14th International Symposium on Equatorial Aeronomy to be held at Bahir Dar, Ethiopia during 19-23 October, 2015.

S. Ramachandran

31. Member, Editorial Board, The Scientific World Journal

Nandita Srivastava

32. Stefan Hepites award of the Romanian Academy for group work on "Genesis and evolution of coronal mass ejections".
33. Guest investigator on ESA's Proba2 solar mission, June-July 2013.
34. Member, scientific organising committee, IAU symposium 300, on "Nature of prominences and their role in Space weather", Paris, June 10-15, 2013.
35. Chaired the session 2.1 at the IAU Symposium 300, on "Nature of prominences and their role in Space weather", Paris, June 10-15, 2013.

36. Member, scientific organising committee, International Study for Earth-Affecting Solar Transients (ISEST) program of SCOSTEP, June 16-20, 2013, Hvar, Croatia.

Sunil Kumar Singh

37. National Geoscience Award-2012, Ministry of Mines, Government of India, in recognition of his significant contribution in the field of Petrology and Geochemistry including Mineralogy, Geochronology and Isotope Geology.

Varun Sheel

38. Main Convener, "Science and exploration of Mars and Venus", 10th annual Asia Oceania Geosciences Society (AOGS) meeting, Brisbane (Australia), June 25-28, 2013.

Kuljeet Kaur Marhas

39. SERB Women Excellence Award for three years, Science & Engineering Research Board (SERB), Department of Science & Technology, Government of India.

Navin Juyal

40. Selected member, expert committee constituted by the Ministry of Environment and Forest, Government of India, to assess the causes of the recent flood in Uttarakhand.

D. Chakrabarty

41. Chairman, Scientific session ST27 (General session on the Ionosphere and Atmosphere) on June 26, 2013 in AOGS, Brisbane, Australia.

Smitha Thampi

42. SERB Women Excellence Award for three years, Science & Engineering Research Board (SERB), Department of Science & Technology, Government of India.

Navinder Singh

43. Member, National Advisory Committee, "Nonequilibrium Complex Systems", February 7-8, 2014, Guwahati.
44. Member, National Advisory Committee, "National Symposium on Mind, Matter and Mathematics - A Dialogue", 2014 at Tehri, Uttarakhand, March 12-14, 2014.

Sanjeev Kumar

45. Member, Primary production working group for Indian Ocean, NERC, India.

L. K. Sahu

46. Member, International Global Atmospheric Chemistry (IGAC)-India Working Group Committee.

Students and Post Doctoral Fellows**Mala Bagiya**

47. URSI young scientist award, 2014.

Vemareddy Panditi

48. American Astronomical Society (AAS)-Solar Physics Division (SPD) Zirin Studentship Award, 2013.

S. Vijayan

49. 2nd prize, Oral Presentation, National Space Science Symposium, Dibrugarh, January 29 - February 1, 2014.

Upendra Kushwaha

50. Best Poster Presentation Award, 28th National Symposium on Plasma Science & Technology, Bhubaneswar, December 3-6, 2013.

Dinesh Kumar

51. Poster Presentation Award, 28th National Symposium on Plasma Science & Technology, Bhubaneswar, December 3-6, 2013.

Shraddha Band

52. 1st Prize in oral presentation, ISMAS Symposium cum Workshop on Mass Spectrometry, Himachal Pradesh, March 9-12, 2014.

Bhavya P. S.

53. 2nd Prize, oral presentation in the ISMAS Symposium cum Workshop on Mass Spectrometry, Himachal Pradesh, March 9-12, 2014.

Midhun M.

54. Conducted Climate change quiz, Training Programme on Climate Science, Divecha Centre for Climate Change, IISc, Benngluru, January 20-31, 2014.

S. G. Reddy

55. Best poster award, Workshop on Recent Advances in Photonics, IIT Delhi, December 17-18, 2013.

A. Aadhi

56. Excellent student paper presentation award, International Conference on Optics & Optoelectronics, Instruments Research & Development Establishment, Dehradun, March 5-8, 2014.

P. Chithrabhanu

57. Best poster award, International Conference on Optics & Optoelectronics, Instruments Research & Development Establishment, Dehradun, March 5-8, 2014.

Indhu Varatharajan

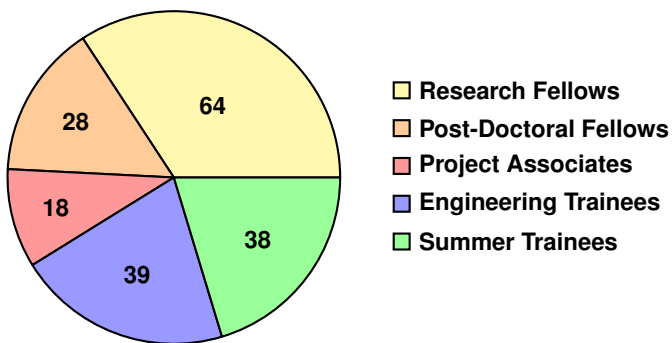
58. 1st prize, Poster presentation, National Space Science Symposium, Dibrugarh, January 29 - February 01, 2014.

Administration

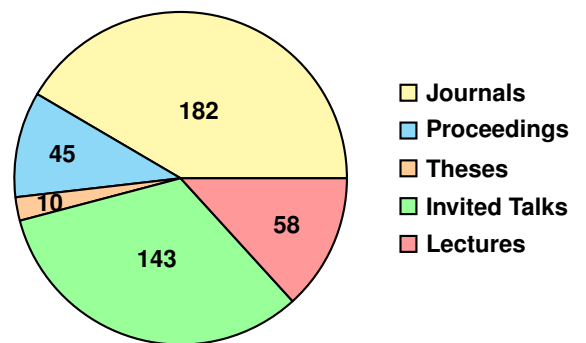
59. PRL has received Second Prize, conferred by Town Official Language Committee (TOLIC), Ahmedabad for excellent contribution towards implementation of Official Language Policy during 2012-2013. A certificate of appreciation has also been given to Shri R. S. Gupta, Hindi Officer-II & OSD.

Human Resource Development

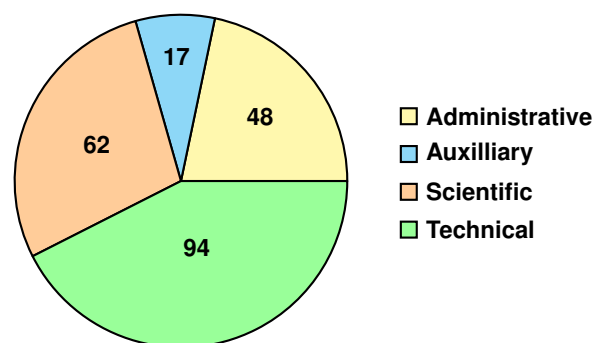
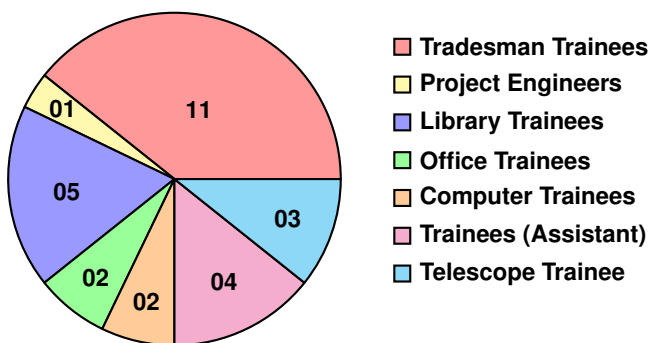
Research & Internship Programmes



Scientific Contributions



Administrative and Auxillary staff structure



Theses Submitted

Vemareddy Panditi

1. "A Study on the Characteristics of Magnetic Field Structure and Evolution of Flaring Solar Active Regions", Mohanlal Sukhadia University, Udaipur, April, 2013.

Siddhartha Chattopadhyay

2. "Quantum Electrodynamical Corrections in Atoms from Coupled Cluster Theory", Mohanlal Sukhadia University, Udaipur, August, 2013.

Susanta Kumar Bisoi

3. "Solar and Solar Wind Studies Using Ground and Space Based Observations, Mohanlal Sukhadia University, Udaipur, October 2013.

Sunil Chandra

4. "Multi-wavelength study of variability in Blazars", Mohanlal Sukhadia University, Udaipur, October 2013.

Arvind Kumar Saxena

5. "Study of Cluster Ions by Mass Spectrometry and Optical Spectroscopy", Mohanlal Sukhadia University, Udaipur, October, 2013.

A. K. Tyagi

6. "Luminescence dating of past seismic and tectonic events: methodological aspects and applications", Gujarat University, Ahmedabad, November, 2013.

Jayati Chatterjee

7. "Isotopic and Geochemical Studies of Saline-Alkaline soils, Water and Sediments of the Ganga river system: Implications to Erosion and Carbon cycle", Mohanlal Sukhadia University, Udaipur, November, 2013.

Arun Kumar Awasthi

8. "Energy Release Processes in Solar Flares", Mohanlal Sukhadia University, Udaipur, December, 2013.

Chinmay Mallik

9. "Atmospheric Trace Gases: Transport and Emission Effects", Mohanlal Sukhadia University, Udaipur, December, 2013.

Koushik Saha

10. "Kinematical Analysis of Ionization and Fragmentation of Molecules", Mohanlal Sukhadia University, Udaipur, December, 2013.

Colloquia/Public Lectures by Visitors

Prof. Mrinal K Sen

CSIR-National Geophysical Research Institute,Hyderabad,India
Uncertainty Quantification in Geophysics

Prof. Jos Lelieveld

Max Planck Institute for Chemistry,Mainz,Germany
The self-cleansing mechanism of the atmosphere

Prof. B.N.Goswami

Indian Institute of Tropical Meteorology,Pune,India
Scalling the Potential Predictability Barrier of the Indian Summer Monsoon Rainfall: An Indian Initiative

Prof. Surendra Singh

University of Arkansas,USA
Floating Frogs and Levitating Lattos

Prof.Girish S. Agarwal

Department of Physics Oklahoma State University,USA
From Quantum Interference to Entanglement

Prof. Dhiraj Bora

Institute for Plasma Research, Gandhinagar
ITER-A Burning Plasma Experiment

Prof. Ram Sagar

Aryabhata Research Institute of Observational Sciences (ARIES), Nainital
Upcoming 4 - meter class optical telescopes at Devasthal Observatory

Prof. Prasanta K.Panigrahi

Indian Institute of Science Education and Research, Kolkata
Viewing Nature Through Wavelet

Dr.Govindaswamy Bala

Center for Atmospheric and Oceanic Sciences Indian Institute of Science,Bangalore
Challenges in Modeling the Global Climate System

Prof. Tapan Nayak

Variable Energy Cyclotron Center, Kolkata
Big Bang to Little Bang-Exploring the Quark-Gluon Plasma at RHIC and LHC

Prof. D. K. Srivastava

Variable Energy Cyclotron Centre, Kolkata
Exploring Quark gluon Plasma with Photons Jets, and heavy quarks

Prof. S. Ananthkrishnan

Dept. of Electronic Science, University of Pune, Pune
Declining solar magnetic fields: Are we heading towards a Maunder minimum?

Prof. Nigel J Mason

The Open University, Milton Keynes, UK
Astrobiology - The Cradle of Life

Prof. E.Arunan

Department of Inorganic and physical Chemistry ,Indian Institute of Science , Bangalore
Molecular Beam Microwave Spectroscopy : Applications in Radio astronomy and Intermolecular Bonding

Prof. K. Asahi

Senior Professor,Department of Physics, Tokyo Institute of Technology
Spin masing and looking for an atomic EDM of nuclear origin

Prof. Ashwin Gumaste

Department of Computer Science and Engineering, Indian Institute of Technology, Bombay

Omnipresent Ethernet: From Concepts to Products - Secure Communications, Networking and Control Framework

Dr. G. Pandithurai

Indian Institute of Tropical Meteorology, Pune

Aerosol-cloud interactions: the uncertain component of climate system

Dr. Y. Sakemi

Nuclear Radiation Physics Group, Department of Physics, Cyclotron and Radioisotope Center, Tohoku University, Japan

Fundamental physics using laser cooled radioactive atoms

Dr. Adam Falkowski

Laboratoire de Physique Theorique in Orsay, France

Higgs after LHC run 1

Prof. Jocelyn Bell Burnell

University of Oxford, Oxford, UK

Reflections on the Discovery of Pulsars

Dr. Sudhir Vempati

Centre for High Energy Physics, IISC, Bangalore

The Top with spin Zero

Dr. Girish S. Setlur

Associate Professor, Department of Physics, IIT Guwahati

Rabi Oscillations in Graphene

Conferences/Symposia/Workshops by PRL

1. "Workshop on Mars Orbiter Mission", PRL, July 26-27, 2013.
2. "ISROs STP Course on Planetary Exploration", PRL, December 11-14, 2013.
3. 14th PLANEX Workshop on "Instrumentation for Planetary Exploration", DD University, Nadiad, January 6-10, 2014.
4. "Workshop on Regional Atmospheric Chemistry: Emerging Trends", PRL, May 6-7, 2013.
5. "From Mantle to the Moon", A scientific meet in Remembrance of Prof. D. Lal, PRL, February 14-15, 2014.

Invited Talks at Conference / Symposia / Workshops

Astronomy and Astrophysics

K.S. Baliyan

1. "Monitoring of Blazars for variability studies from Mt Abu InfraRed Observatory(MIRO)", International Conference on Black holes, Jets, and outflows, Kathmandu, Nepal, October 14-19, 2013.
2. "Long -Term study of blazars for Variability: some interesting results", National Symposium on Gamma-Ray Astronomy, BARC- Mumbai, November 25-27, 2013.
3. "Intra-Night variability in Blazars", National Space Science Symposium, Dibrugarh, January 28- February 1, 2014.

S. Naik

4. "X-ray and IR/Optical Studies of Be/X-ray Binary Pulsars", Lead talk in National Space Science Symposium, Dibrugarh University, Dibrugarh, Assam, January 28-February 01, 2014.
5. "Be/X-ray Binary Pulsars: Multi-wavelength Observations", Transients with ASTROSAT, IUCAA, Pune, January 17, 2014.
6. "X-ray Binaries", Workshop on Analysing Astronomical Data, IUCAA Resource Center, North Bengal University & Calcutta University, December 16-17, 2013.

7. "Detection of Cyclotron Resonance Scattering Feature in 4U 1909+07", 32nd meeting of the Astronomical Society of India (ASI), IISER, Mohali, March 20-22, 2014.

T. Chandrasekhar

8. "Minor bodies of the Solar System", 14th PLANEX Workshop on Instrumentation for Planetary Exploration, DDU University, Nadiad, January 6-10, 2014.

S. Vadawale

9. "Hard X-ray polarimetry with Astrosat-CZTI", MIT-IUCAA Workshop, IUCAA, Pune, January 17, 2014.
10. "Prospects of Hard X-ray polarimetry with Astrosat-CZTI", contributed talk in IEEE Nuclear Science Symposium, Seoul, S. Korea, October 31, 2013.

A. K. Singal

11. "Solar System-An Overview", Planex 14 Workshop, January 6, 2014.
12. "Fanaroff Riley Dichotomy & Malmquist Bias", NSSS, January, 30 2014.

Tanmoy Chattopadhyay

13. "Measuring hard X-ray polarization with Astrosat-CZTI" Conference on 'Accretion onto Black Holes', Goa, September 5-7, 2013.

Anjali Rao

14. "Study of the inner disk radius during early phase of a black hole binary outburst", Conference on 'Accretion onto Black Holes', Goa, September 5-7, 2013.

Solar Physics**A. Ambastha**

15. "Magnetic and velocity field evolution in solar active regions and their role in explosive transients", lead talk on 18th National Space Science Symposium, Dibrugarh, January 29-February 1, 2014.
16. "Solar Physics at USO - A Travelogue", Meeting held at PRL in the memory of Prof. D. Lal, February 14-15, 2014.

Nandita Srivastava

17. "On the role of solar filament plasma remnants in ICMEs leading to geomagnetic storms", 2nd Asia Pacific Solar Physics Meeting, Hangzhou, China, October 22-26, 2013.
18. "Estimating arrival time of Earth-directed CMEs at in-situ spacecraft using COR and HI observations from STEREO", ISEST workshop, Hvar, Croatia June 17-20, 2013.
19. "Kinematics and consequences of coronal mass ejections", Brain Storming Session on Indian Space Science Initiatives, Institute of Radio Physics and Electronics, University of Calcutta, February 12-13, 2014.

Vemareddy Panditi

20. "Helicity Injections by Flux Motions and Its Role in Flares and CMEs", Oral Presentation, SPD meeting, Bozeman, Montana, USA, July 10, 2013.

Planetary Sciences and PLANEX Program**J. N. Goswami**

21. "Planetary Sciences in India: Contribution of Devendra Lal", Devendra Lal Memorial Symposium, La Jolla, California, May 06, 2013.
22. "Indias Mission to Mars", Exchanges at the Frontier (BBC Program), Physical Research Laboratory, October 30, 2013.

23. "Lunar Exploration: Past, Present and Future", Annual meeting of the National Academy of Sciences, Goa, December 05, 2013.

24. "The first ten million years of the Solar System", Inaugural Talk, National Space Science Symposium, Dibrugarh, January 29, 2014.

25. "Chandrayaan-1", Laurel for Team Achievement Award Lecture, International Astronautical Academy, Beijing, September 22, 2013.

26. "Solar System Studies and Planetary Exploration", Tata Institute of Fundamental Research, Mumbai, February 27, 2014.

M. Shanmugam

27. "Indian Moon and Mars mission payloads", in one day seminar on Highlights of Indian Planetary Exploration Programme", DDU, Nadiad, August 10, 2013.

D. Banerjee

28. "Nuclear Instruments for surface/subsurface studies", 14th PLANEX Workshop on Instrumentation for planetary exploration, DDU, Nadiad, January 6-10, 2014.

29. "Planetary Gamma ray spectroscopy", STP Course Planetary Exploration, PRL, Ahmedabad, December 11-14, 2013.

S.V.S. Murty

30. "Mars atmospheric evolution as revealed from martian meteorites", Workshop on Infrared spectroscopy of planetary atmospheres, ISAC, Bangalore, May 8-10, 2013.

31. "Mars orbiter mission science objectives", Workshop on MOM, PRL, Ahmedabad, July 26-27, 2013.

32. "Study of astromaterials to understand formation and evolution of Solar System", IPDEB-2013, S.P. University, Vallabh Vidyanagar, November 15-17, 2013.

33. "Scientific aspects of exploration of Mars", ISG-ISRS-Symposium, Andhra University, Visakhapatnam, December 2-3, 2013.

34. "Earth, Moon and Mars", STP Course Planetary Exploration, PRL, Ahmedabad, December 11-14, 2013.

35. "Science objectives of Mars orbiter mission", International Conference on Microwaves, Antenna, Propagation and Remote Sensing, ICRS, Jodhpur, December 11-14, 2013.

36. "Terrestrial Planets", 14th PLANEX Workshop on Instrumentation for planetary exploration, DDU, Nadiad, January 6-10, 2014.

37. "Trapped noble gas components in meteorites", 18th National Space Science Symposium, Dibrugarh, Assam, January 29-February 1, 2014.

K. K. Marhas

38. "Meteorites, Asteroids and Comets" Structured Training Program (STP) for ISRO Scientists/Engineers, PRL, Ahmedabad, December 11-14, 2013.

Shiv Mohan

39. "Microwave remote sensing of Lunar Surface", Pre-Symposium Tutorials, Andhra University, Visakhapatnam, December 2-3, 2013.
40. "Microwave remote sensing applications", Structural training programme of ISRO, PRL, Ahmedabad, December 13, 2013.
41. "Microwave remote sensing and its applications in planetary studies", 14th PLANEX workshop on Instrumentation for Planetary Exploration" DDU, Nadiad, Gujarat, January 6-10, 2014.

Jayesh P. Pabari

42. "Wireless Sensor and Its Applications", Workshop on Sensors and Its Applications in Engineering Fields, Venus International College of Technology, Kalol, April 26, 2013.
43. "Application of Wireless Sensor Network for Planetary Surface Science", STTP on DSP and Its Application, Parul Institute of Engineering and Technology, Waghodia, December 17, 2013.

K. Durga Prasad

44. "Wireless Sensor Networks for inaccessible terrain studies", 14th PLANEX Workshop on Instrumentation for Planetary Exploration", Nadiad, January 6-10, 2014.

Amit Basu Sarbadhikari

45. "Martian Surface Chemistry and Effects on Atmospheric Spectra", Workshop on Infrared Spectroscopy of Planetary Atmospheres (ISPA); Space Science Instrumentation Facility (SSIF), ISRO Satellite Centre, ISITE Campus, Bangalore; May 8-10, 2013.

Space, Atmospheric , Molecular and Laser Physics**B. Sivaraman**

46. "Radiation Induced Chemistry on Icy Satellite Surfaces Embedded in Magnetospheric Plasma Environment: A New Experimental Facility at PRL", Topical Conference 2013 of Indian Society for Atomic and Molecular Physics, IPR Gandhinagar, 18-20 November 2013 and at "Low Energy Ion Scattering conference" held at IIT Madras, January 18-19, 2014.
47. "Icy Materials", International Conference on Materials and Characterization Technique, VIT, Vellore, March 10-12, 2014.

D. Chakrabarty

48. "Planetary Atmospheric studies", 14th PLANEX Workshop, DDU, Nadiad, January 6-10, 2014.
49. "Significant and complex electric field perturbations in the low latitude ionosphere-thermosphere system during space weather events", session ST01 in AOGS, Brisbane, Australia, June 24-28, 2013.

D. Pallamraju

50. "Investigations of Magnetosphere-Ionosphere Coupling", Brainstorming Workshop on Middle Atmosphere-Thermosphere-Ionosphere coupling processes SRM University, Chennai, April 26-27, 2013.
51. "Sun-Earth interactions", DST-INSPIRE Program, KWC- Sangli, Maharashtra, India, August 01-05, 2013.
52. "Daytime wave characteristics in the lower thermosphere as obtained from the Balloon-borne investigation of Regional Atmospheric Dynamics (BIRD) experiment", 18th National Space Science Symposium, Dibrugarh, India, January 29-February 1, 2014.
53. "Waves in the mesosphere lower thermosphere region", Indian Space Science Initiatives, University of Calcutta, February 12-13, 2014.
54. "Coupling and Dynamics of Atmospheric regions", From Mantle to Moon, A Scientific Meet in Remembrance of Prof. D. Lal, Physical Research Laboratory, Ahmedabad, February 14-15, 2014.

K. P. Subramanian

55. "Significance of Stark Broadening Data in LIBS Analysis", VAMDC Meeting, Ahmedabad, November 21-22, 2013.

R. Sekar

56. "Future direction in the investigation of thermosphere-ionosphere system" in DST brainstorming workshop held at SRM University, Chennai, April 26-27, 2013.

R. Sridharan

57. "The Enchanting Aeronomy", PRL Alumni meet, October 30, 2013.
58. "Remote sensing of Water in Planetary bodies", 14th PLANEX workshop, DD University, Nadiad, December 10, 2013.
59. "Enchanting Aeronomy: Perspectives", delivered the first 'Ravipati Raghavarao memorial Lecture', organized under the aegis of the Hyderabad chapter of INSA, NRSC, Hyderabad, February 28, 2014.

R. P. Singh

60. "Orbital angular momentum of light: Applications in quantum information", International Program on Quantum Information, Institute of Physics, Bhubaneswar, February 17-28, 2014.
61. "Optical vortices through a ground glass plate", International Conference on Optics & Optoelectronics, Instruments Research & Development Establishment, Dehradun, March 5-8, 2014.

S. A. Haider

62. "Response of solar X-ray flares in the ionosphere of Mars", 10th Asia Oceanic Geosciences Society (AOGS) meeting, Brisbane, Australia, June 24-28, 2013.
63. "Meteoroid ablation in the Martian atmosphere: Observation and modeling", 79th Annual Meeting of Academy of Sciences, Bangalore held at Chandigarh during November 8-10, 2013.

S. Lal

64. "Perspectives in atmospheric science and climate change", DST-PURSE sponsored national conference on 'Interdisciplinary Perspectives; Defence studies, Earth System Science and Bio- Medical Science', S. P. University, V. V. Nagar, November 16, 2013.
65. "Geosphere, Biosphere and Atmosphere Interactions: Impact on atmospheric chemistry and climate", NASI Annual session and symposium on 'Space for human welfare' Goa, December 5-7, 2013.
66. "Regional atmospheric chemistry: Future perspectives", Workshop on 'Regional Atmospheric Chemistry: Emerging trends', PRL, Ahmedabad, May 6-7, 2013.
67. "Climate Change: Blowing cold and hot", Refresher course for teachers, S. P. University, V. V. Nagar, January 27, 2014.

S. K. Sharma

68. "Middle Atmospheric Temperature Trends and its association with Ozone", National Space Science Symposium, Dibrugarh, January 29-February 1, 2014.
69. "Study of Total Column Ozone, Water Vapor and AOT over Western Sites of India", International Conference on Tropical Meteorology (INTROMET-2014), SRM University, Chennai, February 21-24, 2014.

S. Ramachandran

70. "Aerosol mixing : Optical and radiative properties", Brainstorming meeting on Atmospheric Chemistry, Ministry of Earth Sciences, New Delhi, April 5, 2013.

71. "Aerosol mixing: Radiative forcing", Workshop on 'Regional Atmospheric Chemistry: Emerging Trends', Physical Research Laboratory, May 6-7, 2013.
72. "Global Warming, Ozone and Aerosols", Seminar on 'Excitements of Research in Basic Sciences', St. Xavier's College, September 19, 2013.
73. "Single particle chemical composition of aerosols", International Discussion Meeting on Low Energy Ion Scattering at Molecular Solids, IIT Madras, Chennai, January 18-19, 2014.
74. "Aerosol Radiative Forcing: Mixing", National Space Science Symposium, Dibrugarh University, Dibrugarh, January 29 - February 1, 2014.
75. "Aerosol Radiative Forcing: Chemical Composition", 6th Review meeting of the Atmospheric Trace Gases - Chemistry, Transport and Modeling (AT-CTM) Project of ISRO GBP, GBPIHED, Mohal, Kullu, March 3-4, 2014.
76. "Aerosol Radiative Forcing and Climate", 1st Climate Science and Policy Workshop, Indian Institute of Technology, Mumbai, March 6 -7, 2014.

V. Sheel

77. "Ion Attachment on Surface of Martian Dust: Effect on Ionosphere", International Discussion Meeting on Low Energy Ion Scattering at Molecular Solids, IIT Chennai, January 18-19, 2014.
78. "Variability of trace gases over Asia: A modeling perspective", ISRO AT-CTM Meeting, G.B. Pant Institute of Himalayan Environment and Development, Kullu, March 3-4, 2014.

Geosciences**A. K. Singhvi**

79. "Relevance of geo-sciences in planning the societal future", Public Lecture at Indian National Science Academy, New Delhi, October 17, 2013.
80. "Some thoughts on Risk from Monsoon floods and consequent vulnerability of societies", Invited talk, Workshop on Flood Risk in Monsoon Asia, National University of Singapore, September 20-25, 2013.
81. "PRL contribution to the Methodology and applications of Luminescence Dating", From Mantle to the moon, A Scientific Meet in Remembrance of Prof. D. Lal, Physical Research Laboratory, Ahmedabad, February 14-15, 2014.

R. Ramesh

82. "¹⁵N study of the Global Nitrogen Cycle", Divecha Centre for Climate Change, Indian Institute of Science, Bengaluru, May 2, 2013.
83. "Climate reconstructions using multiple proxies", International Scoping Workshop of the Belmont Forum, Goa, October 24, 2013.

84. "Dead carbon fraction and mineralogy of speleothems", conference on Earth, Ocean and Atmosphere, IGNA, NGRI, Hyderabad, November 7-8, 2013.
85. "Nitrogen budget in the Indian Ocean: ^{15}N tracer experiments", AP Science Congress, University of Hyderabad, November 14, 2013.
86. "Importance of marine nitrogen cycling", DST-PURSE Sponsored National Conference on Interdisciplinary Perspectives: Defence Studies, Earth System Science and Bio-medical Science (IPDEB - 2013), CISST, S. P. University, V. V. Nagar, November 17, 2013.
87. "Marine dinitrogen fixation in the Arabian Sea", Thermo-Scientific Inorganic Mass Spectrometry User Meet, Goa, November 21, 2013.
88. "Nitrogen cycling in the Indian Ocean", Golden Jubilee Convention of Indian Chemical Society (ICS), Punjab University, Chandigarh, December 7, 2013.
89. "Climate change and marine ecology" key-note lecture in the National Seminar on Climate Change in the Indian Context, M. S. University of Baroda, Vadodara, December 14, 2013.
90. "Paleomonsoon research at PRL", From Mantle to the moon, A Scientific Meet in Remembrance of Prof. D. Lal, Physical Research Laboratory, Ahmedabad, February 14-15, 2014.
91. "Speloclimatology" International Conference in Tropical Meteorology, INTROMET-13, at the SRM University, Chennai, February 24, 2014.
92. "Atmospheric nano-particles: Potential role in chemistry-climate interaction" and "Ocean Acidification: Impacts of carbon dioxide versus other anthropogenic gases", Doon University (Dehradun)-SERB (DST) School (Two lectures), August 5-6, 2013.
93. "Environmental radioactivity: From atmosphere to ocean", MS University (Vadodara)-DST INSPIRE Camp August 9, 2013.
94. "Carbonaceous aerosols from biomass burning emissions in the Indo-Gangetic Plain", IITM, Pune-CAIPEEX Meeting, August 30, 2013.
95. "Atmospheric chemistry and climate change", Workshop on 'Climate science: Recent research' MoES, New Delhi, October 4-5, 2013.
96. "Environmental radioactivity: From atmosphere to ocean", Ahmedabad University (Ahmedabad)-DST INSPIRE Camp, October 23, 2013.
97. "Mass absorption efficiency of brown and elemental carbon in the atmospheric outflow from the Indo-Gangetic Plain", American Geophysical Union Meeting (San Francisco, USA), December 9-13, 2013.
98. "Atmospheric deposition of mineral dust and anthropogenic trace elements", Coordinated Research Project Meeting, BARC, Mumbai, December 21-22, 2013.
99. "Chemical fingerprinting of atmospheric outflow to the Bay of Bengal: Impact of pollution sources", ICARB/ARFI Review Meeting, SPL (Trivandrum), January 8-9, 2014.
100. "Atmospheric chemistry and climate change: Role of nano-particles", Meeting on 'From Mantle to the Moon', A Scientific Meet in Remembrance of Prof. D. Lal, PRL, February 14-15, 2014.

Sunil K Singh

92. "Impact of the Himalayan Orogeny on the contemporary and paleo-Sedimentary Geochemical & Isotope Budgets of the Indian Ocean", NGRI, Hyderabad, May 16, 2013.
93. "Impact of particle release and dust deposition on Nd & Ba concentrations and δ_{Nd} of water column of the Northern Indian Ocean", GEOMAR, Kiel, Germany, September 26, 2013.
94. "Biogeochemistry of the Indian Ocean", Physical Research Laboratory, Ahmedabad; "From Mantle to the moon", A Scientific Meet in Remembrance of Prof. D. Lal, February 14-15, 2014.

M. M. Sarin

95. "Atmospheric chemistry: Regional perspective in a changing climate", National Programme on Atmospheric Chemistry at MoES, New Delhi, April 5, 2013.
96. "Carbonaceous aerosols from Indo-Gangetic Plain and Central Himalaya: Sources and Impact", Workshop on 'Changing chemistry in changing climate', IITM, Pune, May 1-3, 2013.
97. "Atmospheric mineral dust: Transport and chemistry over Indian Region", Workshop on 'Regional atmospheric chemistry: Emerging trends', PRL, May 6-7, 2013.

N. Rastogi

107. "Atmospheric aerosols and climate change", in Contact Programme Workshop on Earth Surface Processes held at Indian Institute of Technology, Gandhinagar, December 09-10, 2013.
108. "Aerosol characteristics over a source region of biomass burning emissions: implications to environmental pollution and climate", in national symposium on Emerging Trends in Physics for Ionizing Radiations, Aerosols and Material Science (ETPRAM-13), Punjabi University, Patiala, December 13-14, 2013.

R. D. Deshpande

109. "Isotopic characteristics of Indian water resources" Karunya University, DST sponsored short term training, Coimbatore, December 10, 2013.
110. "Isotopic characterization of Indian water resources" IOMS users meet, Goa, November 21, 2013.

111. "Groundwater and precipitation isotope fingerprinting results from IWIN Project" National Workshop on Role of Isotopes in Groundwater Management in India, NIH-IAEA-World Bank initiative, NIH, Roorkee, November 13, 2013.
112. "Application of oxygen and hydrogen isotope systematics in glaciology: Level-II training course" Indo-Swiss Capacity Building in Himalayan Glaciology, Jawaharlal Nehru University, October 31, 2013.
113. "Contributions of IWIN National Programme to hydrology in India" International Conference on Advances in Water Resources Development and Management (AWRDM-2013), Panjab University, Chandigarh, October 23, 2013.
114. "Application of oxygen and hydrogen isotope systematics in glaciology: Level-I training course" Indo-Swiss Capacity Building in Himalayan Glaciology, Jawaharlal Nehru University, April 22, 2013.

Sanjeev Kumar

115. "Nitrogen cycle: role in climate and environmental change" Contact Program on 'Earth Surface Processes' by DST, IIT Gandhi Nagar, December 9-10, 2013.

Theoretical Physics

A. R. Prasanna

116. "Enigma of Time", National Symposium on 'Mind, Matter and Mathematics', Tehri, Uttarkhand, March 12-14, 2014.

B. K.Sahoo

117. "Fundamental physics using atoms", Lets love physics symposium, Narmad South Gujarat University, Surat, September 7, 2013.
118. "Relativistic coupled-cluster method for plasma-embedded atomic systems", TC2013, IPR, Gandhinagar, November 18-20, 2013.
119. "Relativistic many-body theories of atomic systems: probing spectroscopy to fundamental physics", SPARC 2014 meeting, TIFR, Bombay, January 28-29, 2014.
120. "Theoretical study of electric dipole moment in ^{129}Xe atom", FPUA2014 meeting, Tokyo, Japan, March 14-16, 2014.

D. Angom

121. "Feshbach Resonances", 'School and Workshop on Physics of Cold Atoms', HRI, Allahabad, February 10-16, 2014. (2 lectures)
122. "Goldstone modes in segregated condensate mixtures", 'School and Workshop on Physics of Cold Atoms', HRI, Allahabad, February 10-16, 2014.

D.P. Dewangan

123. "Some important discoveries in natural sciences", DST INSPIRE Programme, Institute of Life Science, Ahmedabad University, Ahmedabad, October 23, 2013.

H. M. Mishra

124. "Kinetics of chiral transitions in quark matter", workshop on 'Phase diagram of QCD', NISER, Bhubaneswar, July 8-10, 2013.

J. Banerji

125. "Measuring the topological charge of optical vortices", Symposium on 'Non-Equilibrium Statistical Physics and Nonlinear Dynamics (NESP-NLD)', Indian Association for the Cultivation of Science (IACS), January 02-04, 2014.

S. Mohanty

126. "Neutrino depletion mechanisms in IceCube and Gamma Ray Bursts", International Workshop on Baryon and Lepton Number Violation (BLV2013), from the Cosmos to the LHC, MPIK Heidelberg, Germany, April 8-11, 2013.
127. "Higgs Boson", National Space Science Symposium, Dibrugarh University, Dibrugarh, Assam, January 29-February 1, 2014

N. Mahajan

128. "Flavour Physics and CP: Theory Overview", WHEPP XIII, Puri, Odisha, December 12-21, 2013.

N. Singh

129. "An introduction to non-equilibrium transport theories: from Bloch-Boltzmann equation to Mori-Kubo quantum master equations", National Seminar on 'Non-equilibrium Complex Systems', Handique Girls College, Guwahati, February 7-8, 2014.
130. "On the origin of the Thermodynamical arrow of Time: Reconciling Microscopic time reversibility and the macroscopic time irreversibility", National Symposium on 'Mind, Matter and Mathematics - A Dialogue-2014', Tehri, Uttarakhand, March 12-14, 2014.

R. Rangarajan

131. "Resolving the Inflationary Power Spectrum", Field Theoretic Aspects of Gravity - FTAG 2013, IIT Gandhinagar, September 5-8, 2013.
132. "Reheating of the Universe, Gravitinos and Leptogenesis", SUSY and DM, IISc, Bangalore, October 2-5, 2013.
133. "Resolving the Inflationary Power Spectrum", symposium on 'Cosmology and Particle Astrophysics (CosPA 2013)', Honolulu, Hawaii, November 12-15, 2013.
134. "Teaching and Research in Academia", research workshop, Ahmedabad University, November 30, 2013.
135. "Gravitinos, Reheating and the Matter-Antimatter Asymmetry of the Universe", symposium on 'Astro-Particle and Nuclear Physics', Jamia Millia Islamia, New Delhi, January 21-22, 2014.

S. D. Rindani

136. "Anomalous top-quark and Higgs-boson couplings", Discussion Meeting on 'Electroweak Symmetry Breaking and Flavour Physics', IIT. Guwahati, February 20-22, 2014.

S. Goswami

137. "Neutrino less double beta decay in left-right symmetric models", working group talk at BLV 13, Max Planck Institute, Heidelberg, April 8-11, 2013.
138. "Can INO discover CP violation?", plenary talk, INO Meeting, Madurai, September 13-15, 2013.
139. "Neutrino less double beta decay in left-right symmetric models", workshop from Majorana to LHC, ICTP, Trieste, October 2-5, 2013.
140. "Overview of Neutrino Physics", at SANGAM, HRI, March 24-29, 2014. (3 lectures)

V. K. B. Kota

141. "Embedded Random Matrix Ensembles with Lie Symmetries: Results from $U(N)$ Wigner-Racah algebra", International Symposium on 'Symmetries in Science XVI' held in Bregenz, Austria, July 21-26, 2013.
142. "Statistics of Quotients of Successive Spacing's in Random Matrix Theory", mini-conference on 'Annual Theory Discussion Days', Physical Research Laboratory, Ahmedabad, August 26-28, 2013.
143. "Random Matrix Measures for Quantum Many-body Chaos and Localization", 8th Conference on 'Nonlinear Systems and Dynamics (CNSD 2013)', IIT, Indore, December 11-14, 2013.

Lectures at Universities / Institutions

Astronomy and Astrophysics

A. K. Singal

1. "Is there a violation of the Copernican principle in radio sky?", IISER, Pune, March 3, 2014.
2. "In-situ particle acceleration in the lobes of radio galaxies", IUCAA, March 4, 2014.
3. "Equipartition in radio galaxies", IUCAA, March 5, 2014.

K. S. Baliyan

4. "Research in Astronomy & Astrophysics at PRL", Tribhuvan University, Kathmandu, Nepal, October 18, 2013.

S. Naik

5. "Be/X-ray Binary Pulsars", Department of Physics, North Bengal University, December 17, 2013.

T. Chandrasekhar

6. "Diversity of Occultation Phenomena in Astronomy", S.N.Bose National centre for Basic Sciences (SNBNCBS), Kolkatta, November 4, 2013.

Solar Physics

A. Ambastha

7. "A Journey through the Deep Space towards the Origin of the Universe", NIIT University, Neemrana, July 24, 2013.

Wagheesh Mishra

8. "Estimating arrival time of Earth-directed CMEs at in-situ spacecraft using COR & HI observations from STEREO", Colloquium, High Altitude Observatory, Boulder, Colorado, USA, July 11, 2013

Bhuwan Joshi

9. "Observational aspects of magnetic reconnection and energy release in solar flares", Colloquium, Seoul National University, Seoul, South Korea, September 5, 2013.
10. "HXR emission from solar flares: A perspective", School of Space Research, Kyung Hee University, Suwon, South Korea, September 10, 2013.
11. "Solar flares: observations and interpretations", Korea Astronomy and Space Science Institute (KASI), Daejeon, South Korea, September 13, 2013.

Nandita Srivastava

12. "Study of eruptive filaments using SWAP & LYRA observations", Royal Observatory of Belgium, Brussels, Belgium, August 08, 2013
13. "Multi-Application Solar Telescope (MAST) at Udaipur Solar Observatory", Yunnan National Astronomical Observatory, Kunming, China, October 29, 2013

Vemareddy Panditi

14. "On the Magnetic Field Structure and Evolution of Flare/CME Productive Solar Active Regions", Colloquium, PRL, July 31, 2013.

Planetary Sciences and PLANEX Program**Jayesh P. Pabari**

15. "Designing Transmitter and Receiver in Communication System", Parul Institute of Engineering and Technology, Waghodia, March 22, 2014.

S.V.S. Murty

16. "Mars orbiter mission", Colloquium delivered in the Institute of Plasma Research, Gandhinagar, October 21, 2013.

Space, Atmospheric, Molecular and Laser Physics**D. Pallamraju**

17. "What is Space Weather and why should we care about it?" Vigyan Bharati Institute of Technology, Ghatkesar, Hyderabad, May 10, 2013.
18. "Small and large timescale responses of the upper atmosphere using daytime optical investigations", Colloquium delivered in the Indian Institute of Geomagnetism, Navi Mumbai, December 27, 2013.

H. Chandra

19. "Lecture on Ionosphere", Dibrugarh University, April 2013. (16 Lectures)

S. K. Sharma

20. "Space & Atmospheric Sciences: An Overview", CSSTE-AP Course on SATCOM, Space Applications Center, Ahmedabad, August 7, 2013.
21. "Lidar and Radar as Atmospheric Thermometers", VBIT, Hyderabad, November 22, 2013.

22. "Earth's Atmosphere: Its Uniqueness and Importance" M. B. Patel Education Trust and College of Engineers, Kadi, Gandhinagar, February 16, 2014.
23. "Exploration and Science of the Earth's Atmosphere", Physics Department, Panjab University, Chandigarh, March 5, 2014.
24. "LIDAR: A Dynamic Atmospheric Explorer" University of Adelaide, Adelaide, Australia, January 22, 2014.

S. Ramachandran

25. "Internal Feedbacks and External Forcings of Climate System", SERB (DST) School on Science of Climate Change, Doon University, Dehradun, August 2013. (2 Lectures)
26. "Black Carbon Aerosols: Radiative and Climate Impacts", Wadia Institute of Himalayan Geology, Dehradun, August 13, 2013.
27. "Aerosol Radiative Forcing and Climate Impact: Modeling Challenges", Centre for Development of Advanced Computing, Pune, August 29, 2013.
28. "Aerosols and Biogeochemical Coupling", Indian Institute of Tropical Meteorology, Pune, August 29, 2013.
29. "Aerosols, Radiative Transfer and Climate", for M.Sc. (Inter-disciplinary Studies), Sardar Patel University, Vallabh Vidyanagar, Anand, September-October 2013. (6 Lectures)

V. Sheel

30. "Modeling Atmospheric Chemistry over Asia", National Institute of Water and Atmospheric Research (NIWA), Lauder, New Zealand, July 3, 2013.

R. P. Singh

31. "Hanbury Brown Twiss Experiment: Intensity Correlations in Scattered Optical Vortices", Colloquium, Indian Institute of Technology, Kanpur, February 7, 2014.

Geosciences Division**A. K. Singhvi**

32. "Future Earth: Societal Relevance of—and, Scientific Challenges for—Geosciences as Services", Department of Geology, Delhi University, Delhi, February 28, 2013.
33. "Future Earth: Societal Relevance of — and Scientific Challenges for —, Geosciences as Services", Birbal Sahni Institute of Paleobotany, Lucknow, March 4, 2013.
34. "Geology, Luminescence, Climate, Tectonics, Biology, Medicine and their mutualism", National Seminar on Future trends in Physics, St Xaviers College, Ahmedabad, January 30, 2013.

35. "Earth Surface Process: Challenges and Opportunities for Geoscience Services", IIT Gandhinagar- Brain storming session on Earth Sciences, March 15, 2013.
36. "Evolution of the Indian Bid for The International Geological Congress 2003-2013 and the TASKS ahead", Invited presentation at the Brain storming session on Indian Geosciences, Indian National Science Academy, Delhi, August 6-7, 2013.
37. "Some Thoughts On Risks from Monsoon Floods and Consequent Vulnerabilities of Societies, Planning workshop on Flood and Risk in monsoon Asia; Hazard and vulnerability in the past and future", National University of Singapore, Sept 25-26, 2013.

R. Ramesh

38. "Oxygen isotopes and their use in the paleoclimatic studies", Jawaharlal Nehru University, New Delhi, April 12, 2013.
39. "Climate Change", DST-SERB School on Science of Climate Change", Doon University, Dehra Dun, July 12-13, 2013. (2 lectures)
40. "Geophysical Fluid Dynamics", Centre for Earth and Space Sciences", University of Hyderabad, October 7-17, 2013. (12 lectures course)
41. "Geochronological Methods", Indo-Swiss training programme on Capacity Building in Himalayan Glaciology – Level II", Jawaharlal Nehru University, New Delhi, November 5, 2013. (2 lectures)
42. "Statistics", Indian Institute of Technology, Mumbai, December, 2014. (15 lectures)
43. "DST-INSPIRE lectures", K. R. Rangasamy College, Thiruchengodu, August 6–7, 20–21 & 31; September 17–18, 2013. (15 lectures)

Theoretical and Computational Physics

A. R. Prassana

44. "Gravity as a Gauge Theory", Indian Institute for Science, Education and Research, Kolkota, September 16-21, 2013. (2 seminars)
45. "Story of our Universe", Indian Institute for Science, Education and Research, Kolkota, September 16-21, 2013. (2 seminars)

B. K. Sahoo

46. "Fundamental physics using precision spectroscopy" Graduate School of Natural Science and Technology, Okayama University, Japan, March 24, 2014.
47. "Theoretical studies of atomic spectroscopy in Fr atom to probe fundamental symmetries", Radiation Nuclear Physics Group, Department of Physics, Tohoku University, Sendai, Japan, March 25, 2014.
48. "Roles of many-body methods to study atomic EDM of Xe atom", Department of Physics, Tokyo Institute of Technology, Tokyo, Japan, March 26, 2014.

D.P. Dewangan

49. "Quantum transitions between Rydberg states and the correspondence principle", Department of Physics, Missouri University of Science and Technology, Rolla, Missouri, 65409, USA. June 13, 2013.
50. "Research projects, awards and career", DST INSPIRE Programme, Concluding Session, Institute of Life Science, Ahmedabad University, Ahmedabad, October 24, 2013.

N. Singh

51. "A mathematical model for the pseudogap state of cuprate high temperature superconductors", IIT, Ropar, April 16, 2013.

P. Konar

52. "Story of the Higgs - A Journey beyond Nobel Prize", discussion session on 'Topic- Higgs Boson and Nobel Prize', Physics Gujarat arts and science college, Ahmedabad on Nov 30, 2013.

R. Rangarajan

53. "Elementary Particles in the Universe and the Search for the Higgs Boson", INSPIRE programme, Ahmedabad University, October 21, 2013.
54. "Reheating, Gravitinos and the Matter-Antimatter Asymmetry of the Universe", University of Pennsylvania, Philadelphia, October 30, 2013.
55. "Reheating, Gravitinos and the Matter-Antimatter Asymmetry of the Universe", University of California, Irvine, November 5, 2013.
56. "Reheating, Gravitinos and the Matter-Antimatter Asymmetry of the Universe", University of California, Santa Barbara, November 7, 2013.

S. D. Rindani

57. "Study of top-quark anomalous couplings through polarization", Kavli Institute of the Physics and Mathematics of the Universe, University of Tokyo, Japan, June 12, 2013.

B. G. Vaishnav

58. "Research and Career Opportunities in different National Research Organizations", Government Engineering College, Patan, December 13, 2013.

SCIENCE

Astronomy and Astrophysics

Nova V476 Scuti - a nova that formed optically thin dust

Near-infrared spectro-photometric observations of Nova V476 Scuti, made from Mt. Abu, were analysed to identify it as a Fe II type of nova. The near-IR JHK light curve extending for a period of about 59 days after outburst clearly shows the formation of an optically thin dust shell, a phenomenon which is not commonly observed in novae. By fitting black body curves to the spectral energy distributions (SEDs) the temperatures of the dust shell on different epochs have been estimated.

This work was done in collaboration with R.K. Das and Soumen Mondal of S N Bose National Centre for Basic Sciences, Kolkata.

(D.P.K. Banerjee & N.M. Ashok)

Studies of the Be Star X Persei during a Bright Infrared Phase

Near-infrared (NIR) observations from the Mount Abu IR telescope were made of the Be star X Persei during an unprecedented state of IR brightness. The significant new result is that the equivalent widths and line fluxes of the prominent Hydrogen and Helium lines are found to anti-correlate with the strength of the adjacent continuum. Such an anti-correlation effect is not expected and has not been observed earlier in the infrared for any Be star. Different mechanisms were examined, including a Baldwin type effect, that could cause the observed behavior and it is suggested that it originates due to a radiatively warped, precessing circumstellar disk.

(B. Mathew, D.P.K. Banerjee, S.Naik & N.M. Ashok)

Nova KT Eri 2009: infrared studies of a very fast and small amplitude He/N nova

NIR spectroscopic and photometric observations of nova KT Eridani were made during the first 100 days following its outburst in 2009 November. The spectra, typical of the He/N class novae, show strong He I emission lines together with H I and O I emission features, many of which show broad wings with a relatively narrow central component indicative of a bipolar flow. Estimates were made of the distance to the nova, its height above the galactic plane and the ejecta mass. The temporal evolution of the continuum was analysed and the possibility of KT Eri being a recurrent nova was examined.

(A. Raj, D.P.K. Banerjee & N.M. Ashok)

Deployment and commissioning of the spectroscopy section of the new Near-IR spectrograph Camera (NICS)

Diagnosis and repair was successfully carried out of the spectroscopic section of the new Near-IR camera/spectrograph (NICS) which had not been working satisfactorily. Apart from imaging capabilities in the NIR in broad and narrow band filters, the instrument is designed to obtain spectra in the 0.85 to 2.5 micron region at a resolution of 1000. NICS was deployed on the 1.2 m telescope in November-December 2013 and the spectroscopic performance was evaluated and found to be satisfactory. Subsequently, the instrument has given invaluable data on 2 major astronomical events which took place in early 2014. These are (i) the outburst of the Type Ia supernova SN2014J on 21 January 2014 and (ii) the third recorded eruption of recurrent nova V745 Sco on 6 February 2014.

Results from these studies have already been published in the *Astrophysical Journal (Letters)*, and more are expected, which will be described next year.

(D.P.K. Banerjee, V. Venkatraman, N.M. Ashok, & V. Joshi)

Signatures of precession of relativistic jet in blazars

Accretion of matter on the black hole powers the relativistic jet, which dominates the emission at all wavelengths in blazars. The exact mechanisms responsible for the origin, acceleration and collimation of the jet are not well understood. Since central engine is not resolvable by any existing optical facility, variability in flux can be used as a tool to understand the structure and physical processes in the jet.

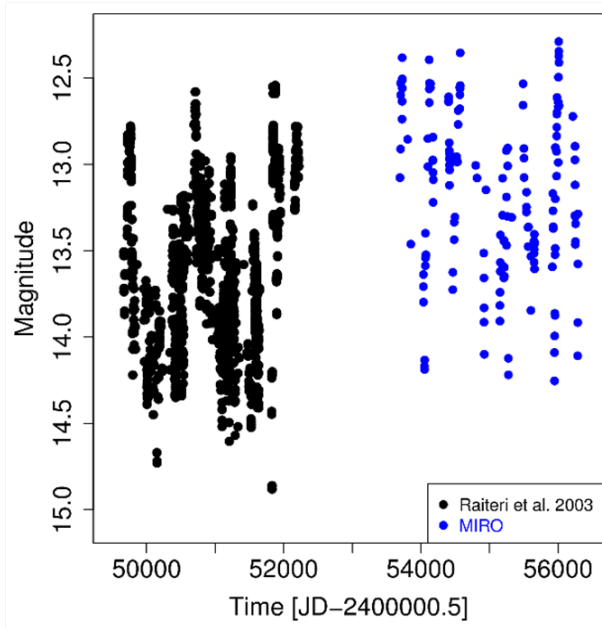


Figure 1: Brightness (Mag) as a function of time (MJD), showing increase and decrease in average brightness of S5 0716+714 during 1995 to 2012.

Blazars show variability in their flux at all frequencies with time scales ranging from years to minutes and appear good candidates for such study. Long duration monitoring of blazars is expected to throw light on the long-term variability patterns of the source, which, in case of blazars, are imprints of the jet structure and dynamics. We have used long-term monitoring data from Mt. Abu Observatory to construct light-curves for blazar S5 0716+714 which show that during 2005-2012, source brightness decreased while it increased during 1996-2003. It was accompanied with decrease in viewing angle (angle between jet direction and line of sight) from about 5 degree to 0.7 degree during 1996-2003 and then increased during 2003-2012 as determined from VLBI images. A decrease in viewing angle leads to enhancement of brightness. Available historical light-curves show a brightness decreasing trend during 1963-1981 and a fast increasing one during 1988-1995. This average brightness behaviour is superposed with slow flares and faster variations as shown in the Figure 1.

Such long-term change in the brightness of the source associated with systematic variation in the viewing angle indicates to precession of the relativistic jet on its axis. According to this, the average brightness of the source should start increasing sometime in 2015. The blazars, thus, are good candidates for studying the precession of the relativistic jet.

(K S Baliyan, S Chandra, & S. Ganesh)

Long Term Intra-night behaviour of S5 0716+71

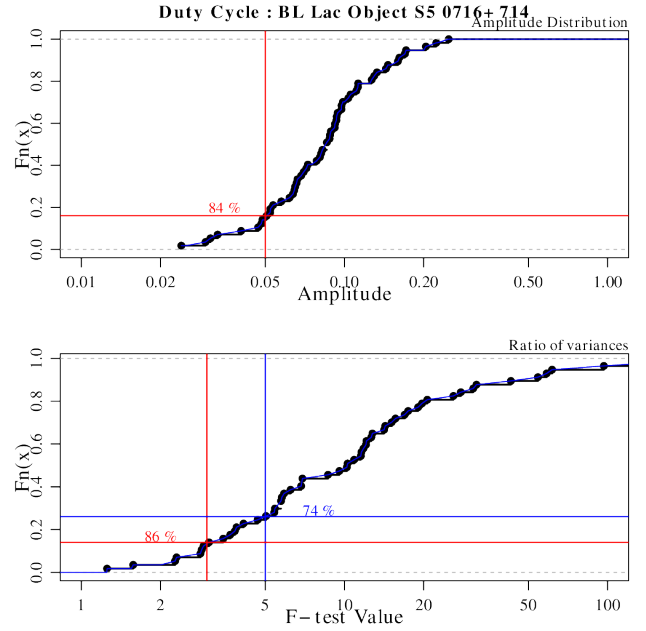


Figure 2: Duty cycle of variation for S5 0716+71. Fraction of total no of nights versus amplitude of variation (top panel: 84% nights with amplitude of variation more than 5%) and F-values (bottom panel: 86% nights as variable at 90% confidence level)

AGNs in general and blazars in particular are highly variable in flux and polarization at various time scales. The physical processes responsible for such variations, intra-night (few hours) variations in particular, are not very well understood. The jet emission is dominated by non-thermal radiation which is highly polarized and variable and any variation is expected to be caused by the activity in the jet. A sample of blazars is being monitored for studying intra-day variability from Mt. Abu IR Observatory for more than 10 years now. Here we report detection of rapid optical variability for the blazar S5 0716+71 observed using optical CCD during last several years consisting of more than 200 nights. In addition to study fast variation, it would also be interesting to see how frequent such intra-night variations are and whether there exists any relationship between intra-night variability and long-term trends. For this study, the light curves are considered for the nights with monitoring longer than 3- hours obtained with very high temporal resolution (45 seconds in R-band). Those nights for which observations are less than one hour or so, are used for generating long term light curves.

All the nights (162) which qualify the above criteria were used to detect intra-night variability by determining the amplitude of variation and corresponding time-scales. The duty cycle of variation obtained for S5 0716+714 comes out to be more than 84% (Figure 2).

The interaction of shocks with local inhomogeneities in the jet appears to cause intra-night variations while micro-variations could be due to small scale perturbations intrinsic to a small cross section of the jet. Another interesting result from this study is that, in general, the amplitude of variation is larger when the source is relatively faint. It is contrary to common belief that amplitude of variation should be larger when activity in the jet is higher, leading to brightening of the source. A detailed study involving several sources is required to address this issue.

(K. S. Baliyan, S. Chandra, & S. Ganesh)

Development of New Optical Imaging Polarimeter

An optical imaging polarimeter has been designed, constructed and tested at PRL for carrying out imaging polarimetry of the extended sources and AGNs using 1.2 m MIRO telescope. It is in the testing phase now. Astronomical polarimetry reveals informations on the distribution of magnetic field in extended sources, intrinsic polarization of a host of sources and dust scattering, which are not otherwise available from other techniques.

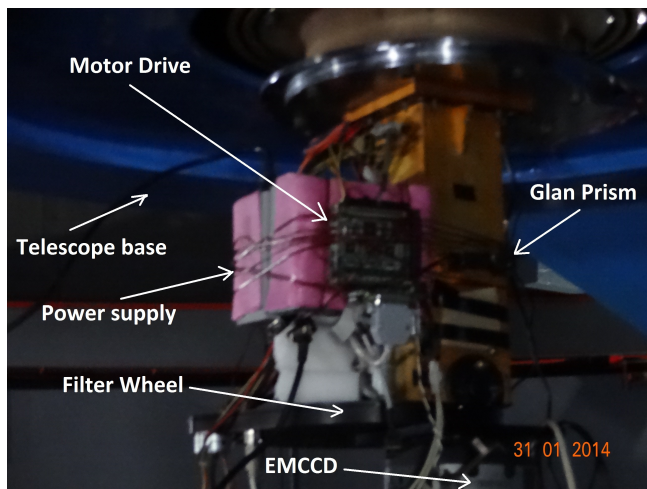


Figure 3: Newly designed and developed PRL Imaging Optical Polarimeter (PIOP) mounted at the 1.2 Mt Abu IR Telescope shows the PRL Optical Imaging Polarimeter (POIP) mounted on the 1.2 m MIRO telescope.

In case of AGNs, generally multi-wavelength emission is dominated by the jet and information on the flux density and optical/radio polarization can be used to glean morphological information about particle acceleration regions and jet magnetic field configuration. The polarimeter is developed around 1024×1024 pixels EMCCD as imaging detector. It uses rotating half wave plate as modulator, rotation being controlled by a stepper motor which completes one rotation

in 48 steps. A Foster prism, as analyzer, splits the beam into ordinary and extra-ordinary orthogonal rays. The polarimeter has a 12-slot filter wheel to accommodate UBVRI broadband filters and a set of narrow band filters. The stepper motor is driven by a timing signal to rotate the half-wave plate and the same signal is used to initiate the exposure (Figure 3).

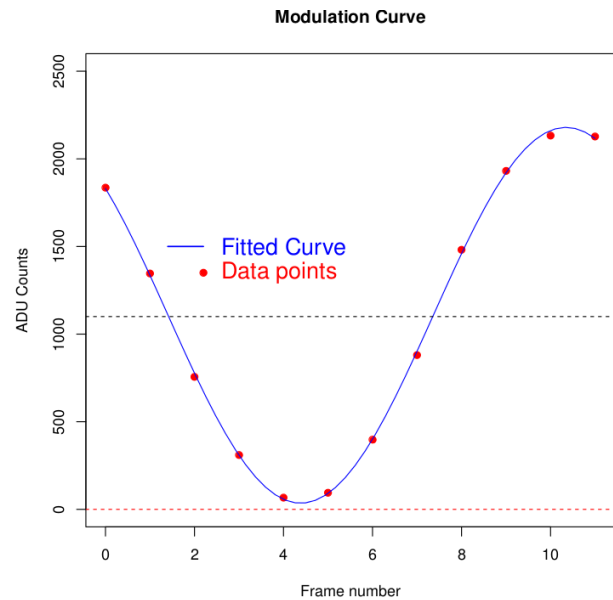


Figure 4: Modulation curve obtained for testing the polarimeter for 100% polarized light using Glan prism.

The instrument is checked for 100% polarized light using source SAO82421, by introducing Glan prism in the light path (Figure.4). The measured degree of polarization is $97.7 \pm 0.4\%$. The instrument has also been used to observe polarization standards. The polarimeter is completely designed and developed in-house, including whole control electronics and hardware fabrication with the help of several engineering trainees and PRL workshop.

(S. Ganesh, A. Mishra, S. Chandra, S. N. Mathur, G. Ubale, & K. S. Baliyan)

A Spatial asymmetry in semi-regular variable UZ Arietis from three epoch lunar occultations in the K band.

Semi-Regular variables (SRVs) are a sub class of Asymptotic Giant Branch (AGB) stars which have a lower amplitude of variability compared to Mira variables. Asymmetry in brightness distribution at the level of milli-arc seconds is known to occur in Miras and has been attributed variously to star spots and stellar rotation or non radial pulsations or inhomogeneous translucent molecular screens. Such studies are very limited for Semi-Regular variables.

UZ Ari IRC +20052 is classified as an oxygen-rich M8 giant. It is an SRV with V magnitude varying from 11.8 to 12.6 and an unconfirmed period of variability of about 163 days. It is high galactic source at a distance of about 140 parsecs. IRAS low resolution spectra indicate the presence of a circumstellar

dust. In this work we report three epoch Lunar occultation observations of a semi-regular variable UZ Arietis spread over 4 years from 2006 to 2010, for the first time. Multi-epoch lunar occultation (LO) observations on the same source provide a means of using the one dimensional high angular resolution technique to deduce the Uniform Disk (UD) angular diameter in different directions across the source. Any two dimensional asymmetry in the source at the level of milli-arcseconds can show up as a significant difference in the UD values measured provided the position angles for the three events are widely different. The first LO was observed in the K band at 2.2 microns with a fast IR photometer and the next two LO events were observed using the fast sub-array (10 pixel X 10 pixel) mode of the NICMOS IR Camera/Spectrometer mounted at the 1.2m telescope of Mt. Abu Observatory (Figure 5).

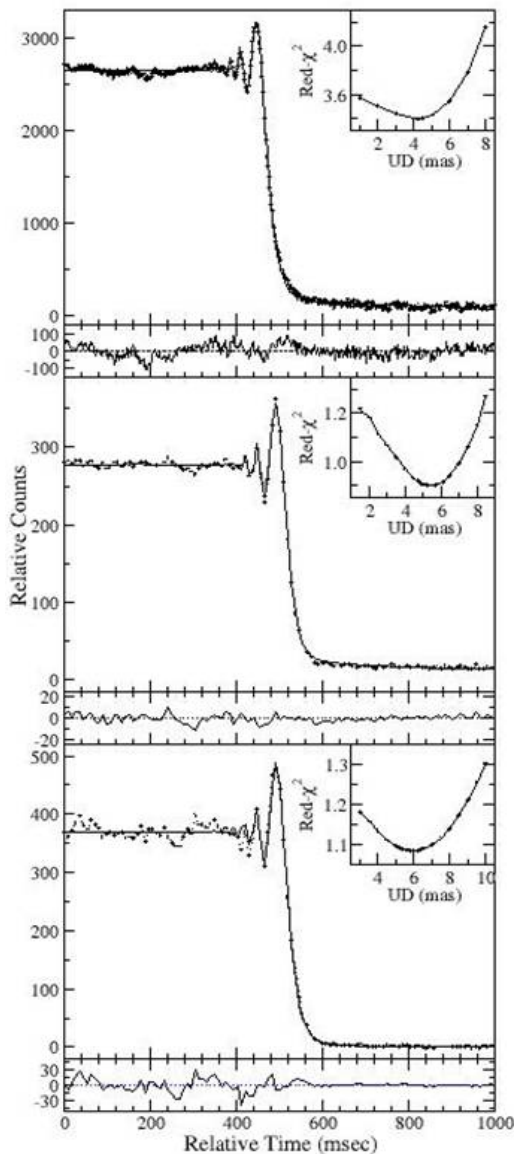


Figure 5: Lunar Occultation light curves of UZ Ari in the K band at 2.2 microns obtained in the 3 epochs, 2006, 2009, 2010, shown along with the model fit and the residuals (Data-model) at the bottom. Inset shows the error curve whose minimum value is the derived uniform disk angular diameter of the source. Optical polarisation observations were also carried out from Mt Abu with PRL Photopolarimeter (PRLPOL) in early 2013 in two epochs.

UZ Ari has several interesting peculiarities. The source has exhibited sporadic water maser emission at 22 GHz. Though the water maser was clearly detected in the period 1983-2001 at a level of about 6 Jansky, recent reports suggest that the maser is no longer detectable. Another interesting aspect of the source is its optical linear polarisation. Significant optical polarisation of about 3% at position angle of about 130 degrees had been observed long ago in 1971 and again in 1976 in the V and R bands. Surprisingly no further polarisation measurements have been carried out on this source for the last 40 years till this work. The uniform disk (UD) angular diameter values at three position angles 63, 98 and 123 degrees across the source show a small but significant difference suggesting the source could be slightly elongated in a direction close to 123 degrees. Completely independent optical polarisation measurements show about 3.2 ± 0.2 % R band linear polarisation with a position angle of 130 ± 2 degrees. (Figure 6).

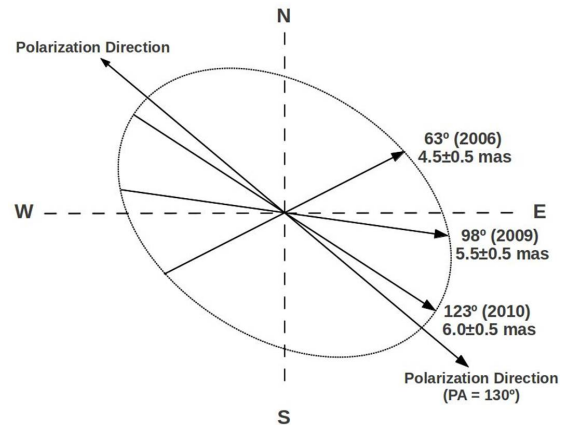


Figure 6: Geometry of the 3-epoch lunar occultation of UZ Ari.

UD angular diameters in milli-arcsec and position angles in degrees are marked. The polarisation direction of 130 degrees is also superposed. It is noteworthy that the polarisation direction of 130 degrees is nearly coincident with the direction of the longest measured angular diameter at position angle 123 degrees. Further this value of polarisation and position angle seem to have remained stable for over 40 years since 1970 till our observations. While the exact cause of this asymmetry in the brightness distribution is not known, the fairly long term stability over decades suggests that it is unlikely to be due to rotating hot or cold spots on the star's surface. Asymmetric mass loss in a preferred direction defined by the polarisation axis is a possibility.

(T. Baug, T. Chandrasekhar, & S. Ganesh)

Detection of a Cyclotron Resonance Scattering Feature in the High Mass X-Ray Binary Pulsar 4U 1909+07

The energy spectra of accretion-powered X-ray pulsars are generally described by phenomenological models consisting of a power law with a high energy cutoff, and a Gaussian function at 6.4 keV for the presence of iron fluorescence

emission. In some cases, a blackbody or bremsstrahlung component is required to describe the presence of excess emission at soft X-rays. Other than these components, a broad absorption-like feature due to cyclotron resonance scattering is often seen in the pulsar spectrum. The magnetic field strength B and the cyclotron resonance energy E_a are related through the relation $E_a = 11.6 B_{12}(1+z_g)^{-1}$ (keV), where z_g is the gravitational redshift and B_{12} is the magnetic field strength in units of 10^{12} G. Detection of a cyclotron scattering resonance feature (CRSF) in the spectrum, therefore, provides the direct measurement of the strength of the pulsar magnetic field. The CRSFs have been detected in the spectrum of about 19 X-ray pulsars.

The high mass X-ray Binary pulsar 4U1909+07 was discovered with the Uhuru satellite in 1974. The spin and orbital periods of the binary pulsar was reported to be 605 s and 4.4 days, respectively. The detection of an OB star in the near-infrared confirmed the system to be an OB supergiant-neutron star HMXB. The pulse profile of the pulsar was found to be strongly energy-dependent. Using Suzaku observation, we detected a CRSF at 44 keV in the pulsar spectrum, which is shown in Figure 7 along with the best-fit model.

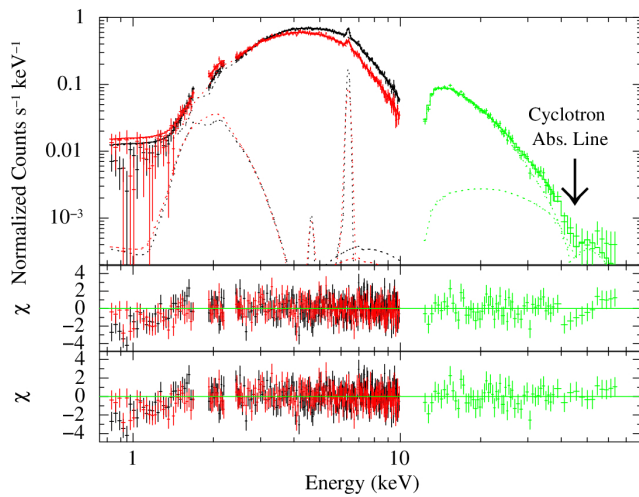


Figure 7: Energy spectrum of 4U1909+07 obtained from the Suzaku observations, along with the best-fit model comprising a partial-covering NPEX continuum model and a blackbody component, narrow iron line emission, and a CRSF. The middle and bottom panels show the contributions of the residuals to chi-square for each energy bin for the partial-covering NPEX continuum model without and with a CRSF component in the model, respectively.

This is the first time that a CRSF has been detected in 4U 1909+07. Several statistical tests on the data and the presence of a clear dip at 44 keV in the normalized Crab ratio confirmed the detection of the CRSF in the pulsar. Using the value of the energy of the CRSF, we estimated the surface magnetic field of the pulsar to be 3.8×10^{12} G. Apart from the CRSF, a weak iron fluorescence emission line at 6.4 keV was also detected in the spectrum.

This work was done in collaboration with B. Paul of RRI, Bangalore.

(S. Naik and G. K. Jaiswal)

X-ray and infrared properties of Be/X-ray binary pulsars

Be/X-ray binaries represent the largest subclass of High-Mass X-ray Binary (HMXB) systems. The compact object in these systems is generally a neutron star (pulsar) whereas the companion is a B- or O-type star that shows Balmer emission lines in its spectrum. The objects in these binary systems are typically in a wide orbit with moderate eccentricity. Though evolutionary model calculations show that binary systems with a white dwarf and Be star or a black hole and Be star should also exist, clear evidence of the existence of such binary systems has not been found as yet. The neutron star in these Be/X-ray binary systems accretes matter while passing through the circumstellar disk of the companion Be star. The abrupt accretion of matter onto the neutron star while passing through the circumstellar disk of the Be companion or during the periastron passage results in strong X-ray outbursts. During such outbursts, the X-ray emission from the pulsar can be transiently enhanced by a factor of more than 10. Be/X-ray binary systems generally show periodic normal X-ray outbursts that coincide with the periastron passage of the neutron star and giant X-ray outbursts that do not show any clear orbital dependence apart from the persistent low-luminosity X-ray emission during quiescent. The neutron stars in the Be/X-ray binary systems are found to be accretion powered X-ray pulsars. As the regular outbursts in Be/X-ray binary pulsars are associated with the periastron passage of the neutron star, it is interesting to study the pulsars in X-rays and the Be companion star in infrared/optical bands during outbursts. For X-ray properties of the pulsar, we use data from several X-ray observatories whereas for infrared study of the Be companion star, we use monitoring data from Mt. Abu observatory.

(S. Naik)

Detection of a variable QPO at 41 mHz in the Be/X-ray transient pulsar 4U 0115+634

Quasi-periodic oscillations (QPOs) in X-ray binary pulsars are known to be related with the motion of blobs of matter in the inner accretion disk. In X-ray pulsars, the QPO frequency ranges from 1 mHz to 40 Hz. The presence of QPOs in the power density spectrum of X-ray pulsars is generally explained with the Keplerian frequency model or the magnetospheric beat frequency model. In Keplerian model, the QPOs arise from the modulation of the X-ray by in-homogeneously distributed matter in the accretion disk, at the Keplerian frequency. In this model, the QPO frequency is same as the Keplerian frequency of the inner accretion disk. In the beat frequency model, blobs of matter orbit the neutron star approximately at the Keplerian frequency of the accretion disk inner edge, accreting at a rate modulated by the rotating magnetic field. This produces power spectral feature at the beat frequency. According to this model, the QPO frequency is equal to the difference between the Keplerian frequency of the inner accretion disk and the spin frequency of the neutron star.

We have detected QPOs at 41 mHz for the first time in the transient pulsar 4U 0115+634, discovered during the UHURU satellite survey, using data from the Rossi X-ray Timing Explorer (RXTE) observatory. The pulsation of the pulsar was first estimated to be 3.6 s and a cyclotron resonance scattering feature (CRSF) was detected at 11 keV. Second, third and fourth harmonics of the CRSF are later detected in the pulsar spectrum from RXTE and BeppoSAX observations.

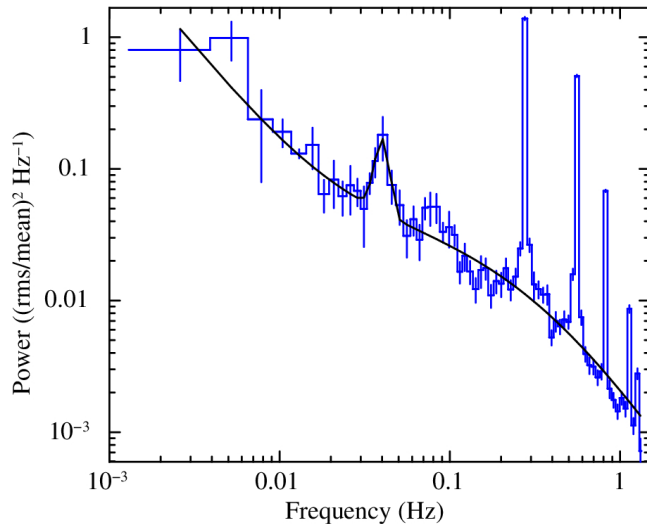


Figure 8: The power-density spectrum of 4U 0115+63 from RXTE/PCA observations on 1999 March 25, clearly showing presence of newly detected 41 mHz QPO. The 3.6 s pulsation and its harmonics are seen at higher frequencies. The solid line represents the fitted model comprising of a power-law continuum, a Lorentzian function and a Gaussian function.

During an outburst, detection of QPOs at 62mHz was reported. Apart from the 62 mHz QPO, another low-frequency QPO at 2 mHz was detected in RXTE observations of the pulsar during 1999 March–April outburst. In our work, we used RXTE observations during X-ray outbursts in 1999 March–April, 2004 September–October and 2008 March–April. The frequency of the newly detected QPO at 41 mHz was found to vary in 27–46 mHz range. This QPO was detected only in 11 out of 95 pointed RXTE observations (one such QPO is shown in (Figure 8) during three outbursts. Though simultaneous presence of multiple QPOs is rarely seen in accretion-powered X-ray pulsars, we detected multiple QPOs in the power-density spectrum of 4U 0115+634.

This work was done in collaboration with S. N. A. Jaaffrey and M.R. Dugair of MLSU, Udaipur.

(S. Naik and G. K. Jaisawal)

A study of solar wind density modulation index during solar cycle 23

We have made a detailed study of variations in the density modulation index ($\Delta N/N$), the ratio of the rms electron density fluctuations (ΔN), to the absolute solar wind density (N), in the inner heliosphere spanning over distance ranging from 0.2 AU to 0.8 AU for the period 1998–2008, covering solar

cycle 23. The density modulation index is of vital importance for understanding the turbulent dissipation and consequent local heating of the solar wind. It also plays a crucial role in understanding the propagation of energetic electrons, through the heliosphere, generated by solar flares and other energetic solar surface phenomena. The ΔN have been deduced using ground-based interplanetary scintillation (IPS) observations at 327 MHz from the Solar Terrestrial Environment Laboratory (STEL), Nagoya University, Japan. Prior to this, the scintillation index measurements are appropriately normalized to remove the effect of source size as it is well known that the scintillation indices are, in general, function of source size and distance from the sun. The absolute density, on the other hand, has been obtained from the space-borne Advanced Composition Explorer (ACE) mission. However, ACE density measurements are effectively at a distance of 1 AU at the Lagrangian point L1. Thus, for estimation of density at the location of the relevant scintillating sources, spreading over distances of 0.2–0.8 AU, the measured ACE densities at 1 AU are extrapolated in the sunward direction using an electron density model that derives the electron density distribution from the solar corona to 1 AU. Our analysis shows that the typical value of the $\Delta N/N$ ranges from 1% to 10%, consistent with earlier findings. In addition, we find that the density modulation index does not vary with heliocentric distance r from the sun. A steady decline in ΔN , a good proxy for the solar wind micro-turbulence levels, has been reported earlier for the period 1995 to 2008. Our investigation of the long-term temporal variations of the density modulation index over the distance 0.2–0.8 AU also show a similar decline during the period 1998–2008. So it appears reasonable, from the linear relationship between the density fluctuations and magnetic field fluctuations, to conclude that this decrease in $\Delta N/N$ is connected to the unusual solar magnetic activity during the long and deep solar minimum at the end of the solar cycle 23.

(P. Janardhan and S. K. Bisoj)

Variation of the inner disk radius during the onset of 2010 outburst of MAXI J1659

Majority of the black hole binaries are transient X-ray sources, spending most of the time in quiescent state with a luminosity below the detection limit of all sky X-ray monitors. This state typically lasts for few years with the episodes of quiescence separated by transient outbursts. The luminosity of the source increases by orders of magnitude during outbursts which typically last for few months. Almost all the transient black holes show a common property of following a Q-shaped track in the hardness-intensity diagram during outbursts. These diagrams show that an outburst starts with the source in the hard state and as the outburst progresses the source switches between soft and hard states. The source reaches the hard state again when it enters into the quiescence. These properties are explained with a disk truncation model which says that the inner accretion disk extends close to the innermost stable circular orbit (ISCO) and it is truncated at larger radii during hard states. Since the outburst starts with the source in the hard state, it is presumed that the disk is truncated at larger radii during early stages of the outburst. However, the early stages of the outburst are not easy to

detect because the source becomes detectable only when the luminosity reaches a significant fraction of the peak luminosity. Therefore, the direct observational evidence for a truncated inner disk during early hard state is not available.

We studied a transient black hole candidate MAXI J1659-152 which was detected during early stages of the outburst with a rapid follow-up and dense coverage by Swift/XRT. We analyzed total 80 spectra using a novel technique of simultaneously fitted, in groups of ten, spectra to constrain the geometric parameters of the binary system. With this method, we studied the variation in the inner disk radius and found a very systematic behavior with the progress of the outburst. The disk was found to be truncated at few hundred Schwarzschild radius during early stages of the outburst. We noticed that as the outburst progresses, the disk radius moves closer to the black hole. This probably, is the first observational evidence of the accretion disk closing-in during the early stages of the outburst.

(A. Rao, S. V. Vadawale)

Estimation of detection efficiency in plastic scintillator: Implications on the lower energy limit and sensitivity of a hard X-ray focal plane Compton polarimeter

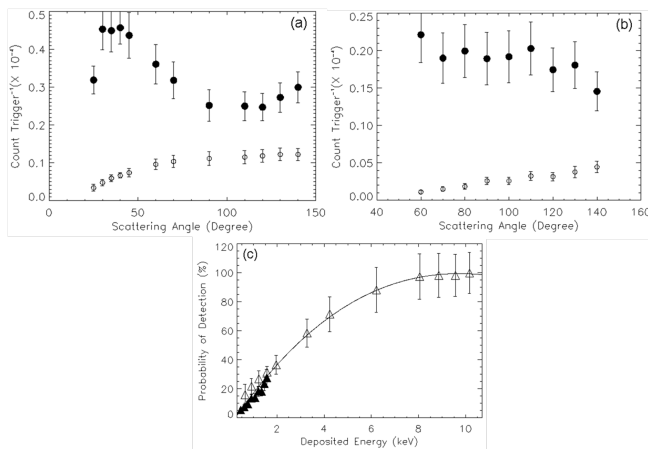


Figure 9: (a) Observed count rate, normalized with respect to the total number of triggers in plastic for incident photons of 59.5 keV as a function of scattering angles; (b) and same for incident photons of 22.1 keV. Open and filled circles stand for coincidence and non-coincidence modes respectively. (c) Detection Probability of plastic scintillator as function of deposited energy in plastic, obtained by the semi-analytical modeling of the observations.

With the recent technological advances it has become possible to design a focusing X-ray telescope in hard X-ray range. Following X-ray telescope provides improvements in sensitivity by several orders of magnitude and this development has raised feasibility of having sensitive X-ray polarimetric observations in hard X-ray range, which were impossible so far. In this context we have initiated development of hard X-ray polarimeter based on the principle of Compton scattering, which can be used at the focal plane of a hard X-ray optics. Sensitivity of such polarimeter significantly depends on the low energy threshold of the active scatterer which is typically made of a plastic scintillator. In order to understand the low energy behavior of the plastic

scatterer, we carried out a Compton scattering experiment using the same plastic scintillator. The experiment involves detection of the Compton scattered X-rays from plastic using an independent detector (CdTe) at different scattering angles for a known energy X-ray beam.

Our experimental set up employs the same principle of the coincident detection of Compton scattered event and provides the opportunity to systematically test the detection efficiency of the plastic scatterer at different deposited energies. Figure 9(a) and 9(b) show the experimental results for two radio-active X-ray sources, ^{109}Cd (X-ray line energy of 22.16 keV) and ^{241}Am (X-ray line energy of 59.5 keV) as a function of scattering angle in coincidence and non-coincidence mode. We modeled our observations by a semi-analytical model using the knowledge of scattering cross-sections and geometry of our setup to obtain the final detection probability as a function of the energy deposited in the plastic scatterer during the Compton scattering event as shown in Figure 9(c).

It can be seen that at lower energies (0.4 - 3.0 keV), probability of detection increases linearly with the deposited energy and then reaches around 100 % at 7 keV and saturates thereafter as expected. This result has significant implication on the lower energy limit of operation of focal plane Compton polarimeters and thus their sensitivity.

(T. Chattopadhyay, S. V. Vadawale, M. Shanmugam, S. K. Goyal)

Prospects of hard X-ray polarimetry with Astrosat-CZTI

Astrosat is the forth-coming Indian satellite dedicated to the multi-wavelength astronomical observations. Cadmium Zinc Telluride Imager (CZTI), one of the five payloads, is a large area pixelated (pixel size 2.5 mm) detector for hard X-ray spectroscopy in 20 - 100keV energy range. Such pixelated detectors working in event mode can also work as Compton polarimeters, where the double pixel events arising due to Compton scattering of a photon in one pixel and absorption of that photon in another pixel constitute the basic azimuthal angle distribution. Using this property of the detectors, we explored the feasibility of using CZTI for X-ray polarization measurements for celestial sources. We carried out detailed Geant4 simulations for CZTI to estimate sensitivity of CZTI. Figure 10 shows the polarimetric sensitivity of CZTI in terms of the minimum detectable polarization (MDP) in the energy range of 100 - 300 keV as a function of source intensity in Crab units. Exposure times of 1 Ms and 500 ks are denoted by asterisks and triangles respectively. Since, the modulation factor depends on the angle of polarization; sensitivity of the instrument is also polarization angle dependent. This provides an opportunity to confirm the polarization measurement by repeating the observations with different orientation of the spacecraft. For a Crab like source, expected MDP is 10% in 500 ks exposure. Our analysis shows that the Astrosat-CZTI will be the most sensitive instrument for hard X-ray polarization measurements in this energy range.

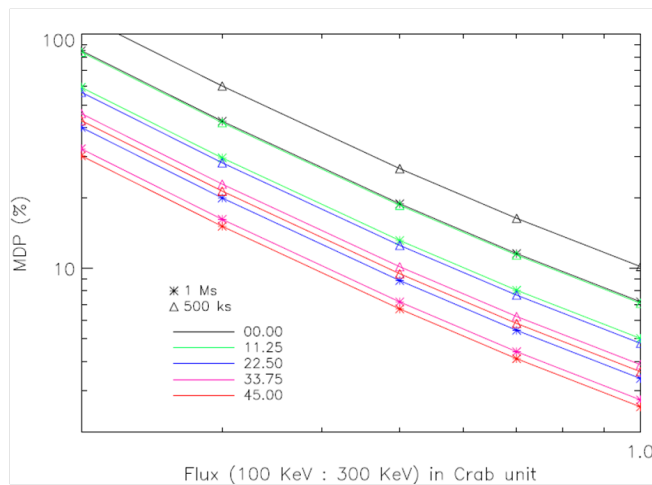


Figure 10: Polarimetric sensitivity of Astrosat-CZTI in terms of minimum detectable polarization (MDP) as function of source intensity and polarization angle. Random background is assumed to be $10 \text{ counts s}^{-1} \text{ cm}^{-2}$.

(T. Chattopadhyay, S. V. Vadawale)

The PARAS spectrograph stability and some new results

The PRL optical fiber-fed high-resolution cross-dispersed echelle spectrograph (PARAS) was commissioned at the Mt Abu 1.2 m telescope a couple of years back with science observations continuing since April 2012. The spectrograph has shown remarkable stability on Radial-Velocity standard stars at sub-2m/s (1.5m/s – 1.9m/s) over a period of about two years. Such stability thus gives us the ability to detect planets of mass down to 10-earth mass with a period of a few days around bright stars up to 7^{th} magnitude and Jupiters and Brown Dwarfs up to 10^{th} magnitude. Detection of a star at the Hydrogen burning limit: We have found evidence of one of the smallest mass star of $0.087 \pm 0.003 M_{\odot}$ at the hydrogen burning limit in an eclipsing binary system. The primary star mass in the system is between 0.70 to 0.78 Solar-Mass (K2 to K4 spectral type). Figure 11 shows the Radial-Velocity (RV) curve obtained from the PARAS observations.

The period is found to be 16.94 days, with a K-value (semi-amplitude) of 8453m/s and orbital eccentricity (e) 0.16. The magnitude of the primary star is 10.7 mag. The error bars on the data points are about 25m/s. Stellar activity or evidence of a super-Neptune around a K0 Dwarf: We report RV observations from a K0 dwarf star for over a period of three months (Figure 12).

The primary star mass is about 0.8 Solar Mass with 9.04 apparent magnitude in the V-band. The RV observations show periodic oscillations of 3.8 days with a semi-amplitude (K) of about 18 m/s. This could either be an evidence of a super-Neptune with a mass of 0.11 Jupiter-mass ($m \sin(i)$) at a semi-major axis of 0.056AU or stellar activity (stellar photosphere pulsations). We need to observe for a few more months to detect any variations in the period. If it is an exoplanet, then the period will remain

constant over time. The observed period will change over time if it is due to stellar photosphere pulsations alone.

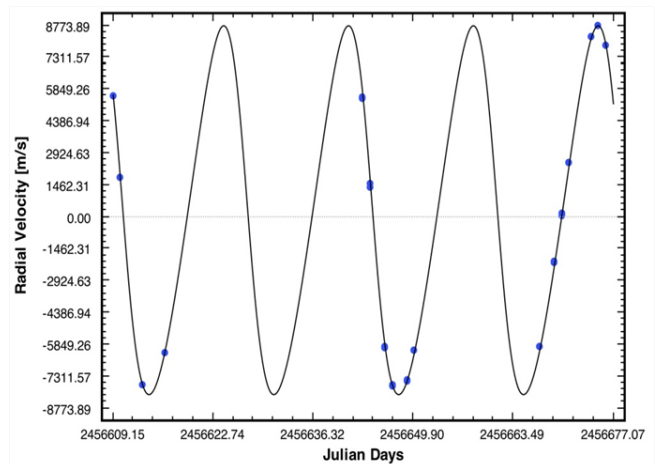


Figure 11: RV curve of an eclipsing binary system showing evidence of secondary star with mass of 0.087 ± 0.003 Solar Mass. One of the lowest mass star known.

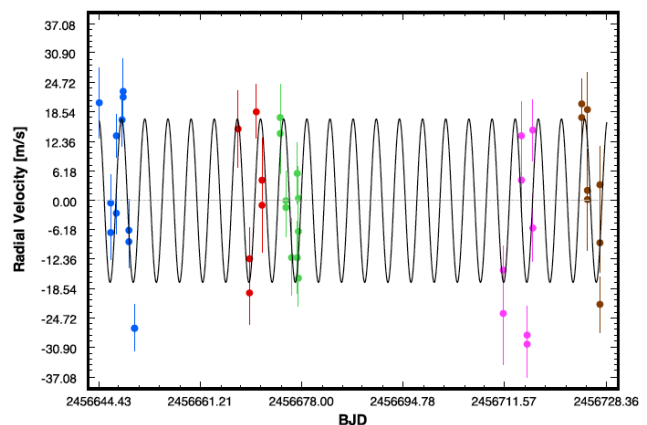


Figure 12: 3.8 days periodic RV variations observed over a period of 3 months from a K0 type dwarf star. The errors on the individual points are between 6m/s to 9m/s.

(A. Chakraborty)

Orientation based Unified Scheme: Some doubts

Using a 408 MHz sample from the equatorial sky region, selected at the same flux-density level as the strong 3CRR sample, it was shown that a fore-shortening in the observed sizes of quasars, expected from the orientation-based unified scheme, is not present. Even the quasar fraction does not match with that expected from the unified scheme, casting strong doubts on the unified scheme. It also threw up an intriguing result that two samples from different sky regions but selected using the same criteria, the relative distribution of radio galaxies and quasars differs qualitatively, not in accordance with the cosmological principle which expects an isotropic sky.

(A. K. Singal & Raj Laxmi Singh)

Thermal and non-thermal energetics of precursor and main phase emission in solar flares:

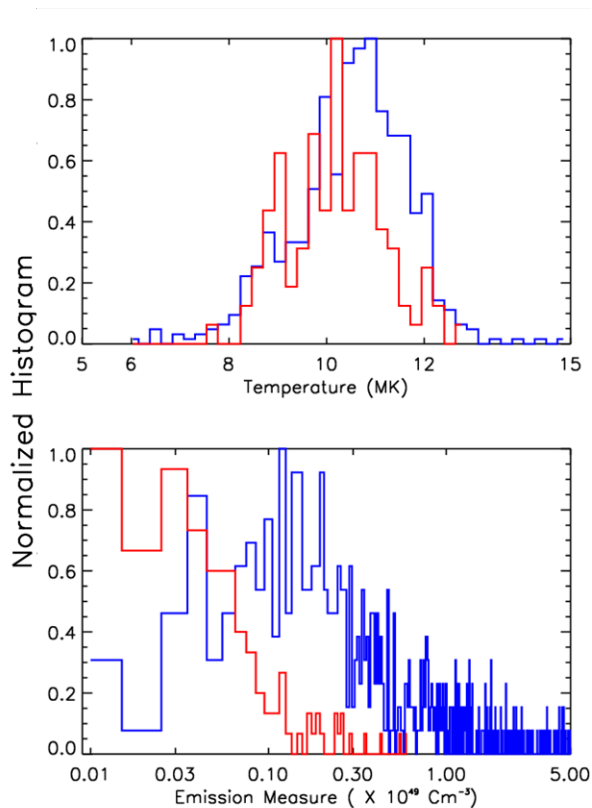


Figure 13: Top and bottom panels represent the Temperature versus EM during the precursor and main phases, respectively.

We study the spatial and spectral evolution of multi-wavelength emission from fifty flare events occurring during year 2003-2012 which shows unambiguous spatially

linked precursor emissions. Preflare multi-wavelength emission is investigated to characterize flare plasma parameters associated with this phase.

Further, we explore their association with flare main phase and estimate the flare plasma parameters viz. temperature emission measure (EM) and non-thermal spectral index (γ). The plasma parameters deduced during the precursor and main phases revealed that though EM during the precursor phase ($0.01-0.1 \times 10^{49} \text{ cm}^{-3}$) was 2 orders less than that of the main phase ($0.08-0.7 \times 10^{49} \text{ cm}^{-3}$), T reached 80% (5-12 MK) of its main phase (9-14 MK) value (Figure 13). Investigation of the temporal, spatial and spectral evolution of the M1.8 flare, which occurred in the active region 11195 (S17E31) on 2011 April 22 revealed a multi-loop system that destabilized systematically during the precursor and main phases. In contrast, hard X-ray emission was absent during the precursor phase, appearing only from the onset of the impulsive phase. The energy released in the precursor phase, was thermal and $\sim 1\%$ of the total flare energy. The study of morphological evolution of the filament in conjunction with synthesized T and EM maps reveals (a) partial filament eruption prior to the onset of the precursor emission and (b) heated dense plasma over the polarity inversion line and in the vicinity of the slowly rising filament during the precursor phase. Based on the multi-wavelength observations, we propose a scheme to unify the energy release during the precursor and main phase emissions in which the precursor phase emission was originated via conduction front that resulted due to the partial filament eruption. Also, the heated leftover S-shaped filament underwent slow-rise and heating due to magnetic reconnection and finally erupted to produce emission during the impulsive and gradual phases.

Part of this work has been done in collaboration of the Indo-US group.

(A. K. Awasthi and R. Jain)

SCIENCE

Solar Physics

The Trigger of a Spectacular Filament Eruption leading to a CME and Flare

Coronal mass ejections (CMEs), prominence filament eruptions, and flares are three different types of large-scale eruptive phenomena that occur in the solar atmosphere. It is believed that they are closely related, different manifestations of a single physical process. Although most CMEs are not associated with flares, a large flare is invariably associated with a CME. CMEs represent ejection of mass and magnetic flux from lower corona into the interplanetary space, and play important role in governing space weather. Several CME models have been developed to describe their pre-eruption structures (or progenitors), initiations, and eruptions based on the available observations. Here, we present results based on our study of a long, dark quiescent filament, located in a weak magnetic field region in the solar north-west quadrant, transiting the solar disk during 20-29 September 2013. After several days of inactivity, the filament began significant restructuring and activation, eventually erupting catastrophically on 29 September 2013 21:22 UT. This eruption was seen in $H\alpha$ images as sudden disappearance of the filament, historically known as a 'disparition brusque' event. On the other hand, SDO-AIA 171 and 304 Å images showed upward rise of filament and CME travelling at a speed of approximately 900 km/s. It was associated with a moderate proton event which continued over next several days, affecting the space weather. We have investigated this event with the primary aim to look for the trigger of the sudden eruption of the quiescent filament. For our study we used GONG $H\alpha$ 6563Å, along with SDO-AIA and HMI data. From the GONG $H\alpha$ images, we found signature of new emerging magnetic fluxes

in the form of a compact brightening which developed adjacent to the filament's central barb (marked as f2 in Figure 14).

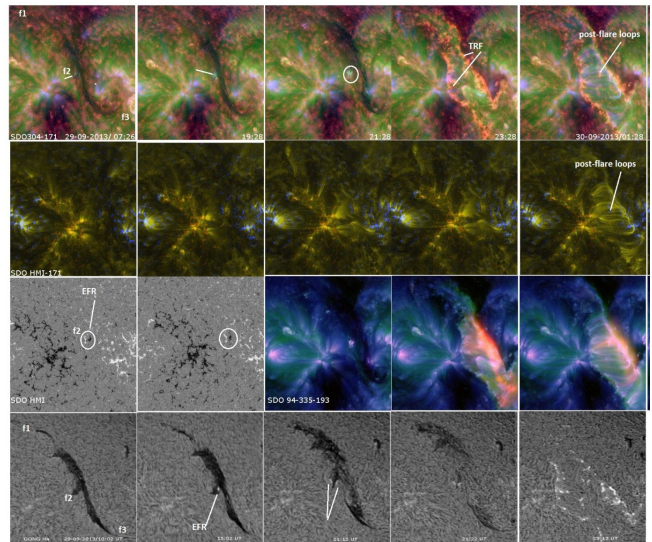


Figure 14: SDO-AIA and HMI images: Temporal sequence of the filament eruption, CME and a two-ribbon flare associated with the transient event observed on 29 September 2013.

SDO-HMI magnetogram movie also indicated the first sign of emerging flux region (EFR) of both signs at the rate of 13.3 (-74.1) Mx/hr on 29 September 2014/02:34 UT over an area of $1.9 \times 10^8 \text{ km}^2$. This process increased both in rate and area

with time. The SDO-images further confirm the EFR, which destabilized the filament flux rope and caused its eventual eruption.

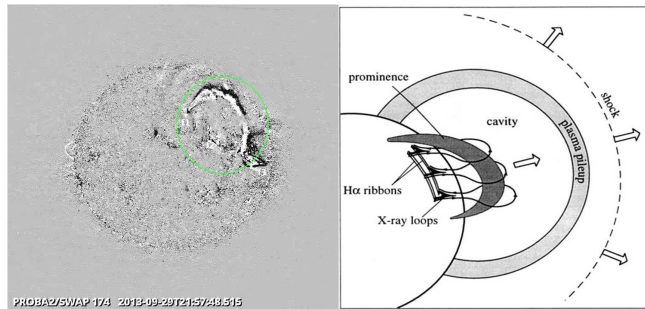


Figure 15(a) Proba2/SWAP difference image of the filament eruption at 21:57 UT; (b) Schematic diagram showing the relationship between the filament eruption, H-alpha flare ribbons, and the CME (adopted from Forbes 2000).

The difference images clearly showed detachment of the filament and its rise at 'f2', i.e., the site of EFR, while it remained connected at its two extreme legs 'f1' and 'f3' (Figure 15a). It is clear that the EFR triggered eruption of the twisted flux rope structure of the filament, leading to a bodily transport of its flux system into the corona and onwards into the interplanetary space as a CME. After a lapse of over 20 minutes of the filament's eruption and CME's launch, a classic long-duration, moderate C-class two-ribbon flare started developing at 21:43UT along the magnetic neutral line delineated by the long filament that lasted over 3 hours. As the flare progressed, host of post-flare loops formed during the decay phase linking the two-ribbons of the flare separating out with time. This indicated a reconnection process taking place below the erupting filament/CME much after the filament eruption occurred.

Thus, we infer that the dark filament was the progenitor of the ensuing CME. Its structure essentially represented a twisted flux rope holding the filament in equilibrium by the overlying magnetic field lines line-tied to the solar surface. The emerging magnetic fluxes near the filament channel destabilized the flux rope by the ensuing rearrangement of magnetic field structures and loss of equilibrium. The magnetic field lines spanning over the flux rope stretched up as the flux rope rose upwards. This led to the formation of anti-parallel magnetic field lines of opposite sign below the flux rope approaching each other. A current sheet formed between the approaching upwards-downward field lines, known to be susceptible to microscopic instabilities which enable resistive or collision-less fast magnetic reconnection. The observed two-ribbon flare in the region below is indicative of this reconnection process. Furthermore, the magnetic reconnection resulted in cutting the line-tied magnetic field lines that removed the restraint for the flux rope, and facilitated rapid eruption and upward acceleration of the flux rope. As a portion of the overlying magnetic loops stretched up extending to the inter-planetary space along with the flux rope, the magnetic structures near the two extreme legs 'f1' and 'f2' of the flux rope slipped onto the solar surface, clearly

demonstrated by the SDO-AIA and Proba2 images. This process as schematically shown in Figure 15b is consistent with the standard CME model.

(A. Ambastha)

A study of the flare associated changes seen in the solar active region NOAA 11719 during an M-class flare

The solar active region NOAA 11719 produced an M6.5 class flare on 11 April 2013 around 06:55 UT, when it was located near the disk-center (N10E08). This flare was accompanied by a type II radio burst, an EIT wave, a full halo CME, and a proton rich event. The flare was well observed by ground- and space-based observatories in various wavelengths and energies, viz., GONG, SOHO/LASCO, SDO, and GOES. The H α images obtained by the GONG instrument located at the Udaipur Solar Observatory show filament activity in this active region before and during the flare. These images also show the evolution of this flare as a two-ribbon structure and the flare ribbons covered the umbra of the sunspot as the flare progressed. The He II 304 Angstrom images obtained from AIA instrument onboard SDO spacecraft show successive expansion and contraction of the flare ribbons during the flare. The flare ribbons as seen in H-alpha and He II 304 Angstrom images are shown in the top panels of Figure 16. We have also examined the flare associated changes in velocity flows and magnetic field properties in the active region using the images obtained from HMI instrument onboard SDO spacecraft.

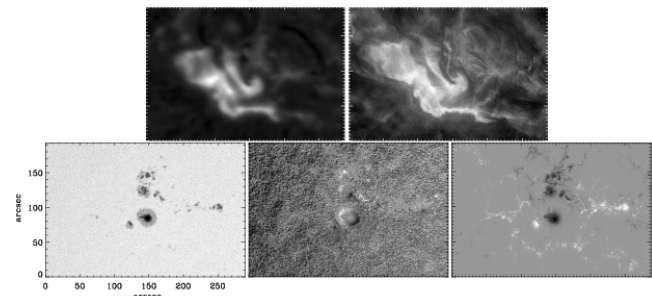


Figure 16: Top panels: The flare ribbons in the active region NOAA 11719 during an M6.5 class flare as seen in H α images (left) obtained from GONG instrument located at Udaipur Solar Observatory and He II 304 Angstrom images (right) obtained from AIA instrument onboard SDO spacecraft. Bottom panels: The images of the active region in continuum intensity, Doppler velocity, and the line-of-sight magnetogram as observed with HMI instrument onboard SDO spacecraft. All the images shown here are the mean images over the time interval 06:50-07:50 UT spanning the flare on 11 April 2013.

We observe changes in the velocity flows in some localized regions of the active region during the flare. The images of the active region in continuum intensity, Doppler velocity, and the line-of-sight magnetogram as observed with HMI instrument are shown in the bottom panels of the Figure 16. In the Figure 17, we show the vector magnetic field

map of the active region obtained from HMI instrument at 06:48 UT on 11 April 2013. In this map, the horizontal magnetic field ($B_h = \sqrt{B_x^2 + B_y^2}$) vectors in blue (yellow) are over plotted on the vertical components of the magnetic field map with iso-contours at +150 G (-150 G). The length of the vectors indicates magnitude of B_h and the arrows show direction. Here, we notice the twist in converging horizontal vector magnetic fields in the south polarity region before the beginning of the flare.

In the Figure 18, we show the time evolution of total line-of-sight magnetic flux and the net vertical current in the north and south polarities of the active region, separately, during 03:00-10:00 UT on 11 April 2013.

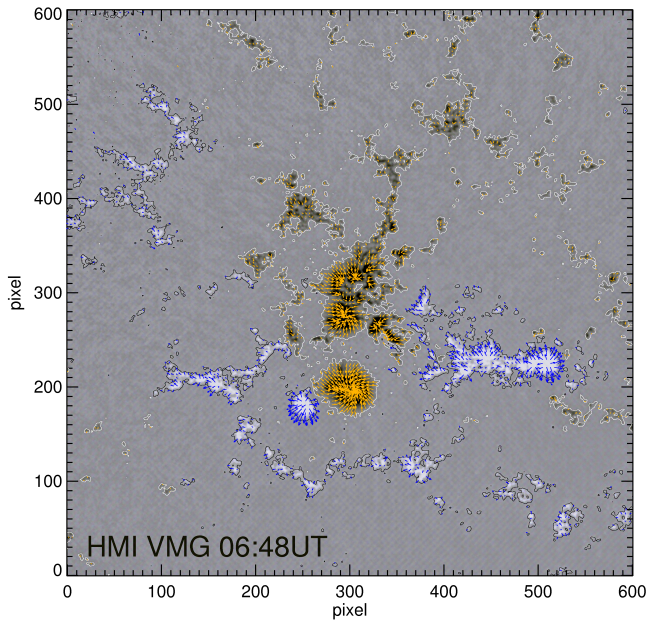


Figure 17: Typical vector magnetogram of the active region NOAA 11719 obtained from HMI instrument onboard SDO spacecraft at 06:48 UT on 11 April 2013. The horizontal magnetic field ($B_h = \sqrt{B_x^2 + B_y^2}$) vectors in blue (yellow) are over plotted on the map of vertical components of the magnetic field with iso-contours at +150 G (-150G). The length of vectors indicates magnitude of B_h and arrows show the direction. The total field-of-view is 300×300 arc-sec² with pixel scale equivalent to 0.5 arc-sec.

The total line-of-sight magnetic flux show continuous decrease in both the polarities of the active region during 03:00-10:00 UT while the flare started at 06:55 UT. The net vertical current starts increasing in both the polarity regions before the onset of the flare and maintains higher values than earlier during the flare. This increase of current is generally considered to be precursor of the occurrence of eruptive events like flares and CMEs as has been reported earlier by several researchers. Further, it is also observed that the north polarity region is having negative net current while the south polarity region is having positive net current. This implies negative signed helicity of the active region flux system, which is consistent with the magnetic channel of inverse-S sigmoid as seen in the He II 304 Angstrom images obtained from AIA instrument.

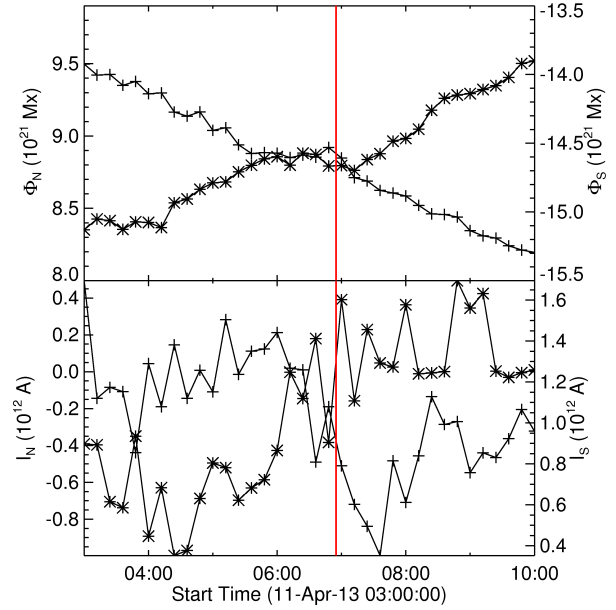


Figure 18: The top panel shows the time evolution of the total line-of-sight magnetic flux in the north and south polarities of the active region NOAA 11719 during the time interval 03:00-10:00 UT on 11 April 2013. The curve with plus sign (+) is for north polarity region while that with asterisks (*) is for south polarity region. The bottom panel shows the time evolution of net vertical current in the north and south polarities of the active region with the aforementioned convention of symbols. The vertical red line represents the start time of the flare as seen in the GOES 1-8 Å soft X-ray flux.

(B. Kumar, A. Raja Bayanna, P. Vemareddy, P. Venkatakrisnan, and S. K. Mathew)

Flare-induced oscillations in the solar active region

It is believed that flares can induce oscillations in the Sun. We study the photospheric and chromospheric oscillations in the solar active region NOAA 11719 during a large two-ribbon flare that occurred in this active region on 11 April 2013. For this purpose, we employ nearly simultaneous observations from HMI and AIA instrument onboard SDO spacecraft and the H-alpha observations from the ground based network of solar telescopes, GONG. The HMI data used here are the Fe I 6173 Angstrom photospheric Dopplergrams taken at a cadence of 45 sec during and before the aforementioned flare on 11 April 2013. The AIA data comprise of the He II 304 Angstrom filtergrams taken at a cadence of 45 sec spanning the flare and pre-flare epochs. The pixel scale in both the HMI and AIA data used here is 0.5 arc-sec per pixel. The GONG instrument located at the Udaipur Solar Observatory fully covered this flare event in H-alpha 6563 Angstrom with a cadence of 60 sec and a pixel scale of 1 arc-sec per pixel. We have used these chromospheric H-alpha images from the GONG, along with the HMI and AIA images to study the flare-induced oscillations in the active region during this large two-ribbon flare. A two-point backward difference filter is applied to the sequence of images to eliminate the slowly varying components and to enhance the fast oscillatory signals in the time domain. These filtered images are

then used to estimate the Power Spectrum of the oscillatory signals before (4:30-06:00 UT) and spanning (06:50-8:20 UT) the flare using the techniques of Fast Fourier Transform.

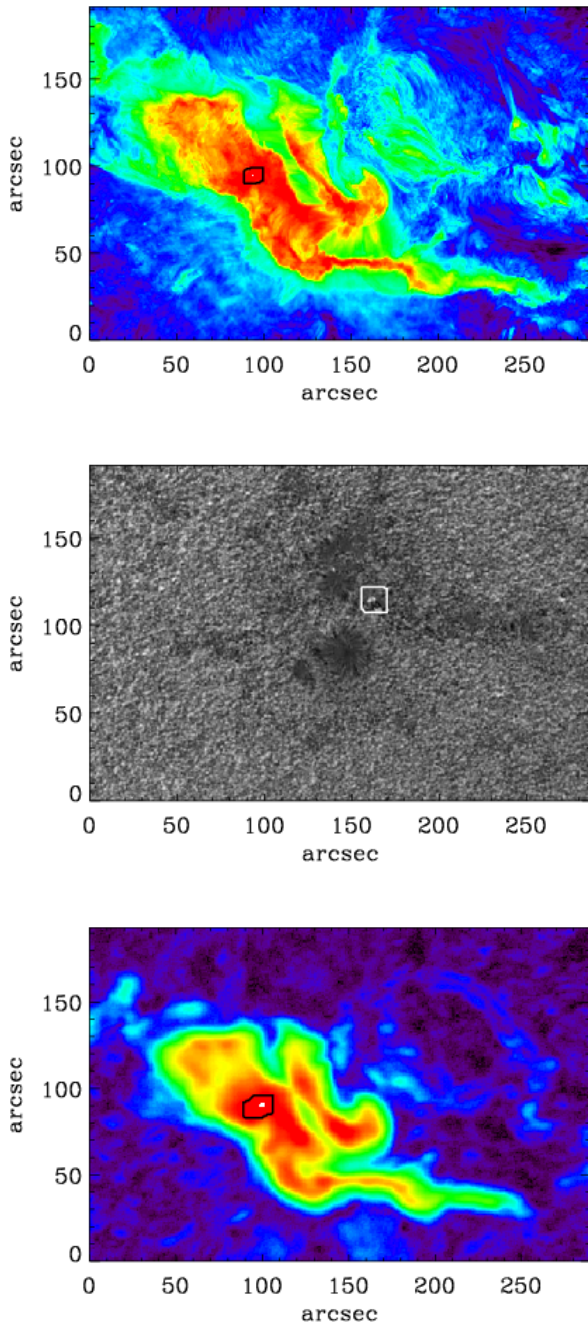


Figure 19: Root Mean Square (RMS) maps of the solar active region NOAA 11719 obtained from the Fe I 6173 Angstrom Dopplergrams from SDO/HMI (top panel), He II 304 Angstrom filtergrams from SDO/AIA (middle panel), and the H-alpha 6563 Å filtergrams from Udaipur GONG instrument (bottom panel) spanning the flare (06:50-08:20 UT) event on 11 April 2013. In these RMS maps, the localized regions with relatively high values of RMS are shown in boxes.

We have also constructed the Root Mean Square (RMS) maps from the filtered images spanning the flare in order to locate the flare affected areas in the active region. In the Figure 19, we show the RMS maps obtained from the Fe I 6173

Angstrom Dopplergrams, He II 304 Å filtergrams, and the H-alpha 6563 Å filtergrams spanning the flare.

In these RMS maps, the localized regions with relatively high values of RMS are shown in boxes. We have selected around 20 pixels in these localized regions and estimated the temporal Power Spectra for these pixels before and spanning the flare. The Power Spectra over these pixels are averaged to deduce a stabler spectrum over these flare affected areas. In the Figure 20, we show the average Power Spectra obtained from the Fe I 6173 Dopplergrams, He II 304 Å filtergrams, and the H-alpha 6563 Å filtergrams for the epochs, before and spanning the flare.

These Power Spectra show the signatures of flare-induced photospheric and chromospheric oscillations in the active region during this large two-ribbon flare.

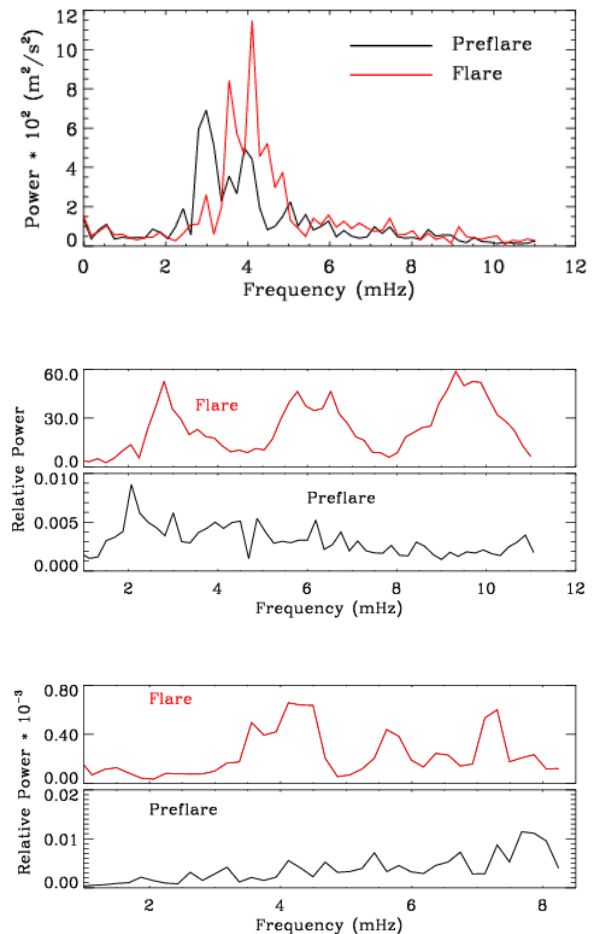


Figure 20: Average Power Spectrum estimated over the pixels located in flare affected areas in the active region NOAA 11719 obtained from the Fe I 6173 Dopplergrams from SDO/HMI (top panel), He II 304 Angstrom filtergrams from SDO/AIA (middle panel), and the H-alpha 6563 Angstrom filtergrams from Udaipur GONG instrument (bottom panel) for the epochs, before (04:30-06:00 UT) and spanning the flare (06:50-08:20 UT) event on 11 April 2013. The signature of flare-induced oscillations is seen in the different layers of the Sun.

It is also observed that the power spectrum of the photospheric velocity oscillations show significant flare-induced enhancement in a localized region of the active region, which is located far away from the sites of the

flare-ribbons as seen in the He II 304 Angstrom and H-alpha 6563 Angstrom images. Such events are rare and require a different explanation than the particle beam model or the model considering the back-reaction of shocks launched at the solar photosphere during the chromospheric evaporation and accompanied by chromospheric condensation during the flares. A detailed study is being done to understand these flare-induced oscillations.

(B. Kumar, A. Raja Bayanna, S. K. Mathew, and P. Venkatakrishnan)

Evolution of Coronal Mass Ejections in the Heliosphere and their Arrival Time prediction at 1 AU

Coronal Mass Ejections (CMEs) are expulsions of huge magnetised plasma from the Sun into the heliosphere which are responsible for major space weather events. The estimation of kinematics and prediction of arrival time of CMEs is of prime concern to a solar-terrestrial physicist; therefore, many reconstruction techniques have been developed for estimation of kinematics of CMEs. It is a useful step to identify the most accurate method for practical purpose of forecasting CME arrival time at the Earth.

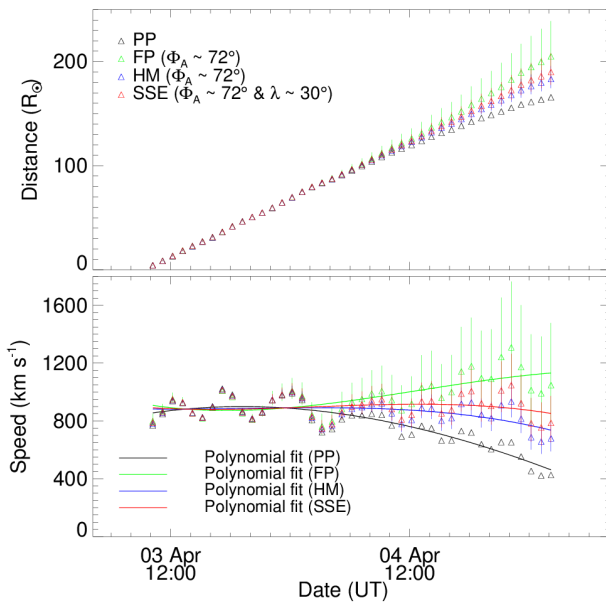


Figure 21: In the top panel, estimated distance profiles based on application of the four single spacecraft methods (Point-P, Fixed-Phi, Harmonic Mean and Self Similar Expansion) for the tracked feature of 2010 April 3 CME is shown. In the bottom panel, speed profiles derived from adjacent distances (solid line shows the polynomial fit) is shown. Vertical lines show the error bars.

To assess the performance of reconstruction techniques in the estimation of arrival time, we selected three CMEs launched with different speeds from the Sun on 2010 October 6, April 3 and February 12 and which propagated into different ambient solar wind environment. We constructed the time-elongation maps (J-maps) for these CMEs using running difference images obtained by coronagraph (COR2: 2-15

Rs), Heliospheric Imagers (HI1: 12-90 Rs and HI2: 70-330 Rs). Using J-maps, we continuously tracked the selected features of these CMEs in the heliosphere. We implemented a total of 10 reconstruction techniques, ranging from single spacecraft methods and their fitting analogues to stereoscopic techniques, on the selected CMEs. We have also used the Drag Based Model (DBM) to estimate the kinematic properties of CMEs for the distance range beyond which a CME could not be tracked in J-maps. Using these techniques, we derived the kinematics and arrival time of selected CMEs. We compared the estimated kinematics and also assessed the relative performance of reconstruction techniques in estimating CME arrival time near the Earth. The estimated arrival times and transit speed of each CME were also compared with the actual values measured in in situ observations near the Earth.

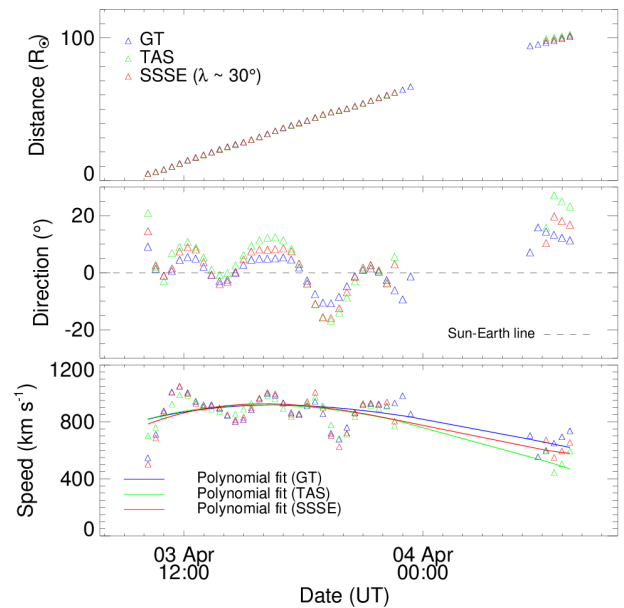


Figure 22: From top to bottom panels, distance, propagation direction (relative to the Sun-Earth line) and speeds profiles are shown for tracked feature of 2010 April 3 CME as derived using three stereoscopic (Geometric Triangulation, Stereoscopic Self-Similar Expansion and Tangent to A Sphere) methods.

The derived kinematics from the four single spacecraft methods, applied to the time-elongation profile of the 2010 April 3 CME extracted from the STEREO-A J-maps, are shown in Figure 21. The uncertainties introduced in the results due to certain assumptions involved in these methods are also quantified and are shown with error bars.

We implemented three stereoscopic methods which use the CME elongation-time profiles derived from two vantage points. Results from the stereoscopic techniques are shown in Figure 22. We also used the three techniques which are based on the fitting of derived time-elongation track of CMEs from the J-maps. We found that stereoscopic methods are always superior to single spacecraft methods to estimate the CME kinematics and hence for the prediction of CME arrival time and speed at 1 AU. Irrespective of CME characteristics, among the stereoscopic methods, the Tangent to a sphere (TAS) method is found to be the best for arrival time prediction.

We also found that Harmonic Mean (HM) method performs the best among the single spacecraft techniques. We also found that use of DBM reduced the errors, particularly for those CMEs which are launched in slow solar wind and are tracked to smaller elongation angle in J-maps. Our study reveals that using remote sensing observations from HIs, the arrival time estimation of CMEs improved than using only observations near the Sun.

This work was carried out in collaboration with Jackie A. Davies of STFC, Rutherford Appleton Laboratory, UK.

(W. Mishra and N. Srivastava)

Interaction of Coronal Mass Ejections in the Heliosphere:

Around solar maximum phase, CMEs are launched from the Sun in quick succession which under certain favourable initial conditions can interact or collide with each other during their heliospheric propagation.

If such an interaction occurs, then various space weather prediction schemes may not be successful unless the post-collision CMEs characteristics are taken into account. Such interacting CMEs on their arrival to the Earth may enhance geomagnetic disturbances. Therefore, CME-CME interactions are important, in particular to understand their nature of collision, kinematics and arrival time near the Earth. We selected three Earth-directed CMEs launched successively during 2011 February 13-15 to study their geometrical and kinematic evolution.

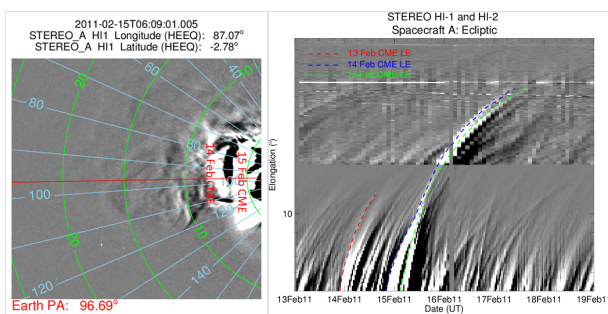


Figure 23: In left panel, collision between February 14 and 15 CMEs is shown in running difference images of HI1-A FOV. Contours of elongation (green) and position angle (blue) is overlaid on the image. The horizontal red line marks the position angle of the Earth. In right panel, time-elongation map (J-map) for STEREO-A using running difference images of HI1-A and HI2-A is shown. The tracks of February 13, 14 and 15 CMEs are shown in red, blue and green, respectively.

At this instant, the angle of separation between the twin STEREO spacecraft was 180° , therefore, both spacecraft observed these CMEs as limb CMEs. The CMEs of February 13 and 15 were fast, with speeds of 500 and 900 km s^{-1} , respectively; while CME of February 14 was slow with a speed of 300 km s^{-1} in COR2 field-of-view (FOV). We examined the difference in geometrical evolution of slow and fast CMEs during their propagation. Examining the running difference images, we noticed that CME of February 15 approached

and caught up with the CME of February 14 in HI1 FOV (left panel of Figure 23). Further, we constructed the J-maps in the ecliptic plane for these CMEs as shown in right panel of Figure 23. Tracking the CMEs continuously in the heliosphere, we estimated their de-projected kinematics in COR and HI FOV using various reconstruction techniques. We found strong evidence of interaction and collision between CMEs of February 14 and 15 around 8 Rs in COR2 FOV and around 28 Rs in HI1 FOV, respectively while CME of February 14 caught the CME of February 13 between 138-187 Rs in HI2 FOV. The estimated kinematics of these CMEs before and after their collision is shown in Figure 24.

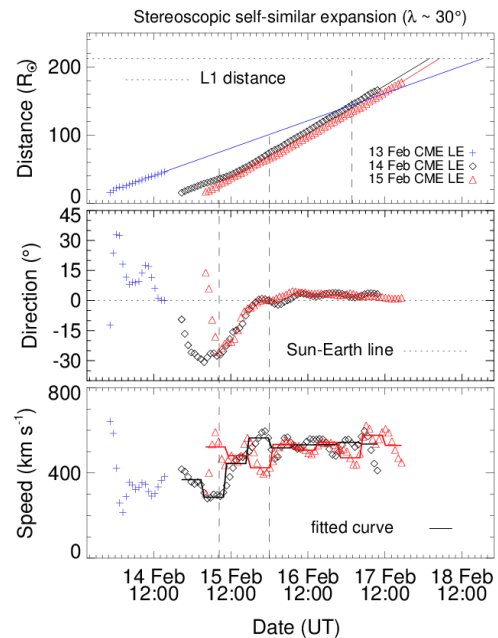


Figure 24: From top to bottom, distance, propagation direction and speed (as obtained using SSSE method) of three selected CMEs are shown. In the top panel, horizontal dashed line marks the heliocentric distance of L1 point. In the middle, dashed horizontal line marks the Sun-Earth line. In the bottom panel, speed shown with symbols are estimated from differentiation of adjacent distance points while speed shown with solid line is determined by differentiating the first order polynomial for estimated distance for each five hour interval. From the left, first and second vertical dashed lines mark the start and end of the collision phase of February 14 and 15 CMEs. In the top panel, rightmost vertical dashed line marks the inferred interaction between February 13 and 14 CMEs.

(W. Mishra and N. Srivastava)

Contraction and disruption of coronal magnetic fields during the failed eruption of a filament and associated M6.2 flare

We have carried out a multi-wavelength study of the failed eruption of an active region filament that occurred in NOAA 10646 on 2004 July 14 using TRACE, RHESSI, and NoRH observations. The associated M6.2 flare exhibited significant pre-flare activities for 30 minutes in the form of sequential brightening of low lying coronal loops and simultaneous contraction of large overlying loops. In the beginning the speed of contraction was 6 km s^{-1} which increased to

25 km s^{-1} during the last ten minute interval. The X-ray observations taken by GOES and RHESSI reveal a very gradual variation of intensity during the pre-flare phase and at the time of the peak flux, X-ray sources are observed up to 12-25 keV energy band from low lying coronal loops.

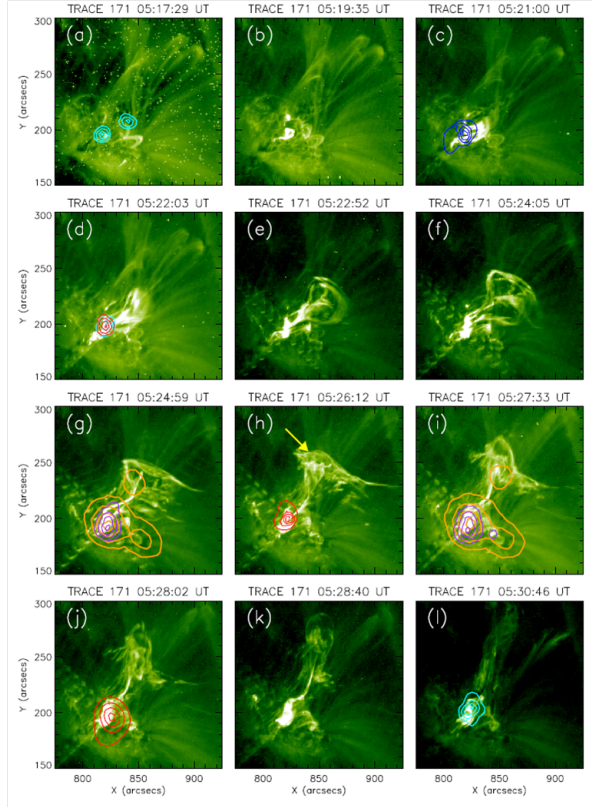


Figure 25: A few representative TRACE 171 Å images showing the evolution of a failed filament eruption and associated HXR and MW sources. Color codes for HXR and MW sources: 12-25 keV (cyan), 25-40 keV (red), 40-100 keV (blue), 17 GHz (yellow), and 34 GHz (magenta).

The onset of the filament eruption is accompanied with the impulsive rise of HXR and MW emissions and the respective light curves indicate multiple peaks. The HXR and MW sources during the impulsive phase show complicated temporal and spatial evolution. Apart from prolonged HXR and MW emissions from the foot-point region, MW sources at 17 GHz were observed intermittently from coronal heights. Following the peak phase of the flare, the filament eruption was suppressed and halted by the overlying field lines at a height of $5 \times 10^4 \text{ km}$. The complete failure of the eruption is further supported by the SOHO/LASCO observations which did not show any coronal mass ejection (CME) associated with this flare. The pre-flare observations at the flare site and its coronal environment provide evidence for the breakout model of solar eruptions as the triggering mechanism for the onset of fast rise of the filament. However, the kinematic and morphological evolution of filament at later stages is quite complicated and suggests complex interaction of magnetic flux rope of rising filament and overlying coronal loops (Figure 25).

(B. Joshi and U. Kushwaha)

Activation phases of a solar prominence eruption and associated flare-CME event

We have analyzed multi-wavelength observations of a solar erupting prominence and accompanied M1.8 flare that occurred in active region NOAA 11548 on 2012 August 18. The erupting prominence undergoes interesting morphological evolution and eventually leads to a partial halo coronal mass ejection (Figure 26).

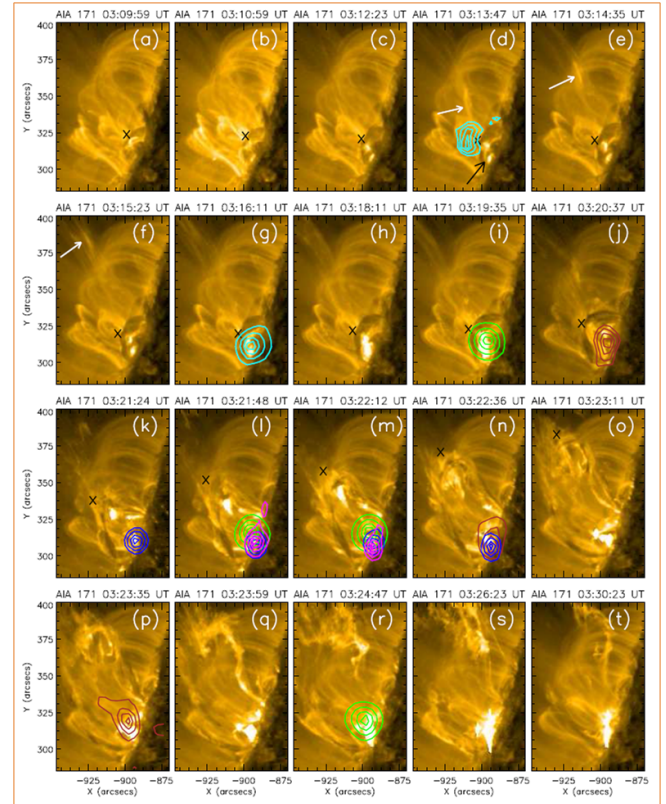


Figure 26: Series of AIA 171 Å images showing prominence activation, expansion and eruption in AIA/SDO field of view. The cross symbol (x) indicate the apex of rising prominence. The RHESSI X-ray sources in several energy bands are shown by different colors: 10-15 keV (sky), 12-25 keV (green), 25-50 keV (blue), 50-100 keV (blue), and 100-300 keV (magenta).

The availability of simultaneous multi-wavelength measurements obtained from RHESSI, SDO, SOHO, STEREO, and NoRH provide us with a unique opportunity to understand the crucial physical processes during activation, expansion and propagation of the prominence. Prior to the prominence destabilization and onset of the flare, significant activities were observed in the overlying coronal region, such as, jet like eruption, writhing motion of a rising flux rope, and localized EUV sources. The X-ray light curves of the flare clearly indicate a pre-cursor phase during which the prominence undergoes a slow evolution with a constant velocity of 9 km/s.

Complex type III radio bursts were observed prior and during the flare impulsive phase which suggest opening of coronal field lines and ejection of energetic particles into the inner heliosphere. The fast rise phase of the prominence began

with the impulsive non-thermal HXR emission up to 150 keV. During this phase, the prominence speed was found to increase almost linearly with a constant acceleration of 390 m s^{-2} , reaching a maximum of 232 km s^{-1} at a height of 44 Mm above the solar surface. From SOHO/LASCO observations, we were able to clearly track the associated CME up to a height of $16 R_{\odot}$. The velocity of CME is observed to decrease from 1260 km s^{-1} to 400 km s^{-1} with a constant deceleration of 83.74 m s^{-2} .

These observations reveal that although the slow rise phase of the prominence was associated with the heating in the core region, eruption of the prominence was likely triggered due to the breakout reconnection initiated at the overlying magnetic loops during the pre-impulsive phase of the flare.

(U. Kushwaha and B. Joshi)

Quasi-Static 3D Magnetic Field Evolution in Active Region NOAA 11166 During X1.5 Flare

We analysed a flare of X-class involving main quasi-elliptical ribbon in addition to two elongated remote ribbons. Such flares of elliptical geometry occur in a specific configuration of magnetic topology, under different evolving conditions of boundary fields. We interpret the observations based on quasi-static force-free model that led us to have insight into the topological scenario of flaring AR.

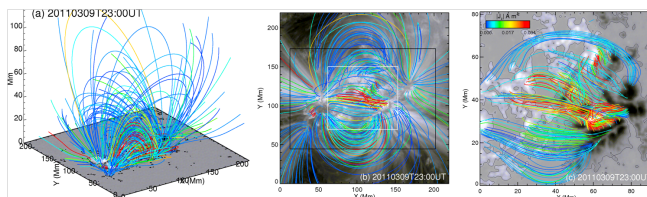


Figure 27: Field extrapolation and magnetic field structure of AR 11166 on March 9, 2011 at around 23:00UT. (a) Traced fieldlines shown on normal component of field at the boundary, in the full computation domain of $300 \times 300 \times 300$ grid cells displayed in the perspective 3D view (b) Fieldlines plotted on the AIA 171A passband image as viewed in the projected 2-D plane, Note that the field line's orientations well resemble the plasma tracers. The black rectangular box represents the field-of-view (FOV) of the AR displayed in Figure 14 and the white one indicates the flaring region covering the extended ribbons, hereafter refer as region of interest (ROI), (c) the ROI with fieldlines that land within the FOV. In all (a-c) panels, the fieldlines are color coded according to the vertical current at the lower boundary ($J_z [z=0]$) as shown with color scale in (c).

We used coronal imaging information in different wavelengths corresponding to different heights from Atmospheric Imaging Assembly (AIA), and photospheric Vector magnetic field observations from Helioseismic Magnetic Imager (HMI) on board Solar Dynamic Observatory. Using photospheric magnetic fields as boundary conditions, we constructed 3D-magnetic above the AR by potential and non-linear force-free field (NLFFF) approximations at every 12 minutes around the time of X1.5 flare occurred in NOAA 11166 on March 9, 2011.

For time frame at 23:00 U.T., in Figure 27 (a-c), the field lines are traced and plotted in colour code according to the vertical current at their footpoints on the boundary. From the oblique view, the field lines originating from sunspots are overlying (up to the heights of 110Mm) to those low-lying (below 40mm) at the flaring region with current flowing comparatively higher along them. In panel (b), the same fieldlines are plotted over 171Å channel image for comparing them with coronal plasma tracers as proxies of fieldlines. Plasma structures from major sunspots resemble those with less current flowing fieldlines, indicating potential field approximation a valid model to them. However, compact, stressed locations generally observed at flaring sites as here, having complicated structures are difficult to model even with general NLFFF approximation. Most sheared (in red-) fieldlines are located along the PIL around SSP. It is worth to mention that this is the only location that differs with the rest when compared to that of PF modelled magnetic structure, suggesting non-potential, higher energy state.

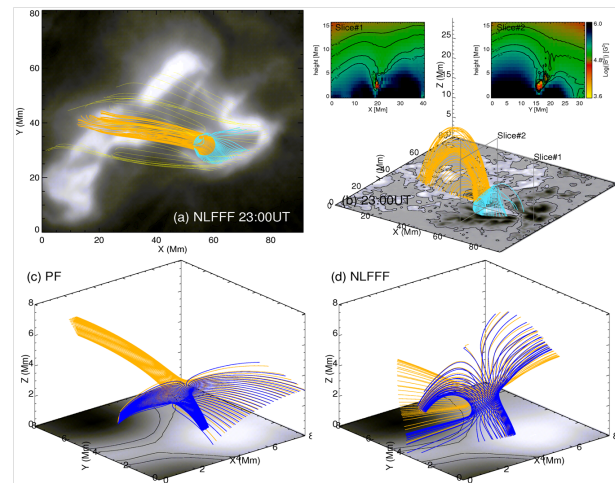


Figure 28: Fan-Spine topology in AR 11166 (a) Top view of topological skeleton with dome shaped fan fieldlines (cyan) landing along ribbon and spine fieldlines (orange) connecting remote ribbon RB3. Note that the fieldlines from about outer edge of the ribbon RB1 are deployed in yellow, showing its obvious connectivity with extended remote ribbons RB2 and RB3. (b) Same structure plotted on B_z boundary map depicted in 3D view. The field $|B|$ is extracted in the cross-section planes of slice#1, slice#2 containing the null point and displayed in the insets. Note the null location approximately at 2.11Mm in both inset plots. (c) Close-up view of the magnetic structure in PF model around the null in the volume of 8Mm side of cube. Fieldlines below (above) the fan plane are colored in blue (orange) for clarity. Evidently, it delineates fan-spine topology with fan fieldlines constructing Σ -surface, inner and outer spine fieldlines as γ -line.(d) Same as panel (c) in NLFFF model. Presence of fan-spine topology is obvious. Spiral nature of fieldlines (in blue) indicates presence of current and twist resulting complicated structure around the null.

Those field lines which are little away from PIL in surrounding negative flux are connecting remote positive flux regions, passing over isolated positive polarity SSP and covering it like dome shaped structure. Such configurations are possible locations to form null points with a specific topology related to the reconnection. We found null points in every frame of PF model from 20:00 UT to 23:36 UT. However, in the NLFFF model fields, the algorithm did not find any null in few frames, might be the reason pertinent to the noise and computational errors. In the NLFFF field, the location of null is (78.04, 43.55, 3.76) at 23:00 UT frame in the ROI. In all other frames, null

point is observed about this grid cell at a height of about 2.11Mm and above. The reason to find no null after 23:36 UT in either model would likely be related to structural change of magnetic configuration by reconnection and signifies the topological change during flare.

In Figure 28(b), the same structure is shown in oblique 3D view, over plotted on B_z distribution on the boundary, making it clear the above picture of topology. For reassurance, the field strength $|\mathbf{B}|$ distribution in the horizontal, vertical planes of slice#1 and slice#2 are extracted. They are shown in insets with logarithmic scale in the same panel. Note that small field (yellow) spread around the null extending along the spine direction, further confirms the existence of magnetic null. In panel 28(c), the fan-spine topology is shown in a small cubical volume of $8 \times 8 \times 8 \text{ Mm}^3$ side, centred on the null.

At this scale, the unwanted noise in the numerically extrapolated field did not yield directly to find such topology, until we smooth the field with a boxcar of 3 grid cells. Fieldlines at a radius of 0.7 Mm from null are traced on either side of the fan plane. Clearly we can notice that the fan surface extends to intersect along ribbon RB1, outward spine (orange) reaches to remote ribbon RB3 and inner spine (blue) lands at middle part of the positive polarity SSP. Similarly, from the NLFFF solution (panel (d)), the existence of fan-spine topology is obvious. Because of tilted fan plane orientation with spine, fieldlines that observed in fan plane in PF solution are becoming aligned with spine. In addition, spiral nature of fieldlines in fan plane delineates twist and current forming complex topological structure around the null. Thus we identify and confirm the presence of 3D coronal null-point with associated fan-spine topology associated to the ribbons in the flaring region. In Summary, we envisioned the existence of a particular type of topological structure associating the null point. The existence of null points in the magnetic structure of the active region is of fundamental significance to 3D-reconnection process. The flare location with HXR emission is well coincides with the null point location implying possibility of null point reconnection. Moreover, ribbon RB1 is almost co-spatial with the intersection of fan-surface with the lower boundary, and outward spine falls on ribbon RB3. Fieldlines from outer edges of RB1 linked to extended regions of remote ribbons RB2 and RB3, explaining topological relevance of observed ribbon emissions, according to flare models. This work is in collaboration with Dr T. Wiegmann of MPI, Lindau, Germany.

(P. Vemareddy)

Evolution of Observed Net Current in the Solar Active Region NOAA 11158

The generation of electric current in astrophysical plasma has been clearly explained by E.A. Parker in terms of the distortion of the magnetic field by external forces applied by a field free plasma. According to this, the net current flowing across the photospheric layer of a sunspot must be zero. However a clear evolution of the observed net current from zero value to a large non-zero value was seen

during the emergence of magnetic flux in NOAA AR 10930. Although Parker does warn about the detection of spurious net currents due to inadequate spatial resolution of present day magnetographs, it remained a mystery as to why this admittedly spurious net current showed such a systematic evolution. In this paper, we study the evolution of the net current in AR 11158 for the N and S polarity sunspots of the active region as a whole and then examine the evolution in the two different regions which produced several CMEs and flares. We identify plausible locations that account for the systematic evolution of the observed, non-neutralized, net current. AR 11158 emerged on February 11, 2011 with prominent, major sunspots appearing on the disc with positive (north) polarities P1, P2, P3 and negative polarities N1, N2, N3 (south) as shown in a typical vector magnetogram in Figure 29.

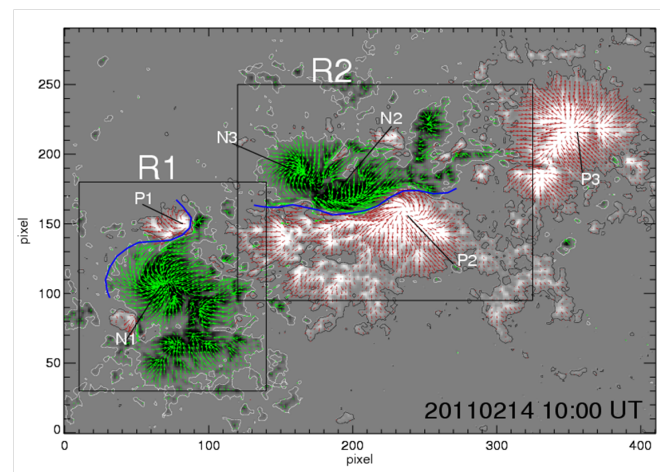


Figure 29: Typical Vector magnetogram of AR 11158 at 10:00UT on February 14, 2011. The horizontal field vectors in red (green) are over plotted on vertical component of magnetic field map with iso-contours at 150G (-150 G). The dominant sunspot polarities are marked as P/N* within the rectangular regions of interest R1 and R2 (sub-regions) for further correspondence. The blue solid curves represents the polarity inversion lines (PILs) separating positive and negative vertical flux regions. The field of view is $207 \times 146 \text{ arcsec}^2$ (1 pixel = 0.5 arcsec).

The horizontal field vectors are almost parallel to the polarity inversion lines (PILs) between N1, P1 and N2, P2. Such an alignment is known as sheared configuration where field lines become stressed to store magnetic energy. Thus there are two such R1 and R2 (shown in rectangular boxes) with high activity. According to the soft X-ray flux information of GOES, this AR produced 15 C, 2 M and one X class flares that are mainly associated with sub-region R2, and many CMEs associated with R1, during 13-16, February, 2011 with continued activity till disk transit on February 21.

For evolution study, the integrated magnetic flux and vertical currents (IN, IS) in both polarities are plotted separately, as a function of time, respectively the entire AR (top panels), region R1 (middle panels), region R2 (bottom panels) in Figure 30. This study of observational analysis, infers the following major conclusions. The net current in each polarity over the entire AR exhibits systematic evolution with decreasing trend in the first half of the observation time changing to an increasing trend after a major flare.

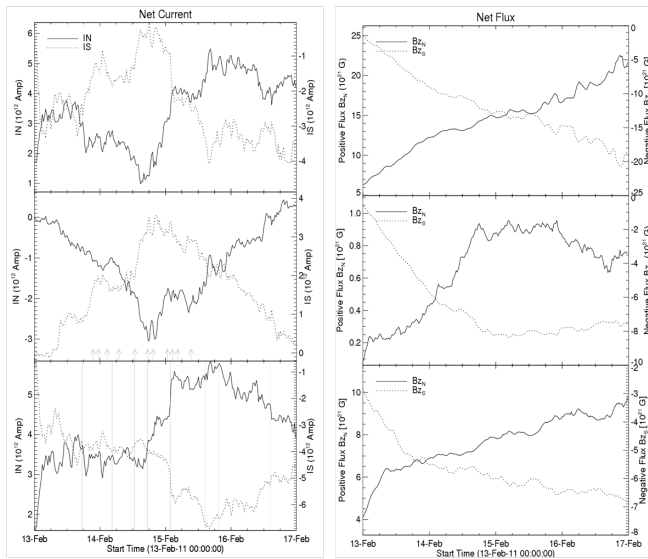


Figure 30: Evolution of magnetic flux (vertical current) over entire AR 11158, sub-region R1, sub-region R2 in top, middle and bottom panels of first (second) column, respectively. Vertical lines (Bottom right panel) indicate the initial timings of flares and arrows (middle right panel) are that of CMEs, and the same will be used in later plots without mentioning further.

The net current in the first phase is mainly contributed from sub-region (R1) having dominant rotating sunspots caused by emergence of a twisted flux rope, whereas in the second phase it is contributed from sub-region (R2) having dominant large shear motions caused by emergence of twisted strands of a flux rope. The systematic evolution of the observed net current is seen to be correlated with the length of strongly sheared PIL in both, R1 and R2. The non-observability of a field free plasma interface at the PIL (due to lack of resolution) is very likely to be the reason for non-observability of neutralization of the observed net current.

This work is in collaboration with S. Karthikreddy of IIST, Thiruvananthapuram.

(P. Venkatakrishnan and P. Vemareddy)

Formation of magnetic islands and their ejections: A numerical study

The high Lundquist number $S (\approx 10^{14})$ of the solar corona renders it a near-ideal magnetofluid where the condition of flux-freezing holds valid. Under this condition of flux-freezing the coronal magnetofluid can be partition into contiguous subvolumes of fluid each of which entraps its own subsystem of magnetic flux. During any dynamical evolution, these subvolumes are expected to press into each other and in the process two subvolumes can come arbitrarily close by ejecting out the interstitial fluid. Then, depending on the orientations of magnetic field lines on the two interacting subvolumes, the magnetic field at the common surface of interaction may become discontinuous and a current sheet (CS) is formed there. In a near-ideal system this discontinuity

in magnetic field never attains its true mathematical limit, since the developing current sheets decay through magnetic reconnection as a minimum threshold in local S is achieved where the otherwise negligible Ohmic dissipation becomes important.

If length of these developing CSs is sufficiently larger than the corresponding thickness, then magnetic islands (closed magnetic field lines) are formed through magnetic reconnection. Such formation of magnetic islands are observed in laboratory plasma devices like the Tokamak where it leads to a loss in confinement. Also, the ejection of closed magnetic field lines--nomenclatured as magnetic ejecta; are widely observed at the solar atmosphere.

In the following we numerically demonstrate the formation of magnetic islands through magnetic reconnection using the Implicit Large Eddy simulation (ILES) mode of the numerical model EULAG-MHD, a magnetohydrodynamic extension of the standard EULAG. For the purpose, we consider an incompressible viscous magnetofluid with infinite electrical conductivity where the initial magnetic field is the superposition of two linear force-free fields, and has the same morphological structures as the coronal magnetic field. Here simulations are carried out for a uniform grid resolution of 96^3 in a physical domain of extensions 10Mm in the three directions of the Cartesian geometry; morphed in a computational domain of size $(2\pi)^3$ while the time is normalized to the Alfvén transit time. The computations are performed as the magnetofluid relaxes from an initial static state via viscous relaxation.

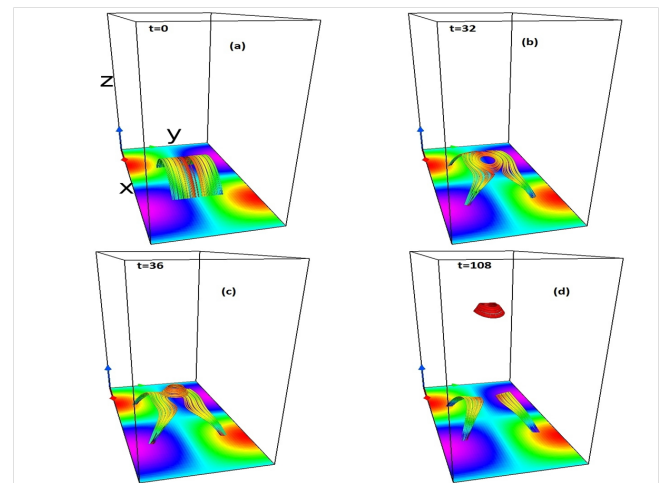


Figure 31: Time Evolution of magnetic field lines showing the formation and ejection of magnetic islands.

The solenoidality of the evolving magnetic field is maintained by imposing an open boundary condition at the vertical boundaries (z direction) while the lateral boundaries (x and y) are assumed to be periodic. The evolution of magnetic field lines are depicted in Figure 31. Because of the periodicity, in Figure 31 we have displayed only half of the physical domain in the y -direction since similar features are expected to be repeated in the other half of the domain. The physical steps of the evolution are the following. The initial non-zero Lorentz

force pushes two oppositely directed field lines (Figure 31a) about the line $y = \pi/2$ toward each other. Noteworthy is the initial amplitude of Lorentz force, which because of the chosen boundary conditions is significant only at the lower z -constant planes and is maximum at $x = \pi/2, 3\pi/2$ along the line $y = \pi/2$. The resulting push then deforms the bottom of a magnetic field line more than its top which generates the two X-type nulls at $x = \pi/2$ and $3\pi/2$ – as depicted in Figure 31b.

Subsequently, the neighbouring field lines get reconnected at the X-type nulls by a model dependent residual magnetic diffusivity characteristic of an Implicit Large Eddy Simulation generated in response to under-resolved scales. This magnetic reconnection results in formation of the closed magnetic structures - nomenclatured as magnetic islands. These islands form an isolated flux systems in a sense that the closed reconnected field lines are not topologically identical to the initial open field lines. The increase in size of these magnetic islands with time can be attributed to an increase in the reconnected flux. The magnetic ejecta then liftoff in the vertical (as shown in Figures 31 c–d) since the magnetic pressure below a magnetic island is greater than the same above the island – a reminiscent of the initial Lorentz force distribution in the vertical.

This work is done in collaboration with Piotr K. Smolarkiewicz of European Center for Medium-Range Weather Forecast, Reading, UK.

(D. Kumar and R. Bhattacharyya)

Formation of magnetic discontinuities through viscous relaxation

A magnetofluid with infinite electrical conductivity evolves with magnetic field lines being tied to the fluid parcels---referred to as the flux freezing or frozen-in condition. Under this condition of flux freezing, it is always possible to identify fluid surfaces (identified by the overlaying material elements) to local magnetic flux surfaces (MFSs) across which the magnetic flux is zero. To further focus on ideas, let us consider a volume of magnetofluid as a stack of such MFSs, albeit of complex geometry. In an evolving magnetofluid, these flux surfaces are expected to contort non-uniformly in response to an unbalanced force resulting in deforming field lines lying on it. In a favorable condition, the net effect may culminate into pushing localized portions of two flux surfaces towards each other. As a result of this pushing between portions of two interacting MFSs the interstitial fluid gets squeezed out, bringing local portions of the two interacting MFSs arbitrarily close, such that an infinitesimally small resistivity can become significant. Depending on the orientations of magnetic field lines on the two MFSs then, the magnetic field may get discontinuous and hence according to Amperes law form current sheet (CS) which is an enhanced volume current density localized at the common surface of interaction. Recognizing that this common surface of interaction is also a part of the interacting MFSs, tracking the evolution of MFSs gives a direct visualization and hence a better physical understanding of the process

of CS formation. The ubiquity of CS formation in an equilibrium magnetofluid satisfying the frozen-in condition is addressed by the Parker's magnetostatic theorem which is based on a general failure of a continuous interlaced magnetic field in maintaining simultaneously the local force-balance, along with the preservation of global magnetic topology as a consequence of flux-freezing. To be in conformity with these analytical requirements for generation of CSs, the following numerical demonstration utilizes the physical process of viscous relaxation where a hydromagnetic fluid evolves to a terminal quasi-steady state while preserving its magnetic topology. Towards such a viscous relaxation, the magnetofluid is considered to be incompressible, viscous and having infinite electrical conductivity. The initial non-equilibrium magnetic field is constructed from a linear force-free field (lfff).

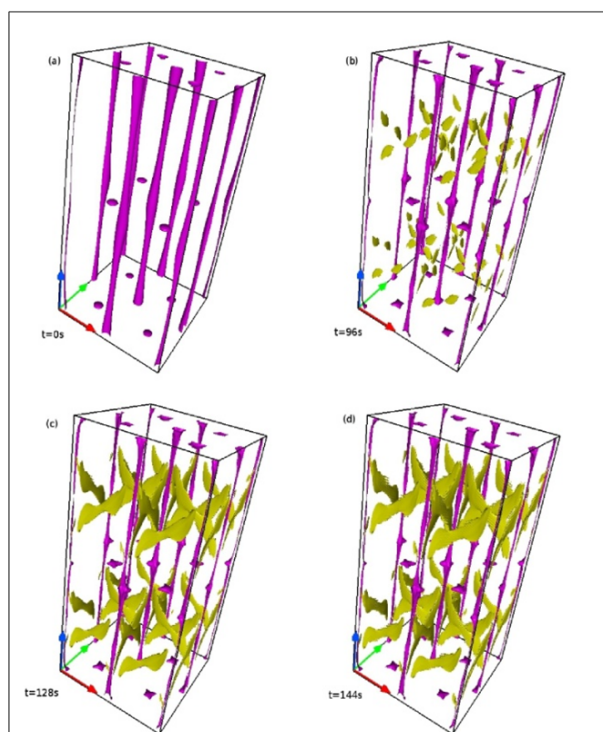


Figure 32: Time sequence of magnetic nulls (in pink) overlaid with J-30 surface (in yellow).

This construction is based on the understanding that the magnetic topology of the lfff is complex enough in terms of interlaced magnetic field lines along with the presence of 2D and 3D nulls. In addition, the lfff is a special solution of a force-free equilibrium which is also realizable in the solar corona. For a direct visualization of the development of CSs, we have further represented the initial magnetic field in terms of three pairs of local MFSs and advected these MFSs instead of the magnetic field. The preservation of the initial magnetic topology is achieved by relying on the second-order-accurate non-oscillatory advection scheme MPDATA (Multidimensional Positive Definite Advection Transport Algorithm). The simulations are carried out for a grid resolution of $128 \times 128 \times 256$ in a triply periodic Cartesian domain of horizontal (x and y) extent 2π and vertical (z) extent $2s_0\pi$ where s_0 is a constant, measuring the deviation of the initial magnetic field from the corresponding lfff. The initial fluid

velocity is assumed to be zero. The results are summarized below.

Figure 32 depicts the evolution of magnetic nulls overlaid with a selected isosurface of maximum current density $|J|_{max}$ having an isovalue which is 30% of its maximum value. Hereafter, we refer to this isosurface as J-30. An important property of this J-30 surface is in its appearance at spatial locations away from the magnetic nulls. This is a key finding of this work since CSs are generally expected to be formed near the magnetic nulls.

To further explore the origin of CSs away from the nulls, in Figure 32, we have plotted the evolution of a single local MFS overlaid with a selected isosurface of the corresponding component current density having an isovalue: 60% of the maximum total current density; referred to as the J_1-60 .

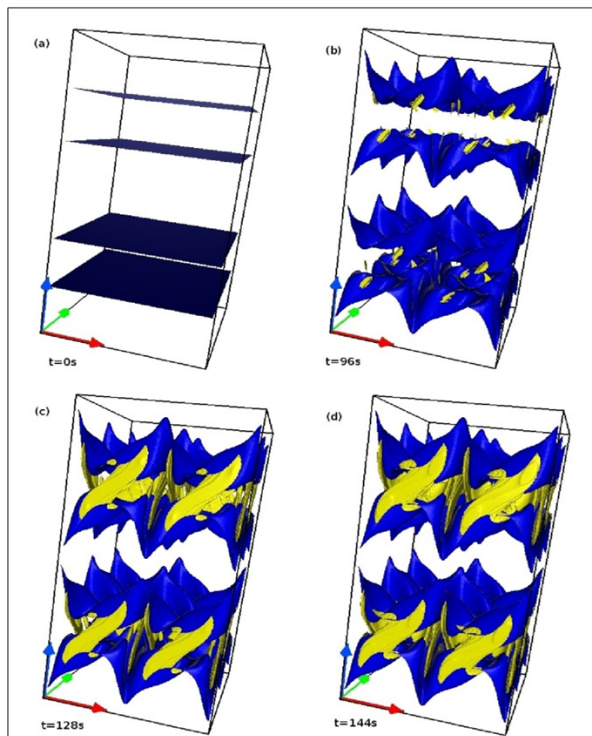


Figure 33: Time sequence of single flux surface (blue) overlaid with J_1-60 surface (in yellow).

Figure 33 clarifies the important finding that the appearance of J_1-60 surface is due to contortions of the corresponding local MFS. Evolution of other local MFSs further confirm that CSs are forming because of a favourable contortion of these flux surfaces in a way to bring portions of the same flux surface having oppositely directed field lines close to each other and thereby increasing the gradient of magnetic field. A contortion away from the magnetic nulls is then responsible for the appearance of CSs at spatial locations not co-located with the magnetic nulls and hence is supportive of the Parker's magnetostatic theorem in its generality.

(S. Kumar and R. Bhattacharyya)

Narrow-band imaging system for Multi-Application Solar Telescope at Udaipur Solar Observatory: Characterization of Lithium Niobate etalons

Multi-Application Solar Telescope (MAST) is a 50 cm off-axis Gregorian telescope, which has been installed at the lake site of Udaipur Solar Observatory. For near simultaneous photospheric and chromospheric observations, a narrow band imager has been developed as one of the back-end instruments for this telescope. The narrow band imaging is achieved using two Lithium Niobate (LN) Fabry-Perot etalons (FP_1 and FP_2) working in tandem as a filter. Etalons in tandem effectively increases the free spectral range (FSR) and the spectral resolution of the system. Wavelength tuning of this filter is achieved by changing voltage, and temperature of the etalons using the electro-optic property of the LN material. In order to characterize the etalons, a Littrow spectrograph was setup, in conjunction with a 15 cm Carl Zeiss Coud solar telescope. Calibration of the etalons was carried out for the solar spectral lines at Fe I 617.3 nm, and Ca II 854.2nm, which are formed in photosphere and chromosphere respectively. In our experiment, the temperature tunability was used to fix the initial position of the transmission channel at the optimum wavelength position. Then the desired spectral lines were scanned using voltage tuning. Temperature tuning of FP_1 shows that etalon kept at any temperature between 27°C and 33°C would allow us to scan full line profile of both the spectral lines by applying voltages in the range of ± 3 kV. Similarly it was found that the optimum temperature for FP_2 is 35°C .

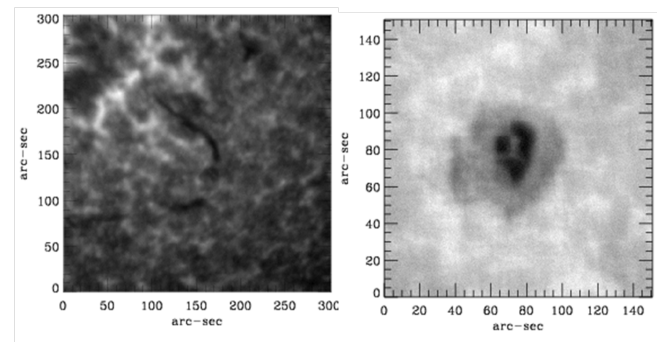


Figure 34: Images obtained by tuning the filter in the line center of 617.3 nm (left) and 854.2 nm (right). Observations in 617.3 nm were obtained on 3 April 2013; the sunspot observed was a part of the active region NOAA AR 11711 located at S17E24 on the solar disk. Observations in 854.2 nm were obtained on 8 March 2013, the filament that is seen in the image was located on the disk at S35E25 near NOAA AR 11689.

At this temperature, transmission channel of FP_2 could scan the line profile of the two lines optimally by applying voltages in the range of ± 3 kV. Tuning the etalons by voltage allowed us to find the cross-over voltages (the voltage where the transmission channel of FP etalon coincide with solar spectral line center) and voltage tuning rates. Voltage tuning rates of the etalons were used to estimate the r_{13} coefficient of the Lithium Niobate etalons and it is found to be 5.2 pm/V and 4.5 pm/V at 617.3 nm and 854.2 nm, respectively. Free spectral range and Full width at half maximum of the FPs in tandem were estimated to be 0.67 nm and 0.015 nm, respectively at 617.3 nm and 1.0 nm and 0.02 nm, respectively at 854.2

nm. A Coud telescope with a clear aperture of 15cm was used to obtain the test images at both the lines using the information obtained from the characterization of the etalons. Observations were obtained by tuning the etalons in tandem across different wavelength positions on both the spectral lines.

Figure 34 shows a magnified view of images taken in the line center of 617.3 nm and 854.2 nm, respectively. For 617.3 nm line, the images were obtained from -150 mÅ to +210 mÅ from the line center, with a step of 30mÅ, whereas line profile of 854.2 nm is scanned from -225 mÅ to +150 mÅ in a step of 75 mÅ.

Using similar observations obtained for the quiet Sun, we retrieved the profiles for both the spectral lines (Figure 35) by estimating the mean intensity of the quiet Sun images. It is evident that due to the limited tunability of the filter, we could not retrieve the complete line profile of 854.2 nm line.

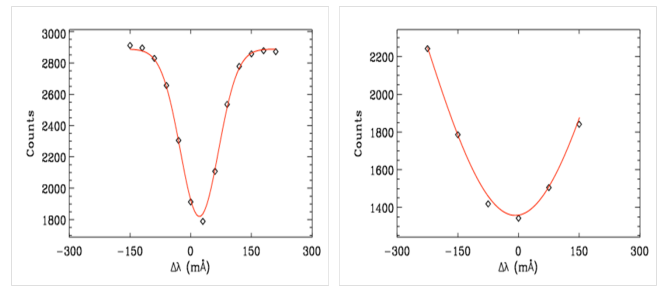


Figure 35: Retrieved line profiles of 617.3 nm (left) and 854.2 nm (right) using quiet sun observations. Line profile of 617.3 nm is scanned at 13 wavelength positions from -150 mÅ to +210 mÅ with $\delta\lambda = 30$ mÅ. Line profile of 854.2 nm is scanned only in the core at 5 wavelength positions from -225 mÅ to +150 mÅ with $\delta\lambda = 75$ mÅ. This system will be integrated with the upcoming solar telescope, MAST towards the middle of 2014.

(A. Raja Bayanna, S. K. Mathew, P. Venkatakrishnan and N. Srivastava)

SCIENCE

Planetary Sciences and PLANEX Program

The irradiation product Si-32 in the early Solar System

Both astrophysical observations of young stellar objects and cosmochemical observations from meteorites suggest that a fraction of the dust and gas of the solar accretion disk has been irradiated by cosmic rays emitted by the young forming active Sun.

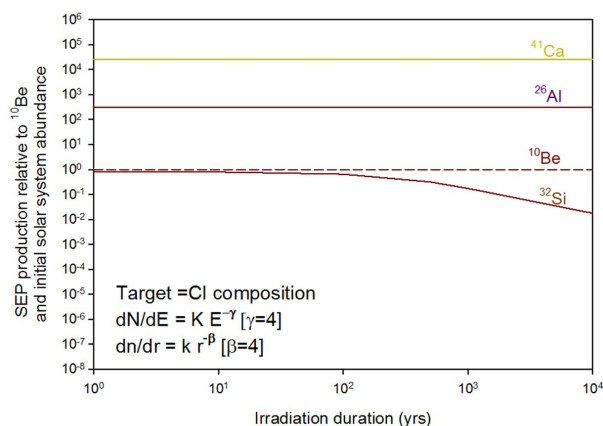


Figure 36: Ratio of calculated to measured solar system initial ratios of ^{26}Al , ^{41}Ca , ^{10}Be and ^{32}Si relative to their reference isotopes, by SEP interactions plotted as a function of irradiation duration. The irradiated objects were assumed to be of CI (solar) composition following a power-law distribution in size ($dn/dr \propto r^{-4}$) with the spectral exponent of the SEP $\gamma=4$. The SEP fluence was adjusted to produce an initial $^{10}\text{Be}/^{9}\text{Be}$ ratio of 1×10^{-3} , for all irradiation duration.

We have performed a calculation for production of ^{32}Si along with ^{10}Be , ^{26}Al and ^{41}Ca in early solar system due to irradiation, with a target of carbonaceous chondrite (CI) composition at asteroidal distance (2-3 AU). Various parameters such as alpha to proton ratio, gamma factor in the

power law spectrum of the irradiation, Be abundance in target CI condensate and beta factor in grain size distribution have been optimized to match the experimentally measured initial value of $^{32}\text{Si}/^{28}\text{Si}$ in CV CAIs. The initial values for $^{26}\text{Al}/^{27}\text{Al}$, $^{41}\text{Ca}/^{40}\text{Ca}$ and $^{10}\text{Be}/^9\text{Be}$ were 5×10^{-5} , 1.4×10^{-8} and 1×10^{-2} respectively. ^{32}Si cross-section for the production has been taken from TALYS (<http://www.talys.eu/>). The simulated T-tauri phase produces excesses of ^{26}Al and ^{41}Ca which has been observed previously and the latter are accepted to be stellar products in the early solar system. ^{10}Be is an irradiation product as it hardly survives in stellar conditions.

Figure 36 indicates that the short-lived radionuclides ^{32}Si and ^{10}Be can be produced together assuming a Be abundance of 100 ppm, with a condition gamma ~ 4 , beta ~ 4 , and the initial values of $^{32}\text{Si}/^{28}\text{Si}$ is determined to be 5×10^{-8} . Though the variation in initial conditions can vary $^{32}\text{Si}/^{28}\text{Si}$ values significantly, the most probable values based on ^{10}Be initial values observed in early condensates indicates a range between 1×10^{-7} to 5×10^{-8} for $^{32}\text{Si}/^{28}\text{Si}$.

(K. K. Marhas)

Noble gas and nitrogen components in Sutter's Mill

Sutter's Mill is a CM carbonaceous chondrite breccia which fell in April 2012. We studied nitrogen and noble gases with the objectives of finding cosmic ray exposure age, as well as to look for trapped gas components of local and interstellar origin. Two splits were analysed by both stepwise pyrolysis and combustion in order to better recognise and decouple several trapped and in situ produced components. We have also analysed acid residues by combustion to look for signatures from interstellar diamonds and SiC. The nitrogen content measured by combustion (363 ppm) and by pyrolysis

(402 ppm) are in agreement, though the release pattern of $\delta^{15}\text{N}$ by combustion and pyrolysis are different.

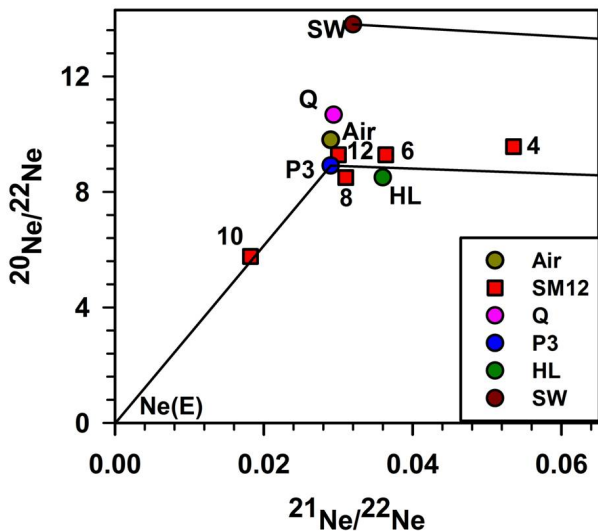


Figure 37: Neon three isotope plot for Sutter's Mill pyrolysis data. Numbers given against each point represent extraction temperature in 100's of °C. Prominent local and interstellar components are also plotted (SW-Solar wind; air-Earth's atm.; P3, HL and Q trapped Ne compositions of interstellar and solar nebular origin).

A low $\delta^{15}\text{N}$ of -16.8 ‰ is observed during combustion at 500°C (probably from nano-diamonds), whereas a high value of 71.2 ‰ is seen in pyrolysis at 1200°C (probably from an inorganic component). He and Ne are dominated by trapped components whereas no clear signal of cosmogenic ^3He is apparent. In the Ne three isotope plot (Figure 37), the pyrolysis data of 400°C and 600°C fall along the mixing line of Ne-Q and cosmogenic Ne and give $^{21}\text{Ne}_c$ of 0.11×10^{-10} ccSTP/g, yielding an exposure age of ~5,500 years, for an average shielding depth production rate of 2×10^{-9} ccSTP/gMa. This extremely young exposure age suggests that the object broke only after reaching the inner solar system. Ne-E is clearly seen at the 1000°C (pyrolysis) and 800°C (combustion) steps. Clear excesses of ^{124}Xe and ^{136}Xe and ^{86}Kr due to Xe-HL and Kr-H are visible at the 800°C pyrolysis step and a lower limit of interstellar diamond abundance of 250 ppm could be derived based on the ^{136}Xe excess, assuming the Xe to be a mixture of Xe-Q and diamond component (Xe-HL). About 8% of Xe is released in pyrolysis subsequent to combustion, with enhanced $^{129}\text{Xe}/^{132}\text{Xe}$ ratio of 1.13, compared to a value of 1.05 during combustion, suggesting a retentive host phase for radiogenic ^{129}Xe . A small amount of bulk sample has been processed through HF/HCl cycles and later oxidised by HNO_3 to produce oxidised C-rich residue and analysed for Ar, Kr and Xe by combustion. The 600°C and 700°C fractions of this sample show an HL component of Ar, Kr and Xe.

This work is carried out in collaboration with Dr. P. Jenniskens, SETI Institute, California, USA.

(S.V.S. Murty, P.M. Ranjith Kumar and R.R. Mahajan)

Silicon Isotope composition in different phases of Enstatite Chondrites

The small and less studied group of Enstatite chondrites are unique amongst the primitive meteorites as they are thought to originate in a region of nebula where the C/O ratio was somewhat higher and hence more reducing than the solar value. The elements that are mainly lithophile under more oxidizing conditions tend to be siderophile (e.g., Si) or chalcophile (e.g., Ca, Mg, Mn, Cr, Na, K) in reducing conditions where parent bodies of enstatite chondrites might have formed. Also they appear to have undergone significant refractory lithophile element (RLE) fractionation, as evinced by low Mg/Si, Al/Si ratios, compared to other primitive meteorites. In particular E chondrites exhibit no isotopic variations in O, N, Mo, Ni, Cr, Ti and Sr relative to terrestrial composition, which, in most cases, is not true for the ordinary and carbonaceous chondrite groups. This has led some authors to suggest that E chondrites are the primary building blocks of Earth.

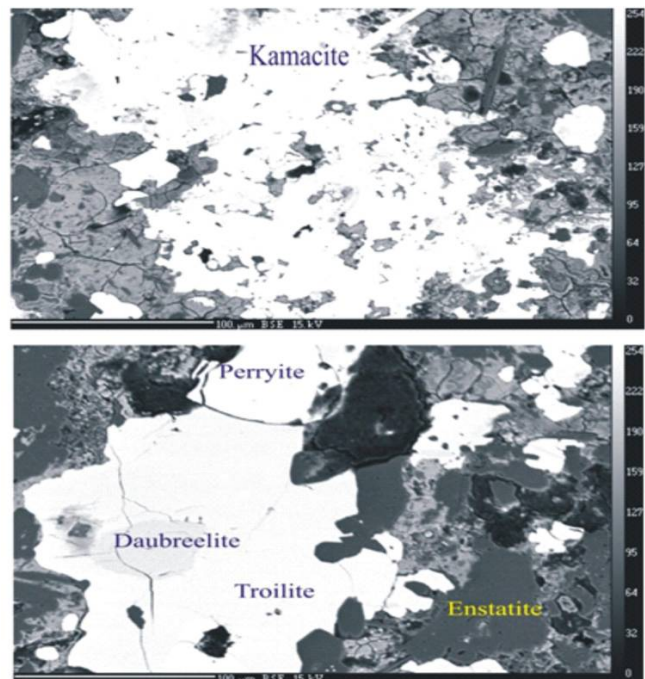


Figure 38: BSE images of minerals in EH3 meteorite.

But, one isotope system which appears to differ from this trend is silicon as with respect to Si isotopes, E chondrites are known to be the lightest macroscale solar system objects so far analysed. Petrography, texture and mineral chemistry of several silicates, sulfides and metallic phases have been investigated using reflected light microscopy, BSE imaging (Figure 38) and quantitative EPMA analysis in two Enstatite chondrite namely PCA 91 461(EH3) and ALH 81 021 (EL6).

The individual minerals investigated includes the following: Enstatite (MgSiO_3), Albite ($\text{NaAlSi}_3\text{O}_8$), troilite (FeS), daubreelite (FeCr_2S_4), niningerite [$(\text{Mg}, \text{Fe}, \text{Mn})\text{S}$], schreibersite ($(\text{Fe}, \text{Ni})_3\text{P}$), kamacite (Fe-Ni alloy), and Perryite ($(\text{Ni}, \text{Fe})_5(\text{Si}, \text{P})_2$). The composition of Enstatite seems to be

uniform in chondrules and matrix with $\sim 60\%$ SiO_2 . Apart from Silicates, Kamacite and Perryite were found to be two metallic phases with high abundance of Silicon, containing ~ 3 and ~ 14 wt% Si respectively. These two phases and Enstatite will be further investigation using MC-ICPMS in order to understand the nature of Si isotope fractionation between metallic phases and silicates in Enstatite chondrites.

(J. Sikdar and V. K. Rai)

Katol meteorite, a highly shocked L6-7 chondrite

Katol chondrite shower fell in Nagpur district, Maharashtra on 22nd May, 2012, and 27 fragments weighing ~ 3.5 kg have been collected by Geological Survey of India. Using mineral chemistry, petrography and oxygen isotopic composition we have classified it as troilite-metal nodule bearing highly equilibrated L6-7 (S6) ordinary chondrite with metamorphic equilibrium temperature of 900°C - 950°C and calibrated equilibrium shock pressure of 60 GPa. Homogenised olivine and low- Ca pyroxene composition (PMD $< 2\%$), well crystallised grains of high- Ca pyroxene, a new Wo- rich low- Ca pyroxene phase (Wo: 3.22) and presence of microchondrules are some textural-chemical characteristics that refer to primary and secondary properties. Tertiary properties include planar fracture (PF), planar deformation features (PDF) in olivine and large-scale maskelynitisation (size frequently ranges up to $200\ \mu\text{m}$) of secondary plagioclase.

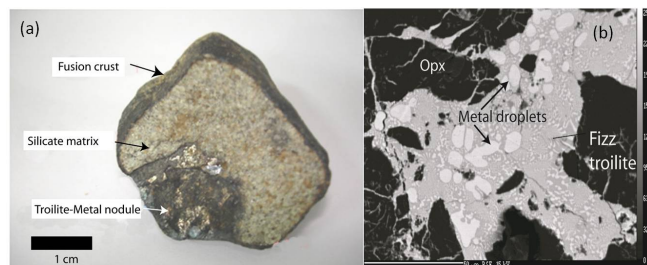


Figure 39: (a) Broken surface of Katol meteorite shows fusion crust, silicate matrix and troilite-metal nodule; (b) image of fizzed troilite and metal droplets within troilite-metal nodule.

We found a large nodule in Katol (Figures 39a, 39b) that mostly comprises immiscible troilite- metal melt and intensely fractured silicates without any silicate-melt phase. Melt veins of different generations filled with variable proportion of metal-sulphides refer to multiple shock veining events in the same location where brittle silicate host under shear deformation was converted to in-situ breccia, cataclastic fragments (angular to subrounded) and pulverized silicate matrix often analogous to pseudotachylites.

This nodule is an end-product of impact- induced frictional melting. Spatially focused frictional heating during impact produced shock veins, filled with immiscible troilite-metal melt. Multiple set of different generations of fractures,

melt veins and shock- melt ejecta are related to multiple shock events due to high-energy impact. Immediately after impact, re-equilibration of heterogeneously distributed heat promoted metamorphism has occurred, adjacent to zones of maximum impact heating. Thus overall shock induced texture of the troilite-metal nodule is quite different from those of host chondrite in the immediate neighbourhood as the latter was subject to equilibrium shock pressure without shear deformation. Additionally, high-P phases like impact-produced glass (maskelynite from plagioclase and olivine composition glass) and ringwoodite (γ -polymorph of olivine) are observed only in troilite-metal nodule. Shock thermal history of Katol corresponds to peak shock pressure of ~ 90 GPa and calibrated post-shock temperature of $\sim 900^\circ\text{C}$ to 650°C . Cosmic ray produced radioactive (^{60}Co) and stable (noble gas) isotopes have been studied in Katol, to understand its pre-atmospheric size and interplanetary sojourn. Activity of ^{60}Co , larger than in Kendrapada meteorite (pre-atmospheric radius of 50-150 cm) and clear presence of ^{36}Ar , ^{82}Kr and ^{128}Xe produced by (n, γ) reactions on ^{35}Cl , ^{81}Br and ^{127}I respectively indicate that the pre-atmospheric radius of Katol is ≥ 100 cm. Based on cosmogenic ^{21}Ne amount an exposure age in the range of ~ 50 Ma is derived, for a pre-atmospheric radius of 100-150 cm. More detailed studies are in progress.

(D. Ray, S. Ghosh, R.R. Mahajan, A.D. Shukla, P.M. Ranjith Kumar and S.V.S. Murty)

Thermal history of iron meteorites

We have investigated three iron meteorites (2 falls from India and one find from USA) to study their metal, sulphide, phosphide and carbon phases, to look for unusual phase assemblages and to derive their thermal history.

Kavarpura: Kavarpura iron meteorite (~ 6800 g, single piece) fell in Jhunjhunu district, Rajasthan on 29th August, 2006. Structurally, it is inclusion- free 'Fine Octahedrite' with Widmansttten pattern (mean kamacite band- width of 0.27 mm) and a variety of plessites (finger- cellular- and black plessite). Chemically, it is high- Ni (9.5 wt%) IVA group with very low P. It has suffered severe shock up to 600 kb as evident from matte- textures of ϵ - kamacite. Post-shock annealing is the most conspicuous event of Kavarpura iron and it is reflected in the asymmetric M-shaped Ni-profile or, small-scale fluctuation in the Ni-minimum of cloudy taenite zone (CTZ) if shocked under medium to high shock pressure (Figure 40a). We estimated a cooling rate ($^\circ\text{C}/\text{Ma}$) of Kavarpura in the range between 225 and 450 with a mean value 320 (Figure 40b).

Bhuka: Bhuka iron meteorite (2420g, single piece) fell in Barmer district, Rajasthan on 25th June, 2005. It is structurally classified as Fine Octahedrite (mean kamacite band width of 0.275 mm) with several macro inclusions (max. $10\ \text{mm} \times 5\ \text{mm}$) of silicates and micro inclusions (600 to $50\ \mu\text{m}$) of graphites.

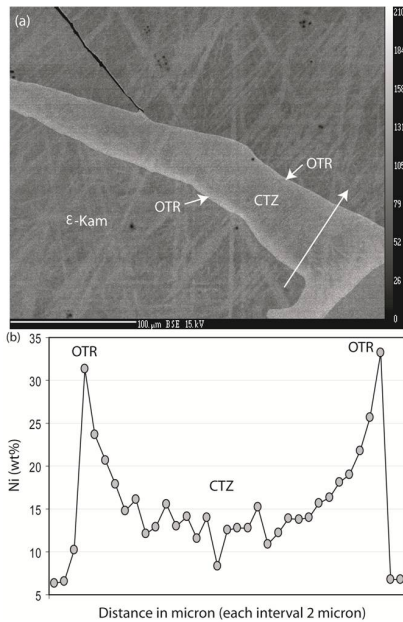


Figure 40: (a) Annealed taenite within ϵ - kamacite matrix, outer taenite rim (OTR) and CTZ-cloudy taenite zone in Kavarpura meteorite; (b) M' shaped Ni-profile across the annealed taenite.

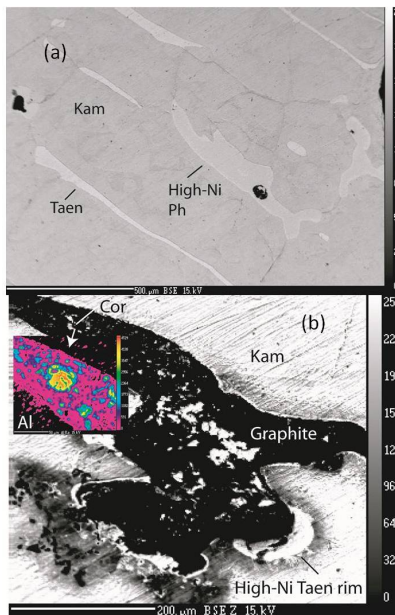


Figure 41: (a) Taenite (Taen) lamellae and high-Ni Phosphide (Ph) within recrystallised Kamacite (Kam) in Bhuka; (b) Graphite inclusion rimmed by high-Ni Taenite (Taen). Corundum (Cor) are also present.

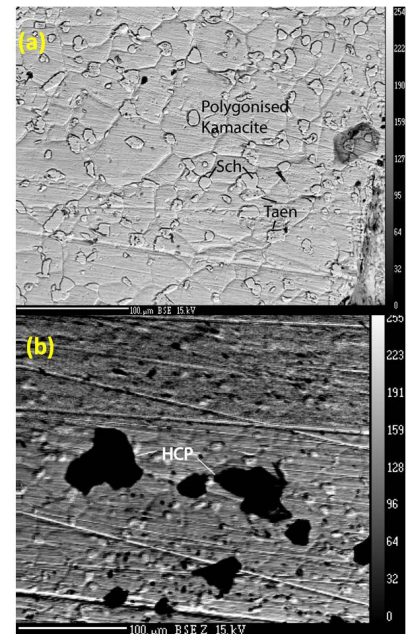


Figure 42: (a) Schreibersite and taenite within highly recrystallised kamacite matrix in Washington County meteorite; (b) High carbon phase (HCP) in kamacite matrix.

Besides kamacite bands and taenite lamellae that form Widmanstten texture, we note several textural features like polygonised kamacite, tiny taenite blebs, amoeboid-shaped patchy taenite, swathing taenite around graphite inclusions and P- rich taenite (Figures 41a, 41b). BSE and X- ray images of the large graphite inclusions (maximum: 600 μm) report several micro-inclusions that include (i) corundum (30 to 50 μm in size and nearly pure Al_2O_3) grains with spinel inclusions, (ii) free SiO_2 or, tridymite, (iii) mixed phase of Fe- silicates and phosphates, (iv) anorthite, (v) Fe- Ti- Al spinel, (vi) P-rich taenite, (vii) kamacite and (viii) rare grains of troilite. Study on nature of silicate inclusions are presently in progress. Chemically, it belongs to low-Ni (8.4 wt%) IAB group. We estimate a cooling rate of $\sim 40^\circ\text{C}$ Ma for Bhuka.

Washington County: This iron meteorite (5750g) probably fell in 1916 at Washington County, Colorado, USA. In absence of primary cooling textures, Washington County was structurally 'ataxite' and chemically 'Ungrouped' as proposed by earlier workers. Severe reheating due to high degree of shock accounted for complete destruction of all primary textures and formation of the thoroughly recrystallised new texture which is a granulated kamacite matrix decorated with evenly distributed particles of high- Ni taenite and Ni-rich schreibersite (Figure 42a). Present study reports the occurrence of high carbon phase (HCP) which is sporadically distributed in the polygonised kamacite matrix as largely angular grains and appears pitch black in BSE images (Figure 42b). Based on the abundance of metals and non- metals, their paragenesis, phase compositions, bulk Ni and plots of Ga, Ge, Ir and P against Ni (not shown here) we re-classify Washington County into structural group, 'Reheated Medium Octahedrite' and chemical group IIIB of

IIIB. Metallographic cooling rate of Washington County is estimated to be $100^\circ\text{C}/\text{Ma}$ based on its bulk Ni- content and the experimentally calibrated cooling rate curve of IIIAB chemical group.

(D. Ray, S. Ghosh and S.V.S. Murty)

Diverse mineral paragenesis and igneous crystallization history of olivine-phyric shergottite Tissint

Tissint is a new shergottite of the Martian meteorite group. It was a witnessed fall in July 2011 in the Morocco desert, and characterized as an olivine-phyric shergottite. In this study, we performed petrographic analysis of two mounted and polished grains of Tissint. Petrogenetic history of this meteorite and its relationship with other shergottites were derived based on detailed geochemical analyses of the constituent phases, using EPMA for major-element and LA ICP-MS for minor- and trace-element study. The megacryst assemblage consists of olivine (up to 0.4 mm) and pyroxene lath (up to 0.5 mm long). The finer-grained groundmass (Figure 43) mainly consists of olivine, pyroxene, maskelynite, and phosphates. The total range of olivine compositions is Fo_{60-16} , with more-fayalitic compositions measured in the rims of large olivine and in the groundmass olivine grains. Minimum cooling-rate estimate yields values of $\sim 0.5^\circ\text{C}/\text{hr}$, based on Fo-zonation in olivine megacrysts. Pyroxenes become increasingly iron-rich from core to rim, in general, where Mg-rich orthopyroxene, pigeonite and augite tend to Fe-rich pigeonite and augite. Pyroxenes are LREE-depleted from core to rim like other olivine-phyric shergottites. Throughout

the rock, individual groundmass maskelynites are unzoned but inter-granular compositions exhibit a range of anorthite contents (An_{70} to An_{60}). REE data shows strong positive correlation between P_2O_5 and REE in maskelynite, indicating that those with elevated REE abundances have likely resulted through interaction with REE-rich phosphate. This interaction could have occurred via shock processes. Plagioclase in Tissint is most calcic and only restricted in very anorthitic range compared to the most depleted and most primitive shergottites. Variable cooling events are observed in this study from the fresh textural domains. The pyroxenes of Tissint display patchy zoning with irregular pattern of zonation, which indicates multi-staged growth phenomenon in an open system.

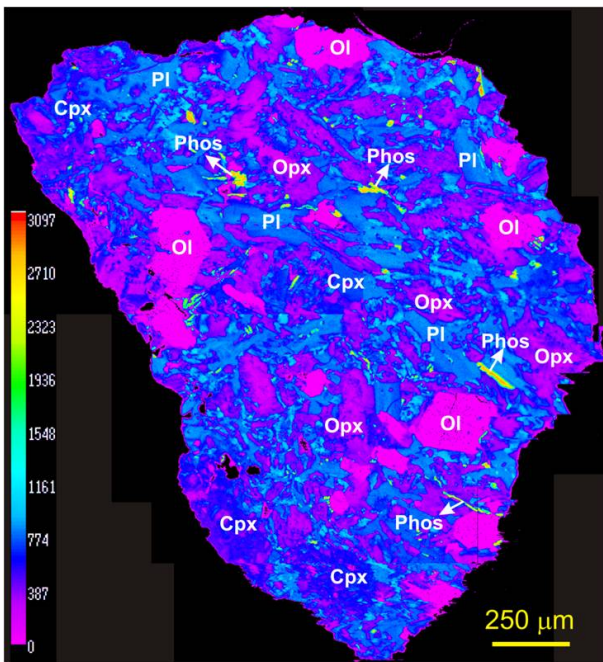


Figure 43: X-ray Ca K-alpha image of Tissint meteorite section.

This work is carried out in collaboration with Dr. E. Babu, NGRI, Hyderabad.

(A. Basu Sarbadhikari and S.V.S. Murty)

Remote sensing of Moon and Mars

Spectral characterization of young basalts on the Moon using M^3 data from Chandrayaan-1

A comparative assessment of the mineralogy of young basalts (~1.2 Ga to ~2.8 Ga) from the western nearside (WN), Moscoviense basin (M), and the Orientale basin (O) of the Moon has been made using Level 2 Moon Mineralogy Mapper (M^3) data from the Chandrayaan-1 mission.

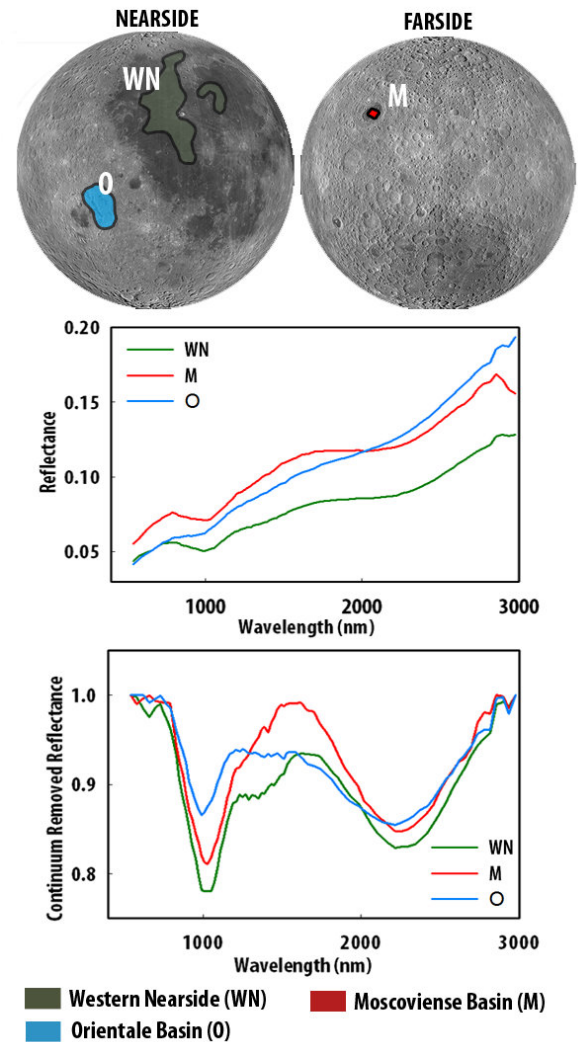


Figure 44: LROC-WAC mosaics of the Moon showing outline of young basalt exposures studied. They span from ~1.20 Ga – 2.76 Ga. Representative M^3 spectra (both normal and continuum removed) from western near side basalts, Moscoviense basin and Orientale basin have been plotted showing their characteristic spectral behavior. The western nearside basalts are olivine rich, the ones in the Orientale basin are rich in clinopyroxene, and those in the Moscoviense basin show signatures of Fe-rich glasses along with clinopyroxenes.

Spectral data characteristics of the individual units have been generated from fresh small craters to minimize the complications due to space weathering. Representative spectra for individual units and the derived spectral parameters (Band centers and Integrated Band Depth Ratio) have been used to study composition of these young basalts. A modified approach of Gaffey (for olivine-pyroxene mixtures) and the methodology of Adams (for interpreting pyroxene type) have been used to improve our understanding of the spectral behaviour of these basalts. The study of late phase (~1.20 Ga – 2.76 Ga) volcanism across the Moon in widely distributed basins has revealed that they show diverse spectral behaviour suggesting plausible compositional heterogeneity in their source regions. Most of the young basalts of Oceanus Procellarum are characterized by abundant olivines and they show complex volcanic history

(Figure 44). Vast exposures of olivine concentrated units having higher abundance of olivine content than high-Ca pyroxenes are emplaced in the northern Oceanus Procellarum region. Mostly, they show distinct stratigraphic gradation with the immediately underlying units of relatively lower olivine content. The Moscoviense unit shows signatures of Fe-rich glasses along with clinopyroxenes. The basalts of Orientale basin are typically devoid of olivine and are rich in high-Ca pyroxene. Thus, mineralogy of these mare basalts which erupted during the late stage volcanism vary across the Moon's surface; yet, broader observations reveal apparently higher FeO content in the younger basalts of western nearside and Orientale region.

However, non mare mixing, coarse spectral and spatial resolution of the data, local variations in the thickness of individual basalt units, fractionation during basalt emplacement, and plausibility of vertical mixing are some factors that might complicate the interpretations.

(I. Varatharajan, N. Srivastava, S.V.S. Murty)

Degradation of Moreux crater: Record of recent and episodic glaciation in Protonilus Mensae region of Mars

Morphologic characteristics of ice-rich landforms in the Martian mid-latitudes record evidence for significant degradation of the landscape in response to spin-axis/orbital parameter-driven shifts in the Late Amazonian climate. These landforms are spatially distributed across the mid-latitudes and their co-existing presence has so far not been observed from a single crater to infer how exactly a terrain has degraded while Mars was undergoing major-moderate-minor shifts in its Late Amazonian climate. We have therefore carried out an in-depth investigation of Moreux crater (~135 km, centered at 41.66°N, 44.44°E in the Protonilus Mensae region) for identification of features associated with recent and episodic glacial events and for emphasizing on the role played by these glacial events in the degradation of the crater. Evidence for extensive modification of the crater rim/wall, floor and central peak by emplacement of multiple scales of ice-rich landforms that represents large history of glacial activities was found. From our results we document phases of major-moderate-minor glacial activities as (1) piedmont lobes/lobate debris (Figure 45), aprons/linear valley fills (500-100 Ma), (2) viscous flow features (100-5 Ma) and (3) gullies/thermal contraction crack polygons (5-0.4 Ma).

The randomly distributed narrow channels observed within/around Moreux helped us to envisage that the glaciation might have been more extensive and much earlier in the history than the formation of LDA/LVF in this region. We suggest that central peak of Moreux probably acted as the locus for accumulation of ice/snow and the diversity of glacial/periglacial features within the crater was possibly controlled by differences in the amount of accumulated ice/snow and the rate at which the terrain responded to the shifts in climate during the periods of higher obliquity. Taken together, these ice-rich deposits within Moreux suggest that sequential degradation of the crater has occurred over the last tens of millions of years of Martian history.

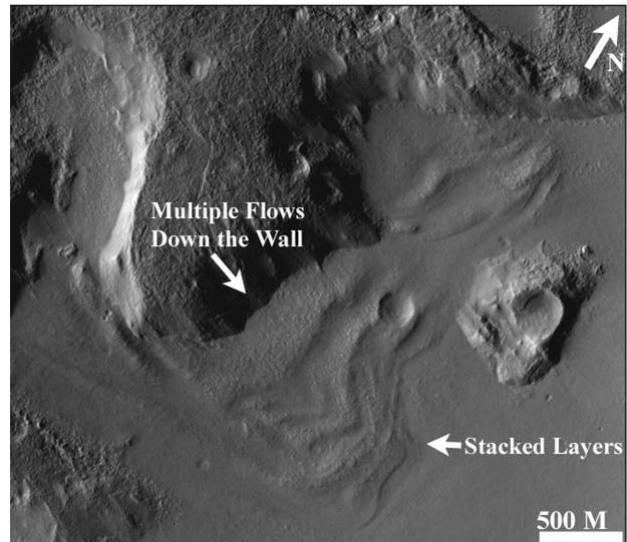


Figure 45: Lobate debris apron merging and distorting down gradient to form patterns similar to linear valley fills.

(R. K. Sinha and S.V.S. Murty)

Geomorphic insights from multiple modes of gully formation on Mars

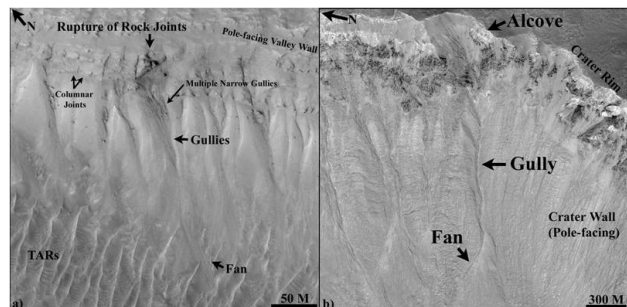


Figure 46: Gully formation on Mars: (a) Discharge of groundwater from the space between the rock joints, and (b) accumulation of ice/snow within alcoves during past ~5 Ma that melted and formed gullies.

Gullies on Mars (Figure 46) are among the most spectacular features discovered at locations supporting top-down flow of liquid water under suitable P-T conditions that prevailed during the past 5 Ma. We have conducted geomorphic investigation of gullies observed from a geological suite of craters located northeast of Argyre basin (38.1°S, 28.6°W). From our observations, we validate and present that groundwater and snowmelt were the ultimate source for forming gullies on Mars. For the first time, evidence for existence of a possible aquifer within the interior of a crater is presented. Overall, the gullies were found to develop by at least 5 different modes during the past ~5 Ma which we broadly grouped under (1) an older phase for down slope flow on equatorward faces; (2) a moderate phase for top-down melting on eastward/westward slopes; and (3) a younger phase exclusively on pole-facing slopes. On addressing the problem of gullies forming over eastward/westward slopes,

we established that it is the sublimated ice/snow packs from within/around of Argyre basin, which possibly sourced the melt water for gullies over east/west wall of craters lying within the nearby latitudes. Further, we showed that orientation of local undulated topographic faces played a key role in controlling the distribution of gullies over the preferred pole/equator facing slopes. In addition to this, we deciphered the origin of relatively new bright deposits within gully channels and tested their possible link with flow of water on contemporary Mars. In all the modes we found role of microclimatic shifts to be significant, which has at certain favourable times, at certain locations, accumulated the volatiles (ice and snow), facilitated flow of water and formation of gully-like features.

(R. K. Sinha, S. Vijayan and S.V.S. Murty)

Multi layered ejecta craters in the equatorial region of Mars

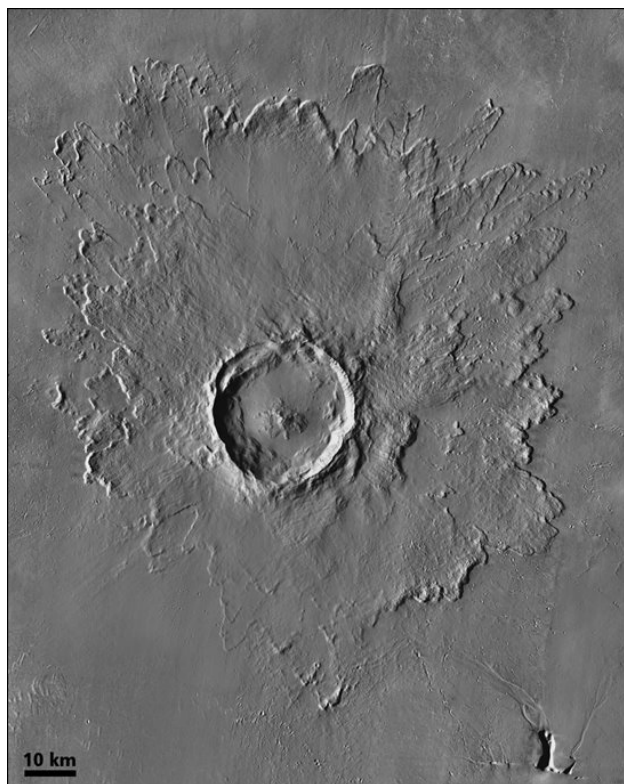


Figure 47: A multiple layer ejecta crater on the Northern hemisphere of Mars showing different layered patterns.

Martian impact craters often have distinct ejecta patterns, which distinguishes them from other planetary craters. Among them, the multi layered ejecta (MLE) craters are dominant on the equatorial region of Mars. Ejecta morphology helps to identify regions that have contained or still harbour volatile-rich reservoirs on the equatorial region of Mars, where the pole ward dominance is well established. The equatorial presence indicates that the Mars wide obliquity range ~ 45 degree (high obliquity) and < 30 degree (low obliquity) could play probable role in transporting the volatile rich material under such circumstances.

However, this holds good for the younger craters which are formed within few Ma. Among MLE craters, four different types of inner morphology were observed, those having a crater floor that is 1) flat, 2) has a peak, 3) has a pit and 4) has a summit pit. The formation of the inner morphology is based on the impactor size, velocity and the target medium. The formation and their distribution provide details like i) their target surface nature, ii) role of volatile content and iii) regional climatic activity influencing the formation. MLE craters (Figure 47) on the highland region have older formation age than the craters formed on the resurfaced Northern hemisphere (younger). We derived two parameters, the ejecta mobility (EM) (fluidity of the ejecta at the time of emplacement) and maximum ejecta extent for each crater to understand their features. On the northern hemisphere, the maximum EM was obtained as 2.6 for the crater (dia. ~ 92 km) located on the resurfaced region. Similarly, for the southern hemisphere, EM was 2.8 and the crater (dia. ~ 50 km) was located on the Tyrrhena volcanic provinces. The volatile activity can also be deciphered using the sublimation pits on the inner and outer region of the craters. The inner sublimation pits help to identify the extent of depth up to their presence, whereas observation on ejecta infers the top concentration. The absence of sublimation pits on several directions over the ejecta indicates the distribution variation in volatile below the surface.

Relating the differences to the location of crater, elevation of terrain, orientation of slopes, and the nature of target material along with the inner and outer morphology of MLE craters brings out the role of target material and volatile concentrations during the impact emplacement. This categorization delineates the past climatic activity and infers their activity over the time scale.

(S. Vijayan, R.K. Sinha and S.V.S Murty)

Lunar regolith thickness estimation using simulated brightness temperature

Passive microwave radiometry is a potential technique to understand the surface and subsurface characteristics of planetary bodies. A simulation based study has been carried out to understand the emission from the lunar surface and interpret it to understand the subsurface characteristics. The present effort is towards developing a dual frequency regolith depth index involving use of frequencies expected in Chandrayaan-2 lunar orbital mission. In this simulation, brightness temperature has been simulated at L (1.25 GHz) and S (2.1 GHz) band using a variety of expected conditions on lunar surface. We have used a three layer model described by variability in its dielectric properties which are influenced by regolith density and $\text{FeO} + \text{TiO}_2$ contents, for the simulation. Simulated values of brightness temperature were used to define an index called regolith depth index, which describes variability due to regolith thickness. The inversion of regolith depth was done for Apollo landing sites. Inversion was also done using single frequency. Estimated regolith depth using dual frequency index based model were compared with single frequency based approach. It was

observed that dual frequency derived thickness correlated with measured data better as compared to single frequency. The thickness of regolith is consistent with the formation age given in the incremental order as Apollo A12, A15, A11, A17, A14 and A16 with the oldest dating back to Imbrium age. Among these, the first three regions are well within the ~5 m range of thickness (Figure 48), but the next two regions (A17 and A14) show significant change in thickness, likely due to lateral/vertical mixing.

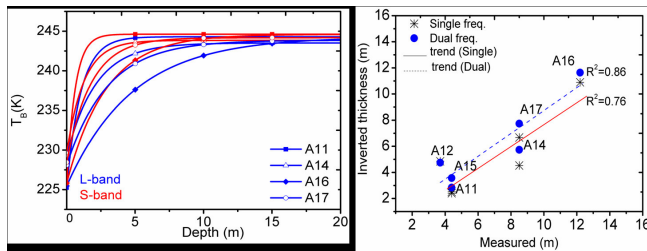


Figure 48: Estimated regolith thickness using the inversion method developed.

Incorporating the effect of vertical mixing of FeO+TiO₂ over these two regions using their in situ measured FeO+TiO₂ showed probable variation up to ~1 m in the estimated thickness. This study has been carried out for evaluating the potential of expected Chandrayaan-2 L-band and S-band passive microwave observations. A dual frequency based regolith depth index is proposed which has shown improved performance over single frequency based approach. The prevalence of regolith mixture is inevitable; thus, along with the lateral mixture model, incorporating vertical mixing will provide reasonable regolith thickness.

(S. Vijayan, S. Mohan and S.V.S. Murty)

Radar ejecta distribution from Mini SAR data

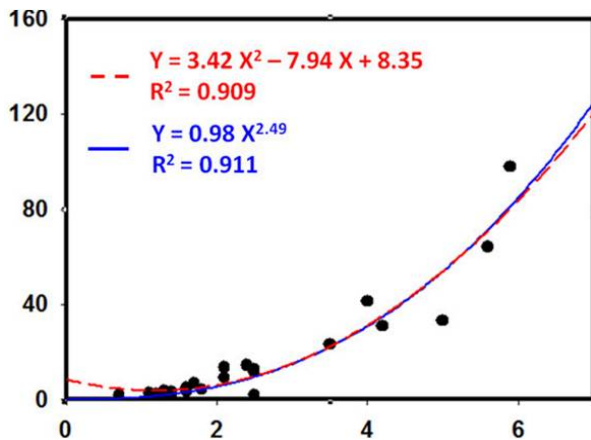


Figure 49: Correlation between crater diameter and SAR derived spatial ejecta extent.

Impact cratering is a major surface sculpturing process in case of airless bodies such as Moon and also one of the primary factors for redistributing the excavated material across the

lunar surface. Mini-RF, highly sensitive to surface roughness is able to provide detailed morphological imageries with unprecedented resolution and quality.

Thus, measurements on ejecta extent are possible using radar images. Such measurements provide knowledge on the extent of area influenced by impacting process. In this study, detailed quantification of ejecta matter for small craters (< 6 km) on the basis of their amount of spatial deposition has been attempted. For this purpose, circular polarization ratio (CPR) and S₁ (displaying intensity) from Miniature Radio Frequency (Mini-RF) instrument onboard Lunar Reconnaissance Orbiter (LRO) were acquired to characterize the radar backscatter of a large number of craters for deriving spatial ejecta blanket coverage. Further, optical Wide Angle Camera (WAC) imageries onboard LRO have been used for comparison purpose. In order to accurately estimate the total ejecta deposition, its characterization into finer and coarser material has also been done for 22 small sized craters ranging in diameter from 0.7 to 5.6 km, having a minimum depth of 2 m to a maximum of 930 m, from Rimae Sirsalis, a highland-mare mixed region. The estimated ejecta extent is related with crater geometrical properties like depth, diameter and volume. Results indicate that there exists a definite non-linear relationship between crater diameter and ejecta distribution as shown in the Figure 49. The present study provides a new method of observing ejecta distribution using radar and its relationship with crater geometrical parameters.

(A. J. Desai, S. Mohan and S.V.S. Murty)

Radar Polarimetric parameters of permanently shadowed region of lunar craters

The permanently shadowed regions (PSR) on Lunar Poles, possible repositories of volatiles, have been a subject of research and significant debate. Initial results from Chandrayaan-1's Mini SAR categorized lunar craters in PSR and identified craters having deposits of water ice. Craters with Ice deposits are known to have elevated Circular Polarization Ratio (CPR) because of volumetric scattering and Coherent Backscattering Opposition Effect (CBOE). Surface or single bounce scattering from dry, fine-grained regolith give CPR less than unity but increase in surface roughness at wavelength scale or high degree of surface roughness will results in high CPR. This produces an ambiguity between water ice and high degree of surface roughness, as both give elevated CPR. The higher values of CPR may be caused by surface slope, rocks, wavelength-scale surface roughness and dielectric constant. In an attempt to reduce the ambiguity on radar detection of water ice at the permanently shadowed regions near the lunar poles, circular polarization ratio (CPR), linear polarization ratio (LPR) and degree of linear polarization (DoLP) of impact craters has been analyzed using Mini SAR radar data from Chandrayaan-1 mission. Eleven anomalous and nine fresh craters of Lunar North Pole were selected for this study. M-chi decomposition technique has been used to decompose the image into single bounce scattering, double bounce scattering and volume scattering. CPR gives elevated values because of

both high level of surface roughness and deposits of water ice. M-chi decomposition and CPR are used together to identify the area having only volume scattering, showing the deposits of water ice at anomalous craters. Polarimetric parameter like LPR and DoLP help in understanding the surface-subsurface scattering of fresh and anomalous craters at lunar poles. LPR indicates about the target scattering contribution from surface and sub surface. Degree of Linear Polarization (DoLP) depends on surface physical properties (the dielectric constant and relative amount of surface vs. subsurface scattering), radar incidence angle, and the amount of spatial averaging across surfaces. In this study, it has been observed that LPR shows two different signatures in the anomalous craters but unique single signature in fresh craters.

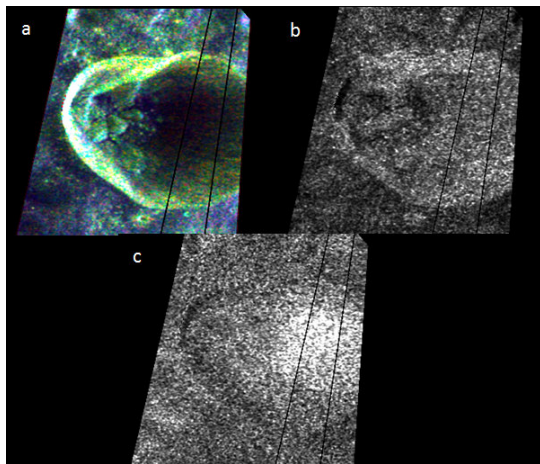


Figure 50: Hermite crater (20km; 87.8°N, 47.1°W) is an anomalous crater; (a) shows the m-chi decomposition of the image where Blue shows Single bounce scattering, Green shows Volume/diffused scattering and Red is double bounce scattering; (b) CPR image, showing roughly similar high CPR values at both interior and exterior of the crater; (c) LPR image showing two distinct signatures inside the crater.

Figure 50 indicates two distinct signature of LPR inside hermite crater, which is indicative of two scattering mechanism in anomalous craters. Hermite crater (20km; 87.8°N, 47.1°W) is an anomalous crater; (a) shows the m chi decomposition of the image where Blue shows Single bounce scattering, Green shows Volume/diffused scattering and Red is double bounce scattering; (b) CPR image, showing roughly similar high CPR values at both interior and exterior of the crater; (c) LPR image showing two distinct signatures inside the crater.

(S. Choudhary, S. Mohan and S.V.S. Murty)

Tool development for the analysis of Shallow radar data

Shallow Radar (SHARAD) onboard Mars Reconnaissance Orbiter (MRO) spacecraft is primarily for the detection of subsurface structure and ice deposits at deeper layer of MARS surface. In view of the difficulty in identifying the subsurface layer due to weak signal, an automated method for the detection of subsurface layer using digital technique is attempted. For this purpose, radargram from SHARAD has been acquired covering part of North Pole Layer Deposit

(NPLD). The procedure involves the detection of first return and separating various subsurface returns using segmental, thresholding and noise reduction method. The procedure allows the detection of subsurface layers and their boundaries. The tool would be helpful in segregating the radargram for identifying returns at various depths. Figure 51 shows the typical output from the radargram showing one of the data from NPLD.

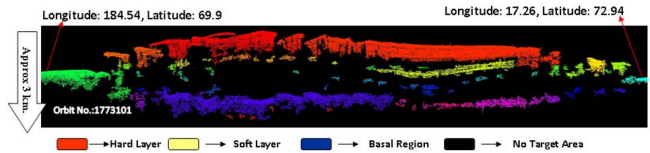


Figure 51: A typical result showing MARS NPLD region with subsurface layered deposits.

(R. R. Bharti, S. Mohan and S.V.S. Murty)

Development of payloads for planetary exploration missions

Moon Electrostatic Potential and Dust Analyser (MESDA) for Chandrayaan-2 Lander

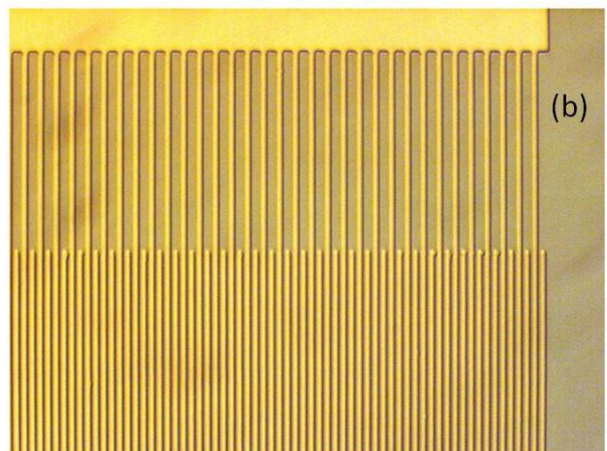
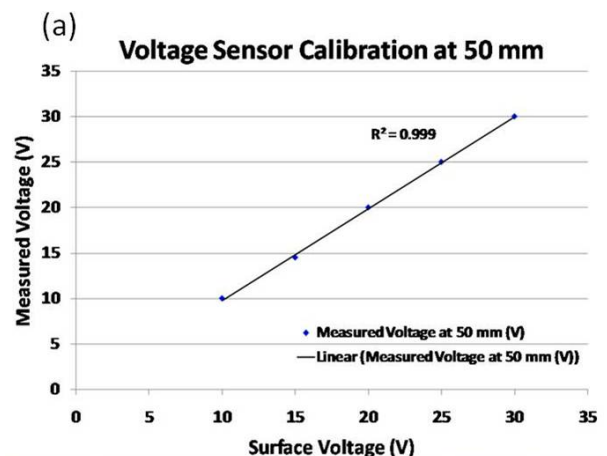


Figure 52: (a) Calibration plot of prototype of voltage sensor for LSPD and (b) Image of first IDT on GaAs substrate with Gold metallization for LDD.

To study the lunar electrostatic and dust environment, a Moon Electrostatic Potential and Dust Analyzer (MESDA) payload has been proposed for Chandrayaan-2 lander. There are two independent instruments in the MESDA payload viz., Lunar Surface Potential Detector (LSPD) and Lunar Dust Detector (LDD).

The LSPD will measure lunar electrostatic surface potential at ~ 50 mm from the lunar surface, whereas the LDD will detect the presence of charged dust particles at a similar altitude using an Inter Digitated Transducer (IDT) dust sensor. Design and development of sensors and front end electronics for both the instruments have been initiated. A prototype of the LSPD has been developed and initial measurements have been carried out in the laboratory. A calibration curve of the prototype of voltage sensor is depicted in Figure 52a. For the LDD, an IDT dust sensor with one micron inter-electrode spacing is under fabrication in collaboration with Micro Electronics Group, SAC. The image of the first IDT is shown in Figure 52b. The IDT has been attempted on GaAs substrate with Gold metallization. Further work on MESDA is underway.

(J. P. Pabari, M. Mariaammal, S. K. Goyal, D. Banerjee and Y. B. Acharya)

Lunar Electrostatic and Dust Levitation Modelling

The surfaces of airless, non-magnetized bodies in our solar system are directly exposed to the solar wind plasma and UV radiation, causing dust grains on their surface to be electrically charged. These electric fields can exceed surface forces (cohesion) and gravity for small dust particles, causing electrostatic dust levitation. Dust levitation almost certainly occurs within a few meters of the lunar surface, creating 'lunar horizon glow' as captured by Surveyor lander camera during early lunar missions. The Surveyor lander observed $\sim 5 \mu\text{m}$ grains levitating 3-30 cm above the lunar surface.

The characteristics of lunar dust were later investigated during Apollo mission and dust grains ($\sim 0.1 \mu\text{m}$) in the lunar exosphere were observed up to ~ 100 km altitude. NASA's Lunar Atmosphere and Dust Environment Explorer has been launched with the primary objective of characterizing lunar atmosphere and dust environment. To study the lunar electrostatic and dust environment, a Moon Electrostatic Potential and Dust Analyzer (MESDA) payload has been proposed for Chandrayaan-2 lander. Model calculations have been carried out for locations near the terminator to understand the nature of the dust dynamics parameters. Figure 53 shows the maximum radius of the dust grain which is levitated versus the lunar surface potential. The results indicate that for average solar wind conditions $\sim 0.1 \mu\text{m}$ charged dust grains can be levitated above the lunar surface for an electrostatic potential value of ~ 3.5 Volts, assuming an electron temperature of 10 eV and an electron density of $\sim 5 \text{cm}^{-3}$ respectively.

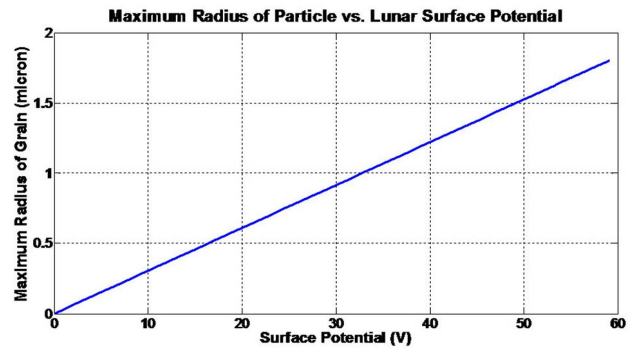


Figure 53: Modelling results of maximum radius of levitated dust versus surface potential on the moon.

(J. P. Pabari and D. Banerjee)

CHaSTE Payload for Chandrayaan-2 Lander - Prototype development

Precise information about heat exchange within the uppermost surface regolith of the Moon is necessary for obtaining an equilibrium balance between external (solar) and internal (due to radioactive decay and accretion) heat fluxes to aid us in understanding the thermal state of the Moon. Recent observations direct towards existence of more internal heat than thought earlier. To derive more accurate lunar thermal models, it is very important to know the extent and the spatial variability of the insulating fluffy layer and thermal properties of the upper 100-200 mm of the lunar regolith. For this purpose, an in situ surface thermal probe experiment 'CHandra's Surface Thermal Experiment' (CHaSTE) on board Chandrayaan-2 Lander is proposed. This experiment is being developed jointly by PRL and SPL, Trivandrum. The objective of the proposed experiment is in situ investigation of thermal profile within the top 10 cm of lunar regolith at the Chandrayaan-2 landing site (at a high latitude location) to understand the thermal properties of the near surface region of the moon.

The experiment basically contains three modules: (i) *Thermal Probe* containing a series of temperature sensors and a heater, to be inserted inside the lunar regolith by means of an appropriate deployment mechanism; (ii) *Electronics Box* housing the necessary electronics, and to be placed in a controlled environment on the lander and (iii) *Deployment Mechanism* with a spindle based forward penetration mechanism to be used for deploying the probe. The mechanism will be stowed during flight and deployed after landing. A laboratory prototype (Figure 54a) of the probe and its electronics has been designed and tested as a proof of concept of the proposed experiment. The structure of the probe was designed by machining a Teflon (FEP) rod into an aerodynamic shape. Another version of the probe using ABS plastic material was also designed using rapid prototyping. A T-shaped four-layer Sensor PCB was designed and fabricated for mounting the sensors, heater and probe interface connector. Eight two-wire PT1000 sensors and a small flat resistance heater were mounted on the T-shaped

PCB and the PCB was embedded in the T-slot provided in the structure in such a fashion that the sensors and heater are parallel to the surface of the probe. Bread board models of probe electronics and command/control electronics were also designed for testing the integrated system. Experiments under various conditions (Ambient, Vacuum and Field) were conducted to characterise the performance of the designed prototype of CHaSTE. Result of one such experiment is shown in Figure 54b.

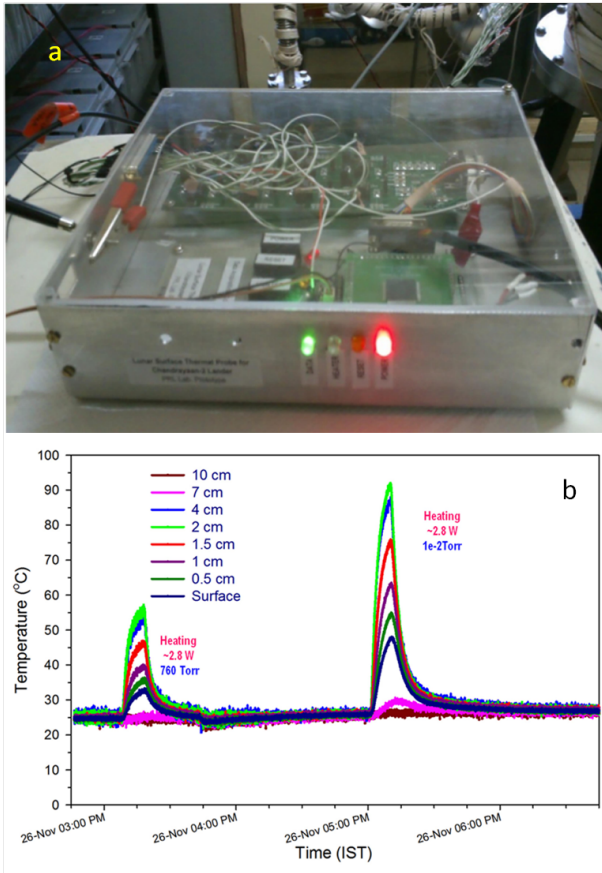


Figure 54: (a) Prototype Probe and Electronics designed at PRL; (b): Response of the probe during active heating - role of surrounding atmosphere in heat propagation.

(K. Durga Prasad, V. Mani Teja, V.K. Rai and S.V.S. Murty)

Effect of grain size and porosity on surface thermal behaviour of the Moon

The outer-most porous layer of the Moon principally dictates the propagation of solar heat influx to the interior layers and thus needs to be better understood. However, the nature or behaviour of this outer-most layer is not well-constrained due to lack of sufficient experimental data. We have initiated efforts in understanding the behaviour of the top few centimetres (~10 cm) of the lunar surface by means of laboratory experiments. We have designed and tested a chamber with necessary experimental setup to carry out these experiments under simulated lunar environment conditions. Experiments were carried out to initially understand the effect

of pressure/interstitial gases and grain size on the thermal behaviour of the sample. These experiments were currently carried out with fine grain sand. Experiments were conducted to simulate daytime surface temperature of the Moon (~125°C) for uniform as well as 2-layered stratigraphies.

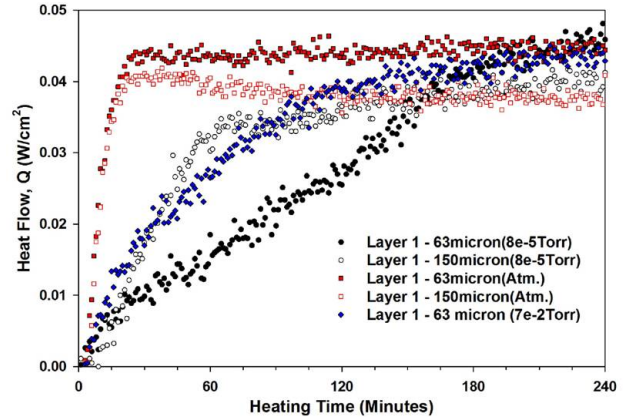


Figure 55: Temporal variation of heat flow within the sample stratigraphy for variable pressures and grain sizes.

Figure 55 shows the temporal evolution of heat flow due to a porous layer made of 63 μm size soil, for different pressure conditions - Atmospheric, 7×10^{-2} torr and 8×10^{-5} torr (indicated with solid symbols). Variations due to a porous layer made of 150 μm soil are also shown for atmospheric and 8×10^{-5} torr pressures in the same Figure 55 as open symbols. A pressure dependence of heat flow within the sample stratigraphy is clearly evident from the Figure 55. These results thus indicate that the behaviour of heat transfer within porous media under vacuum is appreciably different from that under atmospheric conditions. This has several implications in understanding the heat flow within the surface regolith of the Moon.

(K. Durga Prasad and S.V.S. Murty)

Comparison of laboratory XRF measurements from APXS (Alpha Particle X-ray Spectrometer) with Geant4 Simulation Results

The Alpha Particle X-ray Spectrometer (APXS) on-board Chandrayaan-2 rover aims at measuring elemental composition of the lunar surface using a Silicon Drift Detector SDD with improved energy resolution (150 eV at 5.9 keV). The objective of the APXS instrument is to analyze several soil and rock samples along the rover traverse for the major elements by detecting characteristic X-rays in the energy range of 1 to 25 keV. APXS instrument is configured as a single package and is mounted in the front side, beneath the rover chassis at a height of 180 mm from the lunar surface viewing the sample area of 220 mm diameter. The APXS assembly consists of a stack of three PCBs for detector signal readout and processing and shutter with motor to protect the detector and radio-active sources from lunar dust (during rover traverse). The shutter is positioned close to the circular periphery of the source holder with minimum gap of < 1

mm. The inner side of the shutter will be coated with desired material of known chemical composition for the calibration of APXS instrument as and when required. We have carried out XRF measurements in the laboratory using Alpha Particle X-ray Spectrometer which provides energy resolution of 150 eV at 5.9 keV, when the detector is cooled to -35°C . These measurements are carried out using six ^{55}Fe X-ray sources (^{244}Cm alpha source are under procurement) for various target materials at different detector to target heights to experimentally quantify the change in the XRF intensity with detector to sample height. The total activity of ^{55}Fe source is ~ 60 mCi (10 mCi each). The measured XRF data is compared with GEANT4 based Monte-Carlo simulation by developing a model similar to APXS, and carried out the simulation for similar operating condition & source activity. We used Al and Ti targets for both XRF measurements and in the GEANT4 simulations.

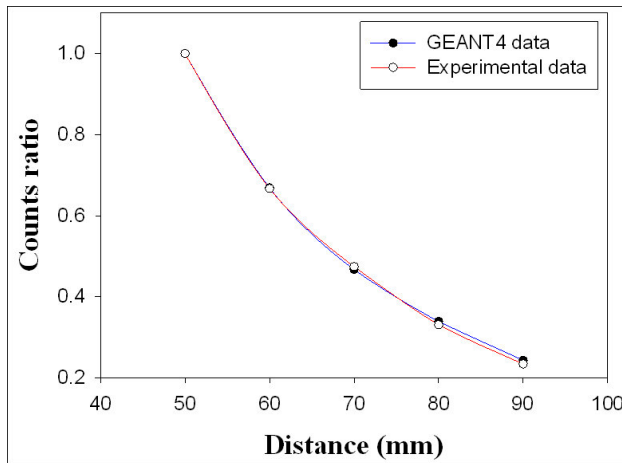


Figure 56: Dependence of XRF intensity for various detector to Ti target heights, where experimental measurements are compared with GEANT4 simulation.

The XRF spectra was measured for Ti target at a height of 90 mm with integration time of 3600 seconds. In the spectra, we observed the energy lines at 4.5 keV and 4.9 keV from Ti target, 5.9 keV and 6.4 keV due to scattered X-rays from ^{55}Fe source and 3.0 keV and 3.2 keV lines are likely due to Argon present in air. It is shown that the XRF intensity decreases by a factor of 5 when the sample to detector distance is changed from 50 mm to 90 mm. The GEANT4 simulation carried out for similar detector to sample distance yielded results that closely matches with XRF data as shown in Figure 56. Similarly for Al target, the XRF intensity decreases about 100 times when the sample to detector distance is varied from 10 mm to 60 mm.

To experimentally confirm the XRF peak due to Ar in air (as observed in Figure 57), we have made an air-tight enclosure of Perspex. The enclosure is flushed with dry nitrogen and observed that the Ar peak disappeared after sufficient flushing (Figure 58). XRF measurement with height gives an indication that the APXS would require about 5-6 hours integration time to have meaningful data when mounted at 180 mm above the lunar surface. The Qualification Model (QM) PCB layouts for APXS payload has been completed, and we aim to complete the qualification tests later this year.

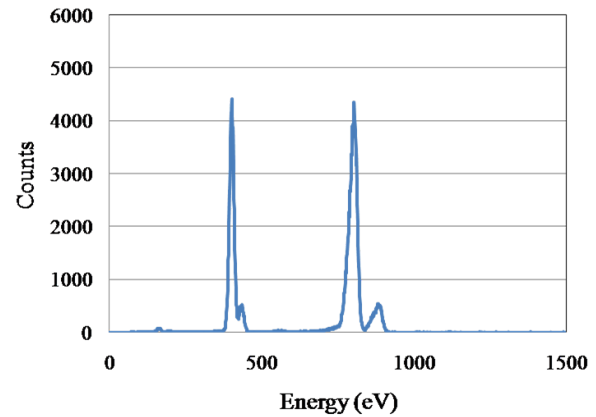


Figure 57: XRF measured inside the enclosure in the presence of air and without any target.

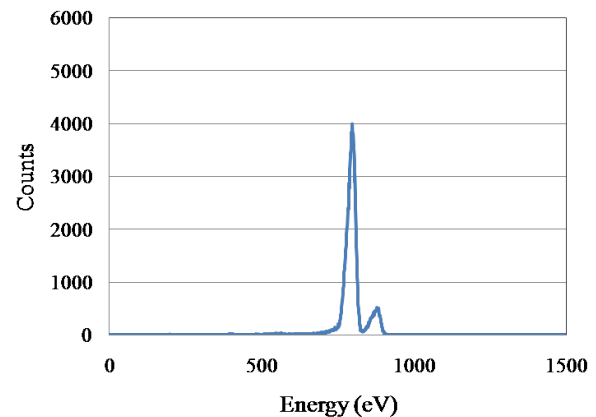


Figure 58: XRF measured inside the enclosure after flushing with dry nitrogen and without any target

(M. Shanmugam, S.K. Goyal, A. Patel, Y.B. Acharya and S.V.S. Murty)

High count rate measurement from Solar X-ray Monitor for Chandrayaan-2 Orbiter

One of the scientific experiments onboard Chandrayaan-2 orbiter is the remote X-ray Fluorescence spectroscopy for measuring abundances of the major rock forming elements of the lunar surface. The experiment involves measuring spectra of fluorescent X-rays from lunar surface which are generated due to the incident solar X-rays. Since the flux of fluorescent X-ray lines critically depend on the flux and spectrum of the incident solar X-rays which are highly variable, it is essential to have simultaneous measurement of X-ray from the Sun in order to have quantitative interpretation of the lunar X-ray fluorescence spectra.

The Solar X-ray Monitor (XSM) onboard Chandrayaan-2 orbiter will accurately measure the real time solar X-ray spectrum using state-of-the-art Silicon Drift Detector (SDD).

At PRL, we are developing XSM payload for Chandrayaan-2 Orbiter. XSM instrument consists of two packages namely XSM sensor package and XSM processing electronics package. XSM sensor package consists of SDD module coupled with Charge Sensitive Pre-Amplifier (CSPA), Shaping amplifier, HV supply for SDD module, controller for the peltier cooler and the moving mechanism. The XSM analog front end electronics include two independent channels of shaping amplifiers with two peaking times of $0.8 \mu\text{s}$ and $0.2 \mu\text{s}$ respectively. The slow channel is optimized for high energy resolution up to incident count rate of ~ 100 kcounts/s, whereas the fast channel is used to independently count the total number of X-ray interactions on the detector so as to have proper dead time correction of the recorded X-ray spectrum.

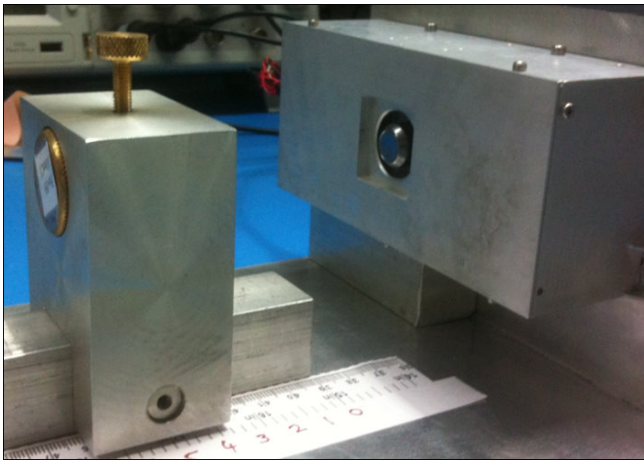


Figure 59: Experimental arrangement for high count rate measurement using ^{55}Fe source.

The developed engineering model of the XSM payload provides energy resolution of ~ 200 eV at 5.9 keV for the pulse peaking time of $0.8 \mu\text{s}$ by cooling the detector to -35°C . The XSM instrument is characterized for count rates up to 150 kcounts/s using ^{55}Fe X-ray source. This was carried out by designing a test setup such that the centre of the detector is matched with the source centre by mounting the source in a movable guide as shown in Figure 59. By changing the distance between the source and the detector, the incident X-ray rate on the detector is varied and the spectra was acquired. From this experiment, it is shown that the energy resolution maintained ~ 200 eV at 5.9 keV up to 70 kcounts/s and varies to 350 eV at 150 kcounts/s as shown in Figure 60. Energy resolution measurement is also carried out for the pulse peaking time of $1.2 \mu\text{s}$ for count rates up to 150 kcounts/s. It is shown that the energy resolution at lower count rate is ~ 180 eV at 5.9 keV and the resolution is stable for the count rates up to 45 kcounts/s and changes drastically at higher count rates (Figure 60). Based on this result, we have chosen $0.8 \mu\text{s}$ pulse peaking time for XSM experiment.

The developed instrument is also tested for stability of spectral peak position with count rate. It is well known that the spectral peak position changes with pulse peaking time and count rate. We tested the developed system for peak position stability for the pulse peaking time of $0.8 \mu\text{s}$ and $1.2 \mu\text{s}$. It is shown that the peak position change is within 2 ADC channels for

the count rate up to 70 kcounts/s and changes from 296 ADC channels to 280 ADC channels at 150 kcounts/s for the pulse peaking time of $0.8 \mu\text{s}$. For $1.2 \mu\text{s}$, the change in peak position is quite drastic with count rate as shown in Figure 61. We also implemented paralyzable dead time in the event processing which enables to select only clean events which are not affected by previous events for generating spectra. We have digitally implemented selectable paralyzable dead times of $3 \mu\text{s}$, $5 \mu\text{s}$, $7 \mu\text{s}$ and $10 \mu\text{s}$. The data was acquired with no dead time and with $10 \mu\text{s}$ and shown that the energy resolution at low count rate is similar in both cases and improves ~ 10 eV at 150 kcounts/s with $10 \mu\text{s}$ paralyzable dead time for the pulse peaking time $0.8 \mu\text{s}$ and it is ~ 35 eV for $1.2 \mu\text{s}$ peaking time.

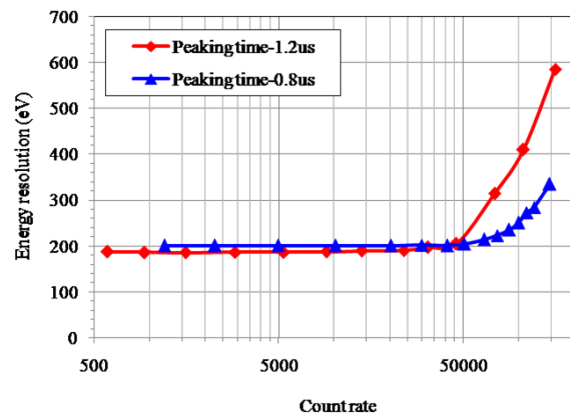


Figure 60: Energy resolution versus count rate for different pulse peaking time.

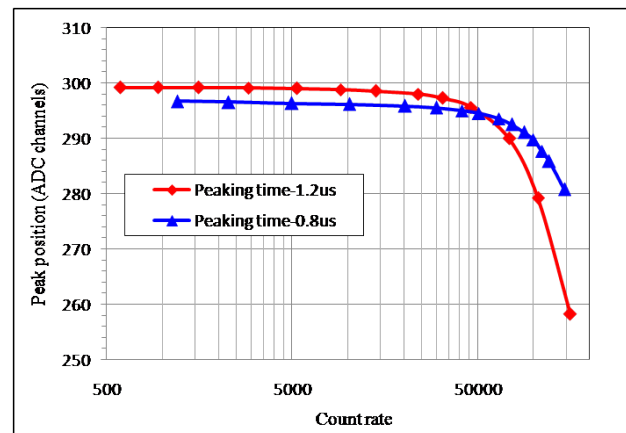


Figure 61: Peak energy position versus count rate for different pulse peaking time.

We also observed that the peak stability has improved to ~ 2 ADC channels with $10 \mu\text{s}$ dead time for the pulse peaking time $0.8 \mu\text{s}$ and for $1.2 \mu\text{s}$, peak stability improves to ~ 4 ADC channels. Similarly, high count rate measurement using X-ray gun is also completed.

(M. Shanmugam, A. Patel, S.K. Goyal, Y.B. Acharya and S. Vadawale)

Development of a $\text{LaBr}_3:\text{Ce}$ Gamma Ray Spectrometer (GRS)

An important technique for remote sensing studies of chemical composition of planetary surfaces is gamma ray spectroscopy which has been used previously to study surface composition of the Moon, Mars and Asteroids at various spatial resolutions. We are developing a $\text{LaBr}_3:\text{Ce}$ gamma ray spectrometer for a future planetary mission. Previously, the performances of the shaping amplifier and the processing electronics sub-systems have been tested with the $\text{LaBr}_3:\text{Ce}$ detector. The energy resolution at 1.274 MeV with present GRS configuration was measured using a ^{22}Na radioactive source, and is estimated to be $\sim 3.2\%$.



Figure 62: Bread-board model of GRS electronics developed in PRL combining shaping and processing electronics within a single PCB.

The linearity of the developed GRS has been checked by plotting the variation of ADC channel with gamma ray energy, and the data acquisition software enables us to obtain the counts from the bread-board model.

Recently, we have designed a new bread board model which combines both shaping and processing electronics into a single board to reduce the possibility of additional noise due to cable connection between shaping and processing electronics board. A 14-bit ADC is used for digitization of signal, so that the input voltage can be set from -10 V to +10 V. The required control signals for ADC and peak detector are generated through Actel A3PE250 FPGA. The bread-board model is shown in Figure 62.

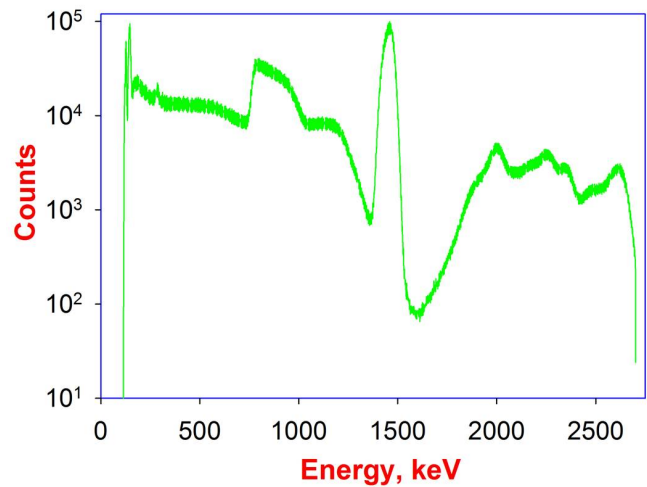


Figure 63: Background spectra measured using $\text{LaBr}_3:\text{Ce}$ GRS with in-house electronics enclosed within a 4-inch thick lead shield chamber; integration time was ~ 3 days.

After calibration measurements, a gamma ray background spectra has been measured for 3 days, and is shown in Figure 63. Measurements of gamma ray spectra have been carried out on K, U and Th standards and soil samples from Thaltej campus for determining the composition of U, Th and K using both $\text{LaBr}_3:\text{Ce}$ and HPGe gamma ray spectrometers.

(D.K. Panda, D. Banerjee and A.D. Shukla)

SCIENCE

Space, Atmospheric, Molecular and Laser Physics

Quantification of absorbing aerosol type over the Indo-Gangetic Plain

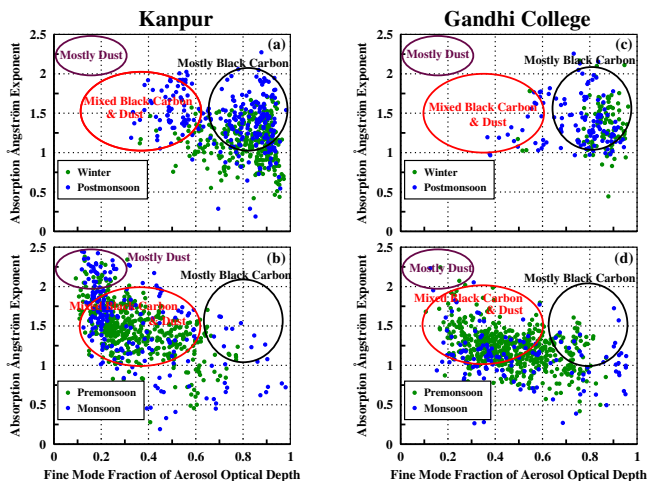


Figure 64: Absorption Ångström exponent plotted as a function of fine mode fraction of aerosol optical depth in different seasons over Kanpur and Gandhi College in the Indo-Gangetic Plain. The ellipses in different colors represent categories of absorbing aerosols, namely, Mostly dust, mixed Black Carbon and dust, and mostly Black Carbon.

Aerosol size distribution, absorption and extinction Ångström exponents over Kanpur (an urban location) and Gandhi College (a rural site) in the Indo-Gangetic Plain (IGP) are examined to determine the absorbing aerosol type. Mostly Black Carbon (BC) and BC mixed with dust dominate (>95%) the absorbing aerosol abundance over the IGP. In Kanpur

mostly dust contribution is higher than over Gandhi College, while over Gandhi College the concentration of mostly BC is significantly higher than that over Kanpur (Figure 64). Fine mode absorbing aerosols mainly emitted from anthropogenic sources (biomass burning and downwind transport of fossil fuel aerosols) are comparatively more abundant over Gandhi College than over Kanpur throughout the year.

Dust mixed with BC remains higher over Kanpur during all the seasons than over Gandhi College because of its proximity to the Thar desert and due to the transport of dust. Mostly dust aerosols are absent over Gandhi College throughout the year. It is clear that Kanpur and Gandhi College located in IGP are governed by different aerosol types in different seasons. This study brought out the spatiotemporal heterogeneity, and quantified the absorbing aerosol type over the IGP which is crucial while estimating the aerosol radiative effects.

This work was done in collaboration with Sumita Kedia, Centre for Development of Advanced Computing, Pune.

(S. Ramachandran)

Influence of mixing on aerosol heating over an urban region

Influence of aerosol mixing state on aerosol heating rate over an urban region is investigated using measured spectral aerosol optical properties and a radiative transfer model. Aerosol heating rates are calculated for external mixtures, and for mixing states have been determined corresponding to

single scattering albedo (SSA) obtained from ground-based near surface (using Aethelometer and Nephelometer) and columnar measurements from Ozone Monitoring Instrument (OMI) on board Aura satellite. SSA from ground-based measurements is lower than columnar SSA throughout the year owing to the abundance of absorbing aerosols near surface. In winter, mineral dust coated with water soluble aerosols emerges as the most probable mixing state for ground-based SSA (0.7), while black carbon coated with water soluble is found to be the most probable mixing state for columnar SSA (0.95), thus, suggesting that aerosol mixing states can vary for different SSA at the same location. Aerosol heating rate obtained for external mixture is higher than the heating rate obtained for ground-based SSA, while it is lower than the heating rate estimated for columnar SSA (Figure 65) which is consistent with SSA values. High aerosol heating rate ($\geq 1 \text{ Kd}^{-1}$) is confined to < 3.5 km during winter (Figure 65) and post-monsoon, while aerosol heating (0.5 Kd^{-1}) extends up to 6 km during pre-monsoon and monsoon due to deeper boundary layer and presence of dust at higher levels. These findings on the mixing state of aerosols for different SSA values over urban regions will serve as useful inputs in reducing the uncertainties associated with aerosol radiative effects.

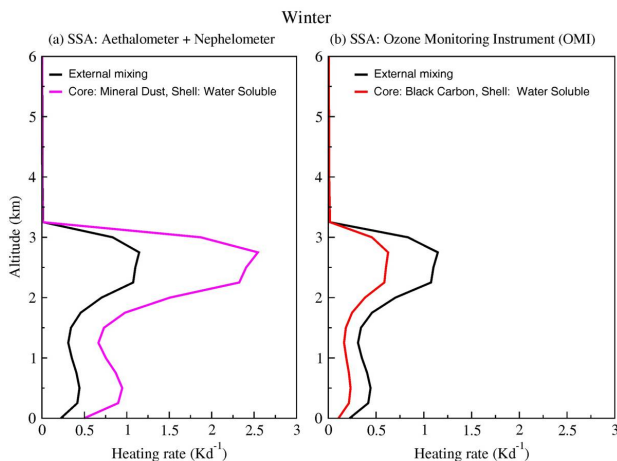


Figure 65: Aerosol heating rate (Kd^{-1}) profiles for external mixture and core-shell mixing scenarios over an urban region (Ahmedabad) during winter. Heating rates are estimated for aerosol mixing state obtained correspond to single scattering albedo from (a) ground-based (Aethalometer and Nephelometer) and (b) column (OMI onboard the Aura remote sensing satellite).

This work was done in collaboration with R. Srivastava, Indian Centre for Climate and Societal Impacts Research, Ahmedabad.

(S. Ramachandran and T.A. Rajesh)

Aerosol-precipitation interactions over India and surrounding oceanic regions

Aerosol and cloud characteristics over the Arabian Sea, India and the Bay of Bengal during summer monsoon in the last decade exhibit large regional, intra-seasonal and inter-annual variations. AOD and rainfall exhibit significant

negative correlation over All India and the Bay of Bengal; correlation between the two is positive over the Arabian Sea. AOD is expected to decrease during heavy rainfall due to wet removal as seen over All India and the Bay of Bengal. However, a positive correlation between AOD and rainfall anomalies can arise due to (a) inefficient removal of aerosols by wet deposition, (b) replenishment of aerosols due to natural sources (especially sea salt), and (c) growth of existing water soluble aerosols in high ambient relative humidity conditions ($> 80\%$) that exist during summer monsoon season. Cloud effective radius shows significant positive correlation with rainfall over India and the Arabian Sea, while it is negatively correlated with rainfall over the Bay of Bengal. The negative correlation between cloud effective radius and rainfall could occur due to a combination of variability in meteorological conditions and an inverse aerosol indirect effect caused by heterogeneous ice nucleation. This analysis on aerosol, cloud and rainfall characteristics over land (India) and the adjacent oceanic regions (Arabian Sea and Bay of Bengal) reveals that the aerosol-cloud interactions and the related aerosol indirect effects can vary on spatial scales.

This work was done in collaboration with Sumita Kedia, Centre for Development of Advanced Computing, Pune.

(S. Ramachandran)

Aerosol optical properties from ground-based and remote sensing observations in south Asia

Seasonal and inter-annual variability in aerosol optical depth (AOD) and aerosol size distribution are investigated using ground-based measurements (sun photometers and sun/sky radiometers), MODIS (MODerate Imaging Spectroradiometer) and MISR (Multiangle Imaging SpectroRadiometer) satellites over Ahmedabad, Gurushikhar, Karachi, Kanpur and Gandhi College. Karachi and Ahmedabad AODs are two times higher than those over Gurushikhar, a high altitude remote site. AODs over Kanpur and Gandhi College in the Indo-Gangetic basin are higher than those measured over Ahmedabad, Gurushikhar and Karachi. Comparison between ground-based and MODIS (Terra and Aqua) retrievals show that aerosol optical depths do not change significantly in an hour and much of the diurnal AOD variation is captured well by the two MODIS (Terra with an overpass at 1030 hrs, and Aqua with an overpass at 1330 hrs) instruments. The temporal difference (about an hour) between the ground-based and remote sensing measurements contributes negligibly to the observed differences in AODs. The differences between ground-based and remote sensing (MODIS and MISR) AODs vary on spatial scales. During the study period (2006-2008) MODIS underestimates AODs over western India by about 0.04, while over the Indo-Gangetic Plain MODIS overestimates AOD by 0.06 in (Kanpur) and underestimates AOD by 0.07 (Gandhi College) with respect to ground-based AODs. During the same period MISR underestimates AODs in the range of 0.02-0.17 over Ahmedabad, Gurushikhar, Karachi and Kanpur, while in Gandhi College MISR overestimates AOD by 0.2 when compared to ground-based AODs. These results on spatial and seasonal variations in

aerosol optical characteristics will be useful in improving the remote sensing aerosol retrieval algorithms over the south Asian region.

This work was done in collaboration with Sumita Kedia, Centre for Development of Advanced Computing, Pune.

(S. Ramachandran)

Seasonal and inter-annual variability of tropospheric ozone over an urban site in India: A study based on vertical profiles over Hyderabad

This study is based on the analysis of ozone profiles over Hyderabad, measured during the years 2006-2008 using the Measurement of Ozone and Water Vapor by Airbus In-Service Aircraft (MOZAIC) data. Tropospheric profiles of O_3 show clear seasonality with high and low values during the pre-monsoon and monsoon seasons, respectively. Analysis of back trajectory and fire count data indicates major roles for long-range transport and biomass burning in the seasonal variation of O_3 . Typically, lower levels of O_3 in the monsoon season were due to the flow of marine air and negligible regional biomass burning, while higher levels in other seasons were due to transport of continental air into Hyderabad. In the upper troposphere, relatively low levels of O_3 during the monsoon and post-monsoon seasons were associated with deep convection. In the free troposphere, levels of O_3 also show year-to-year variability as the values in the pre-monsoon of 2006 were higher by about 30 ppbv compared to 2008. The year-to-year variations were mainly due to transition from El Niño (2006) to La Niña (2008). The higher and lower levels of O_3 were associated with strong and weak wind shears, respectively. Typically, vertical variations of O_3 were anti-correlated with the lapse rate profile. The lower O_3 levels were observed in the stable layers, but higher values in the mid-troposphere were caused by long-range transport. In the PBL region, the mixing ratio of O_3 shows strong dependencies on meteorological parameters. A Chemistry Climate Model (CCM-version 2 of MRI, Japan) reasonably reproduced the observed profiles of O_3 except for pre-the monsoon season.

(L. K. Sahu and V. Sheel)

Measurements of atmospheric volatile organic compounds (VOCs) using a proton-transfer-reaction time-of-flight mass spectrometer (PTR-TOF-MS)

Volatile organic compounds (VOCs) play important roles in the chemistry of the troposphere and can affect the earth's climate. Measurements of these species are rare over the Indian subcontinent and surrounding marine regions. Traditionally, gas chromatography (GC) based methods have been used for the detection of VOCs in the atmosphere. Recently, a new instrument known as Proton Transfer Reaction Time of Flight Mass Spectrometer (PTR-TOF-MS) has been installed in PRL for carrying out highly sensitive and rapid real-time detection of VOCs. This instrument

also provides high mass resolution and thus improves the analytical information contained in the mass spectra of atmospheric air. This is for the first time that the TOF based measurements of VOCs are being carried out in India. As shown in Figure 66, the PTR-TOF-MS based measurements in an urban site of Ahmedabad show clear separation of isomeric compounds like furan and isoprene, ketene and propene, etc. Measurements from 27 November 2013 to 28 February 2014 show large diurnal and day-to-day variations of VOCs. The oxygenated VOCs (OVOCs) make major contributions compared to other VOCs in ambient air. Among the VOCs, methanol is one of the most abundant VOCs with a daily mean of 21 ± 6 ppbv at Ahmedabad. The mixing ratios of most of the VOCs showed highest values during morning and evening hours which coincide with the traffic during rush hours in Ahmedabad. The meteorological condition has been one of the important factors causing large day-to-day variations in the levels of various VOCs. In this study, the mixing ratios of isoprene (C_5H_8), acetonitrile (CH_3CN), and benzene (C_6H_6) have been measured with the objective of being used as tracers for biogenic, biomass burning, and vehicular origins, respectively. In future, simultaneous measurements of VOCs and oxides of nitrogen (NO_x) will be conducted as ozone (O_3) chemistry depends on the ratio of VOCs to NO_x .

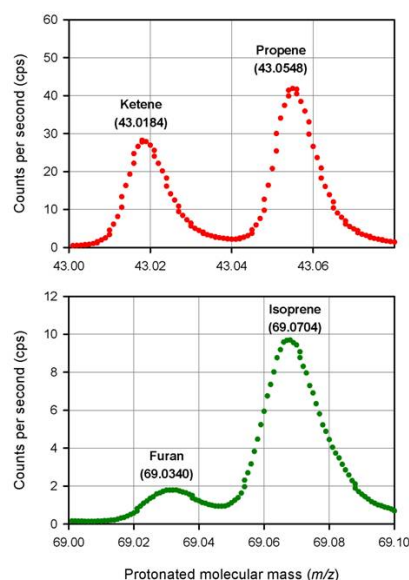


Figure 66: High mass resolved PTR-TOF-MS spectra of isomeric compounds like ketene and propene (top) and furan and isoprene (bottom) in ambient air at Ahmedabad.

(L. K. Sahu and P. Saxena)

Source and process studies for trace gases over Ahmedabad

Measurements of O_3 , CO , NO_x and SO_2 were made over Ahmedabad during varying meteorological conditions (May-October, 2011) to study the effect of meteorology and air masses on the concentrations, variability and

inter-relationships of these gases. The levels of CO and SO₂ observed over Ahmedabad were, in general, not very high compared to other major urban regions in India and Asia. On the other hand, NO_x levels, impacted by vehicular emissions, were found to be substantially elevated. A sudden increase in trace gas levels was observed during post-monsoon months, with average concentrations of primary pollutants being more than twice of pre-monsoon values. This change is brought about by a concurrent change in prevailing winds. Levels of CO, NO_x and SO₂ showed unique relationships with wind direction depending on the source contributions. Very good correlations are observed between CO and NO_x indicating co-emissions of these species. SO₂ values, as well as SO₂/NO_x ratios are higher when wind is from the eastern sector of the city which contains a thermal power station and a few industrial clusters (Figure 67). The SO₂/NO_x slope for point sources over Ahmedabad is found to be 0.4 while it is 0.03 for mobile sources.

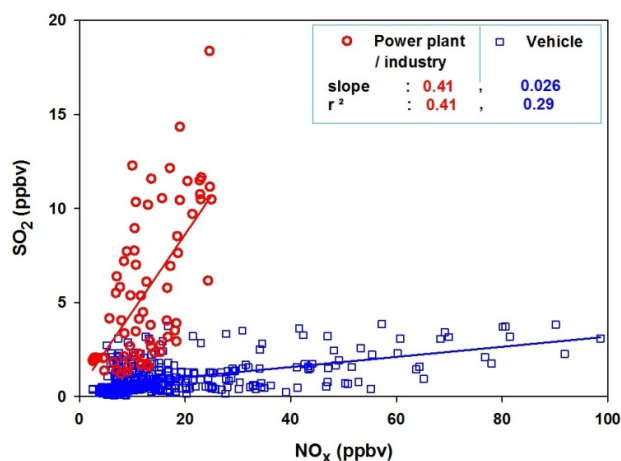


Figure 67: Relationships between SO₂ and NO_x over Ahmedabad during May-October, 2011.

Further, reduced sulfur gases (RSCs) were measured for the first time over Ahmedabad using a gas chromatograph set-up developed at PRL. The set-up was able to determine the atmospheric concentrations of two RSCs viz., COS and CS₂ for most of the analyses during February-October, 2013.

(C. Mallik, S. Venkataramani and S. Lal)

Greenhouse gases over Ahmedabad

Carbon dioxide (CO₂) and methane (CH₄), are the two most important human-influenced greenhouse gases contributing to more than 75% to the total radiative forcing. Carbon monoxide (CO) plays an important role in atmospheric chemistry and acts as an indirect greenhouse gas by perturbing the OH-CH₄-O₃ chemistry. The sources and sinks of these gases are poorly quantified and characterized, especially over Asian region. Climate change predictions require better understanding of the sources and sinks of these gases as well as changes in their levels. This necessitates their accurate measurements in different regions

of India. Simultaneous measurements of these gases have been initiated at PRL using a state of the art laser based analyzer. Average diurnal variation for the month of November 2013 is shown in Figure 68. While all the three gases show afternoon minimum and increase in the evening hours due to changes in source strengths and boundary layer dynamics, diurnal variation in CO₂ is different. CO₂ shows a slight increase from mid-night to early morning due to respiration process by biosphere. The noon time dip is also linked to the photosynthesis effect in addition to other boundary layer and anthropogenic sources. Hence, the amplitude of the diurnal variation in CO₂ gives information related to the biosphere. The average levels of CO₂-CH₄ and CO, at Ahmedabad during November, 2013 were 417.2 ppmv, 2.4 ppmv and 690 ppbv respectively, which are much higher than the background levels.

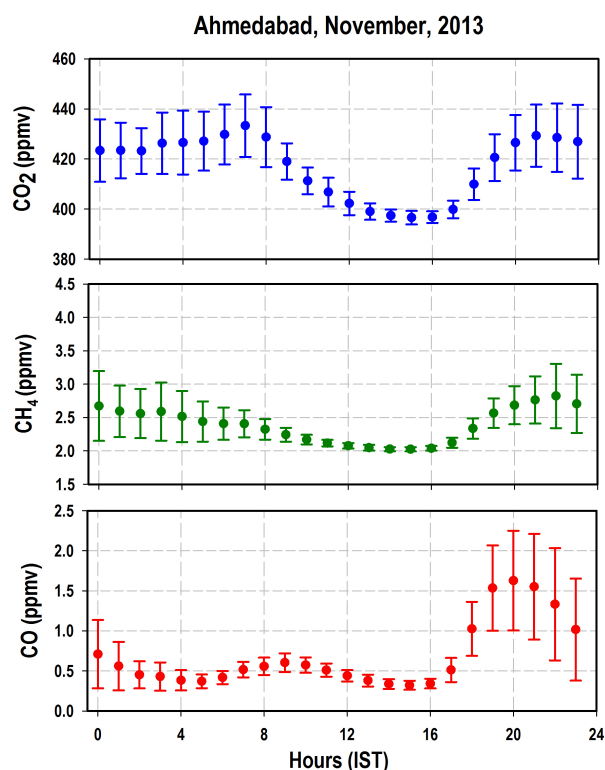


Figure 68: Average diurnal patterns of CO₂-CH₄ and CO over Ahmedabad during November, 2013.

(N. Chandra, S. Venkataramani and S. Lal)

Role of biomass burning and long range transport on trace gases over Asia

Anthropogenic emissions in Asia are increasing due to rapid urbanisation and industrial growth. Trace gases like CO and O₃ emitted in the Asian region are susceptible for long range transport and are known to affect regions as far as the Indian Ocean. We study the seasonality in the vertical distribution of CO and O₃ over Asia using the MOZAIC aircraft data and

chemistry transport models. The objective of this study is to investigate the effect of biomass burning and long range transport, on the variability of these trace gases. While the PBL CO is predominantly influenced by strong winds, bringing regional background air from marine and biomass burning regions, under calm conditions, CO levels are elevated by local emissions. Back trajectories and fire count map indicate the role of long-range transport and regional biomass burning on the lower tropospheric O₃. On the other hand, in the free troposphere, seasonal variation reflects the impact of long-range transport associated with the ITCZ and biomass burning. The inter-annual variations were mainly due to transition from El Niño to La Niña conditions.

In collaboration with M. Kajino, Meteorological Research Institute, Tsukuba, Japan.

(V. Sheel and L. K. Sahu)

Longitudinal variation in the Electrical conductivity in the stratosphere over low latitude regions– Balloon borne results

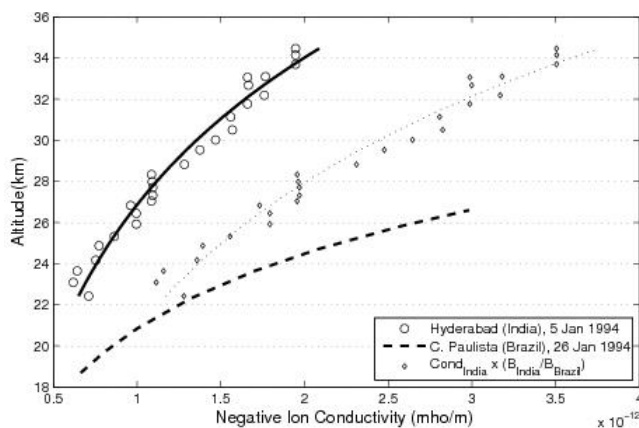


Figure 69: The conductivity profile obtained from Hyderabad on 5 January 1994 and that obtained from Cachoeira Paulista, Brazil for January 26 1994 (Reproduced from Saba et al., 1999). The curve with dotted lines and diamond symbols gives an 'expected' profile for conductivity variation for Brazil, obtained by considering only the difference in the magnetic field over the two locations.

During Indian Middle Atmospheric Conductivity Campaign (1982-1994), the vertical profiles of stratospheric conductivity were measured using different techniques, from a low-latitude station, Hyderabad (17.5°N, 78.5°E Geographic, 8.5°N magnetic lat), to investigate the stratospheric conductivity variations over low latitude regions, including long term variations. In the present study, the conductivity profile obtained from Hyderabad on 5 January 1994 is compared to that obtained from Cachoeira Paulista, Brazil (22°44S 44°56W geographic, 11°57S, 22°32E geomagnetic) on 26 January 1994, to understand the longitudinal variations. The longitudinal difference in the magnetic field strengths is expected to cause longitudinal differences in the sources of ionizing agencies such as cosmic ray fluxes, and hence the conductivity. The observations also show that stratospheric

conductivity over Cachoeira Paulista, Brazil, is significantly higher than that observed over Hyderabad. However, the difference is more (especially at higher altitudes) than that could be explained simply by the magnetic field variations over these two locations (Figure 69). Since Cachoeira Paulista is near the South Atlantic Anomaly region, it is expected to have additional effects of particle precipitation, especially over higher altitudes

(S. P. Gupta and S. V. Thampi)

Study of Mesospheric Temperature Inversions over Sub-tropical Location using Lidar and Satellite Observations

Characteristics of Mesospheric Temperature Inversions (MTIs) are studied using ~250 nights of Rayleigh Lidar data collected over Mt. Abu (24.5°N, 72.7°E) during the period of 1997 to 2003 for the first time from an Indian sub-tropical location. Three MTI events have been investigated and a detailed statistical analysis has also been performed. A strong MTI event, with amplitude of about 30 K, at altitudes between 60 and 70 km was observed on 30 December 2003. It was accompanied by strongly perturbed mesospheric zonal winds as observed by TIMED Doppler Interferometer (TIDI) onboard Thermosphere Ionosphere Mesosphere Energetics and Dynamics (TIMED). Two MTI episodes during March and December 2000 were investigated, which shows that MTI can persist for few days and its amplitude varies gradually. These episodes of MTIs exhibit different characteristics, viz., height of occurrence, magnitude of inversion and separation between multiple MTIs. Ozone observed by Halogen Occultation Experiment (HALOE) onboard Upper Atmospheric Research Satellite (UARS) also showed significantly higher variability during strong MTI events. Statistical analysis revealed that the frequency of occurrence of MTIs is maximum during winter and minimum during summer. These features are in contrast to the low-latitude observations. The average magnitude of MTIs is ~ 20 K and has prominent seasonal variability. The average height of occurrence of MTIs is found to be lower over Mt. Abu than that Gadanki.

(S. Sharma, H. Chandra, S. Lal and Y. B. Acharya)

Formation of meridional circulation cell in thermosphere during Sudden Stratospheric Warming (SSW) events

Oxygen dayglow emissions at multiple wavelengths (557.7 nm originating at ~ 130 km, 630.0 nm 230 km, and 777.4 nm at peak of F-region) over a low-latitude location, Hyderabad showed systematic enhancements in intensities after one-to-two days of the occurrence in the peak of SSW events during the years 2010 – 2013. Further, the enhancements are seen to be present throughout the day (Figure 70).

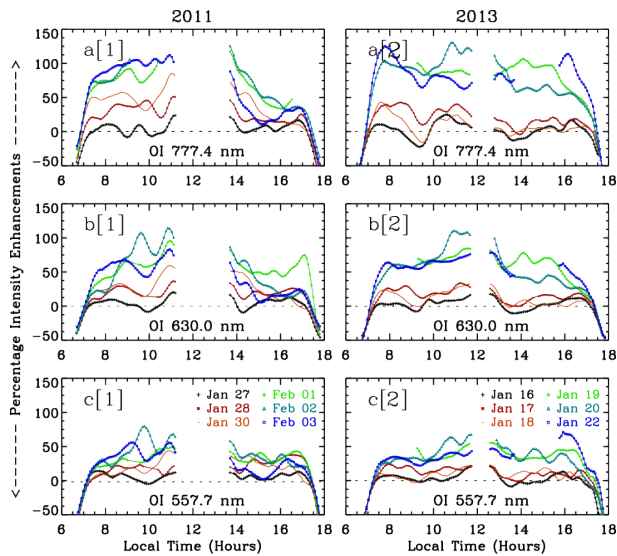


Figure 70: Intensity variations in the oxygen dayglow emissions in-and-around the SSW events during 2011 and 2013 are shown. It can be seen that the intensity enhancements systematically increase after one-to-two days from the peak of the SSW event day (Jan 31 and Jan 18 for 2011 and 2013, respectively).

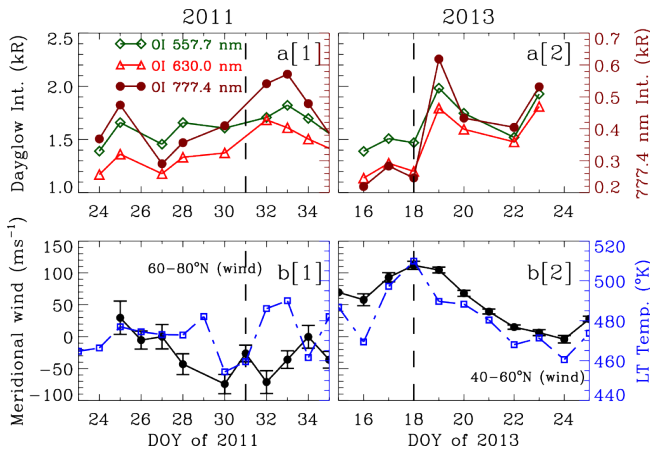


Figure 71: (a) The daily averaged dayglow emission intensities at low-latitudes for OI 557.7, 630.0, and 777.4 nm are shown. Dashed vertical line depicts the day of peak SSW event. (b) SABER measured lower thermospheric (LT) kinetic temperature (squares) over arctic latitudes and TIDI measured lower thermospheric daily averaged zonal-mean wind (at 110 km altitude). Notably, the winds are either equatorward (negative) or are reducing in magnitudes of the poleward (positive); especially from-and-after the peak of the SSW occurrence that coincides with enhancement in dayglow intensities.

It has been verified that these rises in intensities are not due to tidal effects, geomagnetic storm effects, or to the movement of the ionospheric layer to lower heights as a consequence of counter-electrojet that did occur on these occasions. Commensurate with the intensity enhancements in the integrated daytime emission (data for a couple of years 2011 & 2013 are shown in Figure 71 the lower thermospheric temperatures (measured by the Sounding of the Atmosphere using Broadband Emission Radiometry, SABER) at high latitudes and the equatorward (or reducing in poleward) meridional winds (measured by TIMED Doppler Interferometer, TIDI) show increased magnitudes. Based

on these measurements, it is proposed that a meridional circulation in thermospheric winds is set up during SSW events which enabled transport of oxygen from high-to-low latitudes.

This additional source is believed to be responsible for the observed enhancement in the daytime optical emission intensities over low-latitudes.

(F. I. Laskar and D. Pallamraju)

Development of a Near Infra-Red Imaging Spectrograph (NIRIS) for mesospheric temperature measurements

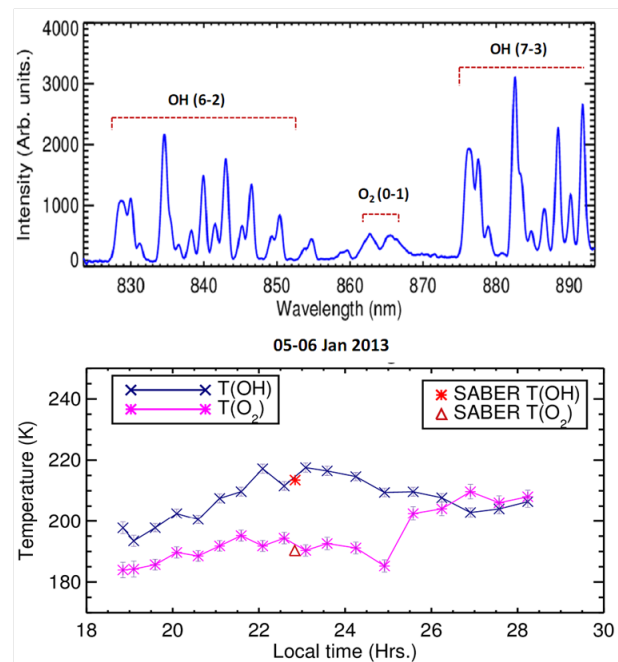


Figure 72: Night time spectrum obtained from NIRIS. OH (6-2) band $P_1(2)$ and $P_1(4)$ rotational lines (at 840 and 846.5 nm, respectively) are used for OH rotational temperature calculation. O_2 866 and 868 nm band lines are used to calculate O_2 rotational temperatures. Bottom: Nocturnal rotational temperatures derived using NIRIS from Gurushikhar, Mount Abu on 05-06 January 2013. SABER kinetic temperatures at ~ 87 km and ~ 94 km altitudes during satellite overpass of the observational site are also shown for comparison.

Neutral dynamics of the mesosphere can most efficiently be investigated by measuring the temporal variability in temperatures. One of the most accurate methods to derive the mesospheric temperatures is by recording the OH and O_2 rotational line spectra at high spectral resolution. The rotational levels of OH and O_2 are sensitive to the ambient temperatures and so, by obtaining the ratio of airglow emission intensities at chosen wavelengths, it is possible to obtain information of the temperatures from where they emanate (87 and 94 km, respectively). To enable such a measurement a grating spectrograph has been developed after suitably modifying the one which was primarily designed for recording spectra at ultra-violet wavelengths. After

modification, the present instrument, NIRIS, records spectrum in the 823 to 894 nm wavelength region and achieves a dispersion of $0.07 \text{ nm pixel}^{-1}$ and a resolution of 0.21 nm at 840 nm . A sample high resolution spectra obtained is shown in Figure 72 (top panel) and the temperature so derived (with uncertainty of $\pm 3\text{K}$) for the whole night in Figure 72 (bottom panel).

The temperatures compare well with satellite-based Sounding of Atmosphere by Broadband Emission Radiometry (SABER) kinetic temperatures. NIRIS has been commissioned for operation at the Optical Aeronomy Observatory at Gurushikhar, Mount Abu (24.6° N , 72.8° E) and is running on automated basis in a programmed manner since January 2013.

(R. P. Singh, D. Pallamraju, K. Phadke, and R. Narayanan)

Global characterization of mesospheric temperatures during Sudden Stratospheric Warming (SSW) events

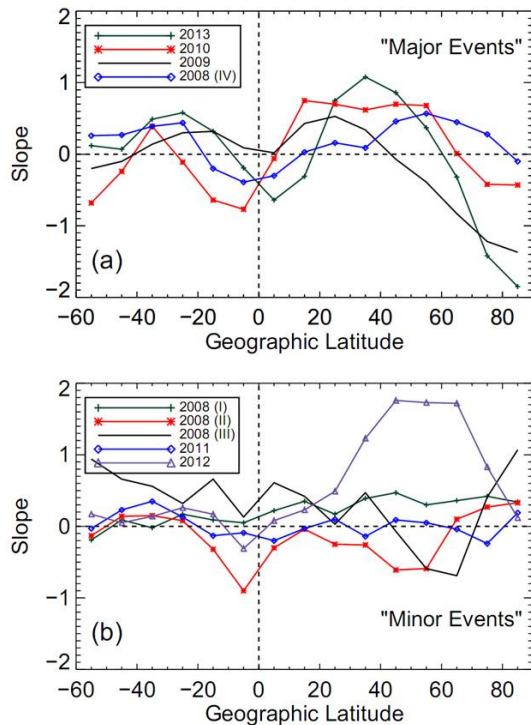


Figure 73: (a) Slopes derived from stratospheric vs mesospheric temperatures regression analysis with respect to the geographic latitude are shown for four major SSW events. (b) Similar plots as shown in the top panel but for the minor SSW events. One may note a “double-humped” structure in temperature gradients with respect to the geographic equator, especially during major SSW events. Such characterization in mesospheric temperatures across latitudes brings to light hitherto unknown intriguing nature of the latitudinal coupling that exists during the SSW events.

Mesospheric rotational temperatures as derived from $\text{O}_2(0-1)$ and $\text{OH}(6-2)$ band nightglow emissions originating at 94 and 87 km altitudes, respectively were obtained from Mount Abu (24.6° N , 72.8° E) using Near InfraRed Imaging Spectrograph

(NIRIS) showed enhancements during the major SSW event of January 2013. The effects of SSW on the mesospheric temperature at high latitudes have been extensively studied using different techniques in comparison to those over low- and mid-latitude regions. To understand the observed enhancement in mesospheric temperatures from Mount Abu in the context of SSW, a detailed investigation was carried out for nine SSW events that occurred over the past six years (2008-2013) using SABER (Sounding the Atmosphere using Broadband Emission Radiometry) data. The longitudinal mean mesospheric temperatures at different latitudes of northern and southern hemispheres have been derived. For every event, the mesospheric temperatures in a latitude bin of 15° were plotted with respect to SSW temperatures, the slopes of which indicate mesospheric heating (+ve slope) or cooling (-ve slope) over that latitude with respect to stratospheric temperatures. It is found that the well-known mesospheric cooling at higher latitudes during SSW periods turns to mesospheric warming at mid-latitude regions in both the hemispheres which is more prominent in northern hemisphere compared to the southern hemisphere. It is found that major SSW events shows a “double-humped” structure in mesospheric temperature enhancements with two crests over tropical to mid latitudes and a trough over the geographic equator (Figure 73).

(R. P. Singh and D. Pallamraju)

Vertical Coupling of Atmospheres: Dependence on Solar Activity and Sudden Stratospheric Warming (SSW)

Comprehensive behavior of the low-latitude upper atmosphere during SSW events at varying levels of solar activity has been studied. The equatorial electrojet (EEJ) strength and the total electron content (TEC) data from low-latitudes during the year 2005-2013 are used in this study. There were six major and three minor SSW events in this duration, wherein the solar activity wherein average sunspots varied from 5 to 55. Signatures of the large scale planetary wave (PW) type features have been found to be of different strengths in both the measurements for different solar activity levels and SSW strengths. The spectral amplitudes of quasi-16 day scale amplitudes in the EEJ and TEC during the three very strong SSW events of 2006, 2009, and 2013 are found to be very high and of significant magnitude during the minor events of the low solar activity period of 2005-2011. The SSW occurred around the new moon phase in all these events with varied background conditions. In summary, in addition to the effect of SSW strength and solar forcing it seems that the occurrence time of the SSW events with respect to lunar phase has a role to play in enhancing the PW amplitudes constructively or otherwise and thereby influence the effectiveness of the vertical coupling.

This work done in collaboration with B. Veenadhari at IIG, Navi Mumbai.

(F. I. Laskar and D. Pallamraju)

Long Term Changes in the Ionosphere over Indian low latitudes: Impact of greenhouse gases

Increased concentration of greenhouse gases due to anthropogenic activities warm the troposphere and have a cooling effect in the middle and upper atmosphere. Ionospheric densities and heights are affected due to cooling. Carbon dioxide is one of the most dominant gases for the cause of long term ionospheric trends along with other radiatively active trace gases. Regular ionospheric soundings made over Ahmedabad (23.1°N, 72.7°E), during 1955-2003 are examined to study the long term changes in the critical frequencies (f_oF_1 , f_oF_2) of the various ionospheric layers and the height of the maximum ionization ($h_P F_2$). A decrease in f_oF_2 (1.9 MHz for midday, 1.4 MHz for midnight) and $h_P F_2$ (18 km for midday, 17 km for midnight) are noted. An increase is noted in f_oF_1 (0.4 MHz). The f_oF_2 data are also examined over an equatorial station Kodaikanal (10.2°N, 77.5°E), situated near the magnetic equator for the years 1960-1995 and a decrease of 0.5 MHz for midday and 0.7 MHz for midnight are noted in ~35 years.

(S. Sharma and H. Chandra)

Three dimensional wave characteristics of neutral waves obtained by combined balloon and ground based measurements

Using combined balloon-borne optical (ultraviolet oxygen OI 297.2 nm airglow originating at ~120 km), and ground-based optical (visible oxygen OI 557.7 nm dayglow with a representative altitude of ~100 km), radio (the F-region of the ionosphere h'F at ~200 km), and magnetic measurements (equatorial electrojet ~105 km) the neutral wave characteristics in the daytime Mesosphere Lower Thermosphere (MLT) region have been obtained. All the wave parameters in three dimensions, namely scale sizes in the zonal (λ_x), meridional (λ_y), and vertical (λ_z) directions, wave periodicities (τ), horizontal phase speeds (c_H), and horizontal (θ_H) and vertical (θ_V) propagation directions have been obtained. They are λ_x :40-80 km; λ_y :200 km, λ_z :20-40 km; τ :16-30 minutes; c_H :21-77 ms⁻¹; θ_H :11°-22°; and θ_V :59°-63°. Such detailed characterization of waves in the daytime MLT region has not been done before by experimental means. Further, simulation studies carried out elsewhere show that the waves of the characteristics derived by our measurements are capable of propagating to ionospheric heights of 175 km. Furthermore, spectral analysis between the fluctuations in all these parameters showed common coherence periods in the range of 16-30 minutes in all these parameters that are separated in altitude and latitude, indicating a coupled behavior of the atmospheres and a possible means of coupling between the daytime and the nighttime phenomena.

This work was carried out in collaboration with S. Chakrabarti, University of Massachusetts, Lowell, USA and T. K. Pant, SPL.

(D. Pallamraju, R. P. Singh, F. I. Laskar, and R. Narayanan)

On the pre-midnight ascent of F-layer in the June solstice during the deep solar minimum in 2008 over the Indian sector

In contrast to the usual downward movement of F-layer during nighttime over the dip equator (Thumba, India and Fortaleza, Brazil), upward movement of F layer has been observed in the June solstice of the solar minimum years. This upward movement of the F layer during midnight hours can be due to electro-dynamical and/or chemical processes. In order to delineate this, drift (electro-dynamical) measurements on-board the Communication/Navigation Outage Forecasting System (C/NOFS) satellite are used in this investigation. This elicits that the midnight upward drift over the Indian sector during the northern summer months of 2009 (solar minimum year) is the largest and electro-dynamical in nature. In contrast, it is shown that upward midnight drift over Fortaleza during this period is chemical (recombination effect) in nature. Long-term lower mesospheric wind data from India reveals that the phases of both the meridional and zonal components of the diurnal tide regress while the phase of the meridional component of the semidiurnal tide significantly advances with decreasing solar activity with concomitant increases in amplitudes during the summer months. These observations suggest the possible semidiurnal tidal influence on the pre-midnight rise of F layer over the Indian sector in the June solstice during low solar activity.

This work is done in collaboration with B. G. Fejer (CASS-USU, USA), S. Gurubaran (IIG), T. K. Pant (SPL, VSSC) and M. A. Abdu (INPE, Brazil).

(D. Chakrabarty and R. Sekar)

Evidence for collisional damping of gradient drift waves during solar eclipse event over the dip equator

Comparison of rocket observations of electron density and fluctuations in it on a solar eclipse vis-à-vis a control day revealed the absence of gradient drift waves at lower altitudes during eclipse day despite the presence of strong gradient in the altitude profile of electron density. Based on these observations, the importance of collisional quenching of the gradient drift waves at lower altitudes during solar eclipse is brought out.

(R. Sekar, S. P. Gupta and D. Chakrabarty)

Zonal variations in the daytime thermosphere obtained from optical dayglow emission intensities

Low- and equatorial-latitude upper atmosphere responds to variations in the equatorial electrodynamic processes. To investigate this behaviour of the daytime upper atmosphere

across longitudes data has been obtained along the zonal direction from a low latitude location, Hyderabad (Geographic: 17.5°N, 78.5° E; Geomagnetic: 8.6°N, 151.8°E). Multi-wavelength high spectral resolution imaging spectrograph (MISE) has been used for this study. MISE obtains oxygen dayglow emissions intensities over a large field-of-view (of 140°) at 557.7nm, 630.0nm, and 777.4nm wavelengths which originate from altitudes of around 130 km, 230 km, and peak of the ionospheric F-region, respectively. The zonal variation in oxygen emission intensities has been obtained and the tidal contribution at each location has been removed. The resulting periodicities of the waves are in the range of 0.5 to 3.0 hours. Wave number spectral analyses is carried out to obtain the scale sizes of waves in the zonal direction and are found to be in the range of 200 - 400 km at an altitude of 230 km as obtained by the oxygen 630.0 nm emission dayglow. These initial results obtained from the OI 630.0 nm emission dayglow (that correspond to 230 km) will be augmented by those at OI 557.7 nm (~130 km) and OI 777.4 nm (peak of the F-region) to get a more detailed picture of the waves and their dynamics that exists in those altitude ranges.

This work is done in collaboration with T. Vijayalakshmi and M. Anjireddi at JNTUH.

(D. K. Karan, D. Pallamraju, and K. Phadke)

Signature of storm and substorm effects on 630.0 nm airglow intensity from Thumba – a case study

Narrow spectral band (0.3 nm) and narrow field-of-view observations of OI 630.0 nm airglow intensity from Thumba (a dip-equatorial station) reveal distinctive effects of storm and substorm induced electric fields in thermospheric neutral airglow emission intensity. These observations bring out the efficacy of 630.0 nm airglow observations to address the complex relationship between geomagnetic storm and magnetospheric substorm and their effects on the low latitude ionosphere-thermosphere system.

This work is done in collaboration with Tarun K. Pant (SPL, VSSC).

(D. Rout, D. Chakrabarty, R. Sekar, R. Narayanan, and S. V. Thampi)

Multi-wavelength nightglow emission intensity variability and plasma neutral coupling

A new CCD-based multiwavelength nightglow photometer has been developed in-house and it has been automated for programmed operation on continuous (nightly) observations since 2013 from the optical aeronomy observatory in Gurushikhar. This photometer makes near-simultaneous measurement of nightglow emissions at OI 630.0 nm (that

originates at an altitude of ~250 km), OI 557.7 nm (~100 km), Na 589.0 nm (90 km), and Na 589.6 nm (90 km). The vertically separated optical emission altitudes enable investigations of interactions between the lower emission altitude (~E-region) and the ones from higher altitudes (F-region). The OI 557.7nm nightglow emission predominantly originates due to three body collision mechanism (at ~100 km) and behaves in a fashion similar to that of the sodium emissions. However, on occasions, it can have a significant contribution due to dissociative recombination and so it behaves in similar fashion with that of the OI 630.0nm emission at higher altitude. Further, there are occasions when the simultaneously operating digisonde from Ahmedabad showed in-phase movement of the F-layer with the intensity variation of the OI 630.0 nm emission. These intense plasma neutral interactions as obtained by multiwavelength airglow emissions intensities and digisonde are currently being investigated in greater details.

(D. Pallamraju, K. Phadke, R. Narayanan, R. P. Singh, and R. Sekar)

A new digital radio beacon receiver for ionospheric Total Electron Content (TEC) measurements: Initial results

A new GNU Radio Beacon Receiver (GRBR) system for ionospheric Total Electron Content (TEC) measurements has been fabricated in-house and installed at PRL (Figure 74).

The GRBR uses the FPGA (Field Programmable Gate Array) based Universal Software Radio Peripheral (USRP) and the open-source software toolkit for the software radio, GNU Radio. GNU Radio is an excellent software toolkit for implementing the Software Defined Radio systems. Its front-end is based on the script language Python, while the software for the digital signal processing is written in C++. The USRP is operated as a two-channel receiver connected to a host computer through the USB 2.0 interface. By selecting specific daughter boards to feed the analog signals, the USRP is used to receive the 150 and 400 MHz transmissions from high inclination LEO satellites, which gives the line of sight relative TEC values. A new iterative algorithm was formulated to convert these relative TECs to absolute TECs based on the earlier work elsewhere. Unlike many other popular methods which require measurements from two stations for absolute TEC determination, this approach can be used to obtain the absolute TEC with data from only one receiving station. Comparison of TECs derived from a collocated GPS receiver shows that the absolute TECs estimated by this method provide reliable estimates over regions with large spatial gradients (due to the presence Equatorial Ionization Anomaly (EIA), in this case) and could bring out the temporal variation of EIA (Figure 75).

This study reiterates the potential of radio beacon measurements in capturing the large-scale plasma transport processes in the low latitude ionosphere.

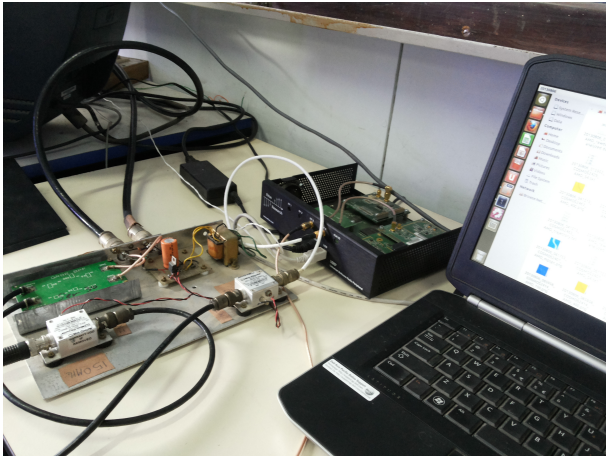


Figure 74: Photograph of the GRBR system installed at PRL.

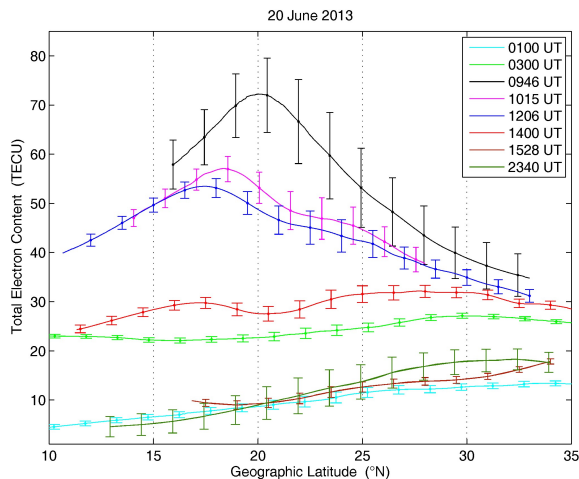


Figure 75: Examples of the latitude variation of TEC at different times on a typical day, derived from GRBR observations.

This work was done in collaboration with M. Yamamoto, Kyoto University.

(S. V. Thampi, Y. B. Acharya, D. Chakrabarty, M. B. Dhadania, M. Bhavsar, M. Bagiya, K. A. Phadke, and A. S. Manke)

Longitudinal extent of Space Weather effect:

Solar and IMF data from satellites along with ionosonde and ground magnetic data at equatorial stations in different longitude sectors were examined in detail for the space weather event of January 2004. The magnetic storm starting at 0130 UT on 22 January 2004 can be divided into two phases, first phase up to 1000 UT when interplanetary magnetic field IMF-Bz was highly fluctuating around a small positive value and the second phase after a sudden large southward turning of IMF-Bz at 1030 UT. The first phase

produced strong spread-F at Jicamarca, Sao Luis and Ascension Island and caused complete inhibition of spread-F at Thumba and Waltair in India. It generated weak spread-F at Ho Chi Minh City in Vietnam and strong spread-F at Hainan and Chung Li. The strong spread-F at Hainan and Chung Li were caused by the positive IMF-Bz during the first phase of the storm and not by the negative pulse of IMF-Bz at 1000 UT. The second phase with southward turning of IMF resulted in the disappearance of equatorial type of sporadic-E in the American sector.

This work is done in collaboration with scientists at Space Physics Laboratory; Andhra University; Institute of Physics, Vietnam Academy of Sciences; Jicamarca Radio Observatory, Peru and Digisonde International, Lowell, USA.

(R. G. Rastogi, H. Chandra, and P. Janardhan)

First results on forecasting the 'spatial occurrence' pattern of L-band scintillations and its 'temporal evolution'

After successfully forecasting (>95%) the temporal evolution of L-band scintillation over a given location, Trivandrum (8.5°N, 76.9°E, dip latitude 0.5°N), an attempt has been made here to generate the spatial-temporal maps of the occurrence pattern of L-band scintillation over the Indian region. The day time $[f_oF_2]^2$ fluctuations are used to forecast the temporal evolution of perturbations during the course of the night over Trivandrum. It is assumed that the electron density perturbations retain their characteristics throughout the night and traverse eastward with a uniform velocity during the course of the night. This implies that when the integrity of wave train of electron density perturbations is retained, any particular feature that passes over Trivandrum would have crossed over another location west of Trivandrum at an earlier time dictated by the zonal velocity. With this, it is fairly reasonable to generate the probable spatial and temporal pattern of L-band scintillation with the basic inputs on perturbations and their zonal velocity. The plausible correlation between the total duration of scintillation and the base height of the F-region ($h'F$) at 1930 LT has been explained in terms of the favourable background neutral atmospheric conditions. Our own earlier results have revealed the relation between $h'F$ at 1930 LT and the probable maximum latitudinal extent of the scintillation has specified the upper limit for the latitudes likely to be affected by the scintillation. It is believed that the present results hold enough potential to generate reliable L-band scintillation forecast maps and provide necessary alerts to the satellite based air navigation users.

This work was done in collaboration with S. Sunda, of Airport Authority of India, T. K. Pant, and R. K. Chaudhary of Space Physics Laboratory, Trivandrum.

(R. Sridharan, M. Bagiya, and L. Jose)

Latitudinal coupling from high to equatorial latitudes during geomagnetic storms

Geomagnetic storms are characterized by a sudden change in the SYM-H index which is associated with the Ring current formation in the magnetosphere. Particle precipitation precedes the formation of the Ring current, which, in addition to forming joule currents at high latitudes, also provides additional source of ionization for neutrals (other than the solar EUV photons). In this study, the behavior of high latitude ionosphere is examined with respect to the ring current (that exists over the magnetic equator) intensity variation (SYM-H index). The database used for this study is the GPS-based Total Electron Content (TEC) obtained from eleven locations (spread over different longitudes in both the hemispheres) and span from January 2011 to March 2012. It has been found that the TEC contribution at high-latitudes due to geomagnetic storms shows a similar behavior with that of the SYM-H over long durations ($\sim 5-10$ days). To obtain the TEC contribution due to the geomagnetic storm alone, quiet day TEC behavior is subtracted from those of the disturbed ones and the residuals are detrended by a 24-hour running average over the duration of the data which removes the ionization contribution due to both the diurnal variation of solar zenith angle and those due to the systematic variation of solar azimuth angle over long durations. These results provide a clear evidence of the high to equatorial latitude coupling as seen in these independent parameters.

(S. Yadav and D. Pallamraju)

Investigations of solar wind magnetospheric ionospheric coupling at high-latitudes

One of the fundamental issues in the physics of solar - magnetospheric-ionospheric (MI) system is to quantify the solar wind energy that is stored and distributed in the MI system. Equatorial ring current formation and particle precipitation are two of the important sinks of energy for particles of solar wind origin, with the latter forming a means of MI coupling over high latitude ionosphere. In the present work, the behavior of high latitude ionosphere has been investigated using Total Electron Content (TEC) measurements from Maitri (Geog: 70.43°S , 11.43°E ; Geomag: 62.49°S , 53.11°E) and Syowa (Geog: 69.06°S , 39.96°E ; Geomag: 70.5°S , 85.40°E) with respect to the enhanced energy inputs into the MI system during disturbed geomagnetic conditions. It is seen that the TEC at these high latitude stations show enhancement in response to the incident energy as characterized by the solar wind energy parameter epsilon (ϵ) which depends on Interplanetary magnetic field strength, B, clock angle (which varies with respect to Bz), and solar wind velocity. A linear fit has been obtained between the TEC enhancement and the energy parameter, (ϵ). It also shows that the observational location needs to be in the sun-earth line (around magnetic local noon) to receive this energy input. Based on this information obtained over a large dataset obtained during 2011 - 12, an empirical formulation has been arrived at using which TEC enhancements over high-latitudes can be

estimated based on solar energy inputs measured by ACE satellite at L1 Lagrange point that go into the calculation of the ϵ parameter.

(S. Yadav and D. Pallamraju)

Indicators for localized regions of heavier species in the lunar surface from CHACE on Chandrayaan-1

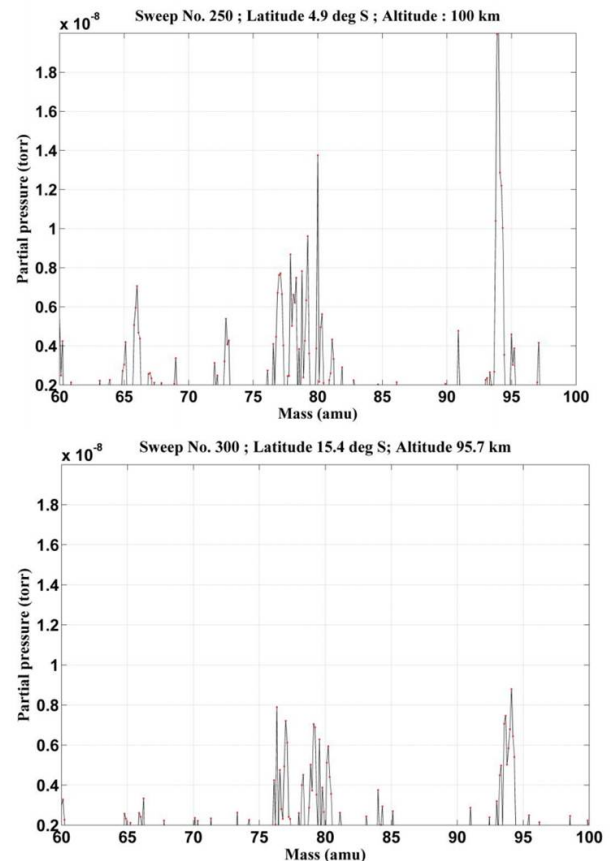


Figure 76: Sample Spectra from different locations highlighting the presence and heterogeneity of heavier species in the Lunar exosphere.

Careful analysis of the 650 spectra obtained from ~ 100 km to the lunar surface and covering a latitude range of (40°N to 85°S) with unprecedented spatial ($\sim 250\text{m}$) and temporal resolution ($\sim 4\text{sec}$) reveals significant grouping of heavier species (>60 amu) in localized regions. Figure 76 depicts some sample spectra corresponding to different lunar latitudes in the longitude region of $12 - 15^{\circ}\text{E}$. These heavier species start showing up from $\sim 5^{\circ}\text{N}$ latitude and continue with their presence with varying strengths as the spacecraft moved towards the South Pole. A mass peak corresponding to 94 amu started appearing $\sim 8^{\circ}\text{N}$ with a partial pressure of 6×10^{-9} torr. It was at its maximum amplitude of 2×10^{-8} torr over latitude of 5°S and lasted up to $\sim 22^{\circ}\text{S}$ beyond which its intensity slowly decreased and eventually merged with the noise level. In general, 80 amu coexisted with 94 amu. However, there are occasions when 80 amu became

stronger than 94 amu by nearly a factor of 2. Mass numbers 77, 78 and 79 that showed up in sweep number $\sim 3.5^\circ\text{N}$ are seen to become stronger intermittently during the MIP (Moon Impact Probe) transit. When the ground trajectory of MIP was projected over the lunar surface, the former crossed over the fringe of the KREEP region rich in potassium and rare earth elements that are associated with large surface heterogeneity. All the above observations are believed to be a reflection of lunar surface heterogeneity and a positive indication for localized regions that are abundant with heavier elements/species.

(R. Sridharan)

Meteoroid ablation and solar EUV/X-ray radiation in the dayside ionosphere of Mars

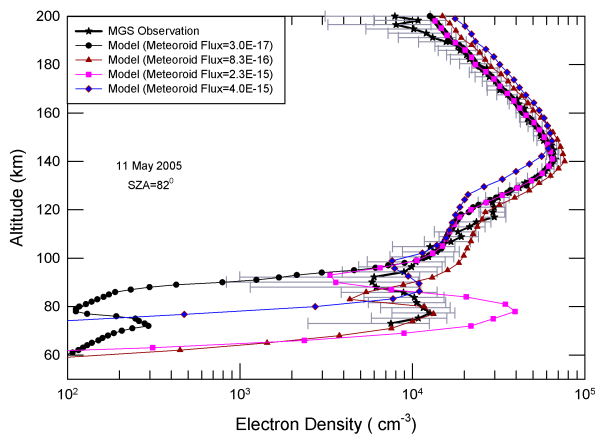


Figure 77: The electron density profile is observed on 11 May, 2005 from radio occultation experiment onboard MGS. The computed electron density profiles on the same day for four incoming meteoroids of different fluxes are also plotted. Comet 10P/Tempel 2 is crossed Martian orbit at a distance of 1.64 AU on May 11, 2005 which contributed to this flux.

A model has been developed which produces three plasma layers simultaneously due to impact of meteoroids, solar X-ray (0.5-9 nm) and EUV (9-102.6 nm) radiation at altitude range 75-85, 100-115, and 135-140 km, respectively in the dayside ionosphere of Mars. The calculated results are compared with the radio occultation measurements made by Mars Express (MEX) and Mars Global Surveyor (MGS) on 18 April, 2004 and 11 May, 2005, when comets P/2003 WC7 (LINEAR Catalina) and 10P/Tempel 2 intersected with the orbit of Mars. The densities of 21 ions (CO_2^+ , O_2^+ , CO^+ , O^+ , NO^+ , N_2^+ , Mg^+ , Fe^+ , Si^+ , MgO^+ , FeO^+ , SiO^+ , MgCO_2^+ , MgO_2^+ , FeCO_2^+ , FeO_2^+ , SiCO_2^+ , SiO_2^+ , MgN_2^+ , FeN_2^+ , and SiN_2^+) and 10 neutral species (Mg, Fe, Si, MgO, FeO, SiO, MgCO_3 , FeCO_3 , MgO_2 and FeO_2) have been computed self-consistently for both days. The model shows that the ions CO_2^+ , N_2^+ , O^+ , CO^+ , O_2^+ , and NO^+ are produced in the upper ionosphere due to impact of solar X-ray and EUV radiation. The metallic ions are formed in the middle ionosphere due to ablation of meteoroids. It is found that the middle ionosphere of Mars

strongly depends on incoming flux of the meteoroids. The meteoroids of fluxes 4.0×10^{-15} and $2.3 \times 10^{-15} \text{ cm}^{-2} \text{ s}^{-1}$ are in good agreement with the observations made by MEX and MGS on 18 April, 2004 and 11 May, 2005 (latter shown in Figure 77), respectively.

This work is carried out in collaboration with Mr. Bhavin Pandya, C.U. Shah College, Ahmedabad.

(S.A. Haider)

Mini-magnetosphere of Mars

The magnetometer experiment onboard MGS discovered a mini-magnetosphere in southern hemisphere (Latitude -46.3° and longitude 198.4° of Mars). In this region aurora is observed in the ultraviolet wavelength region. We have calculated magnetic fields of the mini-magnetosphere. In this model, the direction of the solar wind is perpendicular to the dipole axis and parallel to Mars-Sun line. This calculation shows open field lines of V shaped structure at poles. The electrons/ions which are created in the flux tubes of a closed field line will be trapped in a bouncing motion. The field lines are found to be compressed on both daytime and nighttime due to the inclusion of magnetospheric currents. By putting the current sheet field equal to zero, we have obtained dipole nature of field lines without their deformation. The calculation does not include dipole inclination. Therefore the angular distance between mini-magnetopause crossings and sub-solar point is zero. The position of mini-magnetopause changes with varying solar wind pressure. Observed total magnetic field strength compares well with the model results in the altitude range of 200 to 500 km, where measurements exist. The total field intensity at ~ 200 km is about 250 nT which decreases with altitude, which suggests that Mars should have strong crustal magnetic source in southern hemisphere around the latitudes $30^\circ\text{S} - 50^\circ\text{S}$.

(S.A. Haider)

Response of SEP events in the ionosphere of Mars

An investigation has been carried out on the effects of a large SEP events in the Martian ionosphere and predicted vertical profiles of energy deposition rates, ion, and electron densities. Resultant electron densities, which are produced solely by energetic particle precipitation, exceed 10^4 cm^{-3} between 30 km and 130 km. This density is much greater than that observed below 100 km by radio occultation experiment onboard MGS/MEX. We have also derived approximate expressions for the electron density profile during an SEP event for an altitude above 70 km, where O_2^+ ions (and not water group ions), dominate the ionospheric chemistry. A power law energy spectrum has been used which is valid below 100 km.

(S. A. Haider and V. Sheel)

Effect of Martian dust variability and size distribution on the ionosphere

The dust cycle on Mars and its spatial variability is still not well understood, despite several years of observations of the dust opacity. We have analysed dust climatology for 1999-2012 (8 Martian years) based on dust opacity observed by the Thermal Emission Imaging System onboard Mars Odyssey and the Thermal Emission Spectrometer on board the Mars Global Surveyor to study the temporal variability of dust in the tropics and its effect on the D-region on the ionosphere. The climatology shows distinct and generally repeatable dependence on season, with a large dust storm in 2001 and another one in 2007. Dust mass column loading derived from opacity shows a similar trend. We use our ion-dust model to simulate the effect of the spatial and temporal variability of dust on the ionosphere. We consider a range of dust aerosol size in our model to include the effect of size distribution on the ionosphere. The model couples 35 ions through more than 100 reactions which include ion-neutral collisions, electron neutral collisions, dissociation of positive and negative ions, electron detachment of anions, ion-dust attachment, ion-ion and ion-electron recombination processes. Our calculations indicate that during global dust storms, the D-region of the ionosphere may totally be absent. We also observe that sub-micron size dust particles are a major sink for the ions, compared to larger sized aerosols.

(V. Sheel and S. A. Haider)

Non-radiative relaxation processes and conformational changes in core-excited molecules

Perturbing the inner shells of molecules by removing or exciting the electrons in them leads to a strong coupling of electronic and nuclear degrees of freedom. This coupling often manifests as dissociation of the molecular ion through a variety of intermediate states. These states may belong to a geometry which is different from that of the parent molecule. We have shown that conformational changes do occur under inner shell perturbations and the changes are dependent on the manner in which the vacancy is quenched by transition of high lying electrons and the sharing of the excess energy among the nuclear degrees of freedom. This was shown in photoionisation experiments on molecules such as CS₂ and OCS, perturbed by synchrotron radiation, with photon energy resonant with the L_{1,2,3} edges of sulphur.

This experiment was done in collaboration with the Indus-1 Group of RRCAT, Indore.

(Koushik Saha, S.B. Banerjee, P. Kumar, B. Bapat)

Deducing the role of curve crossing and autoionisation in charge symmetric dissociation of N₂²⁺ and CO²⁺

Dissociation of excited molecular ions can occur through a multitude of decay pathways, depending on the energy of

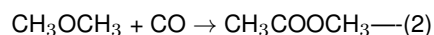
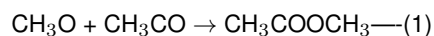
excitation and the density and shape of potential energy curves of the molecular ion. The kinetic energy of the dissociated partners reflects the nature of the excited state potential energy curve, but it is often obscured due to crossing of curves and processes such as autoionisation and tunneling. By combining a kinematically complete fragmentation experiment on CO and N₂ under electron impact and calculation of potential energy curves using the MOLPRO suite of programs at the cc-p5dZ basis set level, we were able to identify the relative contribution of various mechanisms to dissociation of the doubly ionised molecules. The role of non-adiabatic processes and the differences in the dissociation dynamics due to the differences in the point-group symmetries of the molecules was highlighted.

This work is done in collaboration with K.R. Shamsundar of IISER, Mohali.

(A. Pandey and B. Bapat)

Electron impact dissociation of *cis*-methyl acetate astrochemical ice analog

Since the first identification of methanol in Sgr A and Sgr B2 and acetic acid in Sgr B2, Orion KL, and W51, respectively, it is long expected that methyl acetate (CH₃COOCH₃), the simplest ester, could be present in complex chemical network in InterStellar Medium (ISM). Gas grain chemical model suggested that reaction given in *equation 1* leading to the formation of CH₃COOCH₃ in icy mantles. Perhaps carbonylation of dimethyl ether (CH₃OCH₃), reported in the Orion Nebula, could be another reaction route synthesizing CH₃COOCH₃ in ISM icy grains. In fact the carbonylation reaction (*equation 2*) might be the dominant pathway in synthesizing CH₃COOCH₃ as all three molecules were reported to be in the Orion.



After depositing CH₃COOCH₃ molecules on the cold substrate, only *cis*-CH₃COOCH₃ molecules were observed. The dissociation of this molecule under astrochemical ice analog conditions are least understood. Therefore, we had carried out an experiment to understand the dissociation pathway by irradiating CH₃COOCH₃ ices at 85 K using 2 keV electrons. Upon electron irradiation nearly equal amounts of carbon monoxide (CO) and carbon dioxide (CO₂) were synthesized. New IR bands corresponding to ethane (C₂H₆), dimethyl ether (CH₃OCH₃) and methanol (CH₃OH) were also observed. Along with new products the molecules in the ice phase were found to have undergone reorientation.

(B. Sivaraman, R. Mukherjee, K.P. Subramanian)

Radiation induced chemistry on the icy moons of Solar System – higher oxides of carbon and nitrogen on the Jovian and Saturnian icy satellites.

Ion implantation enriches the chemical abundance of a minor constituent on an icy surface, for example, nitrogen and carbon containing species (N_2O , CO_2) on the surfaces of icy satellites. Further processing may lead to the formation variety of molecules containing nitrogen. Such processes can be simulated using laboratory experiments. Energetic electrons at 5 keV were used to irradiate the molecular ices. CO_2 and N_2O ices were irradiated and the chemical pathways leading to the formation of higher oxides of carbon and nitrogen were examined. Pure N_2O and CO_2 ices kept at 85 K irradiated by electrons at 5 keV. New molecules, such as N_2O_2 , N_2O_3 (Figure 78), N_2O_4 , N_2O_5 and CO_3 , CO_4 were observed in N_2O and CO_2 ices, respectively. The identification of higher oxides of carbon and nitrogen has important implications in the complex chemistry on icy satellites. Our results provide data for the gas grain model to estimate the molecular abundances of such species on the surfaces of icy satellites.

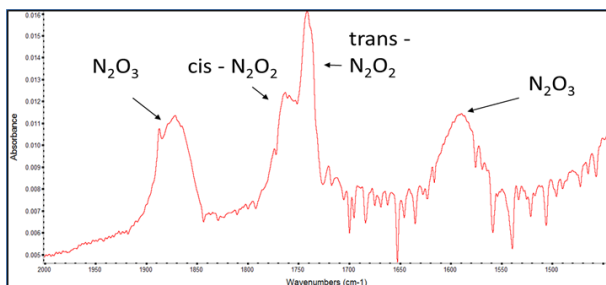


Figure 78: Infrared spectra of N_2O ice analogs after 5 keV electron irradiation at temperature commensurate to icy satellite surfaces.

(B. Sivaraman, R. Mukherjee, A. Saxena, K.P. Subramanian)

Synthesizing the basic unit of benzenoid PAH's: propargyl alcohol to benzene

In combustion chemistry propargyl alcohol ($\text{C}_3\text{H}_4\text{O}$) is known to be the precursor in the synthesis of benzene molecules. The discovery of propenal ($\text{C}_3\text{H}_4\text{O}$) in Sgr B2(N) made propargyl alcohol, an isomer of propenal, an important molecule in the astrochemical context. Therefore, propargyl alcohol ice analogs kept at 85 K were irradiated by 2 keV electrons under astrochemical conditions. Benzene was instantly formed by irradiation and then later was found to be present in the dust surface even after propargyl alcohol sublimation. Our results suggest that soot formation could be from the sublimation of such benzene synthesizing molecular ices.

(B. Sivaraman, R. Mukherjee, K.P. Subramanian)

Vacuum ultraviolet spectra of astrochemical ice analogs

Experiments to record the VUV spectra of astrochemical ices were carried out at National Synchrotron Radiation Research Center (NSRRC), Taiwan. The first run was carried out during the period 21–27 April 2013, where molecules such as ozone, dimethyl ether, butyronitrile, propionitrile, methyl acetate, phenyl acetate and propionic acid were studied during this period.

In the second beamtime period during 31 December 2013 – 6 January 2014, molecules such as diethyl ether, dimethyl ether, acetonitrile, glycerol, ethylene glycol, ethyl acetate and carbon disulphide were studied. VUV spectra of these molecules were recorded starting from 10 K and until sublimation. VUV spectra of these molecules were recorded for the first time. However, the highlight is obtaining the VUV spectra of solid ozone. For the first time, VUV (109 – 220 nm) photoabsorption spectra of high density amorphous and crystalline forms of O_3 (Figure 79) were recorded relevant to both planetary/satellite and InterStellar Medium (ISM) conditions. Absorption in the Hartley region was observed to be very weak or absent when pure O_3 ice was formed in the crystalline phase.

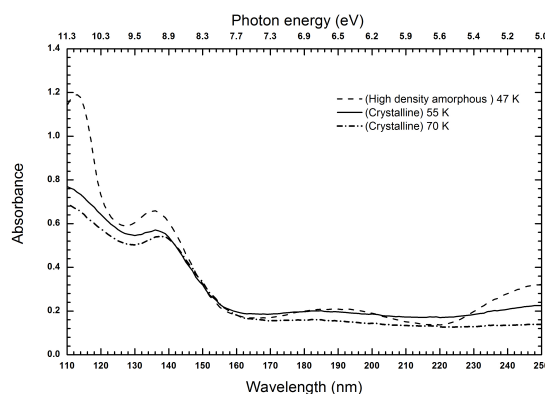


Figure 79: VUV spectra recorded after irradiating O_2 ice at 10 K using 9 eV photons for about 100 mins and then subsequent recording of spectra by warming the ice to 47 K (dashed line) at which temperature the molecular oxygen sublimates to leave a pure O_3 .

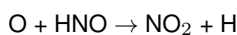
Our results suggest that pure solid O_3 effectively absorbs in the Hartley band but only at temperatures < 70 K. Therefore, absence of Hartley band does not exclude the presence of ozone and our results suggest the need for *in-situ* techniques to detect the presence of O_3 on icy planetary and satellite bodies.

This work is done in collaboration with B.N. Raja Sekhar, RRCAT Indore, N. J. Mason, The Open University-UK, and B.M. Cheng, NSRRC-Taiwan.

(B. Sivaraman and R. Mukherjee)

Oxides of nitrogen on dust grains and their chemical evolution

In order to study the chemical evolution of some oxides of the nitrogen, we have developed a chemical model which includes the gas phase as well as the grain surface chemical network. Our gas phase chemical network mainly consists of the network of Woodall et al. (2007) and the detail chemical network used in Das et al. (2013). The gas phase chemical network consists of 6296 reactions and surface chemical network consists of 288 reactions. Except molecular hydrogen and helium, depletion of all the gas phase neutral species onto the grain surface are considered with a sticking probability one. For the formation of NO_2 , N_2O_3 and N_4O_2 on the interstellar ices, we have taken the following reactions into our consideration:



Binding energies of the surface species are the keys to control the composition of the interstellar grain mantle. Necessary adsorption energies of the surface species are taken from data in literature. As like the adsorption energies of NO , here also, we have assumed the adsorption energies of NO_2 , N_2O , N_2O_3 and N_4O_2 are to be 1210 K. We have considered a dense cloud having number density (n_{H}) = 10^4 cm^{-3} , visual extinction $A(V)$ = 10 and temperature (T) = 10 K for the modelling purpose.

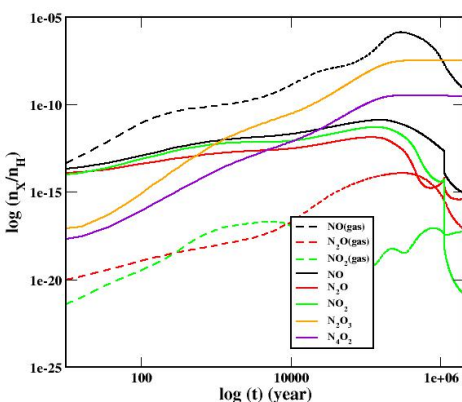


Figure 80: The chemical evolution of the gas phase NO , N_2O and NO_2 along with the chemical evolution of the ice phase NO , N_2O , NO_2 , N_2O_3 and N_4O_2 .

Figure 80 shows the chemical evolution of the gas phase NO , N_2O and NO_2 along with the chemical evolution of the ice phase NO , N_2O , NO_2 , N_2O_3 and N_4O_2 . Beyond 10^5 year, gas phase concentration of NO and N_2O decreases due to heavy depletion to the ice phase. Ice phase NO_2 , NO and N_2O also decreases due to the formation of N_2O_3 and N_4O_2

respectively. It is evident from our model that N_2O_3 and N_4O_2 could be very abundant in the interstellar ices which are in line with our experimental findings. The calculated peak abundances (ratio to total hydrogen abundance) of the ice phase species NO , N_2O , NO_2 , N_2O_3 and N_4O_2 were 1.33×10^{-11} , 5.16×10^{-12} , 1.36×10^{-12} , 3.3×10^{-8} and 2.54×10^{-10} respectively.

This work is done in collaboration with A. Das and L. Majumdar, ICSP, Kolkatta.

(B. Sivaraman)

Understanding the chemical reactions on Titan: Acetonitrile water system as a case study

Complex organic and inorganic species identified in Interstellar medium (ISM) are found to be more common in some of our solar system satellites, such as Titan. Recent spectra from CASSINI CIRS following the Voyager IRIS investigations in the 8 - 500 μm spectral range revealed several molecules constituting H, C and N. The list of molecules ranges from HCN and up to CH_3CN . However, the surface temperature (94 K) and pressure (1.5 bar) conditions that prevail in Titan favours the formation of different heavier nitrile molecules, like propionitrile ($\text{C}_2\text{H}_5\text{CN}$) and butyronitrile ($\text{C}_3\text{H}_7\text{CN}$). Numerous laboratory experiments using discharge setup, photochemical experiments and electron irradiation experiments using various Titan gas mixture analogs lead to the formation of such heavier nitriles. Using the low temperature molecular ices simulation chamber based at IIT Madras we performed experiments using mixture of acetonitrile and water ice analog starting from 10 K and recorded infrared spectra in the 4000-400 cm^{-1} range using Fourier Transform Infrared (FTIR) spectrometer and probing molecules that sublime via mass spectrometry. Ice mixtures formed at 10 K were then warmed to various temperatures, but are not limited to, 30 K, 50 K, 70 K, 90 K, 110 K, 130 K and even to higher temperatures depending on the phase transition as well as sublimation temperature of the ices. The recorded infrared spectra clearly showed an additional band at 3400 cm^{-1} arising from the molecular interaction between the acetonitrile and water molecules. This band disappeared by annealing the sample to phase transition temperature for acetonitrile (around 130 K) where the segregation of acetonitrile molecules in the acetonitrile-water system is proposed from the observed results. Later heating to higher temperatures, up to 160 K, water ice was found to crystallize and then to sublime from the substrate. Our results suggest a stronger acetonitrile-water molecule interaction to be present in the Titan complex chemical reservoir. This interaction suggests chemical pathways for newer molecular synthesis.

This work is done in collaboration with T. Pradeep, IIT-Madras, Chennai.

(B. Sivaraman)

The structure and vibrational frequencies of crystalline and amorphous methyl acetate

Identification of methyl acetate in interstellar medium (ISM) and its spectroscopic studies prompted us to explore the solid phase methyl acetate crystals using numerical calculation. The relaxed structure and vibrational properties have been calculated using SIESTA software at 0 K. In the optimization process, PBE (Perdew, Burke and Ernzerhof) functional and conjugate gradient methods are used, with Double zeta polarized (DZP) basis functions. After optimization of the periodic structures, atomic forces and Born charges are calculated. The relevant bond parameters of methyl acetate are tabulated in Table:1 and compared with the available X-ray crystallographic data.

| Bond Length | Exp. | Calc ^a | Bond Angle | Exp. | Calc ^a |
|-------------|--------|-------------------|------------|--------|-------------------|
| C1-O1 | 1.4529 | 1.3518 | O1-C2-O2 | 122.53 | 122.62 |
| C1-H1 | 0.9052 | 1.1082 | O1-C2-C3 | 111.76 | 112.629 |
| C1-H2 | 0.9482 | 1.1098 | C1-O1-C2 | 114.86 | 114.361 |

Table 1: Comparison of calculated bond parameters with crystallographic data (a) calculated result.

This work is done in collaboration with G. Gopakumar and M. Hada, TMU, Japan.

(B. Sivaraman)

Yb-fiber-laser-pumped, high-repetition-rate picosecond optical parametric oscillator tunable in the ultraviolet

Ultrafast optical sources with wavelength tunability in the ultraviolet (UV) have wide variety of applications including quantum optics, optical data storage, atmospheric sensing, combustion diagnostics, and bio-imaging. Traditionally, such spectral regions are accessed using bulky, complex and power-hungry gas lasers such as excimer lasers, offering limited or no wavelength tuning capability. On the other hand, direct generation of tunable ultrafast radiation in the UV can be realized using nonlinear frequency conversion of the optical parametric oscillators (OPOs) working in the visible and near-IR region. Using such technique we have demonstrated a compact tunable 240-MHz picosecond source for the UV tuned across 317-340.5 nm, with up to 30 mW power at 334.5 nm. The source also provides tunable visible signal in the red, across 634-681 nm, and mid-infrared idler radiation over 2429-3298 nm, with as maximum signal power of 800 mW at 642 nm. The signal pulses have a temporal duration of 12 ps at 665 nm and exhibit high spatial beam quality with Gaussian profile. The signal power is recorded to be naturally stable with a fluctuation of 1.4% rms over 14 hours, while UV power degradation has been observed and studied.

This work was done in collaboration with Prof. Majid Ebrahim-Zadeh from the Institute of Photonic Sciences, Barcelona.

(A. Aadhi and G. K. Samanta)

Experimental generation of ring shaped beams with random sources

The ring-shaped beams from the scattered Laguerre–Gaussian and Bessel–Gaussian beams have been experimentally reproduced. A rotating ground glass plate is used as a scattering medium, and a plano-convex lens collects the scattered light to generate ring-shaped beams at the Fourier plane. The obtained experimental results are supported with the numerical results and are in good agreement with the proposed theoretical results.

(S. G. Reddy, A. Kumar, S. Prabhakar and R. P. Singh)

Measuring Mueller matrix of an arbitrary optical element with a universal SU(2) polarization gadget

A new method for determining the Mueller matrix of an arbitrary optical element and verified it with three known optical elements has been proposed. This method makes use of two universal SU(2) polarization gadgets to obtain the projection matrix directly from the experiment. It allows us to determine the Mueller matrix without pre-calibration of the setup, since the generated polarization states are fully determined by the azimuths of the wave plates. We have calculated errors in determining the Mueller matrix and compared with other techniques, which shows the advantage of our method.

This work was done in collaboration with R. Simon, Institute of Mathematical Sciences, Chennai.

(S.G. Reddy, S. Prabhakar, A. Aadhi, A. Kumar, M. Shah & R.P. Singh)

Annihilation of vortex dipoles in an oblate Bose-Einstein condensate

The annihilation of vortex dipoles, generated when an obstacle moves through an oblate Bose–Einstein condensate, and examined the energetics of the annihilation event have been theoretically explored. We show that the grey soliton, which results from the vortex dipole annihilation, is lower in energy than the vortex dipole. We have also investigated the annihilation events numerically. We observe that the annihilation occurs only when the vortex dipole overtakes the obstacle and comes closer than the coherence length.

Furthermore, we find that noise reduces the probability of annihilation events. This may explain the lack of annihilation events in experimental realizations.

(S. Prabhakar, R.P. Singh, S. Gautam and D. Angom)

Formation of optical vortices through superposition of two Gaussian beams

The phase singularities in the superposed field of two Gaussian beams have been experimentally demonstrated. It is seen that the formation of these singularities depends on the tilt between two Gaussian beams and the separation of their beam axes. By reversing the angle or the position of the beams, one can change the sign of the vortex. We have shown the formation of single as well as multiple vortices by changing the tilt angle and the position of two Gaussian beams. The experimental results are verified with theoretical analysis. We also observe that such a vortex structure can be formed through superposition of two back reflected Gaussian beams from any optical element with two flat surfaces, as illustrated through a beam splitter and a neutral density filter. This technique is very useful for generation of vortices with high-power lasers where one cannot use a spatial light modulator.

(P. Vaity, A. Aadhi and R.P. Singh)

Optical trapping of fluorescent beads

Optical tweezers have been successfully used to trap a variety of particles and biological specimens for numerous applications. Particles which are reflective as well as absorbing could be trapped using beams such as optical vortex. We have set up an optical trap for these fluorescent micro-particles using holographic optical tweezers; we observe that it is not possible to trap fluorescent micro-particles with a Gaussian laser beam or a hollow beam. However, as the fluorescence of these particles gets degraded they could be trapped in custom-made holographic tweezers. Moreover, when a fluorescent particle is brought in the trap containing stably trapped non-fluorescent particle, the stably trapped non-fluorescent particle also escapes from the trap.

This work was done in collaboration with S. N. A. Jaaffrey, Mohan Lal Sukhadia University, Udaipur.

(J. Bhatt, A. Kumar, R.P. Singh)

Quadrature uncertainty and information entropy of quantum elliptical vortex states

The quadrature uncertainty of the quantum elliptical vortex state using the associated Wigner function has been investigated. Deviations from the minimum uncertainty states were observed due to the absence of Gaussianity. We further observed that there exists an optimum value of ellipticity which gives rise to the maximum entanglement of the two modes of the quantum elliptical vortex states. In our study of entropy, we noticed that with increasing vorticity, entropy increases for both the modes. A further increase in ellipticity reduces the entropy thereby resulting in a loss of information carrying capacity. We check the validity of the entropic inequality relations, namely the subadditivity and Araki–Lieb inequality. The latter was satisfied only for a very small range of the ellipticity of the vortex, while the former seemed to be valid at all values.

This work was done in collaboration with A. Banerji, S. Chowdhury and A. Bandyopadhyay of Hooghly Engineering and Technology College, Hooghly and P. K. Panigrahi of Indian Institute of Science Education and Research, Kolkata.

(R.P. Singh)

Spatial distribution of spontaneous parametric down-converted photons for higher order optical vortices

A source of entangled photons (SEP) using spontaneous parametric down-conversion (SPDC) in a non-linear crystal and studied the spatial distribution of photon pairs obtained through the down-conversion of different modes of light including higher order vortices has been developed in the laboratory. We have observed that for the Gaussian pump, the thickness of the SPDC ring varies linearly with the radius of pump beam. In case of the optical vortex beams as pump, two concentric SPDC rings are formed; however, it happens above a critical radius of the vortex beam. The full width at half maximum (FWHM) of SPDC rings increases with increase in the order of optical vortex beams. The presence of a critical beam width for the optical vortices as well as the observed FWHM of the SPDC rings are supported by our numerical results.

(S. Prabhakar, S.G. Reddy, A. Aadhi, A. Kumar, P. Chithrabhanu, G.K. Samanta and R.P. Singh)

SCIENCE

Geosciences Division

Resetting of thermo-luminescence in Sand Dikes Due to Viscous Heating: Theoretical considerations and experimental evidences

The resetting of luminescence (both thermal and optically stimulated) during the formation of sand dike formation was analyzed by computing the transient heat generated due to viscous flow of sand and water mixtures through the overlying sedimentary layers. During the injection of material, the kinematic viscosity of the material plays an important role leading to the generation of a frictional drag between different layers of the material. Due to this drag, a part of the stress during the injection of the dike heats the injected material locally. Calculations suggest that the temperature rise could exceed 350°C, and this is sufficient to reset the luminescence signal as reported by us and others previously. In this study, these theoretical calculations were confronted with experimental data, by a systematic study on a suite of 47 samples collected from the sand dikes in the seismicity prone North East Indian region. For the estimation of transient heat in the sand dike samples, various aspects of luminescence were examined. These included the examination of changes in the sensitivity of 110°C TL glows peak in dike samples. The TL sensitivity after preheat temperature of 300°C, became twice of the sensitivity at first preheat cycle and seven to ten times after preheat of 350°C. Existence of De plateau in temperature range 300-350°C suggested heating up to 350°C. The field data was generally consistent with theoretical predictions. Luminescence studies suggest a minimum of three dike forming events of ($M > 6.5$) at 300 years, 500 years and 1 ka in the study area. Further results and their

implications will be presented. This study formed a part of Mr. Anil Tyagi's (a former student of PRL and now at ITER, IPR) doctoral thesis.

This work was done in collaboration with Prof. R.N. Singh and Dr. Devender Kumar of National Geophysical Research Institute, Hyderabad and Dr. M. K. Murari of Department of Geosciences, University of Cincinnati, USA.

(A. K. Singhvi)

Residual dose of pIR-IRSL signal of feldspar of Tsunami sediments

Feldspar is an attractive luminescence geochronometer of quaternary sediments because of its higher luminescence sensitivity and higher dose saturation limit. However, application of feldspar as natural dosimeter has been obscured by anomalous fading. To overcome this fading issue, the use of post-infrared – infrared stimulated luminescence (pIR-IRSL) at elevated temperature (225-300°C) has provided encouraging results in respect of a lower athermal fading. This is understood on the basis of the fact the trapped electrons that lead to pIRIRSL signal have to recombine with distant recombination centres. A drawback of using this signal is its high residual dose due to hard to bleach components and residual doses of up to 20 Gy have been reported. This limits its applicability to young sediments. We measured the residual doses of pIR-IRSL signal of seven Tsunami

sediments dated to up to 1.3 ka from ~50 km from south of Chennai, India. The residual doses for the present samples were ≤ 3 Gy. The same samples however gave a higher residual dose of 19.5 ± 0.6 Gy for samples with their natural luminescence additionally irradiated to 300 Gy. We suggest that the low residual signal in natural samples arises from a long residence time. The results suggest that the residual dose of pIR-IRSL signal in natural environment could be lower and caution should be taken while measuring pIR-IRSL ages in the laboratory.

(R. H. Biswas and A. K. Singhvi)

Identification of optimum age model for luminescence dating

In Luminescence dating, generally considerable distribution in equivalent doses is seen. These distributions arise from several causes, such as the partial bleaching of sediments, heterogeneous distribution of beta doses, differences in rates of athermal fading, differences in dosimetry at micro-level etc. Out of these, partial bleaching is a single major factor that determines the accuracy of ages for fluvial samples. At present a number of models for estimation of the ages exist. Some of the widely used ones are minimum age models (MAM3, MAM4, minimum 5%, minimum $+2\sigma$), mean age models (Average dose, weighted mean, Central age model and the Leading edge model). Some of these are conceptually similar however application of each of these models result in small but finite differences in ages. Towards this we examined the applicability of these models in giving robust age estimates for samples under controlled laboratory conditions. In this, three samples, one well bleached natural sample, one partially bleached natural sample and one laboratory dosed and bleached sample were taken. For each case ~250 aliquots were measured using the standard SAR procedure. Out of these 250 aliquots 50 sets of 35 aliquots were made using a random selection without replacement. Each of these sets was analyzed using the above mentioned models and the repeatability of dose was checked by means of relative standard deviation (RSD) of the observed set. The models that yielded minimum RSD value were then identified as the models to be used for a particular type of the sample. minimum $+2\sigma$ and minimum 5% in general showed high RSD, on the other hand MAM3 and MAM4 gave less RSD for natural samples. For control sample, however, minimum 5% and minimum $+2\sigma$ model provide best approximates the dose value. A low RSD was found for CAM. Present efforts are to develop more robust statistical checks so as to provide reliable estimates of ages.

This work was done in collaboration with M.K. Murari, University of Cincinnati and Dr. P. Morthekai, Birbal Sahni Institute of Paleobotany, Lucknow.

(N. Chauhan and R.H. Biswas)

OSL Dating of the Coastal Carbonates of Western India and their Implications for the understanding of land-sea interactions

The Saurashtra coast, Western India hosts bioclastic carbonate deposits (termed as the miliolites after sp. miliolidae). These were formed due to a combination of near shore marine, inter tidal, backshore, fluvial and aeolian processes. A considerable debate on the formation processes, their chronology, and the presence of these deposits deep inland, exists and as yet a convergence on the processes and timescales is awaited. Such confusion arises due partly to a questionable chronology based on inappropriate sampling strategies, the use of $^{230}\text{Th}/^{234}\text{U}$ and ^{14}C ages that provide the bulk age of formation of carbonates and are invariably contaminated by detritus and post depositional diagenetic processes. Use of such diagenetically altered ages of formation of carbonates to date e.g. aeolian processes that build carbonate dunes has lead to avoidable confusion. The role of diagenetic processes was elucidated by a few Electron Spin Resonance ages where a significant difference between the age of formation and later cementation was seen.

In the present study we used traces ($<1\%$) of quartz grains trapped in carbonate for optical dating, with the premise that the quartz grains were syn-sedimentary to the carbonate deposition at a given site (either pristine or wind transported grain) and were not significantly affected by post depositional diagenetic and cementation processes. In general, the optical ages were at variance with previously reported radiometric ages. Analyses so far suggest that the ages negate the previously suggested correlation of aeolian deposition with periods of lower sea levels only and, suggest their deposition during a transitional regime. Optical ages also suggest that far inland carbonate deposits were re-worked older carbonate sediments at the coasts. Overall the OSL ages settle some of the existing debates.

This work was done in collaboration with Dr. Nilesh Bhatt, MS University Baroda, Vadodara.

(K. Sharma, A.D. Shukla and A.K. Singhvi)

Hydrogen and Oxygen Isotopic Compositions of Water Vapour over Bay of Bengal during Monsoon

Stable water isotopologues, H_2^{18}O and HDO, are widely used as tracers of the hydrological cycle and reconstructing paleomonsoon. The relative mass difference of O and H isotopes causes isotopic fractionation during phase change of water, including evaporation from open water bodies, condensation in clouds, and below-cloud re-evaporation while the rain falls through the under-saturated atmosphere. Isotopic fractionation during large-scale condensation is believed to be an equilibrium process, obeying the Rayleigh isotopic fractionation model. But isotopic exchange processes in clouds formed due to intense convective activity are more complex. For treating isotopic fractionation during evaporation, a model proposed by Craig and Gordon [hereafter

referred to as CGM], and later modified by Merlivat and Jouzel [hereafter referred to as MJ79], is widely used. MJ79 predicts a relationship between ocean surface relative humidity and d -excess (defined as $\delta D - 8 \cdot \delta^{18}O$) by applying a global closure assumption. Though this leads to a systematic bias in predicting the vapour isotopic values, the relationship between h and d -excess is indeed observed in the marine vapour over the Southern Ocean. This relation is yet to be verified in the tropical oceans, a major moisture source for the global hydrological cycle. We attempted to understand the influence of boundary layer processes and ocean surface conditions on the stable hydrogen and oxygen isotopic compositions ($\delta^{18}O_v$ and δD_v) of atmospheric vapour over the Bay of Bengal (BoB), one of the important sources for monsoon rain. This is the first time such measurements are being reported from the tropics. δD_v and $\delta^{18}O_v$ of ~ 70 water vapour samples collected at 6 and 25 m heights over the sea surface of the Bay of Bengal (BoB) during July-Aug 2012, characterise the isotopic systematics of monsoon vapour. No significant vertical variation was observed in δD and $\delta^{18}O$ of vapour, but the d -excess at these levels did not correlate, suggesting an additional kinetic fractionation. The temporal variations of δD_v and $\delta^{18}O_v$ of marine vapour showed a good relation with air temperature rather than sea surface temperature, indicating ocean skin temperature's control on the equilibrium fractionation during evaporation into the isotopic boundary layer. The control of normalised humidity on d -excess is less prominent in the BoB. Although the distribution of water vapour isotopologues over BoB are primarily determined by the ocean surface conditions, they can be significantly altered by laterally advected isotopically depleted vapour from re-evaporated rain en route, especially during the monsoon.

(P. R. Lekshmy, M. Midhun and R. Ramesh)

Inter- and intra-specific carbon and nitrogen assimilation by dinoflagellate and diatom species

Ocean primary productivity (rate of carbon fixation, measured in $\text{mg Cm}^{-2}\text{d}^{-1}$) is one of the major sinks of atmospheric carbon dioxide, thus an important regulator of the Earth's climate. Primary productivity is mainly determined by the availability of reactive nitrogen in the ocean surface waters. Reactive nitrogen substrates could either be new (NO_3^-) or recycled (NH_4^+ , Urea) nutrients, depending upon the dominant process in the surface ocean. The type of preferred nitrogen substrate uptake by phytoplankton determines the efficiency of the marine biological pump. Generally, NH_4^+ is believed to be preferred over NO_3^- by phytoplankton, when both substrates are present. However, this paradigm has been challenged and it is found that diatoms prefer NO_3^- while NH_4^+ is preferred by dinoflagellates. Understanding of preferred substrate is critical to estimate oceanic nitrogen and carbon budgets. The main problem for such estimates arises because the species do not behave exactly the same way around the globe and there might even exist variability on the intra-specific uptake level, as has previously been demonstrated with other phenotypic traits. Therefore, if we do not take such variations into account, the models for predictions will not be accurate. Marine

phytoplankton species have previously been considered to have unlimited dispersal ability due to their small size and high numbers, and as a consequence, phytoplankton species would have no biogeographic boundaries. Conversely, studies during the past decade have revealed high genetic and phenotypic diversity within and among geographically isolated populations of various phytoplankton taxa. To understand such diversity in uptake rates, we have estimated nitrogen and carbon uptake by genotypes of different species of dinoflagellates and diatoms. The paradigm that phytoplankton prefer ammonium over nitrate when both substrates are present has been tested by using ^{15}N labelled tracers on cultured diatoms and dinoflagellates isolated from the two widespread geographical areas - the Baltic Sea and the Arabian Sea. We found contrary to the paradigm that both taxa preferred nitrate over ammonium, and a significant within-species variation in N assimilation. Carbon uptake rates in the same experiments were estimated using ^{13}C labelled tracer.

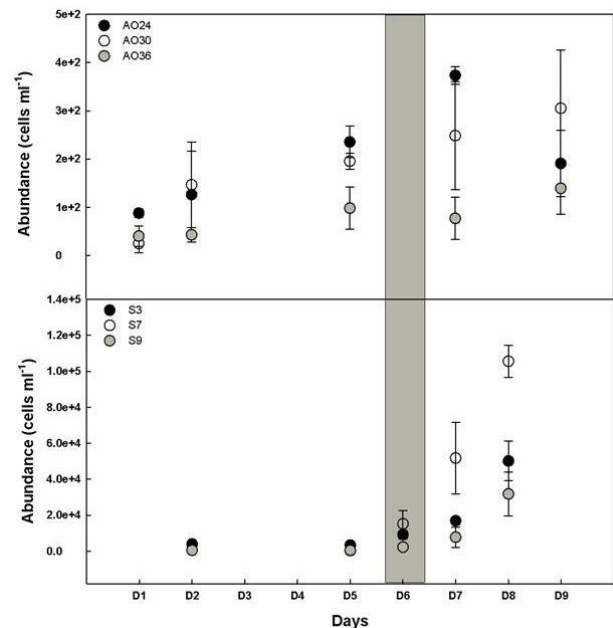


Figure 81: Growth of three monoclonal strains of *Alexandrium ostenfeldii* (AO24, AO30, AO36) and *Skeletonema tropicum* (S3, S7, S9) species in culture experiment 2. Vertical grey bar indicates the day experiment was performed.

(A. Godhe, R. Ramesh and A. Singh)

Development of Methodology for Measurement stable carbon isotopes in Dissolved Inorganic carbon

Two offline methods, a newly developed method by us and an existing one, for the measurement of the stable carbon isotopic composition ($\delta^{13}\text{C}$) of dissolved inorganic carbon (DIC; $\delta^{13}\text{CDIC}$) in natural waters were studied in comparison. The measured $\delta^{13}\text{CDIC}$ values of different water samples, prepared from laboratory Na_2CO_3 , ground and oceanic waters, and a laboratory carbonate isotope standard, are found to be accurate and reproducible to within 0.5%.

(1σ). The extraction of CO_2 from water samples by these methods does not require pre-treatment or sample poisoning and can be applied to a variety of natural waters to address carbon cycling in the hydrosphere. We demonstrated a simpler method (based on a two-end-member mixing model) to estimate the silicate-weathering contribution to DIC in a river system by using the concentration of DIC and its $\delta^{13}\text{C}$. This approach was tested with published data from the Krishna River system as a case study, thereby quantifying the contribution of silicate and carbonate weathering to DIC, particularly during peak discharge.

(N. Gandhi, D. Kumar, H. Laskar, R. R. Mahajan, R. Ramesh, K. Thirumalai and M. G. Yadava)

Age and geochemistry of the Newania dolomite carbonatites

The Newania carbonatite complex of India is one of the few dolomite-dominated carbonatites of the world. Intruding into Archean basement gneisses, the rocks of the complex have undergone limited diversification and are not associated with any alkaline silicate rock. Although the magmatic nature of the complex was generally accepted, its age of emplacement had remained equivocal because of the disturbed nature of radioisotope systems. Many questions about the nature of its mantle source and mode of origin had remained unanswered because of lack of geochemical and isotopic data. Here, we present results of our effort to date the complex using ^{147}Sm - ^{143}Nd , ^{207}Pb - ^{206}Pb and ^{40}Ar - ^{39}Ar dating techniques. We also present mineral chemistry, major and trace element geochemistry and Sr-Nd isotopic ratio data for these carbonatites. Our age data reveal that the complex was emplaced at $\sim 1,473$ Ma and parts of it were affected by a thermal event at ~ 904 Ma. The older ^{207}Pb - ^{206}Pb ages determined by us ($\sim 2,400$ Ma) is deemed to be a result of heterogeneous incorporation of crustal Pb during the post-emplacement thermal event. The thermal event had little effect on many magmatic signatures of these rocks, such as its dolomite-magnesite-ankerite-Cr-rich magnetite-magnesio-arfvedsonite-pyroxhlore assemblage, mantle like $\delta^{13}\text{C}$ and $\delta^{18}\text{O}$ and typical carbonatitic trace element patterns. Newania carbonatites show fractional crystallization trend from high-Mg to high-Fe through high-Ca compositions. The least fractionated dolomite carbonatites of the complex possess very high Mg# (>80) and have similar major element oxide contents as that of primary carbonatite melts experimentally produced from peridotitic sources. In addition, lower rare earth element (and higher Sr) contents than a typical calciocarbonatite and mantle like Nb/Ta ratios indicate that the primary magma for the complex was a magnesio-carbonatite melt and that it was derived from a carbonate bearing mantle. The Sr-Nd isotopic data suggest that the primary magma originated from a metasomatized lithospheric mantle. Trace element modelling confirms such an inference and suggests that the source was a phlogopite bearing mantle, located within the garnet stability zone.

(J.S. Ray, A.D. Shukla, V.K. Rai, N. Awasthi and D.K. Panda)

Chronology of major terrace forming events in the Andaman Islands

Major earthquakes that trigger tsunamis are great natural hazards. The devastations caused by the December 26, 2004 Sumatran earthquake, and the March 11, 2011 Japan earthquake, and associated tsunamis will remain in our memories for a long time. Such events reaffirm the need for studying the cause and effects of large earthquakes of the past and to prepare the world better for the future. In such an effort, to understand the pattern of earthquakes and their effects on the geomorphic evolution, we have studied deformation history in the Andaman and Nicobar Islands, located in one of the most active convergent margins of the world. Focusing on tectonically formed coastal terraces and determining the timing of their formation from the exposed dead corals, we have been able to reconstruct the history of major earthquakes in these islands for the last 40 kyr. Our results in conjunction with the existing radiocarbon age data from coastal terraces of these islands appear to suggest that the frequency of major earthquakes ($M > 7$) in the region has increased during the last 9 kyr. In confirmation with some earlier work, we find evidences for a major earthquake and a tsunami between 500-600 cal yr BP and possibly 4 others during 6-9 cal kyr BP. Our results also indicate that there has been a continuous subsidence of the south Andaman Islands.

(N. Awasthi, J.S. Ray and M.G. Yadava)

Origin of the Mile Tilek Tuff, South Andaman

The Mile Tilek Tuff is one of several consolidated volcanic ash deposits in the Andaman and Nicobar Islands that has preserved evidence of a large scale volcanic eruption in South East Asia. Assumed to be of Mio-Pliocene age, the tuff was thought to have been generated by the Andaman-Indonesian volcanic arc. Little was known about its source volcano because of absence of critical geochemical and isotopic age data. To provide accurate age information and determine its source, we dated the tuff by ^{40}Ar - ^{39}Ar method and measured its trace element contents and Sr-Nd isotopic ratios. The ^{40}Ar - ^{39}Ar plateau age for the whole rock is 0.73 ± 0.16 (2σ) Ma, which suggests that the tuff got deposited much later than previously believed. Chemically, the tuff possesses typical signatures of subduction zone magmatism. Its Sr-Nd isotopic compositions ($^{87}\text{Sr}/^{86}\text{Sr} \geq 0.7073$ and $\epsilon_{\text{Nd}} \leq 0.9$) suggest significant contamination by continental crust, which points to a source volcano in Indonesia. Based on available age information on large scale volcanic eruptions in Indonesia we speculate that the Ranau volcano in south Sumatra could have been the source of the Mile Tilek Tuff.

This work was done in collaboration with K. Pande of IIT Bombay.

(N. Awasthi and J.S. Ray)

Mo isotopes in the northern Indian Ocean, estuaries and rivers

Distribution of dissolved Mo isotopes has been measured in the northern Indian Ocean, the Bay of Bengal and the Arabian Sea employing double spike method by MC-ICP-MS. $\delta^{98}\text{Mo}$ in the open ocean water of the Arabian Sea and the Bay of Bengal indicates conservative behavior with negligible variation with depth. The average $\delta^{98}\text{Mo}$ in five water profiles of the open ocean waters is 2.41 ± 0.05 . $\delta^{98}\text{Mo}$ in seawater seems independent of dissolved oxygen content of the seawater. Even in water column with oxygen minimum zone of the Arabian Sea, it is very much similar to the average open ocean value indicating little impact of sub-oxic condition on the Mo isotope composition. Notable exception is the northern Bay of Bengal which displays quite different $\delta^{98}\text{Mo}$ compared to its open ocean value. Surface water with 32.4 salinity has $\delta^{98}\text{Mo}$ 0.87 whereas deeper water at the same location with 35 salinity has $\delta^{98}\text{Mo}$ 1.93 (Figure 82), much lower than the open ocean value. These deviations in $\delta^{98}\text{Mo}$ at the river mouth could be due to its supply from dissolution of Fe-Mn oxyhydroxide coating, having lighter Mo, of particles due to change in oxidation state in the sub-oxic shelf region.

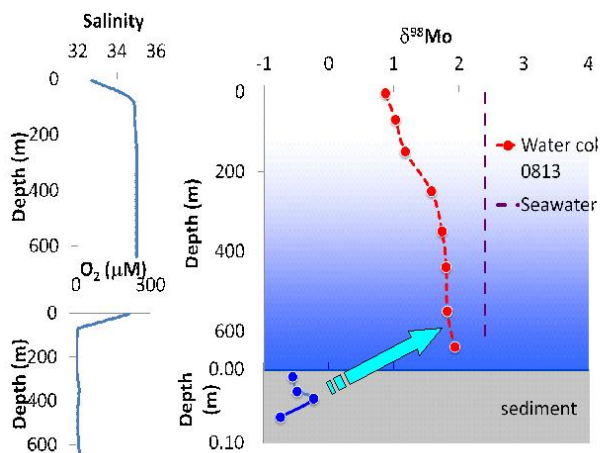


Figure 82: $\delta^{98}\text{Mo}$ in the water column of shelf region of northern Bay of Bengal is isotopically lighter compared to that of open ocean, due to release of lighter $\delta^{98}\text{Mo}$ from Fe, Mn oxy-hydroxide coating of sediments under sub-oxic condition.

(R. Bhushan, V. Goswami, V. K. Rai and S. K. Singh)

Dissolved silicon and its isotopes in water column of the Bay of Bengal: Internal cycling versus lateral transport

Dissolved Si abundance and its isotope composition in water column of the Bay of Bengal (BoB) along the 87°E transect (GIO1 section of International GEOTRACES Program) have been measured to explore its biogeochemistry, distribution in water column and the factor influencing them. The Si abundances are depleted strongly in open ocean surface waters of the Bay of Bengal and characterized by relatively higher $\delta^{30}\text{Si}$ (Figure 83) due to isotope fractionation during biological uptake, whereas the shelf stations show higher Si

concentrations and low $\delta^{30}\text{Si}$ indicating the contributions from the Ganga–Brahmaputra river water and SGD. The combined supply of dissolved Si from the G–B and SGD to shelf waters of the BoB is $\sim 4.7 \pm 1.9 \times 10^{10}$ mol/year. Top ~ 100 m of the Bay of Bengal is under the steady state with dominant supply of dissolved Si through the sporadic meso-scale eddies. The observed $\delta^{30}\text{Si}$ of $\sim 1.34 \pm 0.10$ ‰ in BoB deep waters below a depth of ~ 1500 m is similar within the uncertainty to that reported earlier for the Antarctic Bottom waters. However, the “hot-spots” of dissolved Si concentration in bottom waters, and a feeble similarity in trends of $\delta^{30}\text{Si}$ values in bottom and surface waters indicate a significant role of dissolution of sinking biogenic silica at BoB seafloor.

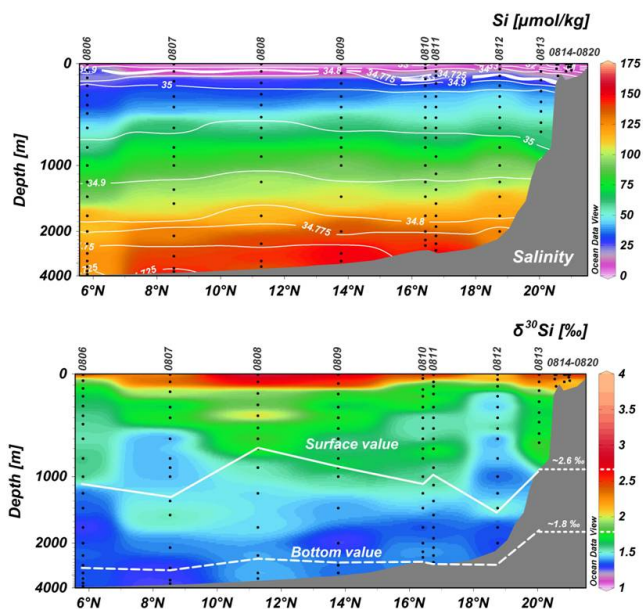


Figure 83: Distribution of Si concentration and $\delta^{30}\text{Si}$ in the Bay of Bengal indicating preferential uptake of lighter Si isotope by diatoms in photic zone resulting in higher $\delta^{30}\text{Si}$ in surface whereas, dissolution of diatoms near sediment water interface cause higher Si and lower $\delta^{30}\text{Si}$ in bottom waters of the Bay of Bengal.

(R. Bhushan, S. P. Singh, V. K. Rai and S. K. Singh)

Weathering in Godavari basin

Water and sediment samples have been collected from the Godavari river system (Figure 84) to study weathering processes and the factors influencing them. Further, its drain through varying rainfall zones make it easier to assess the impact of lithology and rainfall on weathering. Major ions, Sr and Nd isotope compositions are being measured in the dissolved and particulate phases in the Godavari basin to understand the weathering processes in it. Dissolved and particulate $^{87}\text{Sr}/^{86}\text{Sr}$ in this system varies from 0.70887 to 0.72052 and 0.70863 to 0.77809, displaying the basaltic and gneissic influence. Dissolved ϵ_{Nd} shows significant variation -28.7 to -5.6 mimicking the contribution from basalts and gneisses. Dissolved Nd is significantly less radiogenic in the tributaries flowing through the Archean basement. Saline -alkaline soils present in the basin contribute significantly to the dissolved budget of the Godavari. More work is underway to estimate weathering rates and their controlling factors.

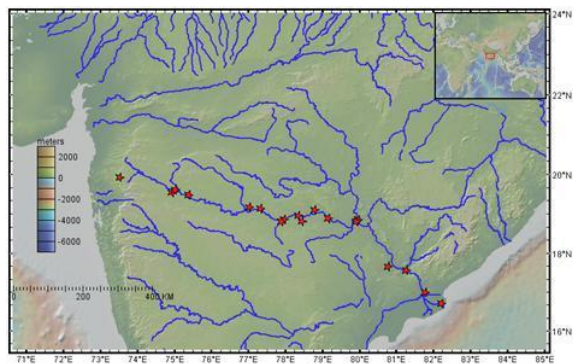


Figure 84: Godavari river is sampled during monsoon of 2013 to study the weathering processes controlled by diverse lithology such as the Deccan basalt and Achaean Gneisses Godvari river system drains through diverse lithology such as the deccan basalt and the Archaean gneisses whose weathering rates are significantly different.

(K. Damodar Rao and S. K. Singh)

Physical Erosion in the Irrawaddy River System

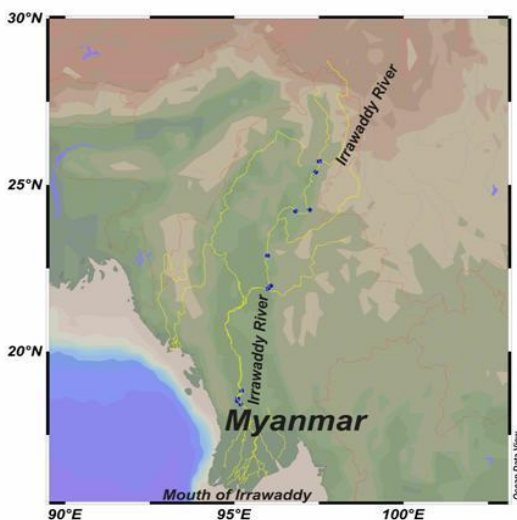


Figure 85: Sampling location of Irrawaddy river system. The silicate fraction of these sediments are being analysed for Sr and Nd isotope composition which has been established to track the sediment sources.

The Irrawaddy River ranks 5th in sediment discharge and 4th in total dissolved load and contributes significantly to the global sedimentary and geochemical budget. Due to poor accessibility the weathering processes and their controlling factors have not been studied in this river system till now despite having global importance. In this study an effort is being made to track the sources of sediments of this large system by analyzing sediments collected from the mainstream and various tributaries of this river system for the first time. Sediments have been sampled all along this river (Figure 85). $^{87}\text{Sr}/^{86}\text{Sr}$ of these sediments displays very small variation, 0.71082 – 0.71813 whereas ϵ_{Nd} varies from -18.5 to -8.8. At its outflow, Irrawaddy have low $^{87}\text{Sr}/^{86}\text{Sr}$ and high ϵ_{Nd} suggesting majority of sediments are derived from calc-alkaline

sources similar to that of Lohit and Dibang rivers of the Brahmaputra. Indo-Burmese and NagaPatkoi ranges also seem to contribute to these isotope compositions.

This study is being done in collaboration with Profs. R.J. Wasson, and Allen Zagler; National University of Singapore.

(K. Damodar Rao and S. K. Singh)

Fluvial landforms and their implication towards understanding the past climate and seismicity in the northern Katrol Hill Range, western India.

The tectonically active Kachchh peninsula in western India lies in the southwest monsoon trajectory and hence provides a rare opportunity to decipher the temporal changes in climate-tectonics interaction in the evolution of the fluvial landforms. Reconstructions based on geomorphology, sedimentology, and geochemistry supported by optical chronology suggest that the fluvial aggradations in the region was initiated during the onset of the Indian Summer Monsoon (ISM) after the Last Glacial Maximum (LGM). The sedimentary characteristics and major elemental concentrations suggest that the sediments are dominated by fluviually reworked milliolites with subordinate contribution from the Mesozoic sandstones and shales and were deposited with the initiation of the ISM after the LGM. Temporal changes in facies architecture and major element concentrations suggest a progressive strengthening of the monsoon between >17 and 12 ka. This was succeeded by an overall strengthened ISM phase with fluctuations after 12 ka and <8 ka. Following this, a gradual decline in the ISM is inferred until around 3 ka. However, presence of the younger valley-fill sediments which are dated to w1 ka are ascribed to a short-lived phase of renewed strengthened ISM in the region before the onset of present day aridity. Based on the morphology of the fluvial landforms, two major events of enhanced uplift can be suggested. The geomorphic expression of the older uplift event dated to >17 ka is represented by the beveled Mesozoic bedrock surfaces which accommodated the post LGM valley-fill aggradation. The younger event of enhanced uplift which is assigned to <3 ka was responsible for the incision of the fill sediments and the Mesozoic bedrock, and the evolution of the present day fluvial landforms. The time averaged incision/uplift rate indicates that the Katrol Hill Range is uplifting at the rate of ~4 mm per year, implying seismically active terrain.

This work was done in collaboration with F. Bhattacharya, B.K. Rastogi from IISR, Gandhinagar, M. G. Thakkar, K.S.K.V. Kachchh, Bhuj and R.C. Patel, Kurukshetra University.

(N. Juyal)

A 1000-year history of large floods in the Upper Ganga catchment, central Himalaya, India

Determining the frequency, magnitude and causes of large floods over long periods in the flood-prone Himalaya is important for estimating the likelihood of future floods.

Towards this we used the slackwater deposits at Bhansawara (in the lower Alaknanda valley) where textural differentiation allowed identification of eleven flood units. The flood units usually have sharp upper and lower boundaries often with either fine sandy or fine sandy clay in the upper few centimetres (the result of waning flood flows) overlying parallel laminated (upper flow regime), ripple laminated (lower flow regime), or massive fine to medium sand with some coarse sand (rapid deposition). There are also some intervals within flood units of alternating sand and sandy clay suggesting fluctuations of flow. Chronology of the flood units is obtained by optical and AMC radiocarbon dating. Based on these a 1000 year history of floods has been reconstructed. The study indicates that all of the floods were large in magnitude which was caused due to the bursting of natural dams in the upper catchment of the Alaknanda river. There is no convincing evidence for a role for glacial outburst floods (GLOFs), and the history of earthquakes does not match the history of floods. It is therefore concluded that rainfall triggered landslide dams, and their rupture as landslide dam outburst floods (LLOFs), played a significant role in flood generation. Preliminary observations suggests that the recent devastating flood of June 2013 was the result of heavy rainfall not landslide dam bursts. The frequency record of the last 1000 year flood shows a non-random pattern. A high frequency between AD 1000 and AD 1300, then a low frequency until a cluster of floods occurred about 200 years ago, then increased frequency. Comparison between the flood history and the record of large floods in Peninsular India, and with independent palaeoclimate records, shows that changes of flood frequency were caused by variations of monsoon rainfall. The cluster of floods ~200 years ago occurred at a time when the monsoon appears to have been at a peak, but the wind speed proxy from which the monsoon peak is inferred increased even more after this time without a commensurate increase in flood frequency. Therefore the cluster cannot be fully explained. Projections of the climate for the end of the current century indicate possible enhancement of monsoon rainfall and rainfall intensity in the Upper Ganga catchment, although the basis for the projection is not strong. Nonetheless it is likely that large floods generated by LLOFs, and heavy rainfall as seen in 2013, will continue, and may increase in frequency.

This work was done with collaboration with R.J. Wasson, National University of Singapore, Y.P. Sundriyal Shipra Chaudhary, S.P. Sati, HNB Garhwal University, Manoj K. Jaiswal, IISER, Kolkata.

(P. Morthekai and N. Juyal)

Geochemical quantification of anthropogenic generated muck in aggravating the June 2013 flood

During June 2013, one of the worst floods in the history of Uttarakhand ravaged the terrain and the people. Maximum human life was lost in the temple town of Kedarnath which was ascribed to the bursting of Chorabari lake behind the temple. The downstream devastation in the lower Alaknanda valley

(around Srinagar) was ascribed to the sediments transported from the paraglacial zone (upper Mandakini valley). However, there was equally strong opinion that the muck generated by Srinagar Hydropower project created the river bed bulking thus flooding the lower town. In order to ascertain the role of natural versus man made (muck) contribution of sediment and flooding we attempted the Chemical Index of Alteration (CIA). CIA is a quantitative measurement of the extent of chemical weathering a rock or sediment has undergone and estimated based on the calculation of the molecular proportion of major elements oxides. Srinagar valley is traversed by the North Almora Thrust which differentiates the quartzite in the northeast and phyllite in the southwest. The phyllite dominated generated during the excavation of tunnel, power house and canal was kept at the banks of the Alaknanda river. Although at places the muck was eroded away, however, it was argued that compared to the sediment transported from the upper catchment (including Chorabari lake), the contribution of the muck (if any) was insignificant. In order to ascertain the local versus long distance contribution of sediment during the flood, sediment are analyzed from Chorabari lake sediment (total 48 samples) and the river bed sediment between Kedarnath to the lower reaches of the Mandakini valley (total 11 samples). The average CIA of 48 samples from Chorabari lake sediment is 58, the flood sediment between Kedarnath and lower Mandakini valley is 45 to 50. The muck CIA is 76 to 71 (close to the phyllite) whereas the river bed flood sediment below the Srinagar barrage varies between 64 to 56. Using the two end member mixing model, (the CIA of the Quartzite and Phyllite) the contribution of muck was found between 47% (proximal to the muck dumping site) to 23% the farthest location downstream of Kirtinagar (Figure 86).

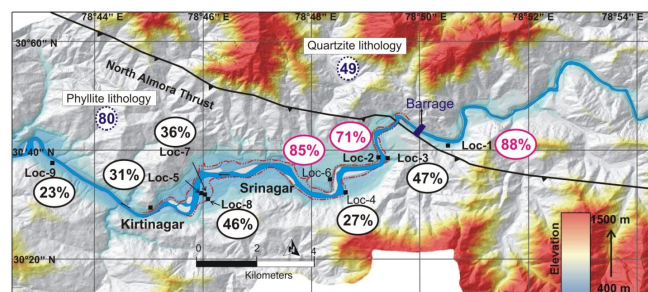


Figure 86. Red ellipsoids (percentage of phyllite in muck). Black ellipsoids (percentage of phyllite in river sediment) Dotted circle represents two end members (phyllite and Quartz) to calculate % phyllite contribution.

The study demonstrate that CIA can be used to differentiate between the short and long distance sediment sources and cautions that the muck generated by hydropower projects should be disposed scientifically in ecologically sensitive Himalayan terrain.

This work was done in collaboration with Y.P. Sundriyal, Naresh Rana, HNB Garhwal University and J. Perumal, Pradeep Srivastava, WIHG, Dehra Dun.

(A.D. Shukla and N. Juyal)

Climate history of Thar Desert: A groundwater based approach

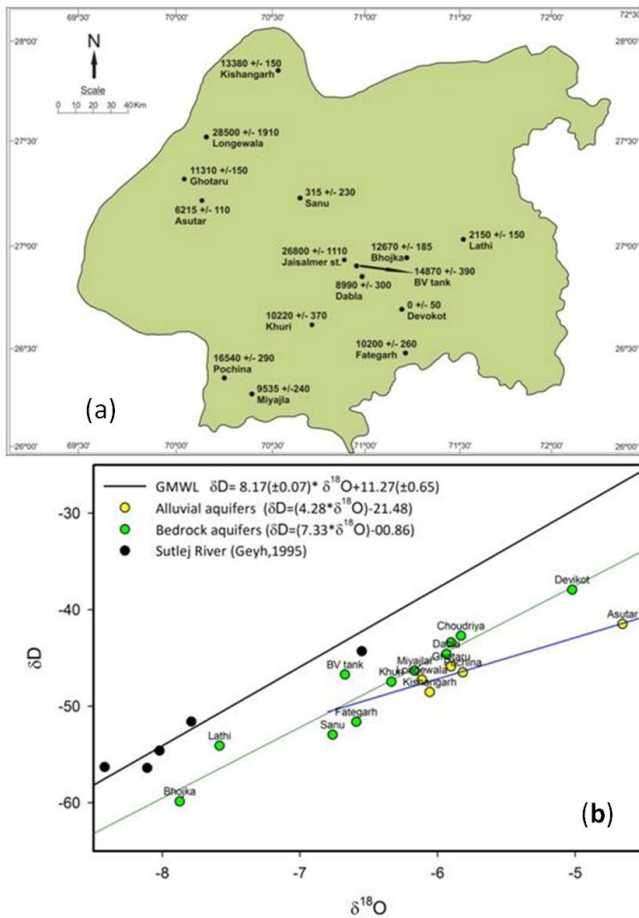


Figure 87:(a) Radiocarbon dates of groundwater samples from Jaisalmer district and (b) plot of $\delta^{18}O$ versus δD of all groundwater samples. Note, most of the samples fall on global meteoric line except sample from Asutar.

Reconstruction of the climate history of extreme arid region like Thar Desert is a challenging task due to the lack of appropriate proxy records. In such regions, groundwater system can be used as a potential archive to study the palaeoclimate. In the present study, different groundwater systems have been studied in the Jaisalmer district to decipher the climate history of the Thar Desert. The rainfall in Jaisalmer district, a part of Thar Desert located in the western margin of the Rajasthan state in India ranges from 50-300 mm/y. The oxygen and hydrogen isotopic composition of ground-water in the Jaisalmer region ranges from -7.87‰ to -4.65‰ for $\delta^{18}O$ and -59.86‰ to -37.92‰ for δD . All these values fall on local meteoric water line confirming meteoric origin of these groundwaters. Radiocarbon age of the Dissolved Inorganic carbon (DIC) of these ground waters provide recharge ages from 28.5 Ka BP to present. There is no recharge for the LGM period in the study area. Post-LGM period from 17 to 6 Ka BP is marked by wet condition with peak at 9-10 Ka BP. From 6 Ka BP to present is a dry period in the study area.

This work was done in collaboration with Dr. J.S. Rathore, JNV University, Jodhpur and Mr. D. Balaji, MS University of Baroda, Vadodara.

(R. Bhushan and A.K. Sudheer)

Mid-Holocene climate and land-Sea interaction along the southern coast of Saurashtra

Even though, the mid-Holocene experienced significant variability both in terms of climate change and sea-level fluctuations, the forcing factors are still debated.

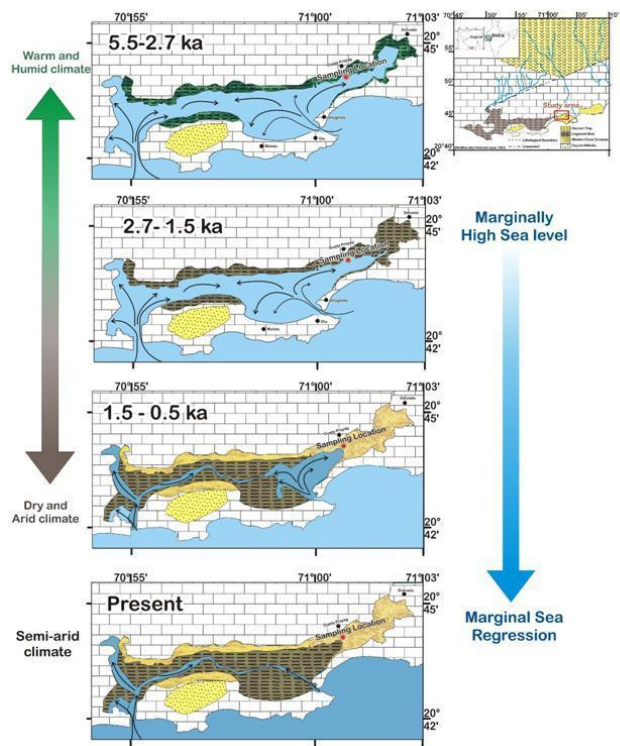


Figure 88: Climatic variability and sea level fluctuation during last 5.5 ka along Diu Island.

Studies have shown that estuarine mud flat sediments responded in accordance with the pace of sea-level and coastal change during Holocene which in turn can be used to reconstruct the climate-variability. In order to ascertain the land sea interactions during the last 5.5 ka, an attempt has been made to study the inactive mudflat of Vasoj Village, NE of Diu Island for geochemical studies supported by the palynological data. The study shows that during the past 5 millennium, the climate has ameliorated from warm and humid conditions to drier conditions along with a marginal change in the sea level, which modulated the sedimentation in the mudflat. This region experienced strengthened monsoonal conditions with marginally high sea level during 5.5 ka and reached to the maximum aridity during 0.5 ka by attaining its

present lagoonal configuration. However, the present climatic condition (semi-arid) was attained probably after 0.5 ka.

This study was done in collaboration with Ms. Shilpa Pandey from BSIP, Lucknow for Palynological studies.

(U. Banerji, N. Juyal and R. Bhushan)

Surface Water Dynamics of the Arabian Sea

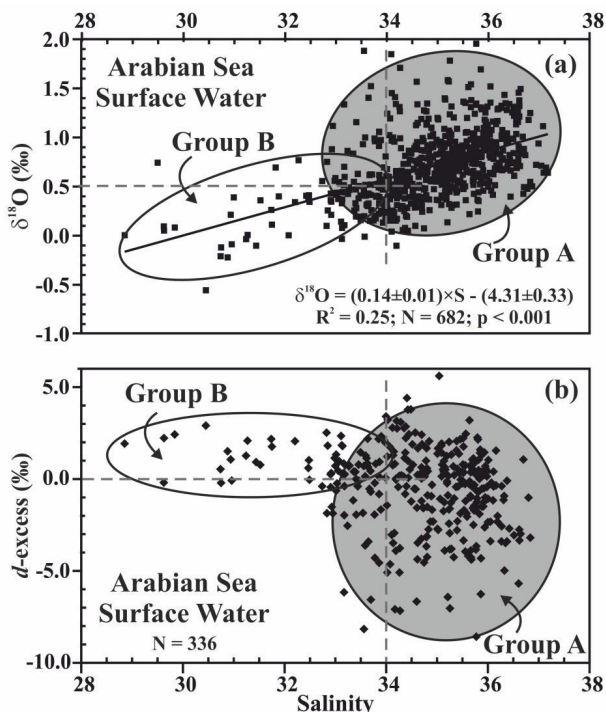


Figure 89: A weak relationship exists between (a) $\delta^{18}\text{O}$ –Salinity and (b) d-excess–Salinity for samples with Salinity < 34, though there is a general geographical correspondence between $\delta^{18}\text{O}$ and Salinity. It seems from the two plots that the surface waters of the Arabian Sea can be separated into two groups, namely Group A (largely open ocean samples) and Group B (largely coastal samples). The samples in Group B (Salinity < 34) have relatively less scatter and narrower range of $\delta^{18}\text{O}$ compared to samples in Group A.

Isotopic compositions ($\delta^{18}\text{O}$ and δD) and salinity of 683 surface water samples from the Arabian Sea (AS) collected during 2008–2011, were measured to understand the factors controlling the spatio-temporal distribution of these parameters. Scatter plots between (a) $\delta^{18}\text{O}$ –Salinity and (b) d-excess–Salinity are shown in Figure 89. Similarly, scatter plots between (a) $\delta^{18}\text{O}$ – δD and (b) d-excess– $\delta^{18}\text{O}$ are shown in Figure 90. From the distributions of $\delta^{18}\text{O}$ and salinity (S), and the relationships between $\delta^{18}\text{O}$ – δD and $\delta^{18}\text{O}$ –S, following inferences have been drawn: (1) there is a broad correspondence between the geographic distributions of the $\delta^{18}\text{O}$ and S; (2) in spite of a large scatter, a statistically significant $\delta^{18}\text{O}$ –S relationship can be identified in much of the investigated part of the AS; (3) the $\delta^{18}\text{O}$ – δD regression line for all samples clumped together has a slope of $3.2 (\pm 0.16)$, much lower than that (7.37) for the global ocean surface water line (GOSWL) which in case of the AS is seen only for samples

with salinity < 34; (4) the linear relationship between $\delta^{18}\text{O}$ and δD breaks down completely in the months of March–May; (5) contrary to the adjoining Bay of Bengal (BOB), both $\delta^{18}\text{O}$ and S progressively increase from equator northwards; (6) the $\delta^{18}\text{O}$ – δD and the $\delta^{18}\text{O}$ –d-excess relationships indicate strong kinetic fractionation due to evaporation from surface waters of the AS throughout the year, with enhancement during summer months.

This work was done in collaboration with Drs. Muraleedharan, P.M. and Sivakumar, K.U. of NIO, Goa, and Kumar, B. and Rao, M.S. of NIH, Roorkee.

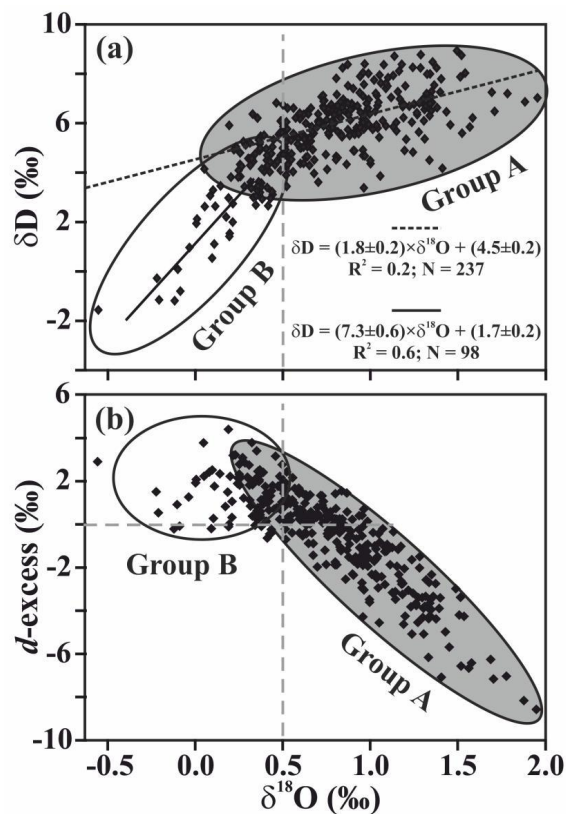


Figure 90: (a) The $\delta^{18}\text{O}$ – δD regression line for surface water samples collected from the Arabian Sea. There is only a poor linear correlation between the two parameters considering all the samples collected from the Arabian Sea. Similar to isotope–salinity plots (the surface waters of the Arabian Sea can be separated into two groups, namely Group A (largely open ocean samples) and Group B (largely coastal samples)). (b) The d-excess– $\delta^{18}\text{O}$ plot for the same samples show a progressive decrease in d-excess values with increasing $\delta^{18}\text{O}$ indicating significant kinetic fractionation due to strong evaporation for samples of Group A.

(R.D. Deshpande, Medha Dave, Raj Laxmi Singh and S.K. Gupta)

Radiocarbon dating of stalagmites to ascertain their time span

While precise approach to date any speleothem is the U–Th disequilibrium method by mass-spectrometry, radiocarbon is still a good tool to understand the time span of such deposits. Moreover, in certain cases when detritus content in

a speleothem is very high, despite applying all the correction approaches, results from U-Th method often lead to ages which are unrealistic. Under such situations only C-14 dating method remains the option to establish tentative chronology of the rare pristine deposits. We have been exploring a few such stalagmites from Andaman Islands with prime intention to reconstruct monsoon of the tropical area. So far these samples have shown high detritus content (Th-232 from 17 to 52 pg/g of stalagmite), therefore corrected ages, for example for the stalagmite AN-2 are: 10.7 ± 6.1 kyr BP at the base and 4.0 ± 4.9 kyr BP at the tip (assuming initial $^{230}\text{Th}/^{232}\text{Th}$ atomic ratio as 20 ppm) which makes the dates unusable. Hence, thirteen closely spaced layers from ~ 28 cm long AN2 were dated giving time span from 4310 ± 120 to 870 ± 90 yr BP. These ages supported with lamination counting will be used to address the climate of the Andaman Islands in the ancient times. In addition to this 10 dates on five stalagmites from Chhattisgarh were obtained, these show various time ranges varying from 1.3 kyr to 13.7 ky B.P. (detritus content and U-Th age are obtained from New Mexico University, U.S.A. under collaboration).

(A.H. Laskar, S. Band, R. Ramesh and M. G. Yadava)

Groundwater Recharge Characteristics in Gujarat

Ground waters from semi-confined and confined aquifers in Gujarat State were isotopically ($\delta^{18}\text{O}$ and δD) characterized to understand the factors governing spatio-temporal variation in isotopic composition and obtain insights about the spatially variable recharge characteristics and possible controlling factors. A total of 391 groundwater samples were collected, mostly from the shallow open wells ($n = 385$) and in a very few cases from the hand pumps ($n = 6$), tapping the groundwater from the first unconfined aquifers in the state of Gujarat, western India. The groundwater sampling was done in two seasons, namely, in the pre-monsoon months of May-June ($n = 197$) and in the post-monsoon months of Nov ($n = 194$), to examine the seasonal variations. In case of the multi-layered alluvial aquifer system such as that in Gujarat, the rate of vertically downward flow of infiltrated water in unsaturated zone is very slow (from < 1 meter up to a couple of meters per year). Also the seasonal variations in isotopic composition are expected to be attenuated below a couple of meters and hence, unconfined ground waters are not expected to have seasonal isotopic variation. However, in this study groundwater is found to exhibit seasonal (pre-monsoon to post-monsoon) variations (Figure 91).

In some regions post-monsoon ground water samples are isotopically depleted in ^{18}O and D compared to pre-monsoon samples. In some other regions, post-monsoon groundwater samples are isotopically enriched in ^{18}O and D compared to pre-monsoon samples. Isotopic depletion in post-monsoon season is possible only when fresh rainwater infiltrates into the unconfined groundwater via preferential pathways or high permeability channels. Similar seasonal variations have also been noticed in d -excess ($=\delta\text{D}-8 \times \delta^{18}\text{O}$) parameter. Based on the observed seasonal variation in $\delta^{18}\text{O}$ and d -excess values, maps of geographical distribution of seasonal differences

have been prepared from which it is possible to identify the regions where there are signatures of preferential recharge, possibly associated with high permeability sub-surface channels connected to surface reservoirs or streams.

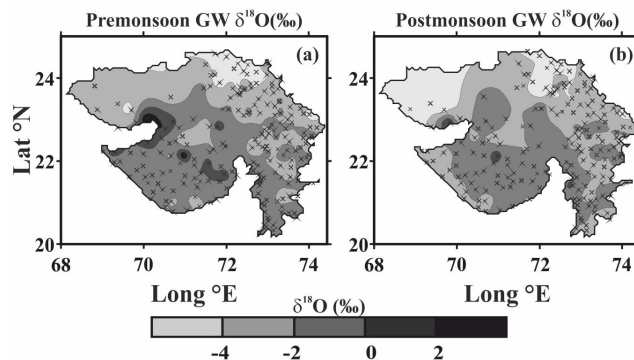


Figure 91: Geographical distribution of $\delta^{18}\text{O}$ of shallow unconfined groundwater of Gujarat in (a) pre-monsoon and (b) post-monsoon seasons.

(R.D. Deshpande and M. Dave)

Tracing sources of dissolved inorganic carbon using $\delta^{13}\text{C}$ in a tropical eutrophic estuary

In aquatic ecosystems, $\delta^{13}\text{C}$ of dissolved inorganic carbon ($\delta^{13}\text{C}_{\text{DIC}}$) can provide information about its possible sources. $\delta^{13}\text{C}_{\text{DIC}}$ is influenced by different inputs and outputs to the system. Inputs, in an estuarine environment, that affect the isotopic signature may include atmospheric CO_2 , respiration of organic matter, surface water and groundwater inflow of aqueous CO_2 and alkalinity, calcite dissolution, and methane oxidation, whereas the outputs include evasion of CO_2 , calcite precipitation, photosynthetic uptake, and water outflow. Since estuaries are directly linked to the human life and ocean, it is important to understand the anthropogenic influences on the carbon dynamics. During this study, we attempted to understand the reasons for spatial and temporal variations in $\delta^{13}\text{C}_{\text{DIC}}$ of the Cochin estuary, a eutrophic tropical estuary in the southwest coast of India, during three different seasons (pre-monsoon, monsoon, and post-monsoon). The dynamic nature of the Cochin estuary was reflected in the measured $\delta^{13}\text{C}_{\text{DIC}}$, which varied from -12.24 to -3.26 ‰ (pre-monsoon), -13.64 to -5.68 ‰ (Monsoon) and -5.35 to $+0.78$ ‰ (post-monsoon). The results indicate the contribution of seawater and freshwater to the $\delta^{13}\text{C}_{\text{DIC}}$ during different seasons. During pre-monsoon and monsoon seasons, sampling locations experienced freshwater input to the estuary and resulted in lower $\delta^{13}\text{C}_{\text{DIC}}$. The range of salinity during December showed the invasion of sea water (high tide) during sampling period, which resulted in higher $\delta^{13}\text{C}_{\text{DIC}}$ than pre-monsoon and monsoon.

This work is being done in collaboration with Dr. G. V.M. Gupta of Centre for Marine Living Resources and Ecology, Cochin, India.

(S. Kumar and P. S. Bhavya)

Primary production in the northern Red Sea

Primarily due to non-scientific considerations, Red Sea remains one of the least studied regions in the world with little data on primary production and related parameters. During a study intended to generate valuable data set and understand the biogeochemistry of the Red Sea, a cruise was undertaken to estimate uptake rates of carbon and nitrogen by phytoplankton, along with concentrations of nutrients and chlorophyll *a*, in the Saudi Arabian waters of the northern Red Sea (23 - 28°N). Concentrations of nitrate, nitrite and phosphate were in traces within the euphotic zone while those of silicon were in excess of 0.5 $\mu\text{mol L}^{-1}$. Concentrations of chlorophyll were very low within the euphotic zone (0.01 - 0.6 $\mu\text{g L}^{-1}$ and 1.53 - 21.5 mg m^{-2}). Rates of carbon uptake at discrete depths ranged from 0.02 to 3 $\mu\text{g C L}^{-1} \text{h}^{-1}$. About 80% of the carbon uptake was attributable to the < 20 μm fraction. Ammonium and urea were taken up in preference and accounted for nearly 90% of the total N uptake. Together, these results indicate that the waters of the northern Red Sea are oligotrophic and that primary production is strongly N-controlled. Analyses of the data and interpretation of the results also led to speculations that the perceived north-south gradient in chl *a* (and possibly in primary production) in the Red Sea is maintained by circulation of chl- and nutrient-rich waters through a series of gyres. There is a greater role for heterotrophy and microbial loop in the trophic dynamics and *in situ* nitrification within euphotic zone is an important source of N for phytoplankton and consequently export of carbon to deep sea could be lesser than that indicated by *f*-ratios.

This work is being done in collaboration with Dr. M. Wafar of King Fahd University of Petroleum and Minerals, Dhahran, Saudi Arabia.

(S. Kumar and P. S. Bhavya)

Modelling biogeochemical cycles in coastal oceans

Several of the key components of carbon cycle are not fully understood or quantified in the coastal oceans, more so in the coastal region surrounding Indian subcontinent, where data is discontinuous and spatially isolated. A study aimed to estimate various components of organic and inorganic carbon and nitrogen pools along with modelling the associated fluxes using *in-situ* and satellite data and study their variability over time using time-series study has been initiated. The study will focus in Gujarat coast using boat trips and continental margins of the eastern Arabian Sea using planned ship cruises. The first field trip related to this study has already been undertaken during March 2014. This study is planned in different phases for five years: (1) *In-situ* measurements of biogeochemical parameters and development of algorithms, (2) field validation of developed algorithms from *in-situ* measurements and assessment and analysis of variability, and (3) implementation of algorithms on satellite data and validation of satellite derived biogeochemical components and fluxes with *in-situ* match-up data.

This work is being done in collaboration with Dr. Mini Raman of Space Application Centre, Ahmedabad.

(S. Kumar and P. S. Bhavya)

Seasonal Variability in Secondary Aerosol Formation over Indo-Gangetic Plain

Indo-Gangetic Plain (IGP) spread over northern India has large amount of gaseous and particulate air pollutants due to emissions from large-scale post-harvest biomass burning, vehicles, industries, and bio-fuel burning. Primary particulate pollutants are compounded by the large emissions of secondary aerosol precursors, resulting in the production of large amounts of secondary inorganic and organic aerosols through multi-phase chemistry. These pollutants cause deterioration of air quality, increase in vulnerability of people to cardiopulmonary diseases, reduction in crop yield, reduction in visibility degradation, and change in Earth's radiation balance. However, poor understanding on the formation of secondary aerosols remains among the major cause of uncertainty in assessing effects of aerosols on climate and air quality. This study presents seasonality in secondary organic and inorganic aerosol formation under the dominance of different source (s) and meteorological conditions in different seasons based on daytime and nighttime hi-vol $\text{PM}_{2.5}$ samples ($n = 149$) collected over Patiala (30.2°N, 76.3°E; 250 m amsl), a site located in the northwest IGP, during October-2011 to September-2012. The samples were assayed for major inorganic ions, elemental carbon (EC), organic carbon (OC) and water-soluble organic carbon (WSOC). The data was classified into five seasons: autumn (Oct-Nov), winter (Dec-Feb), spring (Mar-Apr), summer (May-Jun) and rainy (Jul-Sep), depending upon different meteorological conditions. Characteristic ratios of climatically important species were used as tool to identify their daytime and/or nighttime secondary formation. Different concentration but similar ratio in daytime and nighttime samples would suggest primary sources are dominant and concentration difference could be due to physical processes such as change in boundary layer height, change in source strength. However, different concentration and different ratio could be due to secondary formation through chemical processing of ambient species. The WSOC/OC ratios were on average ~ 1.35 times higher during daytime than that during nighttime in all seasons (except in summer), suggesting at least 35% enhancement in secondary organic aerosols through daytime photochemical reactions. Further, water-soluble fraction of aerosol composition was dominated by WSOC, SO_4^{2-} , NO_3^- , and NH_4^+ , known indicators of secondary organic and inorganic aerosols, suggesting water-soluble fraction of aerosols can be broadly considered as secondary aerosols present in the atmosphere over the study region. Water-soluble fraction of $\text{PM}_{2.5}$ i.e., secondary aerosol fraction varied from 0.31 to 0.62 with higher values (> 0.50) in winter and spring, and lower values (< 0.35) during summer and rainy seasons, reflecting seasonality in secondary aerosol formation. This study improves the understanding on secondary aerosol formation over IGP.

Logistic support for the sample collection was provided by Mr. Atinderpal Singh and Prof. Darshan Singh (Punjabi University, Patiala).

(N. Rastogi)

Impact of South and Southeast Asian continental outflow on aerosol composition over Port Blair, Bay of Bengal

Transport of pollutants through South and Southeast Asian continental outflow and their exchange across air-sea interface can profoundly affect the ocean surface biogeochemistry over the Bay of Bengal. This study presents the PM₁₀ composition and its controlling factors at Port Blair (PB) island located in the Bay of Bengal (BoB) during the late NE-monsoon (February–April) during 2013. PM₁₀ mass concentration ranged from 24 to 65 µg m⁻³ during the study period and interestingly depicted short-period modulation with the periodicity of ~6 days. Even though the PB is located in the middle of ocean, average sea-salt contribution to PM₁₀ was only 3%, anthropogenic and organic together contributed ~60%, EC contributed ~5% and rest including dust was unidentified. Scatter plots between Na⁺ and Cl⁻, Na⁺ and Mg²⁺, and Na⁺ and K⁺ with corresponding seawater lines suggest that all Na⁺ and major fraction of Mg²⁺ in aerosols was also originated from sea-salts, however, significant fraction of K⁺ has been derived from non-sea-salt sources. Strong linear correlation co-efficient between K⁺ and carbonaceous aerosols (OC, EC and WSOC) implicate that the majority of K⁺ could have been originated from biomass burning emissions. The Na⁺ vs Cl⁻ plot indicated near quantitative chloride depletion from sea-salts (range: 57 to 100%, avg: 98%, sd: 7%), and found to be associated with high abundance of SO₄²⁻. Transport of pollutants not only affect marine atmospheric chemistry but the exchange across air-sea interface can have profound impact on the ocean surface biogeochemistry.

Logistic support for the sample collection at Port Blair was provided by Mr. Santosh Kumar Pandey and Dr. S. Suresh Babu (Space Physics Laboratory, Thiruvananthapuram).

(N. Rastogi)

First semi-continuous measurements of water-soluble organic carbon (WSOC) in India using PILS-TOC: Preliminary Results

Semi-continuous measurements of water-soluble organic carbon (WSOC), for the first time in India, were performed using particle-into-liquid sampler (PILS) coupled to total organic carbon (TOC) analyzer with 4 min integration time during January-February 2014 at Patiala located in the Indo-Gangetic plain (IGP). WSOC in ambient aerosols is considered as a measure of secondary organic aerosols (SOA). In parallel to WSOC, mass concentrations of

particulate matter smaller than 1.0, 2.5 and 10 µm aerodynamic diameter (PM₁, PM_{2.5}, and PM₁₀, respectively) were measured with 5 min integration time, and daytime and nighttime PM_{2.5} samples were collected using high volume air sampler. Filter samples were analyzed for major anions, cations, WSOC, organic carbon (OC) and elemental carbon (EC). The concentration of WSOC ranged from 0.1 to 99 µg m⁻³ (average: 15.6, sd: 9.4) during the study period with highest concentration during 'Lohiri' festival. Rain events brought WSOC concentration down to its lowest, however, it came back to seasonal average value within a couple of hours, indicating fast SOA formation. Further, a strong correlation between PM₁ and WSOC (R² = 0.83; slope = 0.113, intercept = 4.7), suggests significant fraction of fine particles are SOA. Diurnal variability of WSOC exhibits bimodal distribution with first peak in the morning (08:00 to 12:00) and second during late evening (18:00 to 22:00), when the combination of lower temperature, higher humidity and relatively high emissions from source (s) occur.

Logistic support for the sample collection was provided by Mr. Atinderpal Singh and Prof. Darshan Singh (Punjabi University, Patiala).

(N. Rastogi and A. Patel)

GEOTRACES inter-comparison of radium isotopes in seawater

As a part of International GEOTRACES programme, we participated in the inter-calibration of radium isotope composition of the coastal seawater. Analytes included ²²³Ra, ²²⁴Ra, ²²⁶Ra, ²²⁸Ra and ²²⁸Th. RaDeCC system is used to measure short lived nuclides, ²²³Ra and ²²⁴Ra. The long-lived nuclides, ²²⁶Ra and ²²⁸Ra were measured by HPGe gamma spectrometry. Nine laboratories joined this activity. One sample set was collected in the coastal region of the Yellow Sea, near Qingdao, China and another in Tolo Harbor of Hong Kong, representing coastal waters of Asian region. The results show most of the data reported by different labs is within two standard deviations of the mean. Radium extraction efficiencies based on two Mn-fiber columns attached in series averaged 95-99%. Results for ²²⁶Ra, ²²³Ra and ²²⁸Th in the Asia inter-comparison are considerably less scattered and ²²⁴Ra results could be probably improved if the samples could reach the laboratory sooner. The results reported from PRL are among the best values reported from all laboratories indicating our high quality measurement capability of radium isotopes in seawater.

(R. Rengarajan)

Upper ocean organic carbon export using naturally occurring radionuclides

The export of particulate organic carbon (POC) from the surface ocean to depth plays a key role in sequestering carbon

from atmosphere into the deep ocean and marine sediments. Short-lived particle-reactive radionuclides ^{234}Th ($t_{1/2}=24.1$ d), ^{210}Pb ($t_{1/2}=22.4$ y) and ^{210}Po ($t_{1/2}=138$ d) have been used for the estimation of carbon export in the ocean. To quantify carbon export, seawater samples were collected to measure depletion of ^{234}Th in the surface waters. Measurements of the integrated ^{234}Th depletion allow quantifying the downward flux of particulate ^{234}Th out of the surface water. In order to convert this flux to a carbon flux, POC/ ^{234}Th ratio of large sinking particles are determined at 200 m depth. ^{234}Th was determined in 4 L seawater samples collected from 9 selected depths from upper 300 m water column using low background beta counting system onboard. We have simultaneously employed disequilibrium in another radionuclide pair, ^{210}Po and its grandparent ^{210}Pb , to predict POC fluxes as there is ample evidence that ^{210}Po is more closely linked to the cycling of organic material within the plankton than is ^{234}Th . For total ^{210}Po and ^{210}Pb analysis, 12 L samples were collected from 12 selected depths up to 800 m with the highest resolution in the upper 150 m of the water column. To characterize spatial and temporal patterns in the magnitude of carbon export from the euphotic zone and evaluate recent changes, samples were collected from 25 profiles from the Arabian Sea, Bay of Bengal and the Indian Ocean during 3 cruises, viz. ORV Sagar Kanya (March-May 2013 and January-February 2014) and RV Sindhu Sankalp (October-November, 2013). Further analysis of these samples are in progress.

(R. Rengarajan, Aswathy, S. Anand)

Geochemical study of the Indo-Myanmar Ophiolite belt

Ophiolite suites (belt) and associated ophiolitic melanges witness the closure of an oceanic domain during continent–continent convergence and present an opportunity to understand the nature of associated mantle material. The ophiolite suite of north-eastern India (Indo-Myanmar Ophiolite) is regarded as the continental extension of the Indonesia island arc which evolved as a result of obduction of the Indian and Burmese plates. Thus the ophiolite belt provides an opportunity to decipher the progress of subduction or under thrusting of the Indian crust vis-a-vis with the active subduction occurring in the Andaman Sea. The objective of the study is to (i) compositional characterization of the ophiolite sequence (ii) estimate the equilibrium condition of the rocks and (iii) understand the nature of the oceanic lithosphere beneath the region. The Indo-Myanmar Ophiolite Belt (IMOB) extends from Pukhpur (Nagaland state) in the north to Moreh (Manipur state) in the south. It consists of different igneous, metamorphic and sedimentary rock components. Ultramafic rocks forming the main component of the belt are consists of mantle sequence of tectonised peridotites with mafic intrusive and pelagic sediments. The preliminary geochemical (major and trace elements) study on some of the selected volcanic rocks collected from the northern part of the ophiolite belt indicate that the rocks are dominated by alkaline basalt. The Primitive Mantle normalized multi element diagram of the analyzed samples show enrichment of LILE compared to HFSE (e.g., Nb, Zr, Ti).

Together with the Ta and Nb depletion and Th enrichment in the samples analysed suggest that the enrichment of these elements occurred during the subduction process. Study is in progress towards compositional characterisation and ascertaining the nature of oceanic lithosphere.

This work is part of a collaborative study with Dr. Bidyandana Maibam, Manipur University, Imphal.

(A.D. Shukla)

Geochemistry and geochronology of dry land fluvial system, western India

Dry land fluvial system in western India emanates from the Aravalli ranges and drains into the Gulf of Cambay and the Gulf of Kachchh. The sedimentary characteristics and textural attributes of the incised alluvial sequences in various river basins of western Indian indicate significant variability in the palaeohydrological conditions. Considering that the region is dominated by the Indian Summer Monsoon (ISM), the temporal changes in sedimentation pattern can be ascribed to the changing strength of the ISM. In the present study we investigated the Banas river which drains through the transitional climatic zone viz. the arid north-west and semi-arid southeast. Optical chronology using the Single Aliquot Regeneration Technique on quartz extract from a 10.5 m thick fluvio-aeolian sequence at Junadeesa (N 24° 13' 6" E 72° 9' 4.96") indicate that deposition occurred between 37 ka to 3.5 ka. Using the detrital proxies weathering and rainfall such as the Al_2O_3 , Fe_2O_3 , TiO_2 , and the Chemical Index of Alteration (CIA) suggests that Banas river experienced an overall strengthened ISM condition during 37 to >22 ka, while the decrease in the detrital proxies after ~22 ka and before 18 ka suggests declining ISM which also corresponds to the Last Glacial Maximum (LGM). The high amplitude fluctuations in CIA indicate short-lived periods of reversal in the overall declining ISM. Following this, a gradual increase in the major elements and CIA are ascribed to a gradual strengthening in ISM which persisted until around 10 ka (early Holocene). After 10 ka a brief decline in geochemical proxies suggests a short-lived reversal in the ISM. This event is then succeeded by gradual improvement in the ISM until around 6 ka (early mid-Holocene). The overall arid climatic condition in Banas basin appears after 6 ka and probably peaked round 3.5 ka. These are the first chronologically constrained climatic reconstruction from the transitional climatic zone of western India suggesting that the late-Quaternary climate variability accords well with the regional climatic pattern obtained from the continental and marine sequences, suggesting that the hydrology of the dry land fluvial system is intimately associated with the winnowing and waxing of the ISM.

This work is part of a collaborative study with Ms. F. Bhattacharyya, ISR Gandhinagar.

(A.D. Shukla and N. Juyal)

Sr and Nd Isotope Composition of Atmospheric Mineral Dust at Ahmedabad: Provenance and Seasonal Variability

Atmospheric aerosol has profound impact on global climate, biogeochemical cycles and human health. Mineral dust is one of the major components in the aerosol budget which comprise ~35% of total global aerosol emission. Asian dust production is estimated to be about 800 Tg / year, which is almost half of world mineral dust emission. To improve our understanding of their sources, transport, deposition and biogeochemical impact, a comprehensive study involving chemical and isotopic composition of ambient aerosols is essential. Towards this, measurements of Sr and Nd isotopic compositions of ambient aerosol at various geographical locations Ahmedabad, Jodhpur, Mout Abu, Cochin as well as over marine region have been initiated. These isotopic signatures are powerful finger print for identifying mineral dust sources and undergo insignificant alteration during transport and atmospheric processes. Ambient aerosol samples collected from Ahmedabad during 2007-2008 using high-volume sampler with an inlet size cut off 10 μm diameter on quartz filters ($8 \times 10''$) are used to study seasonal variability in $^{87}\text{Sr}/^{86}\text{Sr}$. One fourth of the filter samples were cut and leached with 0.6N HCl to remove carbonate/labile fraction. The remaining fraction is digested completely with HF and HNO_3 . Sr is separated using Biorad AG-50w-8x resin column and analyzed for $^{87}\text{Sr}/^{86}\text{Sr}$ on MC-ICP-MS. Preliminary results of Sr isotopic composition at Ahmedabad exhibits significant seasonal variation (0.711 to 0.719) indicating pronounced temporal variability in dust sources and transport in this region. Soil derived from Decan basalt is the major dust source from western and southern region of sampling location with characteristic $^{87}\text{Sr}/^{86}\text{Sr}$ ratio < 0.71 . Thar Desert is situated in north direction with soil probably derived from Aarvalli or Himalaya which has characteristic ratio of ~ 0.75 . Local dust is comprised of alluvial soil transported from Aravalli region with typical $^{87}\text{Sr}/^{86}\text{Sr}$ ~ 0.75 . The seasonal variation in Sr isotopic composition in an annual cycle reflects the differences in source region of mineral aerosol consistent with synoptic scale wind direction over this region and demonstrates that there is significant contribution from dust transported from distant sources at Ahmedabad.

(A. K. Sudheer, Sunil K. Singh, R. Rengarajan and V. K. Rai)

Polar and non-polar organic aerosols from agricultural-waste burning emissions in Northern India:

This study focuses on characteristics of organic aerosols (polar and non-polar) and total organic mass-to-organic carbon ratio (OM/OC) from post-harvest agricultural-waste (paddy- and wheat-residue) burning emissions in Northern India. Aerosol samples from an upwind location (Patiala: 30.2°N , 76.3°E) in the Indo-Gangetic Plain were analyzed for non-polar and polar fractions of organic carbon (OC_1 and OC_2) and their respective mass (OM_1 and OM_2). On average, polar organic aerosols (OM_2) contribute nearly 85% of the total organic mass (OM) from the paddy- and wheat-residue burning emissions. The water-soluble-OC (WSOC) to OC_2

ratio, within the analytical uncertainty, is close to 1 from both paddy- and wheat-residue burning emissions. However, temporal variability and relatively low WSOC/ OC_2 ratio ($\text{Av}: 0.67 \pm 0.06$) is attributed to high moisture content and poor combustion efficiency during paddy-residue burning, indicating significant contribution ($\sim 30\%$) of aromatic carbon to OC_2 . The OM/OC ratio for non-polar ($\text{OM}_1/\text{OC}_1 \sim 1.2$) and polar organic aerosols ($\text{OM}_2/\text{OC}_2 \sim 2.2$), hitherto unknown for open agricultural-waste burning emissions, is documented in this study. The total OM/OC ratio is nearly identical, 1.9 ± 0.2 and 1.8 ± 0.2 , from paddy- and wheat-residue burning emissions. The mass fraction of OM_1 in $\text{PM}_{2.5}$ is nearly identical ($\sim 10\%$) during different emissions (Figure 92). However, the fractional contribution of polar organic mass exhibits significant variability; $\sim 50\%$ during paddy-residue burning emission, $\sim 20\%$ during bio- and fossil-fuel combustion and $\sim 30\%$ during the wheat-residue burning emission (Figure 92).

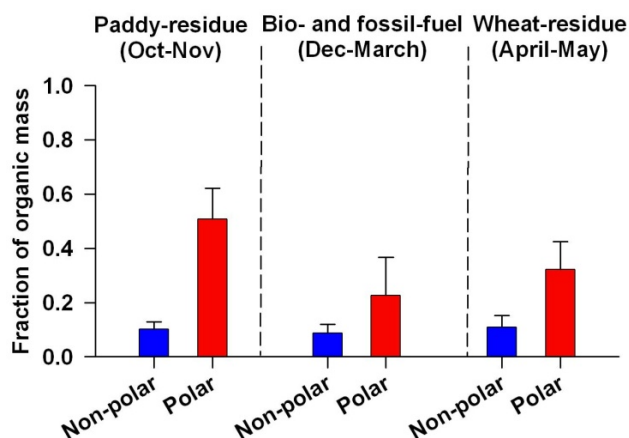


Figure 92: Mass fraction of non-polar and polar organic mass in $\text{PM}_{2.5}$ during post-harvest agricultural-waste burning emissions in the Indo-Gangetic Plain.

(P. Rajput and M.M. Sarin)

Atmospheric polycyclic aromatic hydrocarbons and isomer ratios as tracers of biomass burning emissions:

Emission from large-scale post-harvest agricultural-waste burning (paddy-residue burning during October–November and wheat-residue burning in April–May) is a conspicuous feature in northern India. The poor and open burning of agricultural residue result in massive emission of carbonaceous aerosols and organic pollutants to the atmosphere. In this context, concentrations of atmospheric polycyclic aromatic hydrocarbons (PAHs) and their isomer ratios have been studied for a 2-year period from a source region (Patiala: 30.2°N ; 76.3°E) of two distinct biomass burning emissions. The concentrations of 4-6 ring PAHs are considerably higher compared to 2-3 ring PAHs in the ambient particulate matter ($\text{PM}_{2.5}$). The cross plots of PAH isomer ratios, fluoranthene / (fluoranthene+pyrene) and indeno [1,2,3-cd]pyrene / (indeno [1,2,3-cd] pyrene+benzo [g,h,i] perylene) for two biomass burning emissions, exhibit distinctly different source characteristics compared to those

for fossil-fuel combustion sources in south and south-east Asia (Figure 93). The PAH isomer ratios studied from different geographical locations in northern India also exhibit similar characteristics on the cross plot, suggesting their usefulness as diagnostic tracers of biomass burning emissions (Figure 93).

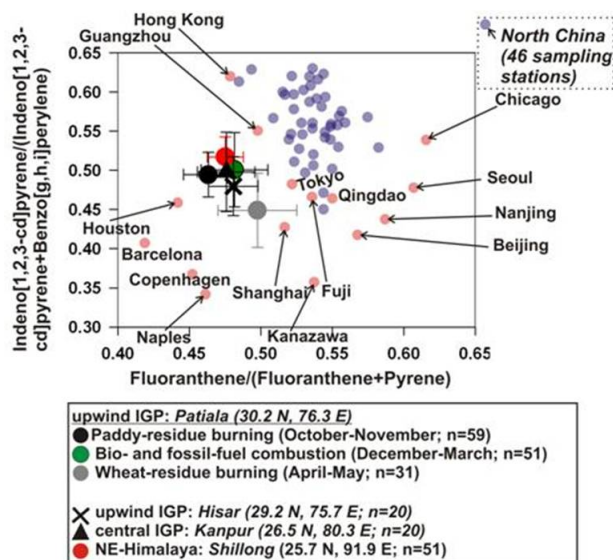


Figure 93: Cross plot of PAH isomer ratios show distinctly different source characteristics in the Indo-Gangetic Plain (IGP) and NE-Himalaya (NE-H) compared to those from the fossil-fuel dominated source regions in south and south-east Asia. The cross plot from Liu et al. (2007) is modified for data from this study.

(P. Raput and M.M. Sarin)

Light absorbing organic aerosols (Brown Carbon) over the tropical Indian Ocean

The first field measurements of light absorbing water-soluble organic carbon (WSOC), referred as brown carbon (BrC), have been made in the marine atmospheric boundary layer (MABL) during the continental outflow to the Bay of Bengal (BoB) and Arabian Sea (ARS). The absorption signal measured at 365 nm in aqueous extracts of aerosols shows systematic linear increase with WSOC concentration, suggesting significant contribution from BrC to the absorption property of organic aerosols. The mass absorption coefficient (b_{abs}) of BrC shows inverse hyperbolic relation with wavelength (from ~ 300 to 700 nm), providing estimate of angstrom exponent (α_P , range: 3 – 19; A_v : 9 ± 3). The mass absorption efficiency of brown carbon ($\sigma_{abs-BrC}$) in the MABL varied from 0.17 to 0.72 m^2g^{-1} (A_v : 0.45 ± 0.14 m^2g^{-1}) (Figure 94). The α_P and $\sigma_{abs-BrC}$ over BoB are quite similar to that studied from a sampling site in the Indo-Gangetic Plain (IGP), suggesting dominant impact of organic aerosols associated with the continental outflow. A comparison of the mass absorption efficiency of BrC and elemental carbon (EC) brings to focus the significant role of light absorbing organic aerosols (from biomass burning emissions) in atmospheric radiative forcing over oceanic regions located downwind of the pollution sources.

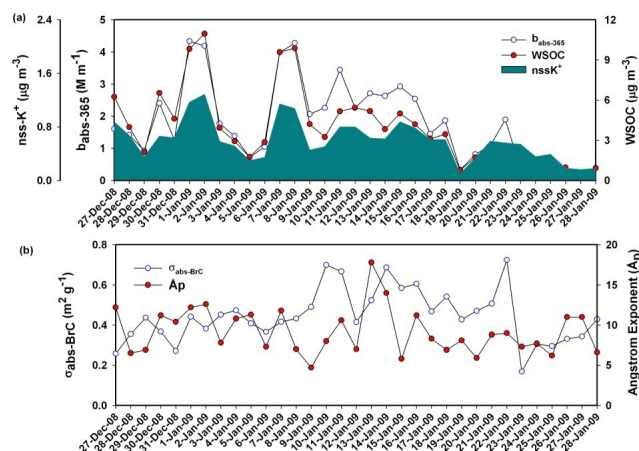


Figure 94: Temporal variability of (a) mass absorption coefficient at 365 nm ($b_{abs-365}$), WSOC and non-sea-salt potassium ($nss-K^+$); (b) mass absorption efficiency ($\sigma_{abs-BrC}$) and angstrom exponent (α_P) of brown carbon (BrC) in PM_{10} sampled from the Bay of Bengal.

(B. Srinivas and M.M. Sarin)

Primary and secondary aerosols from Indo-Gangetic Plain: Impact on CCN, CN concentrations

The number concentrations of cloud condensation nuclei (CCN) and submicron aerosols (CN), along with their chemical composition and optical properties, have been studied during October 2008, October–November 2009 and November 2010 from an urban (Kanpur) site in the Indo-Gangetic Plain (IGP). The concentrations of CCN and CN and their optical properties vary with primary emission and secondary aerosol formation. The CCN (at 0.38% super-saturation) and CN concentrations varied from ~ 3900 to 15000 cm^{-3} and ~ 23000 to 99000 cm^{-3} , respectively. The diurnal variability of CCN and CN show peak concentrations during early morning hours (6 to 9 AM) and nighttime (7 to 10 PM) which is attributable to variability in source strength of carbonaceous aerosols and secondary aerosol formation. The CCN and CN concentrations are $\sim 50\%$ higher during nighttime with simultaneous increase in organic carbon (OC), elemental carbon (EC) and NO_3^- mass concentrations. However, CCN/CN ratios are similar during day and nighttime, suggesting their co-variability with primary and secondary aerosol formation. The CCN/CN ratios are relatively lower (range: 0.11– 0.33) than global average value and those over urban areas (with similar chemical composition in China), suggesting suppressed activation and hygroscopic growth in highly polluted environment of the IGP. The average mass absorption efficiency of EC during daytime (11.7 ± 2.5 m^2g^{-1}) is about factor of two higher than that during nighttime (5.7 ± 1.3 m^2g^{-1}). These results have implications to study morphological features, mixing state and microphysical properties of aerosols under high acidic environment over northern India.

(K. Ram and M.M. Sarin)

SCIENCE

Theoretical and Computational Physics

Dirac Neutrino from flavour mixing and associated discrete symmetries

Flavour symmetries appropriate for describing a neutrino spectrum with degenerate solar pair made from active states and a third massive or massless neutrino are discussed. Appropriate residual symmetries of the leptonic mass matrices are identified and it is demanded that they be subgroups of some discrete symmetry group G_f . G_f can be a subgroup of SU(3) if the third neutrino is massive and we derived general results on the mixing angle predictions for various discrete subgroups (DSG) of SU(3). The main results obtained are (a) the DSG labeled as C-type fail in simultaneously giving correct θ_{13} and θ_{23} (b) All the D-type groups can predict a relation $\cos^2\theta_{13} \sin^2\theta_{23}=1/3$ among the mixing angles which appears to be a good zeroth order approximation. Various $\Delta(6n^2)$ groups with $n>7$ can simultaneously lead also to $\sin^2\theta_{13}$ in the allowed 3 sigma range and we numerically explored prediction for all $n<150$. All DSG of U(3) with order <512 are considered as possible G_f when the third neutrino is massless. Only seven of them are shown to be viable and three of these can correctly predict the mixing angles.

This work is done in collaboration with Ketan M. Patel from INFN, Padova, Italy.

(A. S. Joshipura)

Measuring the charged Higgs mass and distinguishing between models with top-quark observables

The most popular and interesting extension of the standard-model Higgs sector is that which includes an extra scalar doublet, resulting in the so-called two-Higgs-doublet model (THDM). This model has, in addition to three neutral Higgs bosons, a pair of charged Higgs bosons. Depending on how the scalar doublets couple to fermions, there are typically four types of THDM's. Because of the different kinds of couplings in these different types, the production cross sections and decay branching ratios of charged Higgs bosons differ from model to model, in addition to depending on the mass of the Higgs boson itself. The possibility of using top-quark production at the LHC for various studies is a great advantage. Polarization of top quarks, measured using decay distributions can help to distinguish between various production mechanisms. The process of single-top production in association with a charged Higgs boson at the LHC is studied, and it is shown how top-quark polarization and an azimuthal asymmetry A' of the charged lepton arising from top decay can be used in THDM's to determine or constrain the charged Higgs boson mass. Also discussed are some scenarios where these variables can be used even to distinguish between different types of THDM.

This work was done in collaboration with R. Santos of Lisbon University, Lisbon, Portugal and P. Sharma of KIAS, Seoul, S. Korea.

(S. D. Rindani)

Probing chromomagnetic and chromoelectric couplings of the top quark using its polarization in pair production at hadron colliders

The Tevatron, where the top quark was discovered, and the currently functional Large Hadron Collider (LHC), with copiously produced top pairs, enable a detailed study of top-quark properties. In particular, they can be used to test the couplings of the top quark to gauge bosons. Several extensions of the standard model (SM) can give rise to anomalous couplings of the top quark to gauge bosons, in particular, the gluons. This work examines how top-quark polarization, which is predicted to be negligibly small in the SM, can be used to measure chromomagnetic and chromoelectric couplings of the top quark to gluons. Special emphasis is laid on the use of angular distributions and asymmetries of charged leptons arising from top decay as measures of top polarization and hence of these anomalous couplings. It is shown that high sensitivities may be reached at the Tevatron and the LHC with the use of the suggested analysis.

This work was done in collaboration with S.S. Biswal of the Orissa Univ. of Agriculture and Technology, Bhubaneswar and P. Sharma of KIAS, Seoul, S. Korea.

(S. D. Rindani)

Signature of Gibbons-Hawking temperature in the BICEP2 measurement of gravitational waves

BICEP2 has measured B-mode polarization in the cosmic microwave background which is a signal of gravitational waves generated during inflation. There is however a discrepancy between the BICEP2 measurement and the earlier upper bound by PLANCK experiment. We show that the thermal effects of the Hawking-Gibbons temperature on the spectral index of the gravitational waves can reconcile the PLANCK and BICEP2 observations.

This work was done in collaboration with Akhilesh Nautiyal, IMSc, Chennai.

(S. Mohanty)

Higgs instability and Inflation

It has been argued that the well known instability of the Higgs potential makes the standard model incompatible with inflationary scale measured by BICEP2 experiment. We show that taking into account the thermal effects in the deSitter era the Higgs potential at the Hawking temperature is no longer unstable and there is no incompatibility between Higgs and Inflation.

(G. Goswami and S. Mohanty)

One Zero Mass Matrices with Sterile Neutrinos

We investigated the phenomenological implications of the one-zero textures of low energy neutrino mass matrices in the presence of a sterile neutrino. We considered the 3+1 scheme and used the results from a global fit for short baseline neutrino oscillation data, which provided the bounds on the three additional mixing angles. We found that the mass matrix elements connecting only the active states can assume vanishing values in the allowed parameter space for all of the mass spectrum. Among the mass matrix elements connecting the active and sterile states with electron and muon can become small only for the quasi degenerate neutrinos. The element connecting the tau and the sterile state on the other hand, can vanish even for lower values of masses since the 3–4 mixing angle only has an upper bound from current data. The mass matrix element involving only the sterile state stays $< O(1)eV$ in the whole parameter region. We studied the possible correlations between the sterile mixing angles and the Majorana phases to give a zero element in the mass matrix.

This work was done in collaboration with Sivani Gupta and C.S. Kim from Yonsei University, Seoul, Korea.

(S. Goswami and M. Ghosh)

Synergies between neutrino oscillation experiments: an ‘adequate’ configuration for LBNO

Determination of the neutrino mass hierarchy, octant of the 2-3 mixing angle and the CP violating phase in the lepton sector are the unsolved problems in neutrino oscillation physics today. We investigated what is the minimum exposure required for the proposed Long Baseline Neutrino Oscillation (LBNO) experiment to determine the above unknowns. We emphasize on the advantage of exploiting the synergies offered by the existing and upcoming long-baseline and atmospheric neutrino experiments in economising the LBNO configuration. In particular, we do a combined analysis for LBNO, T2K, $NO_{\nu A}$ and INO. We consider three prospective LBNO setups — CERN-Pyhsalmi (2290 km), CERN-Slanic (1500 km) and CERN-Frjus (130 km) and evaluate the adequate exposure required in each case. Our analysis shows that the exposure required from LBNO can be reduced considerably due to the synergies arising from the inclusion of the other experiments.

(S. Goswami, M. Ghosh, P. Ghoshal and S. Raut)

Discovering CP violation with Atmospheric Neutrinos

The measurement of a nonzero value of the 1–3 mixing angle has paved the way for the determination of leptonic CP violation. However, the current generation long-baseline experiments T2K and $NO_{\nu A}$ have limited sensitivity to *the*

CP phase. We showed, for the first time, the significance of atmospheric neutrino experiments in providing the first hint of *CP* violation in conjunction with T2K and NO ν A. In particular, we find that adding atmospheric neutrino data from a magnetized iron calorimeter detector at the India-Based Neutrino Observatory to T2K and NO ν A results in a twofold increase in the range of *CP* values for which a 2σ hint of *CP* violation can be obtained. In fact, in the parameter region unfavourable for the latter experiments, the first signature of *CP* violation may well come from the inclusion of atmospheric neutrino data.

(S. Goswami, M. Ghosh, P. Ghoshal and S. Raut)

Supersymmetric flat directions and resonant gravitino production

Gravitinos are supersymmetric particles that are produced in the early Universe and their presence has very adverse cosmological consequences, referred to as the gravitino problem. We study resonant gravitino production in the early Universe in the presence of supersymmetric flat directions whose large vacuum expectation values (VEVs) break some but not all gauge symmetries. We find that for a large region of parameter space the gravitino abundance is several orders of magnitude larger than the cosmological upper bound. Since flat directions with large VEVs are generically expected in supersymmetric theories this result further exacerbates the gravitino problem.

This work was done in collaboration with Anjishnu Sarkar of LNMIIT, Jaipur.

(N. Mahajan and R. Rangarajan)

Electric dipole polarizability of alkaline-earth-metal atoms from perturbed relativistic coupled-cluster theory with triple excitations

The perturbed relativistic coupled-cluster (PRCC) theory is applied to calculate the electric dipole polarizabilities of alkaline Earth metal atoms. The Dirac-Coulomb-Breit atomic Hamiltonian is used and we include the triple excitations in the relativistic coupled-cluster (RCC) theory. The theoretical issues related to the triple excitation cluster operators are described in detail and we also provide details on the computational implementation. The PRCC theory results are in good agreement with the experimental and previous theoretical results. We, then, highlight the importance of considering the Breit interaction for alkaline Earth metal atoms.

This work was done in collaboration with Dr. B. K. Mani from University of South Florida, USA.

(S. Chattopadhyay and D. Angom)

Goldstone modes and bifurcations in phase-separated binary condensates at finite temperature

We show that the third Goldstone mode, which emerges in binary condensates at phase-separation, persists to higher inter-species interaction for density profiles where one component is surrounded on both sides by the other component. This is not the case with symmetry-broken density profiles where one species is of entirely to the left and the other is entirely to the right. We, then, use Hartree-Fock-Bogoliubov theory with Popov approximation to examine the mode evolution at finite temperature and demonstrate the existence of mode bifurcation near the critical temperature. The Kohn mode, however, exhibits deviation from the natural frequency at finite temperatures after the phase separation. This is due to the exclusion of the non-condensate atoms in the dynamics.

This work was done in collaboration with Dr. S. Gautam from IISc, Bangalore, India.

(A. Roy and D. Angom)

Electric dipole polarizabilities of doubly ionized alkaline-earth-metal ions from perturbed relativistic coupled-cluster theory

Using perturbed relativistic coupled-cluster (PRCC) theory we compute the ground state electric dipole polarizability, α , of doubly ionized alkaline earth metal ions Mg $^{2+}$, Ca $^{2+}$, Sr $^{2+}$, Ba $^{2+}$ and Ra $^{2+}$. In the present work we use the Dirac-Coulomb-Breit atomic Hamiltonian and we also include the Uehling potential, which is the leading order term in the vacuum polarization corrections. We examine the correction to the orbital energies arising from the Uehling potential in the self-consistent field calculations as well as perturbatively. Our results of α are in very good agreement with the experimental data, and we observe a change in the nature of the orbital energy corrections arising from the vacuum polarization as we go from Mg $^{2+}$ to Ra $^{2+}$.

This work was done in collaboration with Dr. B. K. Mani from University of South Florida, USA.

(S. Chattopadhyay and D. Angom)

Annihilation of vortex dipoles in an oblate BoseEinstein condensate

We study the motion of the Gaussian obstacle potential created by a blue detuned laser beam through a phase-separated binary condensate in the pancake-shaped traps. We show that phase-separated binary condensates like ^{85}Rb - ^{87}Rb , with appropriate interaction parameters, can be used experimentally to create obstacle assisted droplet and coreless vortex dipoles. We theoretically analyze the

energetic stability of condensates with normal and coreless vortices. We confirm our analytic and semi-analytic results by numerical solutions of coupled Gross–Pitaevskii equations.

This work was done in collaboration with Dr. S. Gautam from IISc, Bangalore, India.

(S. Prabhakar, R. P. Singh and D. Angom)

Electric dipole polarizabilities of alkali-metal ions from perturbed relativistic coupled-cluster theory

We use the perturbed relativistic coupled-cluster theory to compute the static electric dipole polarizabilities of the singly ionized alkali atoms, namely, Na^+ , K^+ , Rb^+ , Cs^+ and Fr^+ . The computations use the Dirac-Coulomb-Breit Hamiltonian with the no-virtual-pair approximation and we also estimate the correction to the static electric dipole polarizability arising from the Breit interaction.

This work was done in collaboration with Dr. B. K. Mani from University of South Florida, USA.

(S. Chattopadhyay and D. Angom)

Permanent electric dipole moment of Xe atom

The parity (P) and time-reversal (T) odd coupling constant associated with the tensor-pseudotensor (T-PT) electron-nucleus interaction and the nuclear Schiff moment (NSM) have been determined by combining the result of the measurement of the electric dipole moment (EDM) of ^{129}Xe atom and calculations based on the relativistic many-body methods. The accuracies of the reported results are estimated by comparing the calculated dipole polarizability of the above atom with its most precise available experimental data. The non-linear correlation effects are found to be crucial for achieving high accuracy in the calculations. We get lower limits for the T-PT electron-nucleus coupling coefficient and NSM as 1.6×10^{-6} and $1.2 \times 10^{-9} |e| \text{fm}^3$, respectively, by combining our calculations with the available measurement, which, however could improve further when the on-going EDM measurements in the atomic Xe will be successful.

This work is done in collaboration with B. P. Das of Indian Institute of Astrophysics, Bangalore.

(Y. Singh and B. K. Sahoo)

Highly charged ions to probe temporal variation of the fine structure constant

We propose many ions that belong to F-like and Cl-like configurations to probe possible variation of the fine structure

constant by observing their transition lines from the distant astronomical objects. For this purpose, we have developed new relativistic many-body methods to estimate sensitivity coefficients to the variation of the fine structure constant and other atomic properties in many transition lines. To obtain very precise results, we have also incorporated contributions from the lowest order quantum electrodynamics (QED) corrections to the bound electrons and Breit interaction due to the exchange of transverse photons between the electrons. Transitions exhibiting large relativistic effects and lying in the optical wavelengths are being highlighted.

(D. K. Nandy and B. K. Sahoo)

Van der Waals coefficients for the alkali-metal atoms in the material media

The physics of atom-surface of the materials interactions in the experiments are of great interest in many areas of science. The short range interaction between an atom and a material surface can be described by the van der Waals C_3 coefficient using the Casimir-Polder theory. The complication in determining the C_3 coefficients for various atoms and surfaces lies in their dependencies on the dynamic polarizabilities of the atoms and optical conductivity properties of the materials at the imaginary frequencies. As a result, these coefficients are often estimated approximating for a perfectly conducting medium and calculating dynamic polarizabilities using a single oscillator model. Recently, we have developed sophisticated many-body methods and applied to determine polarizabilities of the alkali-atoms very accurately. Using these methods and combining with the observed optical data from various interacting media such as Au (metal), Si (semi-conductor), vitreous SiO_2 (dielectric) and SiN_x (dielectric), we report the C_3 coefficients for many alkali-atoms and demonstrate that these results differ significantly from a perfect conducting medium. We also carry out calculations of the long-range van der Waals coefficients which are very useful in the collision physics.

This work is carried out in collaboration with B. Arora of Department of Physics, Guru Nanak Dev University, Punjab, India.

(B. K. Sahoo)

Reliability tests of the measurements of the hyperfine constants and estimation of the nuclear quadrupole moments of ^{135}Ba and ^{137}Ba isotopes

Direct measurement of the nuclear quadrupole moment (Q) of an isotope is extremely difficult. It is possible to measure their ratios for different isotopes or Q can be determined by combining the measured electric quadrupole hyperfine structure constant (B) with a calculation of B/Q for that isotope. To obtain an accurate value of Q by this procedure, both the measurement and the calculation have to be performed

to high precision. Experimental results are generally considered to be more reliable than the calculations in the many-electron atoms owing to the fact that *ab initio* evaluation of various physical quantities using many-body methods involve a number of approximations at different stages of the calculations. However, measurements from different experiments are not always in agreement and, in certain cases, large discrepancies between the measurements and accurate calculations have been realized. It is therefore essential to scrutinize the accuracies of both the experimental B and calculations of B/Q results when determining the Q values. We have proposed and demonstrated methods to test the validity of the measured values of B and the calculated results of B/Q for a pair of isotopes and using this analysis, we found the most precise Q values of ^{135}Ba and ^{137}Ba as 0.154(2)b and 0.236(3)b, respectively, which differ by about 4% from their previously known values.

This work has been carried out in collaboration with N. C. Lewty, B. L. Chuah, R. Cazan and M. D. Barrett of Centre for Quantum Technologies and Department of Physics, National University of Singapore, Singapore and with B. P. Das of Indian Institute of Astrophysics, Bangalore, India.

(B. K. Sahoo)

Neutrinoless double beta decay and QCD corrections

The possibility of neutrino being a Majorana particle has important and interesting consequences, and therefore is of utmost importance to probe this feature. Observation of neutrinoless double beta decay will confirm the Majorana nature of neutrinos. Since the basic process has a parent nucleus decaying into a daughter and two electrons (but no neutrinos as in the conventional beta decay), a large uncertainty in the prediction of the rate stems from nuclear calculations. Till date the impact of perturbative QCD corrections and evolution under renormalization group has not been studied for the neutrinoless double beta decay. Since the neutrinoless double beta decay constraints imply severe restrictions on the parameter space of any underlying theory, inclusion of such corrections is mandatory to have a correct understanding. It is shown that such corrections can be very significant and can lead to large shifts in the predicted rates.

(N. Mahajan)

Non-perturbative mass of the inflation of slow roll origin

Massless minimally coupled scalar fields pose severe infrared difficulties in de Sitter space. There have been many suggestions to tame this infrared behavior but most of these rely on some ad-hoc or hand waving assumptions. The basic problem lies with the zero mode of the field and it has been suggested that this be handled differently than the non-zero modes. It has been shown that a non-perturbative mass is generated if interactions are considered, including self interactions. The inflation field responsible for the very

rapid expansion of the universe in the very early times is typically considered a massless minimally coupled field and therefore shares all these properties. Here it is shown that even in the absence of interactions at the Lagrangian level, the gravitational perturbation theory which gives rise to non-Gaussianities in the power spectrum can lead to a non-perturbative mass for the inflation, thereby providing a dynamical infrared regulator.

(N. Mahajan)

On the failure of mean-field theories near a critical point

It is well known that mean-field theories fail to reproduce the experimentally known critical exponents. The traditional argument which explain this failure of mean-field theories near a critical point is the Ginzburg criterion. We argue, contrary to the above mentioned traditional view, that diverging fluctuations in real physical systems near a critical point are genuine consequence of the breakdown of the property of statistical independence, and are faithfully reproduced by the mean-field theory. To address the question of why mean-field theories fail to reproduce the known values of critical indices we argue, using the essential ideas of the Wilsonian renormalization group, that mean-field theories fail to capture the long length scale averages of an order parameter near a critical point.

(N. Singh)

Thermodynamical Phase transitions, the mean-field theories, and the renormalization (semi) group: A pedagogical introduction

While analysing second order thermodynamical phase transitions, Lev Landau (the famous Russian physicist) introduced a very vital concept, the concept of an "order parameter". This not only amalgamated the previous fragmentary theoretical understanding of phase transitions (an arsenal of mean-field theories) but also it put forward the important theory of "spontaneous symmetry breaking". Today, order parameter concept is a paradigm both in condensed matter physics and in high energy physics, and Landau theory is a pinnacle of all mean-field theories. Mean field theories are good qualitative descriptors of the phase transition behaviour. But all mean-field theories (including Landau's theory) fail at the critical point (the problem of large correlation length). The problems with large correlation length in quantum many-body systems are the hardest problems known in theoretical physics (both in condensed matter and in particle physics). It was Ken Wilson's physical insights and his powerful mathematical skills that opened a way to the solution of such hard problems.

A perspective on these issues has been addressed. Starting with simple examples of phase transitions (like ice/water; diamond/graphite etc.) we address the following important questions: Why does non-analyticity (sharp phase transitions) arise when thermodynamical functions (i.e., free energies

etc.) are good analytic functions? How does Landau's program unify all the previous mean-field theories? Why do all the mean-field theories fail near the critical point? How does Wilson's program go beyond all the mean-field theories? What is the origin of emergence and universality?

(N. Singh)

Infrared properties of cuprates in pseudogap state: A study of Sharapov-Carbotte scattering rate

Frequency dependent scattering rate of generalized Drude model contains important physics of the electronic structure and of scattering mechanisms. In the present investigation, we study the frequency dependent scattering rate of cuprates (Sharapov-Carbotte scattering rate) at different dopings in the pseudogap phase using the Lorentzian model for the electron-boson spectral function $I^2\chi\Omega$ and the non-constant energy dependent Yang-Rice-Zhang (YRZ) density of states. The increment in the doping concentration shifts the knee point at around ~ 0.17 eV of the $1\omega(\Omega)$ towards the lower frequency which reveals the importance of the electron density of states coming from the pseudogap formation. This corroborates the experimentally observed reduction of pseudogap magnitude with increasing doping.

(P. Bhalla and N. Singh)

Optical conductivity of cuprates from Yang-Rice-Zhang ansatz: Comparison with experiment

We made a theoretical investigation on charge dynamics in weakly coupled CuO_2 planes of the cuprate CNCO in the pseudogap regime by using the phenomenological theory of Yang, Rice, and Zhang (YRZ). With a detailed numerical analysis at various impurity scattering rates (γ imp), we observe that YRZ model is not able to reproduce (in magnitude) the experimentally observed frequency evolution of optical conductivity at a fixed doping level. Further, to analyze the doping evolution of conductivity, we have done a detailed comparison of calculated YRZ conductivity with the experimental one using Two-Component Drude-Lorentz (TCDL) model. We find that YRZ model is capable of reproducing (qualitatively) the experimentally observed doping evolution of Drude-Lorentz parameters, thus it is appropriate for the doping evolution of Drude processes (low energy scale) and processes at the pseudogap (at intermediate energy scale). We also discuss physical reasons of the discrepancy seen in magnitudes.

(N. Singh)

Vacuum stability to constrain a class of B-L models

ATLAS and CMS data at LHC confirmed a narrow range of likely SM Higgs at 125-126 GeV. With existing values of

top mass and strong coupling constant, SM Higgs quartic coupling may run into negative values at a scale below the Planck scale. This vacuum stability problem can be avoided by introducing physics beyond the Standard Model (BSM) in an intermediate scale before Planck scale. We investigated a class of TeV scale BSM models extending SM by introducing new scalar or fermion interactions at the TeV scale while explaining the nonzero Majorana masses of the active neutrinos. Incorporating vacuum stability and perturbativity (triviality) bounds, we constrain the parameters of such models by performing their renormalization-group evolutions.

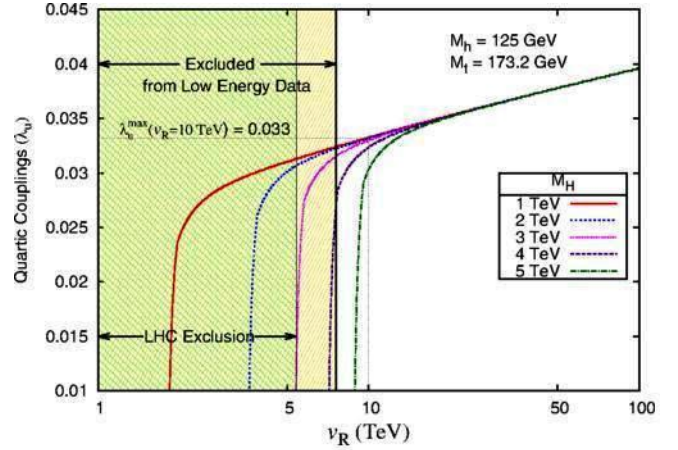


Figure 95: Constraints on the universal quartic coupling λ_u for the LR model with doublet scalars in the low- v_R region for different sets of heavy scalar masses M_H . The yellow shaded region is disallowed from low-energy data ($M_{W_R} > 3.5 > \text{TeV}$) and the green shaded region is excluded from direct searches at the LHC ($M_{W_R} > 2.5 > \text{TeV}$).

This work was done in collaboration with J. Chakraborty, IIT, Kanpur.

(P. Konar and T. Mondal)

Neutrino mass models and exploring at LHC

We consider the generation of naturally small neutrino masses from a dimension-7 operator. Such a term can arise in the presence of a scalar quadruplet and a pair of vectorlike fermion triplets and enables one to obtain small neutrino masses through the TeV scale linear seesaw mechanism. We study the phenomenology of the charged scalars of this model, in particular, the multilepton signatures at the Large Hadron Collider. Of special importance is the presence of the same-sign-tri-lepton signatures originating from the triply charged scalars. The Standard Model background for such processes is small, and hence this is considered as a confirming evidence of new physics. We also looked for events with three, four, five, and six leptons that have negligible contamination from the Standard Model. We further point out the spectacular lepton flavor violating the four-lepton signal that can be the hallmark for these types of models. We also compute the added contributions in the rate for the Standard Model Higgs decaying to two photons via the charged scalars in this model.

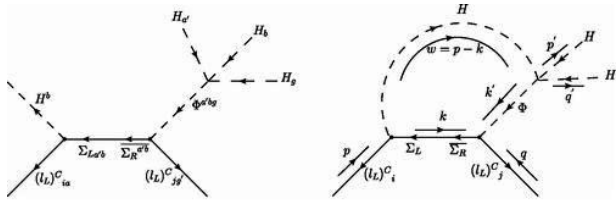


Figure 96: Tree level diagram (left panel) generating dimension-7 seesaw operator and 1-loop diagram (right panel) generating dimension-5 operator for neutrino masses.

(G. Bambhaniya, J. Chakraborty, S. Goswami and P. Konar)

Level spacing statistics and spectral correlations in diffuse van der Waals clusters

Statistical properties of eigen energies, given by nearest-neighbour level spacing distribution $P(s)$, the level number variance $\Sigma^2(L)$, and the Dyson-Mehta $\Delta_3(L)$ statistic, are calculated for van der Waals clusters of different sizes, i.e. three-dimensional bosonic clusters with say N Rb atoms, with N varying from 3 to 40, and interacting through two-body van der Waals potential. For large clusters, it is found that although the so called BGS conjecture seems to be valid, true signatures of quantum chaos are not seen. However, contrasting conjecture of Berry and Tabor is observed with smaller cluster size. For small clusters, due to the existence of large number of quasi-degenerate states in low-lying excitation, Shnirelman peak in $P(s)$ distribution is seen. It is also found that there is a narrow region of intermediate spectrum which can be described by semi-Poisson statistics whereas the higher levels are regular and exhibit Poisson statistics. These observations are further supported by the analysis of the distribution of the ratio of consecutive level spacings $P(r)$ which is independent of the unfolding procedure and thereby provides a tool for more transparent comparison with experimental findings than $P(s)$. The present numerical analysis has been carried out as van der Waals bosonic cluster is relatively a complex quantum system whose experimental realization is possible.

This work was done in collaboration with Dr. (Mrs) Barnali Chakrabarti, Kalyani University, Kolkata and N.D. Chavda (Applied Physics Department, M.S. University of Baroda, Vadodara.)

(V.K.B. Kota)

Poisson to GOE transition in the distribution of ratio of consecutive level spacings

Continuing with the work reported last year on the distribution of the ratio(r) of consecutive level spacings of the eigenvalues of a Poisson (generating regular spectra) spectrum and that

of a GOE random matrix ensemble, analyzed is the transition curve for $\langle r \rangle$, the average of r over the ensemble, for the ensemble generated by the Hamiltonian $H_\lambda = (H^0 + \lambda V) / \sqrt{1 + \lambda^2}$, as a function of the parameter λ . Here, V is a GOE ensemble of real symmetric $d \times d$ matrices and H^0 is a diagonal matrix with a Gaussian distribution (with mean equal to zero) for the diagonal matrix elements. The variances of the H_0 and V matrix elements fixed by the choice that the spectral variance generated by H_0 is same as the one generated by V . This Hamiltonian H_λ generates Poisson system for $\lambda = 0$ and GOE for $\lambda \rightarrow \infty$. Using 1000 member ensembles with d varying from 100 to 1000, curves for $\langle r \rangle$ vs λ are constructed and it is shown that there is a scaling given by the transition parameter $\Lambda \sim \lambda^2 d$, i.e. the $\langle r \rangle$ vs λ curves for different d 's merge to a single curve when $\langle r \rangle$ is plotted as a function of $\lambda^2 d$. Numerically, it is also found that this transition curve generates a map to a 3×3 Poisson to GOE random matrix ensemble. Attempts are being made to solve analytically this 3×3 matrix ensemble. Also, studies of Poisson to GOE transition, in the measure $\langle r \rangle$, in two-body embedded ensembles with a mean-field and in f p -shell nuclei are in progress.

This work was done in collaboration with N.D. Chavda (Applied Physics Department, M.S. University of Baroda, Vadodara.)

(V.K.B. Kota)

Deformed Shell Model Results for Neutrinoless Double Beta Decay of ^{80}Se , ^{82}Se and ^{70}Zn nuclei

Following last year successful work on the calculation of nuclear transition matrix elements (NTME) for the neutrinoless positron double beta decay ($0\nu\beta^+\beta^+$ and $0\nu\beta^+$ EC) of ^{64}Zn , ^{74}Se , ^{78}Kr and ^{84}Sr nuclei, that are in the $A=60-90$ region, using deformed shell model (DSM), started this year are calculations for NTME for the neutrinoless double beta decay ($0\nu\beta\beta$) of ^{70}Zn , ^{80}Se and ^{82}Se nuclei. These are the only candidate nuclei, besides ^{76}Ge , in the $A=60-90$ region. For ^{80}Se and ^{82}Se nuclei, ^{56}Ni is taken as the inert core and employing a modified Kuo interaction in $^2p_{3/2}$, $^1f_{5/2}$, $^2p_{1/2}$ and $^1g_{9/2}$ space, first results for NTME are obtained using DSM wave functions. Comparison with available shell model results indicate that modifications in single particle energies are needed for better description of the ground states of the nuclei involved. Calculations by varying the single particle energy of the $^2p_{1/2}$ and $^1g_{9/2}$ orbitals are in progress. Also in progress are, calculations for ^{70}Zn using Michigan group's $jj44b$ interaction in $^2p_{3/2}$, $^1f_{5/2}$, $^2p_{1/2}$ and $^1g_{9/2}$ space with ^{56}Ni as the core.

This work was done in collaboration with R. Sahu, Berhampur University, Berhampur, Odisha.

(V.K.B. Kota)

Embedded Random Matrix Ensembles in Quantum Physics

Research in the last two decades in particular has resulted in accumulation of large body of new results for embedded random matrix ensembles and it is clear that these random matrix ensembles are indispensable in the study of finite many-particle quantum systems such as atoms, nuclei, quantum dots, small metallic grains, lattice spin models for quantum computers and so on. A first book on this subject was written this year and published by Springer. In this book, starting with an easy-to-read introduction into general random matrix theory, all the necessary concepts for embedded random matrix ensembles are developed from the beginning and reader is carried to the frontiers of present-day research. There are 16 Chapters in the book. First Chapter gives a general introduction and the next two Chapters deal with some general aspects of classical random matrix ensembles. In the remaining part of the book, eight Chapters give results for a variety of embedded ensembles that are mainly classified according to the Lie symmetries of the Hamiltonian of a finite quantum many-body system. Similarly, four chapters are devoted to applications. Last Chapter gives summary and future outlook. Efforts are made to give sufficient details in every Chapter so that an advanced graduate student can follow the mathematics and understand the results of "computer experiments" for embedded ensembles. On the other hand, the book gives an exhaustive review of the field so that a research student can use the material to start working on new questions in the subject of embedded ensembles themselves and in quantum many-body physics using embedded ensembles.

(V.K.B. Kota)

Finite temperature dynamics of vortices in Bose-Einstein condensates

We study the dynamics of a single and a pair of vortices in quasi two-dimensional Bose Einstein condensates at finite temperatures. We use the stochastic Gross-Pitaevskii equation, which is the Langevin equation for the Bose-Einstein condensate, to this end. For a pair of vortices, we study the dynamics of both the vortex-vortex and vortex-antivortex pairs, which are generated by rotating the trap and moving the Gaussian obstacle potential, respectively. Due to thermal fluctuations, the constituent vortices are not symmetrically generated with respect to each other at finite temperatures. This initial asymmetry coupled with the presence of random thermal fluctuations in the system can lead to different decay rates for the component vortices of the pair, especially in the case of two corotating vortices.

This work was done in collaboration with Dr. S. Gautam and Dr. S. Mukerjee from IISc, Bangalore, India.

(A. Roy)

Non-classicality and decoherence of finite superpositions of Fock states

Non-classicality of light is an essential resource in quantum information processing. Negativity in the Wigner function is a signature of non-classicality (Figure 97) and negative volume in the Wigner function is a quantitative measure of non-classicality. A Fock state contains a precise number of photons and is highly non-classical whereas the coherent state, an infinite superposition of Fock states, is most classical. There are, however, many states that are finite superpositions of Fock states (FSFS).

We present a compact and generalized framework to investigate the non-classicality of any arbitrary FSFS. The decoherence of the FSFS is estimated by considering the time evolution of its Wigner function in amplitude decay and phase damping channels. As examples, we determine the non-classicality and decoherence of generalized and reciprocal binomial states.

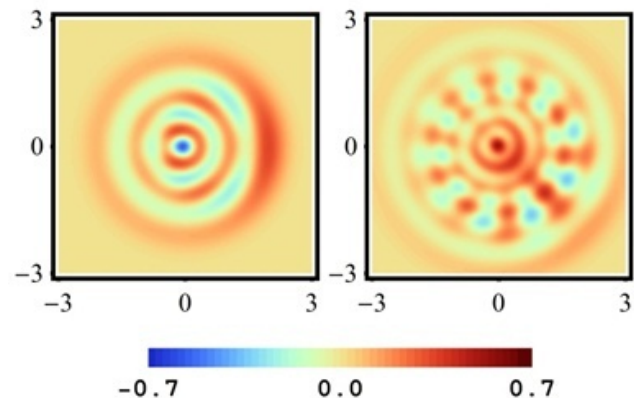


Figure 97: Contour plots of the Wigner function for a generalized binomial state (left) and a reciprocal binomial state (right).

This work was done in collaboration with A. Pathak, Jaypee Institute of Information Technology, Noida.

(J. Banerji)

New low-frequency electromagnetic modes associated with neutral dynamics in partially ionized plasma

The low frequency electromagnetic (EM) modes in inhomogeneous, magnetized partially ionized plasma have been investigated by incorporating neutral dynamics. A general EM dispersion relation has been derived by using a two-fluid magnetohydrodynamics (MHD) model. A detailed analysis shows that the neutral dynamics is playing an extremely important role in physics of magnetized partially ionized plasma by giving rise to new kind of EM modes. It is found firstly that the new instability is linked with compressibility of neutral particles, the collisions between neutral and charged species and the relative streaming in hot/cold, inhomogeneous, magnetized partially ionized plasma and secondly that the neutral dynamics is responsible for the

modified (complex) inertial effect on magnetic field lines. Its consequences on the propagation characteristics of Alfvén wave and cyclotron frequency are discussed. Furthermore, a new mode similar to Langmuir mode is reported. Finally it is discussed how these results may be appropriate for application to space plasma environment.

This study has been carried out in collaboration with A. A. Shaikh, Department of Physics and Astronomy, University of Leicester, Leicester, UK.

(A.C. Das)

PUBLICATIONS

Publication in Journals

Astronomy and Astrophysics

1. Awasthi, A. K., Jain, R., Gadhiya, P. D., et al, 2014, "Multiwavelength diagnostics of the precursor and main phases of an M1.8 flare on 2011 April 22", Mon. Not. R. Astron. Soc., v. 437, p. 2249-2262.
2. Banerjee, D. P. K., Joshi, V., Venkataraman, V., Ashok, N. M., Marion, G. H., Hsiao, E. Y. and Raj, A., 2014, "Near-IR studies of recurrent nova V745 Scorpii during its 2014 outburst", Ap J. Lett., v. 785, p. L11, pp. 1-5.
3. Baug, T. and Chandrasekhar, T., 2013, "Noise reduction methods in analysis of near infrared lunar occultation light curves for high angular resolution measurements", Res. Astron. and Astrophys., v. 13, p. 1363-1380.
4. Bhatt, N. J., Jain, R. and Awasthi, A. K., 2013, "The energetic relationship among geoeffective solar flares, associated CMEs and SEPs", Res. Astron. and Astrophys., v. 13, p. 978-990.
5. Bisoi, S.K., Janardhan, P., Chakrabarty, D., Ananthakrishnan, S. and Divekar, A., 2014, "Changes in Quasi-periodic Variations of Solar Photospheric Fields: Precursor to the Deep Solar Minimum in Cycle 23", Solar Physics, v. 289, p. 41-61.
6. Chakraborty, A., Mahadevan, S., Roy, A., Dixit, V., Richardson, E. H., Dongre, V., Pathan, F. M., Chaturvedi, P., Shah, V., Ubale, G. P. and Anandarao, B. G., 2014, "The PRL Stabilized High-Resolution Echelle Fiber-fed Spectrograph: Instrument Description and First Radial Velocity Results", Pub. Aus. Soc. Pac., v. 126, p. 133-147.
7. Chandra, R., Gopalswamy, N., et al, with Awasthi, A., Jain, R, 2013, "Solar energetic particle events during the rise phases of solar cycles 23 and 24", Adv. Space Res., v. 52, p. 2102-2111.
8. Chattopadhyay, T., Vadawale, S. V. and Pendharkar, J., 2013, "Compton polarimeter as a focal plane detector for hard X-ray telescope: sensitivity estimation with Geant4 simulations", Exp. Astron., v. 35, p. 391-412.
9. Choudhary, D. P., Gosain, S., et al with Awasthi, A. K. and Jain, R., 2013, "Flux emergence, flux imbalance, magnetic free energy and solar flares", Adv. Space Res., v. 52, p. 1561-1566.
10. Chowdhury, P., Jain, R., and Awasthi, A. K., 2013, "Periodicities in the X-ray emission from the solar corona", Ap.J., v. 778, p. 28, pp. 1-9.
11. Dugair, M., Jaisawal, G. K., Naik, S. and Jaaffrey, S. N. A., 2013, "Detection of a variable QPO at 41 mHz in the Be/X-ray transient pulsar 4U 0115+634", Mon. Not. R. Astron. Soc., v. 434, p. 2458-2464.
12. Goobar, A., et al with Banerjee, D. P. K., Venkataraman, V., Joshi, V. and Ashok, N.M., 2014, "The Rise of SN 2014J in the Nearby Galaxy M82", Ap J. Lett., v. 784, p. L12, pp. 1-6.
13. Gopalswamy, N., Xie, H., et al with Jain, R., Awasthi, A.K., 2013, "Height of shock formation in the solar corona inferred from observations of type II radio bursts and coronal mass ejections", Adv. Space Res., v. 51, p. 1981-1989.
14. Hillen, M., Verhoelst, T., et al with Banerjee, D. P. K., 2013, "An interferometric study of the post-AGB binary 89 Herculis I Spatially resolving the continuum circumstellar environment at optical and near-IR wavelengths with the VLTI, NPOI, IOTA, PTI, and the

- CHARA Array”, *Astron. & Astroph.*, v. 559, p. A111, pp. 1-17.
15. Jaisawal, G. K., Naik, S. and Paul, B., 2013, “Possible Detection of a Cyclotron Resonance Scattering Feature in the X-Ray Pulsar 4U 1909+07”, *Ap. J.*, v. 779, p. 54, pp. 1-7.
 16. Joshi, N. C., Uddin, W., Srivastava, with Jain, R. and Awasthi, A. K., 2013, “A multiwavelength study of eruptive events on January 23, 2012 associated with a major solar energetic particle event”, *Adv. Space Res.*, v. 52, pp. 1-14.
 17. Mathew, B., Banerjee, D. P. K., Naik, S. and Ashok, N. M., 2013, “Studies of the Be Star X Persei During a Bright Infrared Phase”, *A. J.*, v. 145, p. 158, pp. 1-9.
 18. Raj, A., Banerjee, D. P. K. and Ashok, N. M., 2013, “Nova KT Eri 2009: Infrared studies of a very fast and small amplitude He/N nova”, *Mon. Not. R. Astron. Soc.*, v. 433, p. 2657-2666.
 19. Singal, A. K. and Singh, R. L., 2013, “Incongruity of the unified scheme with a 3CRR-like equatorial strong-source sample”, *Mon. Not. R. Astron. Soc. Letters*, v. 435, p. L38-L42.
 20. Venkata Raman, V., Anandarao, B. G., Janardhan, P. and Pandey, R., 2013, “Near-infrared monitoring and modeling of V1647 Ori in its ongoing 2008-2012 outburst phase”, *Res. Astron. and Astrophys.*, v. 13, p. 1107-1117.

Solar Physics

21. Joshi, B., Kushwaha, U., Cho, K.S., and Veronig, A. M., 2013, “RHESSI and TRACE observations of multiple flare activity in AR 10656 and associated filament eruption”, *ApJ.*, v. 771, p. 1-14.
22. Joshi, A. D., Srivastava, N., Mathew, S. K., and Martin, S. F., 2013, “Rapid formation and disappearance of a filament barb”, *Solar Physics*, v. 288, p. 191-203.
23. Kumar, D., Bhattacharyya, R., and Smolarkiewicz, P.K., 2013, “Formation of magnetic discontinuities through superposition of force-free magnetic fields: Periodic boundaries”, *Physics of Plasmas*, v. 20, p. 112903, pp. 1-13.
24. Louis, R.E., Mathew, S.K., Puschmann, K.G., Beck, C., and Balthasar, H., 2013, “Formation of a penumbra in a decaying sunspot”, *A&A.*, v. 552, p. L7-10.
25. Mishra, W., and Srivastava, N., 2013, “Estimating the arrival time of Earth-directed coronal mass ejections at in situ spacecraft using COR and HI observations from STEREO”, *ApJ.*, v. 772, p. 70-89.
26. Mishra, W., Srivastava, N., and Davies, J. A., 2014, “A comparison of reconstruction methods for the estimation of coronal mass ejections kinematics based on SECCHI/HI observations”, *ApJ.*, v. 784, p. 135-150.
27. Maurya, R.A., Ambastha, A., and Chae, J., 2014, “Activity-related variations of high-degree p-mode amplitude, width, and energy in solar active regions”, *A&A.*, v. 561, p. A123-A144.
28. Raja Bayanna, A., Kumar, B., Venkatakrishnan, P., Mathew, S.K., Ravindra, B., Mathur, S., and Garcia, R.A., 2014, “On the line profile changes observed during the X2.2 class flare in the active region NOAA 11158”, *Research in Astronomy and Astrophysics*, v. 14, p. 207-220.
29. Sharma, R., Srivastava, N., Chakrabarty, D., Moestl. and Hu, Q., 2013, “Interplanetary and Geomagnetic consequences of January 5, 2005 CMEs associated with solar eruptive filaments”, *J. Geophys. Res.*, v. 118., p. 3954-3967.
30. Vemareddy, P., Ambastha, A., and Wiegelmann, T., 2013, “Magnetic structure of solar active region NOAA 11158”, *Bull. Astron. Soc. India*, v. 41, p. 183-193.

Planetary Sciences and PLANEX Program

31. Bhowmik, S.K., Wilde, S.A., Bhandari, A., and Basu Sarbadhikari, A., 2014, “Zoned Monazite and Zircon as Monitors for the Thermal History of Granulite Terranes: an Example from the Central Indian Tectonic Zone”, *J. Petrol.*, v. 55, p. 585-621.
32. Durga Prasad K. and Murty S.V.S., 2013, “Performance of a small and low-cost chamber to simulate lunar surface environment”, *Acta Astronautica*, v. 89, p. 149-153.
33. Durga Prasad K., Murty, S.V.S. and Chandrasekhar, T., 2013, “A novel wireless light sensing device for planetary and astronomical observations”, *Adv. Space Res.*, <http://dx.doi.org/10.1016/j.asr.2013.04.028>.
34. Jadhav M., Zinner E., Amari S., Maruoka T., Marhas K. K. and Gallino, R., 2013, “Multi-element isotopic analyses of presolar graphite grains from Orgueuil”, *Geochimica et Cosmochimica Acta*, v. 113, p. 193-224.
35. Mishra, R.K. and Goswami, J.N., 2014, “Fe-Ni and Al-Mg isotope records in UOC chondrules: Plausible stellar source of ⁶⁰Fe and other short-lived nuclides in the early solar system”, *Geochim. Cosmochim. Acta* v. 132, p. 440-457.
36. Panchal, R. K. and Pabari, J. P., 2013, “Design of power amplifier and low noise amplifier for 2.4 GHz RF front end in wireless sensor network”, *Int. J. Sci. Eng. Res.*, v. 4, p. 851-858.
37. Ray, D., Misra, S., Widdowson, M., and Langmuir, C.H., 2014, “Search for common parentage for Deccan Continental Flood basalt and Central Indian Ocean Ridge Basalt: A Geochemical and isotopic approach”, *J Asian Earth Sciences*, v. 84, p. 188-200.
38. Ray, D., Misra, S. and Banerjee, R., 2013, “Geochemical variability of MORBs along the slow-spreading Carlsberg-Central Indian Ridge, Indian Ocean”, *J Asian Earth Sciences*, v. 70-71, p. 125-141.
39. Shiv Mohan, Sriram Saran and Anup Das, 2013, “Scattering mechanism based algorithm for improved detection of water ice deposits in the lunar Polar Regions”, *Cur. Sci.*, v. 105, p. 1579-1587.
40. Shiv Mohan, 2013, “Radar Remote Sensing for Earth and Planetary Science”, *Int. J. Sci. Eng. Res.*, v. 4, p. 212-221.

41. Shyam Prasad, M., Rudraswami, N. G. and Panda, Dipak K., 2013, "Micrometeorite flux on Earth during the last ~50,000 years", J. Geophys. Res. (E: Planets), v. 118, p. 2381-2399, pp. 1-47.
 42. Sinha R.K. and Murty S.V.S., 2013, "Geomorphic signatures of glacial activity in the alba Patera volcanic province: Implications for recent frost accumulation on Mars", J. Geophys. Res.: Planets, v. 118, p. 16091631.
 43. Sinha R.K. and Murty S.V.S., 2013, "Evidences of extensive glaciations in Deuteronilus Mensae, Mars: Inferences towards multiple glacial events in the past epochs", Planet. Space Sci., v. 86, p. 10-32
 44. Srivastava, N., Kumar, D., Gupta, R.P., 2013, "Young viscous flows in the Lowell crater of Orientale basin, Moon: Impact melts or volcanic eruptions?", Planet. Space Sci. , v. 87, p. 37-45
 45. Vadawale, S.V., Shanmugam, M., Acharya, Y.B., Patel, A.R., Goyal, S.K., Shah, B., Hait, A.K., Patinge, A. and Subrahmanyam, D., 2013, "Solar X-ray Monitor (XSM) on-board Chandrayaan-2 orbiter", J. Adv. Space Res., <http://dx.doi.org/10.1016/j.asr.2013.06.002>.
 46. Vadawale, S.V., Sreekumar, P., Acharya, Y.B., Shanmugam, M., Banerjee, D., Goswami, J.N., Bhandari, N., Umapathy, C.N., Sharma, M.R., Tyagi, A., Bug, M., Sudhakar, M. and Abraham, L., 2013, "Hard X-ray continuum from lunar surface: Results from High Energy X-ray spectrometer (HEX) onboard Chandrayaan-1", J. Adv. Space Res., <http://dx.doi.org/10.1016/j.asr.2013.06.013>.
- Space, Atmospheric, Molecular and Laser Physics**
47. Chakrabarty, D., Bagiya, M. S., Thampi, S. V., Pathan, B. M. and Sekar, R., 2013, "Signatures of moderate (M-class) and low (C, B class) intensity solar flares on the equatorial electrojet current: case studies", J. Atmos. Sol. Terr. Phys., v. 105-106, p. 170-180.
 48. Cherian, R., Venkataraman, C., Quaas, J. and Ramachandran, S., 2013, "GCM simulations of anthropogenic aerosol-induced changes in aerosol extinction, atmospheric heating and precipitation over India", J. Geophys. Res., v. 118, p. 2938-2955.
 49. Ghosh, D., Lal, S., Sarkar, U., 2013, "High nocturnal ozone levels at a surface site in Kolkata, India: Trade-off between meteorology and specific nocturnal chemistry", Urban Climate, v. 5, p. 82-103.
 50. Gopal, K. R., Lingaswamy, S., Arafath, Md., Balakrishnaiah, G., Kumari, S. P., Devi, K. U., Reddy, N. S. K., Reddy, K. R. O., Reddy, R. R., Azeem, P. A. and Lal, S., 2013, "Seasonal Heterogeneity in Ozone and its Precursors (NOx) by In-situ and Model Observations on Semi-arid Station in Anantapur (A.P), South India", Atmos. Env., v. 84, p. 294-306.
 51. Guharay, A., Reddy, K. Chenna, Chakrabarty, D. and Yellaiah, G., 2013, "Investigation of meteor characteristics over Gadanki using VHF radar observations", Curr. Sci., v. 104, 10, p. 1425-1430.
 52. Haider, S. A., Pandya, B. M. and Molina-Cuberos, G. J., 2013, "Nighttime ionosphere caused by meteoroid ablation and solar wind electron-proton-hydrogen impact on Mars: MEX observation and modeling", J. Geophys. Res. Space Phys., v. 118, p. 6786-6794.
 53. Laskar, F. I., Pallamraju, D., Vijaya Lakshmi, T., Reddy, M. A., Pathan, B. M. and Chakrabarti, S., 2013, "Investigations on vertical coupling of atmospheric regions using combined multiwavelength optical dayglow, magnetic, and radio measurements", J. Geophys. Res. Space Physics, v. 118, p. 4618-4627.
 54. Livingston, J. M., Redemann, J., Shinozuka, Y., Johnson, R., Russell, P. B., Zhang, Q., Mattoo, S., Remer, L., Levy, R., Munchak, L. and Ramachandran, S., 2014, "Comparison of MODIS 3km and 10km resolution aerosol optical depth retrievals over land with airborne sun photometer measurements during ARCTAS summer 2008", Atmos. Chem. and Phys., v. 14, p. 2015-2038.
 55. Mallik, C., and Lal, S., 2014, "Seasonal characteristics of SO₂/NO₂ and CO emissions in and around the Indo-Gangetic Plain", Environ. Monit. Assess., v. 186, p. 1295-1310.
 56. Mallik, C., Lal, S., Venkataramani, S., Naja, M. and Ojha, N., 2013, "Variability in ozone and its precursors over the Bay of Bengal during post monsoon: Transport and emission effects", J. Geophys. Res. Atmos., v. 118, p. 190-209.
 57. Menon, H. N., Shirodkar, S., Kedia, S., Ramachandran, S., Babu, S. and Moorthy, K. K., 2014, "Temporal variation of aerosol optical depth and associated shortwave radiative forcing over a coastal site along the west coast of India", Sc. of the Total Environ., v. 468-469, p. 83-92.
 58. Pallamraju, D., Laskar, F. I., Singh, R. P., Baumgardner, J. and Chakrabarti, S., 2013, "MISE: A Multiwavelength Imaging Spectrograph using Echelle grating for daytime optical aeronomy investigations", J. Atmos. Sol. Terr. Phys., v. 103, p. 176-183.
 59. Rajesh, T. A., 2013, "Software package for aerosol size distribution", Int. J. Scientific Engineering and Tech., v. 2, p. 249-255.
 60. Ramachandran, S. and Kedia, S., 2013, "Aerosol, clouds and rainfall: inter-annual and regional variations over India", Climate Dynamics, v. 40, p. 1591-1610.
 61. Ramachandran, S., and Srivastava, R., 2013, "Influences of external vs. core-shell mixing on aerosol optical properties at various humidities", Environ. Sc.: Processes & Impacts, v. 15, p. 1070-1077.
 62. Rastogi, R. G., Chandra, H., and Yumoto, K., 2013, "Unique examples of solar flare effects in geomagnetic H field during partial counter electrojet along CPMN longitude sector", Earth, Planets and Space, v. 65, p. 1027-1040.
 63. Sahu, L. K., Sheel, V., Kajino, M., Gunthe, S. S., Thouret, V., Nedelec, P., and Smit, H. G., 2013, "Characteristics of tropospheric ozone variability over an urban site in Southeast Asia: A study based on MOZAIC and MOZART vertical profiles", J. Geophys. Res., v. 118, p. 8729-8747.

64. Sahu, L. K., V. Sheel, M. Kajino, M. Deushi, S. S. Gunthe, P. R. Sinha, B. Sauvage, V. Thouret, and H. G. Smit (2014), Seasonal and interannual variability of tropospheric ozone over an urban site in India: A study based on MOZAIC and CCM vertical profiles over Hyderabad, *J. Geophys. Res.*, v. 119, p. 3615-3641.
65. Sahu, L. K., Sheel, V. (2014), "Spatio-temporal variation of biomass burning sources over South and Southeast Asia", *J. Atmos. Chem.*, v. 71, p. 1-19.
66. Sarangi, T., Naja, M., Ojha, N., Kumar, R., Lal, S., Venkataramani, S., Kumar, A., Sagar, R. and Chandola, H. C., 2014, "First simultaneous measurements of ozone, CO, and NO_y at a high-altitude regional representative site in the central Himalayas", *J. Geophys. Res. Atmos.*, v. 119, p. 1592-1611.
67. Segal-Rosenheimer, M., Russell, P. B., Livingston, J. M., Ramachandran, S., Redemann, J. and Baum, B. A., 2013, "Retrieval of cirrus properties by sun photometry: A new perspective on an old issue", *J. Geophys. Res.*, v. 118, p. 4503-4520.
68. Sekar, R., Gupta, S. P., Acharya, Y. B., Chakrabarty, D., Pallamraju, D., Pathan, B. M., Tiwari, D. and Choudhary, R. K., 2013, "Absence of streaming plasma waves around noontime over Thumba in recent times: Is it related to the drift of the dip equator?", *J. Atmos. Sol. Terr. Phys.*, v. 103, p. 8-15.
69. Sharma, R., Srivastava, N., Chakrabarty, D., Mostl, C. and Hu, Q., 2013, "Interplanetary and Geomagnetic consequences of January 05, 2005 CMEs associated with solar eruptive filaments", *J. Geophys. Res. Space Phys.*, v. 118, p. 3954-3967.
70. Sridharan, R., Das, T. P., Ahmed, S. M. and Bhardwaj, A., 2013, "Indicators for localized regions of heavier species in the lunar surface from CHACE on Chandrayaan-1", *Curr. Sci.*, v. 105, p. 1470-1472.
71. Tsunoda, R. T., Thampi, S. V., Nguyen, T. T. and Yamamoto, M., 2013, "On validating the relationship of ionogram signatures to large-scale wave structure", *J. Atmos. Sol. Terr. Phys.*, v. 103, p. 30-35.
72. Ashok Kumar., Vaity, Pravin., Bhatt, Jitendra. and Singh, R. P., 2013, "Stability of higher order optical vortices produced by spatial light modulators", *J. of Modern Optics*, v. 60, p. 1696-1700.
73. Banerji, A., Panigrahi, P.K., Singh, R. P., Chowdhury, S. and Bandyopadhyay, A., 2013, "Quadrature uncertainty and information entropy of quantum elliptical vortex states", *J. Physics A: Mathematical and Theoretical*, v. 46, p. 225303, pp. 1-12.
74. Bhatt, J., Kumar, A., Singh, R. P. and Jaaffrey, S. N. A., 2013, "Optical trapping of fluorescent beads", *J. Exptl. Nanoscience*, p. 1-9.
75. Bhatt, J., Bhatt, S., Buch, S., Singh, R. P. and Jaaffrey, S. N. A., 2013, "Variation of trapping strength with size and number of particles in a single trap", *Optics and Photonics J.*, v. 3, p. 178-183.
76. Giri, D. K., Singh, R. P. and Bandyopadhyay, A., 2013, "Displacement gain dependent fidelity in quantum teleportation using entangled two-mode squeezed light", *Optical and Quantum Electronics*, v. 45, p. 1127-1137.
77. Pandey, A. K. and Bapat, B., 2014, "Effect of transmission losses on measured parameters in multi-ion coincidence momentum spectrometers", *Int. J. of Mass Spectrometry*, v. 361, p. 23-27.
78. Pandey, A. K., Bapat, B. and Shamasundar, K. R., 2014, "Charge Symmetric Dissociation of doubly-ionized N₂ and CO molecules", *J. of Chemical Physics*, v. 140, p. 034319, pp. 1-10.
79. Reddy, S. G., Kumar, A., Prabhakar, S. and Singh, R. P., 2013, "Experimental generation of ring-shaped beams with random sources", *Optics Letters*, v. 38, p. 4441-4444.
80. Reddy, S. G., Prabhakar, S., Aadhi, A., Kumar, A., Shah, M., Singh, R. P. and Simon, R., 2014, "Measuring Mueller matrix of an arbitrary optical element with a universal SU(2) polarization gadget", *J. of Optical Society of America A*, v. 31, p. 610, pp. 1-5.
81. Saha, K., Banerjee, S.B. and Bapat, B., 2013, "A combined electron-ion spectrometer for studying the complete kinematics of molecular dissociation upon shell selective ionization", *Review of Scientific Instruments*, v. 84, p. 073101.
82. Saha, K., Banerjee, S.B. and Bapat, B., 2013, "Three body dissociation of C₂S₂²⁺ subsequent to various S(2p) Auger transitions", *J. of Chemical Physics*, v. 139, p. 164309, pp.1-7.
83. Saxena, Arvind., Prashant Kumar., Banerjee, S. B., Subramanian, K. P. and Bapat, B., 2014, "Dependence of ion kinetic energy and charge on cluster size in multi-photon ionisation of xenon clusters", *Int. J. of Mass Spectrometry*, v. 357, p. 58-62.
84. Saxena, Arvind., Prashant Kumar., Banerjee, S. B., Subramanian, K. P. and Bapat, B., 2014, "Optical spectroscopy of carbon clusters produced in a hollow cathode source", *Spectroscopy Letters*, v. 47, p. 114.
85. Sivaraman, B., Nair, B. G., J.-I. Lo, Kundu, S., Davis, D., Prabhudesai, V., Raja Sekhar, B. N., Mason, N. J., B.-M. Cheng and Krishnakumar, E., 2013, "Vacuum ultraviolet and infrared spectra of condensed methyl acetate on cold astrochemical dust analogs", *The Astrophysical Journal*, v. 778, p. 157, pp. 1-5.
86. Sivaraman, B., Raja Sekhar, B. N., Fulvio, D., Hunniford, A., McCullough, B., Palumbo, M. E. and Mason, N. J., 2013, "Ozone and carbon trioxide synthesis by low energy ion implantation onto solid carbon dioxide and implications to astrochemistry", *J. of Chemical Physics*, v. 139, 074706, pp. 1-10.
87. Vaity, Pravin., Aadhi, A. and Singh, R. P., 2013, "Formation of optical vortices through superposition of two Gaussian beams", *Applied Optics*, v. 52, p. 6652-6656.

Geosciences Division

88. Alappat, L., Seralathan, P., Shukla, A. D., Thrivikramji, K. P. and Singhvi, A. K., 2013, "Chronology of

- Red dune aggradations of South India and its Palaeo-environmental significance*, *Geochronometria*, v. 40, p. 274-282.
89. Awasthi, N., Ray, J.S., Laskar, A.H. and Yadava, M.G., 2013, "Chronology of major terrace forming events in the Andaman Islands during the last 40 kyr", *J. Geol. Soc.*, v. 82, p. 59-66.
 90. Balachandran, S., Pachon, J.E., Lee, S., Oakes, M., Rastogi, N., Shi, W., Tagaris, E., Yan, B., Davis, A., Zhang, X., Weber, R.J., Mulholland, J.A., Bergin, M., Zheng, M. and Russell, A.G., 2013, "Particulate and Gas Sampling of Prescribed Fires in South Georgia, USA", *Atmos. Environ.*, v. 81, p. 125-135
 91. Bhattacharya, Falguni., Rastogi, B.K., Thakkar, M.G., Patel, R.C. and Juyal Navin., 2014, "Fluvial landforms and their implication towards understanding the past climate and seismicity in the northern Katrol Hill Range, western India", *Quatern. Int.*, v. 333, p. 4961.
 92. Bhushan, R., Dutta, K., Agnihotri, R., Rengarajan, R. and Singh, S. P., 2014, "Decadal Variations in Oceanic Properties of the Arabian Sea Water Column Since GEOSECS", *Radiocarbon*, v. 56, p. 313-325.
 93. Biswas, R. H. and Singhvi, A. K., 2013, "Anomalous fading and crystalline structure: Studies on individual chondrules from the same parent body", *Geochronometria*, v. 40, p. 250-257.
 94. Biswas, R. H., Bhatt, B. C. and Singhvi, A. K., 2013, "Effect of optical bleaching on the dosimetric TL peak in $Al_2O_3:C$ for blue and UV emissions", *Radiation Measurements*, v. 59, p. 37-43.
 95. Biswas, R. H., Williams, M. A. J., Raj, R., Juyal, Navin. and Singhvi, A. K., 2013, "Methodological Studies on Luminescence Dating of volcanic ashes", *Quat Geochronol.*, v. 17, p. 14-25
 96. Deshpande, R.D., Muraleedharan, P.M., Singh, R.L., Kumar, B., Rao, M.S., Dave, M., Sivakumar, K.U. and Gupta, S.K., 2013, "Spatio-temporal distributions of $\delta^{18}O$, δD and salinity in the Arabian Sea: Identifying processes and controls", *Mar. Chem.*, v. 157, p. 144-161.
 97. Du, J. Z., Moore, W. S., Hsh, H. F., Wang, G. Z., Jan Scholten, Henderson, P., Men, W., Rengarajan, R., Sha, Z. J. and Jiao, J. J., 2013, "Inter-comparison of radium analysis in coastal sea water of the Asian region", *Mar. Chem.*, v. 156, p. 138-145.
 98. He, C., Li, Q.B., Liou, K.N., Zhang, J., Qi, Li, Mao, Y., Gao, M., Lu, Z., Streets, D.G., Zhang, Q., Sarin, M. M. and Ram, K., 2014, "A global 3-D CTM evaluation of black carbon in the Tibetan Plateau", *Atmos. Chem. Phys. Discuss*, v. 14, p. 7305-7354.
 99. Kothiyari, Girish Ch. and Juyal, Navin., 2013, "Implications of fossil valleys and associated epigenetic gorges in parts of Central Himalaya", *Curr. Sci.*, V. 105, p. 383-388.
 100. Laskar, A. H., Gandhi, N., Thirumalai, K., Yadava, M. G., Ramesh, R., Mahajan, R. R. and Kumar, D., 2014, "Stable carbon isotopes in dissolved inorganic carbon: extraction and implications for quantifying the contributions from silicate and carbonate weathering in the Krishna River system during peak discharge", *Isot. Environ. Health Stud.*, v. 50, p. 156-168.
 101. Laskar, A. H., Yadava, M. G., Ramesh, R., Polyak, V. J. and Asmerom, Y., 2013, "A 4 kyr stalagmite oxygen isotopic record of the past Indian Summer Monsoon in the Andaman Islands", *Geochem. Geophys. Geosyst.*, v. 14, p. 3555-3566.
 102. Laskar, A. H., Yadava, M.G., Sharma, N. and Ramesh, R., 2013, "Late-Holocene climate in the Lower Narmada valley, Gujarat, western India, inferred using sedimentary carbon and oxygen isotope ratios", *The Holocene*, v. 23, p.1115-1122.
 103. Martin, P., M. Rutgers van der Loeff, N. Cassar, P. Vandromme, Francesco d'Ovidio, Stemmann, L., Rengarajan, R., Soares, M., González, H. E., Ebersbach, F., Lampitt, R. S., Sanders, R., Barnett, B. A., Victor Smetacek. and Naqvi, S. W. A., 2013, "Iron fertilization enhanced net community production but not downward particle flux during the Southern Ocean iron fertilization experiment LOHAFEX", *Global Biogeochem. Cycles*, v. 27, p. 871-881.
 104. Midhun, M., Lekshmy, P. R. and Ramesh, R., 2013, "Hydrogen and oxygen isotopic compositions of water vapor over the Bay of Bengal during monsoon", *Geophys. Res. Lett.*, v. 40, p. 6324-6328.
 105. Mishra, S., Chauhan, N. and Singhvi, A.K., 2013, "Continuity of Microblade Technology in the Indian Sub continent: Implications for the dispersal of Modern Humans", *PLOS One*, v. 8, p. e69280, pp. 1-14.
 106. Muthucumarana, R., Gaur, A. S., Chandraratne, W. M., Manders, M., Ramlingeswara Rao, B., Bhushan, R., Khedekar, V. D., Dayananda, A. M. A., 2014, "An Early Historic Assemblage Offshore of Godawaya, Sri Lanka: Evidence for Early Regional Seafaring in South Asia", *J. Mari. Arch.*, v. 9, p. 41-58.
 107. Nagar, Y. C., Ganju, A., Satyawali, P. K. and Juyal Navin., 2013, "Preliminary optical chronology suggests significant dvance in Nubra valley glaciers during the Last Glacial Maximum", *Current Science*, v. 105, p. 96-101.
 108. Nawaz Ali, S. and Juyal Navin., 2014, "Chronology of Late Quaternary glaciation in Indian Himalaya: A critical review", *J. Geol. Soc India*, v. 82, p. 628-638
 109. Nawaz Ali, S., Bishwas, R.H., Shukla, A.D. and Juyal Navin., 2013, "Chronology and climatic implications of Late Quaternary glaciations in the Goriganga valley, central Himalaya, India", *Quat. Sci. Rev.*, v. 73, p. 59-76.
 110. Padro, L. T., Moore, R. H., Zhang, X., Rastogi, N., Weber, R. J. and Nenes, A., 2012, "Mixing state and compositional effects on CCN activity and droplet growth kinetics of size-resolved CCN in an urban environment", *Atmos. Chem. Phys.*, v. 12, p. 10239-10255.
 111. Qurban M.A., Balala, A. C., Kumar, S., Bhavya, P. S. and Wafar, M., 2014, "Primary production in the northern Red Sea", *J Marine System*, v. 132, p. 75-82.

112. Rajput, P. and Sarin, M. M., 2014, "Polar and non-polar organic aerosols from large-scale agricultural-waste burning emissions in Northern India: Implications to organic mass-to organic carbon ratio", *Chemosphere*, v. 103, p. 74-79.
113. Rajput, P., Sarin, M. M., Sharma, D. and Singh, D., 2014, "Atmospheric polycyclic aromatic hydrocarbons and isomer ratios as tracers of biomass burning emissions in Northern India", *Environ. Sci. Pollution Res.*, v. 21, p. 5724 – 5729.
114. Rajput, P., Sarin, M. M., Sharma, D. and Singh, D., 2014, "Characteristics and emission budget of carbonaceous species from agricultural-waste burning in source region of Indo-Gangetic Plain", *Tellus-B*, v. 66, 21026.
115. Ram, K., Tripathi, S. N., Sarin, M. M. and Bhattu, D., 2014, "Primary and secondary aerosols from an urban site (Kanpur) in the Indo-Gangetic Plain: Impact on CCN, CN concentrations and optical properties", *Atmos. Environ.*, v. 89, p. 655-663
116. Ramesh, R., 2013, "Calculating carbon uptake by Oceans", *Geography and You*, v. 13, p. 30-33.
117. Rana, Naresh., Singh, S. K., Sundriyal, Y.P. and Juyal Navin., 2013, "Recent and past floods in the Alakanda valley: causes and consequences", *Current Science*, v. 105, p. 1209-1212.
118. Rastogi, N. and Sarin, M. M., 2013, "Temporal variability in residence time of ambient aerosols using environmental ^{210}Pb ", *Current Science*, v. 105, issue 8, p. 1165–1168
119. Rastogi, N., Singh, A., Singh, D. and Sarin, M. M., 2014, "Chemical characteristics of PM_{2.5} at a source region of biomass burning emissions: Evidence for secondary aerosol formation", *Environ. Pollut.*, v. 184, p. 563-569.
120. Ray, J.S., Pande, K., Bhutani, R., Shukla, A.D., Rai, V.K., Kumar, A., Awasthi, N., Smitha, R.S., and Panda, D.K., 2013, "Age and geochemistry of Newania dolomite carbonatites, India: implications for the source of primary carbonatite magma", *Contrib. Mineral Petrol.*, v. 166, p. 1613-1632.
121. Reddy, D.V., Singaraju, V., Mishra, R., Kumar, D., Thomas, P.G., Rao, K. K. and Singhvi, A.K., 2013, "Luminescence Chronology of inland sand dunes from SE India", *Quat. Res.*, v. 80, p. 265-273.
122. Sarkar, S. D., Mathew, G., Pande, K., Chauhan, N. and Singhvi, A. K., 2013, "Rapid denudation of Higher Himalaya during late Pleistocene. Evidence from Thermochronology", *Geochronometria*, v. 40, p. 304-310.
123. Singh, A., Rajput, P., Sharma, D., Sarin, M.M. and Singh, D., 2014, "Black carbon and elemental carbon from post-harvest agricultural-waste burning emissions in the Indo-Gangetic", *Plain Advances in Meteorology*, p. 179301, pp. 1-10.
124. Singh, A., Ramesh, R. and Godhe, A., 2014, "Inter- and intra-specific carbon and nitrogen assimilation by dinoflagellate and diatom species", *Current Science*, v. 106, p. 867-870.
125. Singh, S. P., Singh, S. K., Bhushan, R., 2014, "Dissolved Boron in the Tapi, Narmada and the Mandovi Estuaries, the Western Coast of India: Evidence for Conservative Behavior", *Estuaries and Coasts*, v. 5, p. 1017-1027.
126. Sridhar, A., Chamyal, L.S., Bhattacharya, F. and Singhvi, A.K., 2013, "Early Holocene fluvial activity from the sedimentology and paleohydrology of gravel terraces in the semi arid Mahi river basin", *J. Asian Earth Sciences*, v. 6, p. 240-248.
127. Srinivas, B. and Sarin, M. M., 2013, "Light absorbing organic aerosols (brown carbon) over the tropical Indian Ocean: Impact of biomass burning emissions", *Environ. Res. Lett.*, v. 8, Id. 044042
128. Srinivas, B. and Sarin, M.M., 2014, "Brown carbon in atmospheric outflow from the Indo- Gangetic Plain: Mass absorption efficiency and temporal variability", *Atmos. Env.*, v. 89, p. 835-843.
129. Tripathy, G. R., Singh, S. K. and Ramaswamy, V.2014, "Major and trace element geochemistry of Bay of Bengal sediments: implications to provenances and their controlling factors", *Palaeogeogr. Palaeoclimatol. Palaeoecol.*, v. 397, p. 20-30,
130. Tripathy, G. R., Singh, S. K., and Bhu, H., 2013, "Re-Os isotopes and major and trace element geochemistry of carbonaceous shales, Aravalli Supergroup, India", *Chem. Geol.*, v. 354, p. 93-106.
131. Verma, V., Biswas, R. H. and Singhvi, A. K., 2013, "Aspects of Infrared radioluminescence dosimetry in K-feldspar", *Geochronometria*, v. 40, p. 266-273.
132. Wasson, R. J., Chauhan, M. S., Sharma, C., Jaiswal, M., Singhvi, A. K. and Srivastava, P., 2013, "Erosion of river terraces as a component of large catchment sediment budgets: A pilot study from the Gangetic Plains", *J. Asian Earth Sci.*, v. 67-68, p. 18-25.
133. Wasson, R. J., Sundriyal, Y.P., Chaudhar S., Jaiswal, M. K., Morthekai, P., Sati, S.P. and Juyal N., 2013, "A 1000-year history of large floods in the Upper Ganga catchment, central Himalaya, India", *Quat. Sci. Rev.*, v. 77, p. 156–166.

Theoretical and Computational Physics

134. Arora, B. and Sahoo, B.K., 2014, "van der Waals coefficients for alkali-metal atoms in material media", *Phys. Rev. A*, v. 89, p. 022511 pp.1-9.
135. Bambhaniya, G., Chakraborty, J., Goswami, S. and Konar, P., 2013, "Generation of Neutrino mass from new physics at TeV scale and Multi-lepton Signatures at the LHC", *Phys. Rev. D* 88, 075006, p. 1-17.
136. Banerji, J. and Pathak, A., 2014, "Wigner distribution, nonclassicality and decoherence of generalized and reciprocal binomial states", *Physics Letters A*, v. 378, p. 117-123.
137. Basak, T., and Mohanty, S., 2013, "130 GeV gamma ray line and enhanced Higgs di-photon rate from Triplet-Singlet extended MSSM", *JHEP*, v. 1308, p. 020, pp. 1-17.

138. Bastero-Gil, M., Berera, A., Mahajan, N. and Rangarajan, R., 2013, "Power spectrum generated during inflation", *Phys. Rev. D*, v. 87, p. 087302 pp. 1-4.
139. B. Dev, P. S., Goswami, S., Mitra, M. and Rodejohann, W., 2013, "Constraining Neutrino Mass from Neutrinoless Double Beta Decay", *Phys. Rev. D*, v. 88, p. 091301(R), pp. 1-4.
140. Biswal, S.S., Rindani, S.D., Sharma, P., 2013, "Probing chromomagnetic and chromoelectric couplings of the top quark using its polarization in pair production at hadron colliders", *Phys. Rev. D*, v.88, p. 074018, pp.1-15.
141. Chakraborty, J., Konar, P., and Mondal, T., 2014, "Constraining a class of B-L extended models from vacuum stability and perturbativity", *Phys. Rev. D*, v. 89, p. 056014, pp. 1-18
142. Chakraborty, J., Mohanty, S., and Rao, S., 2014, "Non-universal gaugino mass GUT models in the light of dark matter and LHC constraints", *JHEP*, v. 1402, p. 074, pp. 1-22.
143. Chakravarty, G., Mohanty, S. and Singh, N. K., 2014, "Higgs Inflation in $f(\Phi, R)$ Theory", *Int. J. Mod. Phys.*, D23, v. 4, p. 1450029, pp. 1-15.
144. Chatterjee, A., Ghoshal, P., Goswami, S., and Raut, S.K., 2013, "Octant sensitivity for large θ_{13} in atmospheric and long baseline neutrino experiment", *JHEP*, v. 1306, p. 010, pp. 1-34.
145. Chattopadhyay, S., Mani, B. K., and Angom, D., 2013, "Electric dipole polarizabilities of alkali-metal ions from perturbed relativistic coupled-cluster theory", *Phys. Rev. A*, v 87, p. 042520 pp. 1-8.
146. Chattopadhyay, S., Mani, B. K., and Angom, D., 2013, "Electric dipole polarizabilities of doubly ionized alkaline-earth-metal ions from perturbed relativistic coupled-cluster theory", *Phys. Rev. A*, v. 87, p. 062504, pp. 1-9.
147. Chattopadhyay, S., Mani, B. K., and Angom, D., 2014, "Electric dipole polarizability of alkaline-earth-metal atoms from perturbed relativistic coupled-cluster theory with triples", *Phys. Rev. A*, v 89, p. 022506, pp. 1-12.
148. Chavda, N.D., and Kota, V.K.B., 2013, "Probability Distribution of the Ratio of Consecutive Level Spacings in Interacting Particle Systems", *Phys. Lett. A*, v. 377, p. 3009-3015.
149. Das, M., and Mohanty, S., 2013, "Generation of scale invariant density perturbations in a conformally invariant Inert Higgs doublet model (Ahmedabad, *Phys. Res. Lab*). Nov 2011 13 pp", *Int. J. Mod. Phys.A*, v. 28, p. 1350094, pp. 1-13.
150. Das, M., and Mohanty, S., 2014, "Leptophilic dark matter in gauged $L_\mu - L_\tau$ extension of MSSM", *Phys. Rev. D*, v. 89, p. 025004, pp. 1-8.
151. Deota, H. N., Chavda, N. D., Kota, V. K. B., Potbhare, V. and Vyas, Manan, 2013, "Random matrix ensemble with random two-body interactions in the presence of a mean field for spin-one boson systems", *Phys. Rev. E*, v. 88, p. 022130, pp. 1-12.
152. Gautam, S., Roy, A. and Mukerjee, S., 2014, "Finite-temperature dynamics of vortices in Bose-Einstein condensates", *Phys. Rev. A*, v. 89, p. 013612, pp. 1-8.
153. Ghosh, M., Ghoshal, P., Goswami S., and Raut, S. K., 2014, "Synergies between neutrino oscillation experiments: an 'adequate' configuration for LBNO", *JHEP*, v. 1403, p. 094, pp. 1-22.
154. Ghosh, M., Ghoshal, P., Goswami, S., and Raut, S.K., 2014, "Can atmospheric neutrino experiments provide the first hint of leptonic CP violation?", *Phys. Rev. D*, v. 89, p. 011301, pp. 1-6.
155. Ghosh, M., Goswami, S., Gupta, S., and Kim, C. S., 2013, "Implication of a vanishing element in the 3+1 scenario", *Phys. Rev. D*, v. 88, p. 033009, pp. 1-20.
156. Gu, P. and Sarkar, U., 2013, "Common Origin of Baryon Asymmetry and Proton Decay", *Mod. Phys. Lett. A*, v. 28, p. 1350159, pp. 1-12.
157. Gupta, S., Joshipura, A.S., and Ketan, M., 2013, "How good is μ - τ symmetry after results on non-zero θ_{13} ?", *JHEP*, v. 1309, p. 035, pp. 1-17.
158. Joshipura, A. S., Mohanty, S. and Pakvasa, S., 2014, "Pseudo-Dirac neutrinos via mirror-world and depletion of UHE neutrinos", *Phys. Rev. D*, v. 89, p. 033003, pp. 1-7.
159. Joshipura, A.S. and Ketan, M., 2013, "Horizontal symmetries of leptons with a massless neutrino", *Phys. Lett.B*, v. 727, p. 480-487.
160. Joshipura, A.S. and Ketan, M., 2014, "A massless neutrino and lepton mixing patterns from finite discrete subgroups of $U(3)$ ", *JHEP*, v. 1404, p. 009, pp. 1-23.
161. Lambiase, G., Mohanty, S., and Prasanna, A.R., 2013, "Neutrino coupling to Cosmological background: A review on Gravitational Baryo/Leptogenesis", *Int. J. Mod. Phys. D*, v. 22, p. 1330030, pp. 1-50.
162. Lewty, N.C., Chuah, B.L., Cazan, R., Barrett, M.D., and Sahoo, B.K., 2013, "Experimental determination of the nuclear magnetic octupole moment $^{137}\text{Ba}^+$ ion", *Phys. Rev. A*, v. 88, p. 012518, pp. 1-8.
163. Mahajan, N., 2014, "Neutrinoless double beta decay and QCD corrections", *Phys. Rev. Lett.*, v. 112, p. 031804, pp. 1-5.
164. Mohanty, S. and Prasanna, A. R., 2013, "Neutrino coupling to cosmological background: A review on gravitational Baryo/Leptogenesis Gaetano Lambiase", *Int. J.Mod.Phys. D*, v. 22, p. 1330030, pp. 1-50.
165. Mohanty, S., Rao, S., and Roy, D. P., 2013, "Reconciling the muon g^{-2} and dark matter relic density with the LHC results in nonuniversal gaugino mass models", *JHEP*, v. 1309, p. 027, pp. 1-16.
166. Nandy, D. K. and Sahoo, B. K., 2013, "Development of relativistic coupled-cluster method for one-electron detachment theory: Application to Mn IX, Fe X, Co XI and Ne XII ions", *Phys. Rev. A*, v. 88, p. 052512, pp.1-12.
167. Nandy, D.K., and Sahoo, B. K., 2014, "Spectral properties of a few F-like ions", *Astron. Astrophys.*, v. 563, p. A25, pp. 1-10.

168. Pakvasa, S., Joshipura, A.S., and Mohanty, S., 2013, "Explanation for the low flux of high energy astrophysical muon-neutrinos", *Phys. Rev. Lett.* v.110, p. 171802, pp. 1-4.
169. Rangarajan, R., and Sarkar, A., 2013, "Kinetic and chemical equilibrium of the Universe and gravitino production", *Astroparticle Physics*, v. 48, p. 37-49.
170. Rindani, S.D., Santos, R. and Sharma, P., 2013, "Measuring the charged Higgs mass and distinguishing between models with top-quark observables", *JHEP*, v. 11, p. 188, pp. 1-20.
171. Roy, A. Gautam, S. and Angom, D., 2014, "Goldstone modes and bifurcations in phase-separated binary condensates at finite temperature", *Phys. Rev. A*, v 89, p. 013617, pp. 1-7.
172. Roy, K., Chakrabarti, B., and Kota, V.K.B., 2013, "Spectral fluctuation and correlation structure of δn statistics in the spectra of interacting trapped bosons", *Phys. Rev. E*, v. 87, p. 062101, pp. 1-8.
173. Sahoo, B.K., Barrett, M.D., and Das, B.P., 2013, "Reliability test for the experimental results of electric-quadrupole hyperfine structure constants and assessment of nuclear quadrupole moments of ^{135}Ba and ^{137}Ba ", *Phys. Rev. A*, v. 87, p. 042506, pp. 1-4.
174. Sahu, R., Srivastava, P.C., and Kota, V.K.B., 2013, "Deformed shell model results for neutrinoless positron double beta decay of nuclei in the $A = 60-90$ region", *J. Phys. G: Nucl. Part. Phys.*, v. 40, p. 095107, pp. 1-18.
175. Prabhakar, S. Singh, R.P., Gautam, S., and Angom, D., 2013, "Annihilation of vortex dipoles in an oblate Bose-Einstein condensate", *J. Phys. B*, v 46, p. 125302, pp. 1-8.
176. Shaikh, A. A., and Das, A. C. 2013 "New low-frequency electromagnetic modes associated with neutral dynamics in partially ionized plasma", *Ann. Geophys.*, v. 31, p. 983-993.
177. Singh, Y., Sahoo, B.K., and Das, B.P., 2013, "Correlation trends in the ground-state static electric dipole polarizabilities of closed-shell atoms and ions", *Phys. Rev. A*, v. 88, p. 062504, pp. 1-11.
178. Singh, Y., Sahoo, B.K., and Das, B.P., 2014, "Ab initio determination of the P - and T -violating coupling constants in atomic Xe by the relativistic-coupled-cluster method", *Phys. Rev. A*, v. 89, p. 030502(R), pp. 1-5.
179. Singh, A., Puri, S., Mishra, H., 2013, "Kinetics of phase transitions in quark matter", *Europhys. Lett.*, p. 52001, pp. 1-17.
180. Singh, A., Puri, Sanjay., Mishra, H., 2013, "Domain growth in chiral phase transitions: Role of inertial dynamics", *Nucl. Phys. A*, v. 908, p. 12-28.

Library & Information Services

181. Nishtha, A. & Rajaram, S., 2013, "Theses Submitted by Doctoral Students of Physical Research Laboratory, India: A Citation Analysis", *Serials Review*, v. 39, p. 114-120.
182. Nishtha, A., 2013, "Publication Pattern of scientists of Physical Research Laboratory (PRL), Ahmedabad, India", *Library Philosophy and Practice*, P. 901, pp. 1-19.

Publications in Proceedings of Conference/ Symposia/ Workshops

Astronomy and Astrophysics

1. Bisoi, Susanta Kumar. and Janardhan, P., 2012, "Observations of a geomagnetic SI^+ – SI^- pair and associated solar wind fluctuations", in: Solar and Astrophysical Dynamos and Magnetic Activity, Proceedings of the IAU, IAU Symposium, 294, pp. 543-544.
2. Bisoi, Susanta Kumar and Janardhan, P., 2012, "Peculiar behavior of solar polar fields during solar cycles 21-23: Correlation with meridional flow speed", Solar and Astrophysical Dynamos and Magnetic Activity, Proceedings of the IAU, IAU Symposium, 294, pp. 81-82.
3. Bisoi, Susanta Kumar. and Janardhan, P., 2012, "Interplanetary scintillation signatures in the inner heliosphere of the deepest solar minimum in the past 100 years", Solar and Astrophysical Dynamos and Magnetic Activity, Proceedings of the IAU, IAU Symposium, v. 294, pp. 83-84.
4. Bisoi, Susanta Kumar. and Janardhan, P., 2012, "Asymmetry in the periodicities of solar photospheric fields: A probe to the unusual solar minimum prior to cycle 24", Solar and Astrophysical Dynamos and Magnetic Activity, Proceedings of the IAU, IAU Symposium, v. 294, pp. 85-86.
5. Chandrasekhar, T., 2013, "Lunar Occultations in the infrared: evolution from single element detectors to sub-arrays", ASI conference series, v. 9, p. 37- 41.

6. Vadawale, S. V., Chattopadhyay, T., Rao, A.R., 2013, "Prospects of hard X-ray polarimetry with Astrosat-CZTI", IEEE proc. NSS/MIC/RTSD, DOI: 10.1109/NSSMIC.2013.6829697.

Solar Physics

7. Joshi, B., Kushwaha, U., Cho, K. S., and Veronig, A. M., 2014, "Signatures of magnetic reconnection during the evolutionary phases of a prominence eruption and associated X1.8 flare", Proceedings of the IAU Symposium on Nature of Prominences and their role in Space Weather, , v. 300, pp. 424-425.
8. Joshi, A. D., Bong, S. C., and Srivastava, N., 2014, "A Statistical Study on Characteristics of Disappearing Prominences", Proceedings of the IAU Symposium on Nature of Prominences and their role in Space Weather, v. 300, pp. 422-423.
9. Srivastava, N., Joshi, A. D., and Mathew, S. K., 2014, "On the onset of recurrent eruptions of a filament observed during August 2012", Proceedings of the IAU Symposium on Nature of Prominences and their role in Space Weather, v. 300, pp. 495-496.
10. Sharma, R., Srivastava, N., Jackson, B. V., Chakrabarty, D., Lockett, N., Yu, H.S., Hu, Q., and Moestl, C., 2014, "Evolution of the 5 January 2005 CMEs associated with eruptive filaments in inner heliosphere", Proceedings of the IAU Symposium on

Nature of Prominences and their role in Space Weather, v. 300, pp. 491-492.

11. Sharma, R., Srivastava, N., and Chakrabarty, D., 2014, "Role of filament plasma remnants in ICMEs leading to geomagnetic storms", Proceedings of the IAU Symposium on Nature of Prominences and their role in Space Weather, v. 300, pp. 493-494.

Planetary Sciences and PLANEX Program

12. Ghosh, S. and Ray, D., 2014, "Microtextures and geochemistry of glass and clast lithologies of Impact-melt from Lonar crater.", 45th Lunar and Planetary Science Conference, Abstract No. 1197.
13. Goyal, S.K., Shanmugam, M., Vadawale, S.V., Banerjee, D., Acharya, Y.B. and Murty, S.V.S., 2013, "Laboratory XRF Measurements Using Alpha Particle X-Ray Spectrometer of Chandrayaan-2 Rover: Comparison with GEANT4 Simulation Results", IEEE proc. NSS/MIC/RTSD-1695.
14. K. Durga Prasad and Murty, S.V.S., 2014, "Effect of grain size and porosity on surface heat influx on the moon", 45th Lunar Planet. Sci. Conf., 1236.
15. Misra, S., Mazumder, A., Andreoli, M.A.G., and Ray, D. 2014, "Large meteorite impacts, volcanism and possible environmental disruption at the Jurassic-Cretaceous boundary.", 45th Lunar Planet. Sci. Conf., abstract no. 1017.
16. Misra, S., Ray, D. and Andreoli, M.A.G., 2013, "Carbonate-rich impact-melt from Morokweng impact structure, South Africa.", Large Meteorite Impacts and Planetary Evolution V, abstract no. 3063.
17. Murty, S.V.S. and Ranjith Kumar, P.M., 2014, "Volume correlated solar noble gases in washington county iron meteorite", 45th Lunar and Planetary Science Conference, 1110.
18. Ray, D. and Misra, S., 2014, "Depth-dependent mantle sources for high- and low Ti mare basalts - an investigation through trace element geochemistry", 45th Lunar Planet. Sci. Conf., 1091
19. Ray, D., Ghosh, S. and Murty, S.V.S., 2014, "Kato meteorite: a rare shower of troilite-metal nodule bearing shock Melted I6-7 chondrite", 45th Lunar Planet. Sci. Conf., 1300
20. Rishitosh K. Sinha., Vijayan S. and Murty, S.V.S., 2014, "Modes of gully formation around north east of argyre basin and the role of volatile discharge due to microclimatic shifts.", 45th Lunar Planet. Sci. Conf., 1670.
21. Ruj, T., Dasgupta, N., Ray, D., and Misra, S., 2014, "Were MORB-like mare basalt generated in absence of any plate tectonics like set up in early Archean.", 45th Lunar Planet. Sci. Conf., 1076.
22. Shanmugam, M., Acharya, Y.B., Mazumdar, H.S., and Vadawale, S.V., 2013, "Dependence of the Leakage Current on the Performance of the Silicon Drift Detector Based X-Ray Spectrometer", IEEE proc. NSS/MIC/RTSD-1741.

23. Shanmugam, M., Vadawale, S.V., Acharya, Y.B., Patel, A. and Goyal, S.K., 2013, "Characterization of High Count Rate Capability of Solar X-Ray Monitor on-Board Chandrayaan-2: The Second Indian Mission to the Moon", IEEE proc. NSS/MIC/RTSD-1686.
24. Vijayan S., Rishitosh K. Sinha. and Murty, S.V.S., 2014, "Characteristics of craters with multi layered ejecta in the equatorial region of mars", 45th Lunar Planet. Sci. Conf., 1676.
25. Vijayan S., Shiv Mohan and Murty, S.V.S., 2014, "Simulated lunar brightness temperature in l- and s- band and regolith thickness estimation using an index-based approach", 45th Lunar Planet. Sci. Conf., 1682.

Space, Atmospheric, Molecular and Laser Physics

26. Aadhi, A., Apurv, C. N., Singh, R. P., and Samanta, G. K., 2014, High-power, continuous-wave, solid-state, tunable source for the ultraviolet, International Conference on Optics & Optoelectronics, paper OP-LAA-5, p. 145.
27. Chithrabhanu, P., Aadhi, A., Reddy, S. G., Prabhakar, S., Samanta, G. K., and Singh, R. P., 2014, A novel entangled system for teleportation of higher dimensional quantum state, International Conference on Optics & Optoelectronics, paper PP-NQQ-12, p. 301.
28. Reddy, S. G., Prabhakar, S., Kumar, A., and Singh, R. P., 2013, "Spatial Intensity Distribution of Optical Vortex Beams", Workshop on Recent Advances in Photonics, paper, p. 41, pp. 1-3.
29. Reddy, S. G., Prabhakar, S., Kumar, A., and Singh, R. P., 2014, "Variation of speckle size with the order of an optical vortex", International Conference on Optics & Optoelectronics, paper OP-OIM-6, p. 397.
30. Reddy, S. G., Kumar, A., Banerji, J., Prabhakar, S., and Singh, R. P., "Optical vortices through a ground glass plate", International Conference on Optics & Optoelectronics, paper IT-OPD-3, p. 487.
31. Saha, K., Banerjee, S.B. and Bapat, B., 2014, "Dissociation of OCS upon various S(2p) Auger decay transitions", J. of Physics: Conference Series, v. 488, p. 012020, pp. 1-6.

Geosciences Division

32. Band, S., Yadava, M.G., Sree, K., Ramesh, R. and Asmerom, Y., 2014, "High resolution precipitation records from a stalagmite of Kotamsar Cave, Chaatisgarh", in: Proc. 28th ISMAS Workshop, (eds. S. K. Aggarwal, P.G. Jaison and A. Sarkar), Indian Society for mass Spectrometry, Mumbai p. 264-266.
33. Bhavya, P.S., Kumar, S., Gupta, G.V.M., Sudheesh, V., Sudharma, K.V., Varrier, D.S., Dhanya, K.R., 2013, "The nitrogen uptake rates in a tropical eutrophic estuary and adjacent coastal Arabian Sea", EUR-OCEANS-hot topic conference-A changing ocean, Las Palmas, Gran Canaria, Spain, E 145 - 146.

34. Bhavya, P.S., Kumar, S., Gupta, G.V.M., Sudheesh, S., Sudharma, K. V., 2014, "Tracing sources of dissolved inorganic carbon using $\delta^{13}\text{C}$ in a tropical eutrophic estuary (Cochin, India)", Proceedings of ¹¹ISMAS Symposium cum Workshop on Mass Spectrometry, ISBN 978-81-904442-6-2, p. 271-273.
35. Deshpande, R.D., 2012, "Application of isotopes in climate change studies ", in: International Meet on Impact of Climate Change on Water Resources (Eds. James, E.J., Jegathambal, P., Brema, J., Priya, K.L.), Kanunya Institute of Technology and Sciences, Karunya University, Karunya Nagar, Coimbatore, India, p. 61-70.
36. Ramesh, R., Mangave, S.R., and Yadava, M.G., 2013, "Paleoclimates of Peninsular India", in: Climate Change and Island and Coastal Vulnerability (Eds. Sundaresan J., et al.), Capital Publishing Company, New Delhi, p.78-100.
37. Rastogi, N., 2012, "Chemical evidences of atmospheric processing of ambient aerosols: Implications", IASTA-Bulletin (ISSN 0971 4510), v. 20, p. 124-125.
38. Rastogi, N., Singh, A., and Singh, D., 2013, "Diurnal Chemical Characteristics of PM_{2.5} over a Source Region of Biomass Burning Emissions in the Indo-Gangetic Plain", Mineralogical Magazine, v. 77, p. 2032.
39. Srivastava, R., Ramesh, R. and Pednekar, S.M., 2013, "Stable isotopic study of Southern Ocean surface waters", in: Scientific and geopolitical Interests in Arctic and Antarctic (eds. R. Ramesh et al), LIGHTS Research Foundation, New Delhi, p.87-92.
40. Wieser, M., Aeschbach-Hertig, W., Schneider, T., Deshpande, R.D. and Gupta, S.K., 2013, "A temperature and monsoon record derived from environmental tracers in the groundwater of Northwest India", Proceedings of International Symposium on Isotopes in Hydrology, Marine Ecosystems and Climate Change Studies, Monaco, March 27 - April 1, 2011, International Atomic Energy Agency, Vienna, p. 7-14.
41. Yadava, M.G., Bhattacharya, Y. and Ramesh, R., 2013, "Application of wavelet transforms to Paleomonsoon data from speleothems", in Wavelets and Fractals in Earth System Sciences (eds. E. Chandrasekar et al.), Chapman & Hall, NY, p. 219-228.
42. Yadava, M.G. and Ramesh, R., 2013, "Estimating the effects of dead carbon fraction and the mineralogy of speleothems on their stable carbon and oxygen isotopic variations", in: Proc. Indo-German Nachkonnnect Seminar on Earth sciences and Society, DAAD & NGRI, Hyderabad.

Theoretical and Computational Physics

43. Kota, V.K.B., 2013, "Interacting Boson Model Applications To Exotic Nuclear Structure in Recent Trends in Nuclear Physics-2012", AIP Conf. Proc., v.1524, p. 52-57.
44. Mahajan, N. and Rangarajan, R., 2014, "Remarks on non-Gaussian fluctuations of the inflaton and constancy of ζ outside the horizon", J. Phys. Conf. Ser., v. 484, p. 012066, pp. 1-4.
45. Mishra, H., Singh, Awaneesh. and Puri, S. 2013, "Kinetics of chiral transitions and domain growth in quark matter", PoS, CPOD2013, p. 022, pp. 1-13.

Books Edited/Review Articles/Technical Notes

Books Edited

1. Kota, V.K.B.,2014, "*Embedded Random Matrix Ensembles in Quantum Physics*", Lecture Notes in Physics, Springer, Heidelberg, v. 884, p. 402.
2. Liritzis, Singhvi, A. K., Feathers, J., Sheng-hua Li, Wagner, G. A., Kadereit, A. and Zacharias, N.,2013, "*Luminescence dating in archaeology, anthropology and geoarchaeology: an overview*", Springer, ISBN: 978-3-319-00169-2(Print), 978-3-319-00170-8 (Online).
3. Masson-Delmotte, V., M. Schulz, A. Abe-Ouchi, J. Beer, A. Ganopolski, J.F. Gonzalez Rouco, E. Jansen, K. Lambeck, J. Luterbacher, T. Naish, T. Osborn, B. Otto-Bliesner, T. Quinn, R. Ramesh, M. Rojas, X. Shao and A. Timmermann, "*Information from Paleoclimate Archives*", Climate Change 2013, Chapter 5, The Physical Science Basis, Contribution of Working Group I to the Fifth Assessment Report of the Intergovernmental Panel on Climate Change [Stocker, T.F., D. Qin, G.-K. Plattner, M. Tignor, S.K. Allen, J. Boschung, A. Nauels, Y. Xia, V. Bex and P.M. Midgley (eds.)].Cambridge University Press, Cambridge, UK.
4. Pabari, J., 2013, "*Investigation of Wireless Sensor Network for Exploration of Lunar Ice-An In-Situ Approach towards Lunar Surface Science*", AP Lambert Academic Publishing, AV Akademikerverlag GmbH & Co. KGGermany, ISBN: 978-3-659-42643-8
5. Ramesh, R., Sudhakar, M., and Chattopadhyay, S.,2013, "*Scientific and geopolitical Interests in Arctic and Antarctic*", LIGHTS Research Foundation, New Delhi, 296, p. 203-211, ISBN: 978-93-5067-908-1.
6. Ray, J. S.,2014, "*The Andaman Archipelago, in Geomorphological Landscapes of India*", Springer-Berlin(Ed. V. Kale), (ISBN 978-94-017-8028-5).
7. Singh, Navinder.,2013, "*On the foundations of statistical mechanics: a brief review*", Modern Physics Letters B, v. 27, p. 1330003, p. 1-29.
8. Vaishnav, B. G., 2013, "*Space Technology in Education–Indian Perspective*", Invited Chapter, The Space Education Phenomena at NASA, Brazil and Beyond, Nova Science Publishers, Inc., NY, July 2013, ISBN:978-1-62618-252-3 (eBook).

Review Articles

1. Ramachandran, S., and Kedia, S.,2013, "*Aerosol optical properties over south Asia from ground-based observations and remote sensing: A review*", Climate, v. 1, p. 84-119.
2. Ramachandran, S., and Kedia, S.,2013, "*Aerosol-precipitation interactions over India: Review, and future perspectives*", Advances in Meteorology, v. 649156, p. 1-20.
3. Rastogi, N.,2012, "*Chemical evidences of atmospheric processing of ambient aerosols: Implications*", IASTA-Bulletin (ISSN 0971 4510), v. 20, p. 124-125.
4. Zuccarello, F., Balmaceda, L., Cessateur, G., Cremades, H., Guglielmino, S. L., Liliensten, J., Dudok de Wit, T., Kretzschmar, M., Lopez, F. M.,Mierla, M., Parenti, S., Pomoell, J., Romano, P., Rodriguez, L., Srivastava, N., Vainio, R., West, M. and Zuccarello, F. P.,2013, "*Solar activity and its evolution across the corona: recent advances*", J. Space Weather Space Climate, v. 3, p. A18-A62.

Technical Notes

1. Pallamraju, D., Optical Aeronomy Studies at Physical Research Laboratory, India, CAWSES Task Group 4 Newsletter, Vol. 8, April 2012.
2. Singh, R. P., Pallamraju, D., and Narayanan, R., Development of Automated Digital Optical Imagers for Photography of vapour cloud releases by rocket, PRL Technical Note, PRL-TN-2012-102.
3. Rajesh, T.A., and Ramachandran, S., 2013, An Integrated Weather Station System, PRL Technical Note, PRL-TN-2013-104.
4. Varun Dongre, F.M. Pathan, Abhijit Chakrabarty, Vaibhav Dixit, 2013, Low Cost, High Precision Temperature Controller, PRL-TN-2013-103.

Promotion of Basic Sciences and Official Language

A special overseas event in PRL: “Exchanges at the Frontier”

The BBC World Service and Wellcome Collection organized “Exchanges at the Frontier”, an exciting series of public events and subsequent radio broadcasts, at PRL Ahmedabad. As the Indian Space Research Organisation launched its first ever Mars Orbiter Mission, the event was organized at PRL and BBC’s Justin Rowlatt and team from BBC world service and Wellcome Collection, UK was at PRL on 30th October, 2013 to speak to Professor J. N. Goswami, Director, PRL about the mission.

The programme was attended by a large and lively audience of the 250 local school children, members of the public and PRL researchers. The discussions were focused on the importance of the Mars mission for India’s scientific status and national pride. The team BBC quoted after the event, “It was perhaps the liveliest audience we’ve ever seen for Exchanges at the Frontier, given to bursting into spontaneous applause and laughter, and eagerly asking questions of our speaker on topics ranging from the technical challenges of the mission to the likelihood of finding aliens on Mars. Given that the subject is of such significance and interest to Indian people, it felt entirely appropriate to be holding the event on home turf, where the garrulous enthusiasm for science and support for India’s ambitious space programme created a brilliant atmosphere in the room”. During the event Prof. Goswami spoke not just about the scientific details of the mission, but about his own early experiences as a budding scientist. He reminisced about his first encounter with space lying on the grass as a child in his home state of Assam, looking out for Sputnik as it passed overhead. It seems likely that for some of the young people in the audience, India’s Mars mission

may prove to be a similarly inspirational first step in their own scientific careers. The audio from this event was recorded and broadcast on BBC World Service on 2nd November, 2013.



Prof. J. N. Goswami and Justin Rowlatt

Lively Audience attending the event at PRL

Glimpses of “Exchanges at the Frontier”

A Scientific meet in the memory of Prof. Devendra Lal

A two-day Scientific Meet “From Mantle to the Moon” was organised in remembrance of Prof. Devendra Lal, a renowned Scientist and former Director, PRL, during Feb. 14-15, 2014 at Physical Research Laboratory, Ahmedabad. The meeting was organised as a mark of tribute to the great person. The meeting provided a glimpse of reminiscences of the Life and Science of Prof. Devendra Lal. The two-day meet comprising seven sessions together presented a glance of different facets of Prof. Lal’s Life and his contributions. Eminent personalities, associates and students of Prof. Lal shared their scientific memoirs during the meeting.



Delegates at a Scientific meet in the memory of Prof. Devendra Lal

Activities on the promotion of Basic Sciences

PRL has been coordinating several programs jointly with the Institutions and learned societies in the region to promote science and create a better scientific environment. Some of the programs include popular lectures by eminent scientists, interactions of scientists with school, college and university students, one day seminars and workshops for students, teachers and researchers, and publication of scientific booklets. In this series following two seminars were supported during the last year.

One day Seminar on Excitement of Research Areas in Basic Sciences, at St. Xavier's college, Ahmedabad, on 19th September, 2013. Eminent scientist from PRL and outside PRL delivered talks in these seminars and interacted with young students about excitement in scientific research. Special sessions on career opportunities in sciences were also organized during the above seminars and in addition to students, teachers and parents had also participated in these discussions.

A Science Awareness Workshop on "New Horizons of Science" sponsored by Indian National Science Academy through PRL was organized by M. B. Patel English Medium Sec. & Hr. Sec. School, Gandhinagar on 15-16 February, 2014. About 1000 students across the schools of Gandhinagar witnessed the symposium and got opportunity to interact with eminent personalities in different disciplines of Science. Most of the presentations were either in Hindi or in Gujarati in very simple form as well as through demonstrations in order to convey the science concepts appropriately to students.



Eminent Scientists and faculty members at the National Seminar on Excitement of Research Areas in Basic Sciences, St. Xavier's College, Ahmedabad.

Science Day Celebration and PRL Scholarship

As has been the practice for several years, a day-long celebration was held on 01 March, 2014 at the Physical Research Laboratory, Ahmedabad to mark the National Science Day (In India National Science Day is celebrated on 28 February every year to commemorate the discovery of Raman effect which was announced by Nobel laureate Sir C. V. Raman on this day). The celebrations aim to attract young minds and motivate them to take up science as one of their career options. National Science Day is also observed to spread the message of importance of science and its application among the people and to accelerate the pace of development among them.



Glimpses of various activities during National Science Day Celebration, 01 March 2014.

PRL Scholarships from the Aruna Lal Endowment Fund, established by late Prof. Devendra Lal, former Director, were awarded to five students on this occasion. The selection was done on the basis of their performances in the state level screening test, poster competition and oral interview. All the five students are to receive ₹10,000/- per year for two consecutive years and for the third year provided the students continue to study in science stream with high academic record.

In addition to the Aruna Lal scholarship, other prizes were awarded like center wise top students (13) in the state level screening test held in February 2014 and poster competitions (12). Most students were accompanied by their teachers. Teachers and students had close interaction with PRL scientists and the judges of the poster competition throughout the day. Also, to give an impetus to young students about the various scientific research being done at PRL, a small science exhibition was organized. All the students and teacher participants visited the exhibits and interacted with PRL scientists. A unique lecture on "career guidance" was also delivered on this day. An interactive lecture with live demonstrations on "Experiments with Lights" was also delivered.

Activities on the promotion of Official Language

As a part of implementation and progressive use of Hindi in PRL, the Hindi Pakhwada was celebrated at PRL from September 14-28, 2013. The highlights of the celebrations included word quiz, essay, elocution, Hamara Karya, self written poetry competition. This time students from the school were invited in the scientific presentation and a question-answer round was conducted. Three best questions were awarded. In the month of July, 2013 the meeting of Town Official Language Implementation Committee (TOLIC) with the Central Government Offices of Ahmedabad was hosted by PRL.

Vishwa Hindi Divas was organized in PRL on 10.1.2014 and a scientific presentation on Udaipur Solar Observatory was given by Prof. Ashok Ambastha.

A workshop on filling online Quarterly Progress Report (QPR) in Hindi was conducted by PRL in February, 2014 in which 40 Central Government Offices in Ahmedabad participated.

A Technical Seminar in Hindi on "National Perspectives of Scientific & Technical Research in PRL" was held at PRL on 14th March, 2014. Fifteen members presented their papers in this Seminar. Shri R.S. Gupta, Hindi Officer-II & OSD delivered lectures in Hindi at workshops held by various Departments like Space Applications Centre, Airport Authority, Food Corporation of India, Income Tax, Doordarshan, ONGC on different topics including Various applications of computers in Hindi.



A Technical Seminar in Hindi on "National Perspectives of Scientific & Technical Research in PRL" : 14 March, 2014.

PRL has been awarded Second Prize for implementation of Rajbhasha with a shield and certificate during the meeting of Town Official Language Implementation Committee (TOLIC) in July, 2013. A shield and certificate was also given to Shri R.S. Gupta, Hindi Officer-II & OSD.

An Orientation Programme for Hindi Officials and Staff was organized by Department of Space in December, 2013 in Shillong which was attended by Hindi Officer-II & OSD. Another Orientation Programme for Hindi Officials and Staff was organized by Department of Space in February, 2014 in Bengaluru which was attended by Shrimati Rumkee Dutta, Hindi Translator and Shri Ashish Sawadkar, Hindi Typist.

Hindi Technical Seminar was organized by Space Applications Centre in October, 2013 which was attended by all the staff and official of Hindi Section. Hindi Workshops are being organized regularly in PRL. Lectures based on the works of different fields in administration in the office are organised in the workshops. The newly appointed employees have successfully completed in-house training of Hindi Typing and got cash prize/increment as personal pay.

Facilities and Services

Computer Centre

To cater to the High Performance Computing needs of our scientists, Computer Centre is equipped with High Performance Compute Cluster having 20 compute nodes, 1 master node with 64GB RAM on each node, 20TB storage capacity and 3.2 TF peak computing performance and 2.2 TF sustained computing performance. The HPC cluster has a Backup node, I/O node, Management node, Storage node, and a Visualization node. The HPC facility is homed in a special chamber that is maintained at controlled temperature and humidity and has a dual UPS system for round the clock operation. The primary network of HPC is with Infiniband and secondary network is Gigabit. Computer Center has SGI server having 16 Intel Xeon processors, 24GB RAM, with 25TB disk capacity. Computer Center also has Dell server having 16 AMD processors, 64GB RAM with 4TB disk capacity, four HP servers, each having four AMD processors, 4 GB RAM, 1.5 TB disk space providing computing power with large disk storage. Computer centre has also IBM Power7 4 CPU based server providing additional computing power. The Internet connectivity is upgraded to 30Mbps through BSNL Optical Fiber Cable. All these computing machines are connected to our high-speed (1Gbps) local area network (LAN) to provide easy, fast and reliable access to more than 300 PCs and a few workstations distributed throughout all the campuses of our laboratory. PRL dispensary in the colony campus opposite IIM is now connected to the Main Campus over an 1Gbps Optical Fiber link. Through this link, the PRL Medical Officers access the Dispensary database housed in the CoWAA cell in computer center.

Through the same Optical Fiber link, the students and PDFs have a round the clock access to PRL LAN/Internet from their rooms via a few Wi-Fi devices installed in the buildings. Students from Thaltej Hostel also can access Internet through a Wi-Fi device installed in the common room in the hostel. The connectivity between Udaipur Solar Observatory (USO), and PRL Main Campus is upgraded to 6 Mbps through BSNL Optical Fiber Cable. Mt.Abu is also connected to PRL main campus over 2 Mbps MLLN link provided by BSNL. Our Thaltej Campus is connected over a Optical Fiber 34 Mbps through BSNL-MLLN link. Thus, round the clock connectivity has been provided to users all the time from Thaltej, USO, and Mt. Abu. Our main campus is also connected to Thaltej via BSNLs 2 Mbps MLLN for voice communication providing intercom telephone facility between the campuses. The Centre provides centralized virus free E-mails by automatically scanning all incoming E-mails. Anti-Spam filter has been centrally installed to fight the Spam mails. The center also provides secure web enabled email service. Internet authorizations, monitoring and reporting functions have been added to have optimal usage of Internet bandwidth. To cater to the High end computing needs, PRL has become resource partner of C-DACs Grid Garuda Project. The Grid Garuda network is integrated to PRL LAN providing seamless access of Garuda resources to PRL scientists. PRL SPACENET connectivity for Data, Intranet, and video conferencing has been established at Main Campus, Thaltej Campus, USO and IR Observatory over IP to interact with ISRO centers. Mathematical, numerical and visualization application software like IMSL, IDL, Mathematica, SigmaPlot, MATLAB, Lahey FORTARN 95, and Statistica etc. have also been installed to cater the needs of the scientific community.

Library & Information Services

PRL Library subscribes to full-text databases like AGU Digital Library, GSA Archive, Nature archive (access from 1987), PROLA, SPIE Digital Library and Science Archive. As no library can be completely self-sufficient, PRL Library also provides document delivery service through ILL. The Library also assists the students in procuring the book-grant books.

In all, 168 books (scientific and general), 61 hindi books and 93 CDs/DVDs were added in the Main, Thaltej and USO libraries during 2013-14. Subscription of seven journals has been added to the existing library collection of 158 journals. Seventy nine (79) book grant requests were processed to assist the students this year. During this period, number of visitors, visiting the library was 3199 and number of documents issued was 2753. The number of ILL requests for articles from other institutes fulfilled by PRL Library was 291 and that of requests of PRL staff fulfilled by other libraries was 299. Number of photocopies made, in house were 23780 and by outside agency were 25908.

The library homepage acts like a window through which it is possible to access the digital content subscribed by PRL as well as open access content. It gives links to 157 online journals out of the 165 journals subscribed by the library. Links have also been provided to a few open access journals in research fields relevant to PRL. The Library Blog has been created to increase the interaction with the library users. The PRL institutional repository consisting of journal articles published by the PRL authors from 1995 to present is also linked through the Library homepage. More than 3200 articles by PRL authors are now part of the repository. All the PRL theses from 1952 onwards (352) are now available full text for PRL users. All the Technical Notes since 1977, published by PRL have been digitized (101) and are available full text for PRL users. E-books page has been redesigned so as give access to the collection by subject as well as by title of the e-book. These collections can be accessed from library homepage (<http://www.prl.res.in/library>). The Library has taken up the digitization of the photographs archive. Scanning of the photographs of about 100 albums is completed. Allocating the metadata (for retrieving the photographs when required), which is the next phase of digitization will start soon.

Workshop

Development of New Optical Imaging Polarimeter

An optical imaging polarimeter has been designed, constructed and tested at PRL for carrying out imaging polarimetry of the extended sources and AGNs using 1.2 m MIRO telescope. Astronomical polarimetry reveals informations on the distribution of magnetic field in extended sources, intrinsic polarization of a host of sources and dust scattering, which are not otherwise available from other techniques. In case of AGNs, generally multiwavelength emission is dominated by the jet and information on the flux density and optical/radio polarization can be used to

glean morphological information about particle acceleration regions and jet magnetic field configuration. The polarimeter is developed around 1024x1024 pixels EMCCD as imaging detector. It uses rotating half wave plate as modulator, rotation being controlled by a stepper motor which completes one rotation in 48 steps. A Foster prism, as analyser, splits the beam into ordinary and extra-ordinary orthogonal rays. The polarimeter has a 12-slot filter wheel to accommodate UBVRI broadband filters and a set of narrow band filters. The stepper motor is driven by a timing signal to rotate the half-wave plate and the same signal is used to initiate the exposure. Figure 98 shows the PRL Optical Imaging Polarimeter (POIP) mounted on the 1.2 m MIRO telescope. The instrument is checked for 100% polarized light using source SAO82421, by introducing Glan prism in the light path (Figure 98). The measured degree of polarization is 97.7 ± 0.4%. The instrument has also been used to observe polarization standards. The polarimeter is completely designed and developed in-house, including whole control electronics and hardware fabrication with the help of several engineering trainees and PRL workshop.

The instrument consists of precise aluminum and brass components with accurate dimensions and surface finish. The system consists of following parts: (1) Half-wave plate gearbox driven by stepper motor for rapidly rotating a half-wave plate. (2) Adjustable mounting block for holding a Foster prism, which can be adjusted in both azimuth and altitude angles for precisely aligning the optical components. (3) Coupling unit machining to hold the above components and also to mount a 12position filter wheel and EMCCD camera as detector.

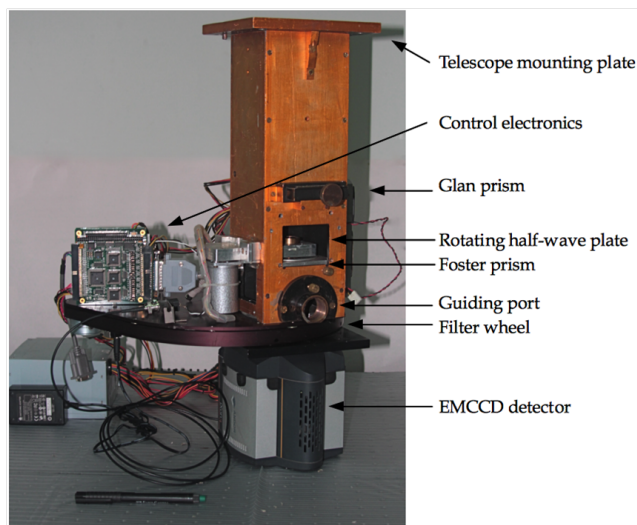


Figure 98: Stepper-motor driven gear box and adjustable mounting block for holding prism for the EMCCD camera detector.

Mirror scanner for airglow photometers

A mirror scanner enables to measure airglow intensities in different directions. Two such mirror scanners were developed in PRL workshop to be augmented on to existing airglow photometers which were reported last year. It involved making of mirror holder, motor coupling for mirror

in the elevation direction, manual rotating plate with aperture for rotation in azimuth direction and fixing the direction in azimuth. After mirror scanner is mounted, it is capable of rotating in a programmed mode with the help of in-house built software. For a campaign in Trivandrum in February, 2014; these scanners were used simultaneously for acquiring data in two photometers for different wavelengths. Both the scanners performed well. The instrument is having machined optical components made from aluminum alloy material. The components are made up of high degree of accuracy and finish to maintain the alignment of the system and interchangeability of the assembly.



Figure 99: Mirror scanner for air-glow spectrometer.

Mechanical design setup for high count rate measurement using X-ray source and X-ray gun for XSM instrument

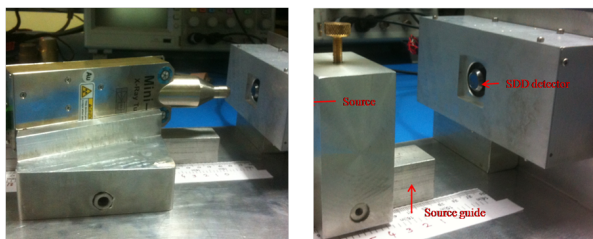


Figure 100: Single stage translation system for mounting xray source and detector.

The developed engineering model of the XSM instruments needs to be tested for various X-ray count rates. In this regard, two mechanism assemblies were designed, one for mounting the X-ray source and another for mounting the X-ray gun. The mechanical design is made such that the centre portion of the detector matches with the X-ray source and gun. The X-ray source and X-ray gun assembly is mounted on a movable

guide by maintaining the parallel axes between them. Using this setup, measurements were carried out satisfactorily.

Multi Wavelength Sun photometer

Multi Wavelength Sun photometer for the measurement of optical properties of aerosols has been designed and developed at Workshop. It is made of solid aluminum cylinder of diameter 90 mm and length 120 mm, housed inside a PVC tube of diameter 110 mm and length 250 mm. The solid aluminum cylinder is designed to hold high grade optical interference filters, multiple baffles, photodiode detectors and signal processing circuit using vertical milling machine VMC-850.

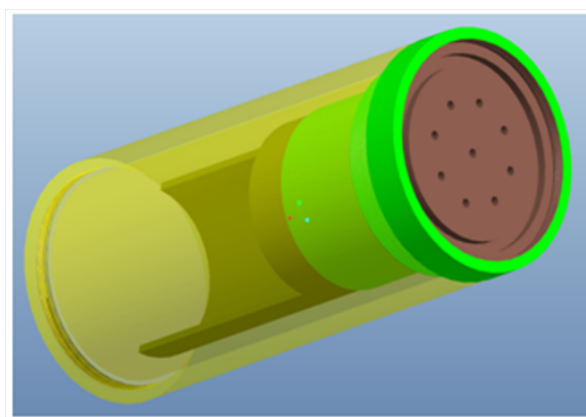


Figure 101: Filter-wheel assembly and the multi wavelength Sun photometer.

UV Laser mounts

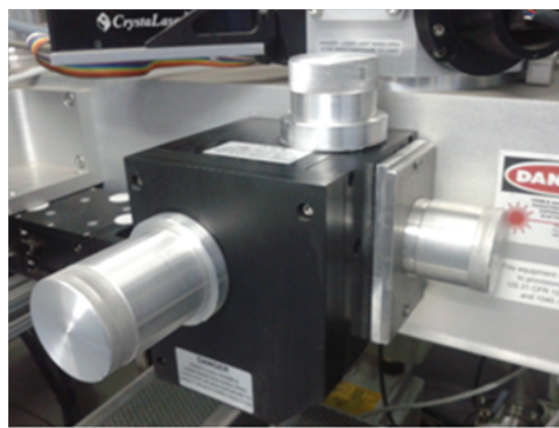


Figure 102: Precision laser mounts with dust protection.

Protection mounts for UV Laser used for particle ablation in Aerosol time of flight mass spectrometer has been designed, developed and installed successfully at ATFOMS Lab. The three mounts were made up of aluminum and have the option of aligning the Laser with much ease. The mount has been designed to protect the Laser system from dust and other objects.

Coral Sampling in the Gulf of Kutch and the Andaman Islands with Underwater Coral Driller

India being a tropical country endowed by four major coral reefs, viz. the Gulf of Kutch, Andaman and Nicobar islands, the Gulf of Mannar and Lakshadweep islands. Corals are animals that secrete calcium carbonate and create carbonate wall-like structures which are known as coral reefs.



Figure 103: Various tools developed at PRL Workshop for underwater coral driller.

They act as an archive by storing the ambient information regarding the sea water chemistry that persisted during the secretion of the calcium carbonate. In order to study the climatic variation and alteration in the oceanographic conditions, it becomes important to study the corals and coral reefs. Therefore, to study recent climatic variability, the underwater coral coring operations were undertaken for

the first time in India on the Porites colonies in the Gulf of Kutch and the Andaman islands. Several samples of live and dead coral cores were raised by using this underwater coral driller procured from M/s Wheeler Tech Corp., USA and the maximum length of the core obtained was ~ 1.3 m. As part of this project, PRL workshop was very instrumental in making suitable developments as required for underwater drilling, field assistance for smooth operation and fabrication of spares that may be lost due to wear and tear during the operations. During the field operations, from PRL workshop tradesman's expertise was very helpful in solving various technical problems at site and resuming the drilling operations at the earliest. This study on corals from various locations from the northern Indian Ocean region has implications towards reconstruction of high resolution climatic records which would help in understanding past sea surface temperature, ocean chemistry and climate.

The workshop helped in developing the corer for its smooth operation in the field. The various tools and tool holders for holding the cutter were developed and fabricated in the workshop as shown in the below figure.

An attachment for Schmidt-Newton 25cm aperture telescope with the main telescope for wide field transit photometry

A new fixture designed and fabricated in workshop as per the requirement. A provision was also provided for adjusting the angle of the telescope with respect to the main 1.2m telescope so that both the telescopes can be aligned parallel to each other with minimum dome obstruction. The fixture and bracket is fitted and aligned with the telescope successfully at IR-Telescope at Mt. Abu and subsequently observations were taken successfully.

in the elevation direction, manual rotating plate with aperture for rotation in azimuth direction and fixing the direction in azimuth. After mirror scanner is mounted, it is capable of rotating in a programmed mode with the help of in-house built software. For a campaign in Trivandrum in February, 2014; these scanners were used simultaneously for acquiring data in two photometers for different wavelengths. Both the scanners performed well. The instrument is having machined optical components made from aluminum alloy material. The components are made up of high degree of accuracy and finish to maintain the alignment of the system and interchangeability of the assembly.



Figure 99: Mirror scanner for air-glow spectrometer.

Mechanical design setup for high count rate measurement using X-ray source and X-ray gun for XSM instrument

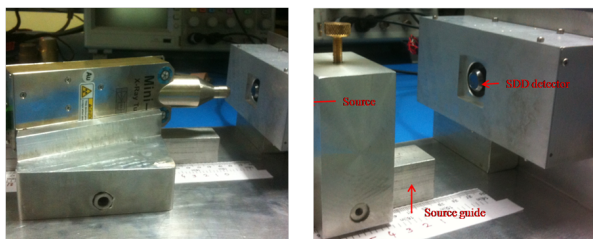


Figure 100: Single stage translation system for mounting xray source and detector.

The developed engineering model of the XSM instruments needs to be tested for various X-ray count rates. In this regard, two mechanism assemblies were designed, one for mounting the X-ray source and another for mounting the X-ray gun. The mechanical design is made such that the centre portion of the detector matches with the X-ray source and gun. The X-ray source and X-ray gun assembly is mounted on a movable

guide by maintaining the parallel axes between them. Using this setup, measurements were carried out satisfactorily.

Multi Wavelength Sun photometer

Multi Wavelength Sun photometer for the measurement of optical properties of aerosols has been designed and developed at Workshop. It is made of solid aluminum cylinder of diameter 90 mm and length 120 mm, housed inside a PVC tube of diameter 110 mm and length 250 mm. The solid aluminum cylinder is designed to hold high grade optical interference filters, multiple baffles, photodiode detectors and signal processing circuit using vertical milling machine VMC-850.

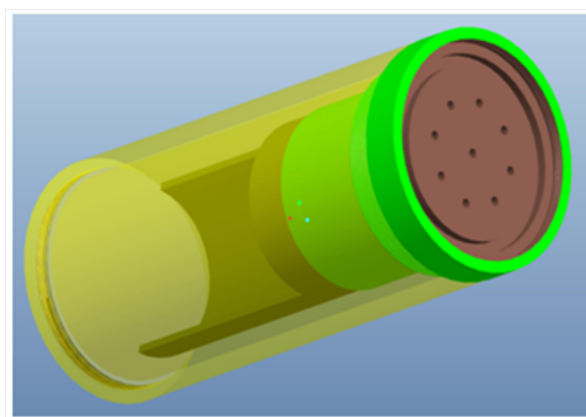


Figure 102: Filter-wheel assembly and the multi wavelength Sun photometer.

UV Laser mounts

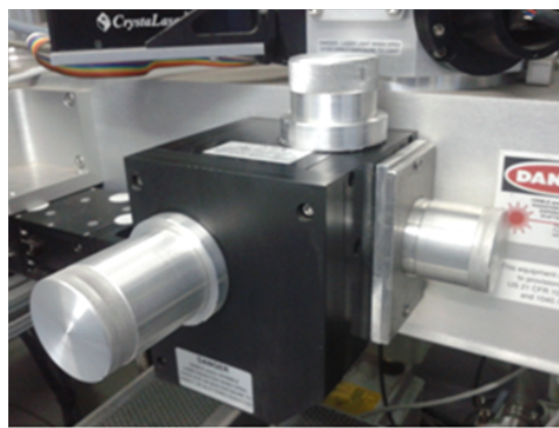


Figure 103: Precision laser mounts with dust protection.

Protection mounts for UV Laser used for particle ablation in Aerosol time of flight mass spectrometer has been designed, developed and installed successfully at ATFOMS Lab. The three mounts were made up of aluminum and have the option of aligning the Laser with much ease. The mount has been designed to protect the Laser system from dust and other objects.

Coral Sampling in the Gulf of Kutch and the Andaman Islands with Underwater Coral Driller

India being a tropical country endowed by four major coral reefs, viz. the Gulf of Kutch, Andaman and Nicobar islands, the Gulf of Mannar and Lakshadweep islands. Corals are animals that secrete calcium carbonate and create carbonate wall-like structures which are known as coral reefs.



Figure 104: Various tools developed at PRL Workshop for underwater coral driller.

They act as an archive by storing the ambient information regarding the sea water chemistry that persisted during the secretion of the calcium carbonate. In order to study the climatic variation and alteration in the oceanographic conditions, it becomes important to study the corals and coral reefs. Therefore, to study recent climatic variability, the underwater coral coring operations were undertaken for

the first time in India on the Porites colonies in the Gulf of Kutch and the Andaman islands. Several samples of live and dead coral cores were raised by using this underwater coral driller procured from M/s Wheeler Tech Corp., USA and the maximum length of the core obtained was ~ 1.3 m. As part of this project, PRL workshop was very instrumental in making suitable developments as required for underwater drilling, field assistance for smooth operation and fabrication of spares that may be lost due to wear and tear during the operations. During the field operations, from PRL workshop tradesman's expertise was very helpful in solving various technical problems at site and resuming the drilling operations at the earliest. This study on corals from various locations from the northern Indian Ocean region has implications towards reconstruction of high resolution climatic records which would help in understanding past sea surface temperature, ocean chemistry and climate.

The workshop helped in developing the corer for its smooth operation in the field. The various tools and tool holders for holding the cutter were developed and fabricated in the workshop as shown in the below figure.

An attachment for Schmidt-Newton 25cm aperture telescope with the main telescope for wide field transit photometry

A new fixture designed and fabricated in workshop as per the requirement. A provision was also provided for adjusting the angle of the telescope with respect to the main 1.2m telescope so that both the telescopes can be aligned parallel to each other with minimum dome obstruction. The fixture and bracket is fitted and aligned with the telescope successfully at IR-Telescope at Mt. Abu and subsequently observations were taken successfully.

Honorary Fellows

J. E. Blamont

P. Crutzen

A. Hewish

K. Kasturirangan

M. G. K. Menon

U. R. Rao

Honorary Faculties

R. K. Varma
FNA, FASc., FNASc., NASI Senior Scientist

S. Krishnaswami
FNA, FASc, FNASc, FTWAS, INSA Senior Scientist

R. G. Rastogi
FNA, FASc, FNASc

S. K. Gupta
FNASc

A. C. Das

A. R. Prasanna

N. Bhandari
FNA, FASc, FNASc, INSA Honorary Scientist

D. P. Dewangan
FNASc

B. G. Anand Rao

S. P. Gupta

H. Chandra

H. S. S. Sinha

U. C. Joshi

R. Sridharan
FASc, FNASc, CSIR Emeritus Scientist

M. M. Sarin
FNA, FASc., FNASc.

Shyam Lal
FNA, FASc., FNASc.

J. Banerji

A. Singal

V. K. B. Kota

T. Chandrasekhar

R. Jain

H. O. Vats

Y. B. Acharya

Academic Faculty

| Name | Designation | Specialization | Academic Qualification |
|---|---------------------|---|--|
| Goswami J. N. <i>FNA, FASc, FNASc, FTWAS</i> | Director | Solar System Studies (Pre-Solar Processes) | Ph.D., PRL, Gujarat. Univ. (1978) |
| Ambastha A. K. | Senior Professor | Solar Plasma Physics | Ph.D., PRL, Gujarat. Univ. (1981) |
| Amritkar R. E. <i>FASc, FNASc</i> | Senior Professor | Nonlinear Dynamics & Chaos | Ph.D., IISc, Bangalore (1978) |
| Ashok N. M. | Senior Professor | Close Binary Stars, Novae/IR spectroscopy | Ph.D., PRL, Gujarat Univ. (1983) |
| Baliyan K. S. | Professor | AGNs, Comets, Atomic Physics, Milky Way | Ph.D., Roorkee Univ. (1986) |
| Banerjee D. | Associate Professor | Thermoluminescence & Planetary Physics | Ph.D., PRL, Gujarat Univ. (1997) |
| Banerjee D. P. K. | Professor | Novae, Be Stars, Planetary Nebulae, IR and Optical Studies | Ph.D., PRL, Gujarat Univ. (1990) |
| Bapat B. | Associate Professor | Atomic & Molecular Processes | Ph.D., T.I.F.R, Bombay Univ. (1997) |
| Basu Sarbadhikari A. | Scientist-SD | Petrology & Geochemistry | Ph.D., IIT, Khargpur (2009) |

| Name | Designation | Specialization | Academic Qualification |
|--|-----------------------|---|-----------------------------------|
| Bhatt J. R. | Associate Professor | Astrophysics | Ph.D., IPR, M.S. Univ.(1992) |
| Bhattacharyya R. | Reader | Plasma Physics | Ph.D., Jadavpur Univ., (2006) |
| Bhushan R. | Scientist-SF | Oceanography and Paleoclimatology | Ph.D., PRL, M.S. Univ. (2009) |
| Chakrabarty A. | Associate Professor | Extra-solar planets, Star Formation & Instrumentation | Ph.D., PRL, Gujarat Univ. (1999) |
| Chakrabarty D. | Reader | Upper Atmosphere and Geomagnetic storm | Ph.D., PRL, M.L.S Univ.(2008) |
| Deshpande R. D. | Scientist-SF | Application of Environmental Tracers in Hydrology | Ph.D., PRL, M.S. Univ. (2007) |
| Goswami S. | Professor | High Energy Physics | Ph.D., Calcutta Univ. (1998) |
| Haider S. A. <i>FASc, FNA, FNASc</i> | Professor | Planetary and Cometary Atmospheres | Ph.D., Banaras Univ. (1984) |
| Janardhan P. | Professor | Solar Radio Astronomy & Space Weather | Ph.D., PRL, Gujarat Univ. (1991) |
| Joshi B. | Reader | Solar Physics, Astronomy | Ph.D., ARIES, Kumaun Univ.(2007) |
| Joshiyura A. S. <i>FNA, FASc, FNASc</i> | Outstanding Scientist | Particle physics | Ph.D., TIFR, Bombay Univ.(1979) |
| Juyal N. | Scientist-SF | Quaternary Geology & Paleoclimate | Ph.D., PRL, M.S. Univ.(2004) |
| Konar P. | Reader | Particle Physics | Ph.D., HRI, Allahabad Univ.(2005) |
| Kumar B. | Scientist-SE | Solar Physics | Ph.D., PRL, M.L.S Univ.(2007) |
| Kumar S. | Reader | Aquatic and Terrestrial Biogeochemistry | Ph.D., PRL, M.S. Univ., (2004) |
| Mahajan N. | Associate Professor | Particle Physics | Ph.D., Delhi Univ.(2004) |
| Marhas K. K. | Associate Professor | Solar System studies | Ph.D., PRL, D.A.V.V Indore (2001) |
| Mathew S. K. | Associate Professor | Solar Magnetic & Velocity Fields | Ph.D., PRL, Gujarat Univ. (1999) |

| Name | Designation | Specialization | Academic Qualification |
|---|-----------------------|---|--|
| Mishra H. | Professor | Strong Interaction Physics & Nuclear Astrophysics | Ph.D., IOP, Utkal Univ. (1994) |
| Mohanty S. | Senior Professor | Astroparticle Physics | Ph.D., Wisconsin Univ. (1989) |
| Murty S. V. S. <i>FASc</i> | Senior Professor | Isotope Cosmochemistry | Ph.D., IIT, Kanpur (1981) |
| Naik S. | Reader | High Energy Astro- physics, X-ray Binaries | Ph.D., T.I.F.R, Bombay Univ.(2003) |
| Pallamraju D. | Professor | Space Weather and Atmospheric coupling processes | Ph.D., PRL, D.A.V.V Indore(1997) |
| Rai V. | Associate Professor | Stable Isotope Cosmochemistry | Ph.D., PRL, M.S Univ. (2001) |
| Ramachandran S. | Professor | Atmospheric AerosolsRadiative & Climate Impacts | Ph.D., PRL, M.S Univ. (1996) |
| Ramesh R. <i>FNA, FASc, FNASc, FTWAS</i> | Outstanding Scientist | Paleoclimatology, Oceanography & Modelling | Ph.D., PRL, Gujarat Univ. (1984) |
| Rangarajan R. | Associate Professor | Particle Physics & Cosmology | Ph.D., Univ. of California, Santa Barbara (1994) |
| Rastogi N. | Reader | Atmospheric & Aerosol Chemistry | Ph.D., PRL, M.L.S Univ. (2005) |
| Ray J. S. | Associate Professor | Isotope Geochemistry | Ph.D., PRL, M.S Univ. (1998) |
| Ray D. | Scientist-SD | Marine Geology & Igneous Petrology | Ph.D., Jadavpur Univ. (2009) |
| Rengarajan R. | Scientist-SF | Atmospheric aerosols & aqueous geochemistry | Ph.D., PRL, M.L.S Univ.(2004) |
| Rindani S. D. <i>FNA, FASc, FNASc</i> | Senior Professor-H | Particle Physics | Ph.D., IIT, Bombay (1976) |
| Sahoo B. K. | Associate Professor | Atomic Physics | Ph.D., Mangalore Univ.(2006) |
| Sahu L. K. | Reader | Atmospheric Science, Trace gases | Ph.D., PRL, M.L.S.Univ., (2005) |
| Samanta G. K. | Reader | Laser and Nonlinear optics | Ph.D., Universitat Politecnica de Catalunya Uni., Barcelona, (2009) |
| Sarkar U. <i>FNA, FASc, FNASc</i> | Outstanding Scientist | Particle Physics | Ph.D., Calcutta Univ.(1984) |

| Name | Designation | Specialization | Academic Qualification |
|---|-----------------------|---|---|
| Sekar R. | Professor | Upper Atmospheric & Ionospheric Physics | Ph.D., PRL, Gujarat Univ.(1991) |
| Sharma S. K. | Reader | Middle Atmosphere & Long Term Atmospheric Changes | Ph.D., PRL, Gujarat Univ.(2010) |
| S. Ganesh | Scientist-SE | Milky Way, Comets, AGN, Astronomical polarimetry | Ph.D., PRL, Gujarat Univ.(2010)) |
| Sheel V. | Associate Professor | Modelling of Lower Atmosphere | Ph.D., PRL, Gujarat Univ.(1996) |
| Shukla A. D. | Scientist-SE | Geochemistry & Cosmochemistry | Ph.D., PRL, M.S. Univ. (2012) |
| Singh A. D. | Associate Professor | Atomic Physics | Ph.D., IIA, Bangalore Univ.(1998) |
| Singh N. | Reader | Theoretical condensed matter and Statistical physics | Ph.D., RRI, Bangalore (2006) |
| Singh R. P. | Scientist-SF | Laser Physics | Ph.D., J.N.U., New Delhi.(1994) |
| Singh S. K. | Associate Professor | Isotope Geochemistry | Ph.D., PRL, M.S. Univ.(1999) |
| Singhvi A. K. <i>FNA, FASc, FNASc, FTWAS</i> | Outstanding Scientist | Palaeoclimatology and Geochronology | Ph.D., IIT, Kanpur (1975) |
| Sivaraman B. | Reader | Low Temperature Astrochemistry | Ph.D., The Open University, UK (2008) |
| Srivastava N. | Associate Professor | Solar Physics | Ph.D., PRL, Ravi Shankar Shukla Univ.(1994) |
| Subramanian K. P. | Professor | Experimental Atomic and Molecular Physics | Ph.D., PRL, Gujarat Univ.(1987) |
| Thampi S. | Reader | Atmospheric Physics | Ph.D., V.S.S.C, Kerala Univ, (2007) |
| Vadawale S. V. | Associate Professor | High Energy Astrophysics and X-Ray Spectroscopy | Ph.D., T.I.F.R, Bombay Univ. (2003) |
| Venkatakishnan P. | Senior Professor-H | Solar Physics | Ph.D., IIA, Bangalore Univ.(1984) |
| Yadava M. G. | Scientist-SF | Palaeoclimate, Radiocarbon dating and stable isotopes | Ph.D., PRL, D.A.V.V., Indore (2003) |

Technical Faculty

| Name | Designation |
|------------------|--------------------|
| Adhiyaru P. R. | Engineer-SE |
| Mahajan R.R. | Scientist-SE |
| Narayanan R. | Scientist-SF |
| Nishtha A. | Librarian-SE |
| Pabari J. | Engineer-SE |
| Rajesh T. A. | Scientist-SE |
| Rao D. K. | Scientist-SE |
| Raval J. | Engineer-SE |
| Shah A. B. | Engineer-SF |
| Shah R. R. | Engineer-SF |
| Shanmugam M. | Engineer-SE |
| Singh Mahendra | Sci./Eng.-SF |
| Vaghela H. R. | Engineer-SE |
| Ubale G. P. | Engineer-SF |
| Venkataramani S. | Scientist-SF |

5. Investments

The trust consistently classifies Fixed Deposits under the head Investments. The fixed deposits are maintained in the custody of Accounts Officer and are physically verified by the Management or its authorized representative(s) periodically.

Surplus out of grants, that of endowment funds are maintained by way of Fixed Deposits and Savings Bank Accounts with Schedule Banks.

6. Inventories

The stock of consumables and medicines are valued at cost which are physically verified by the Management and reconciled with the Stores records.

The stores item purchased and issued immediately to the department are treated as consumed.

7. Retirement Benefits

Retirement Benefits which include Gratuity, Leave Encashment and Pension are treated as payable in the year in which the retirement of employees takes place.

[As per actuarial valuations]:

| | | |
|---------------------------|-------------|-----------------------|
| Gratuity | : ₹. | 9,00,83,690 |
| Half Pay Leave encashment | : ₹. | 47,00,319 |
| Earned Leave encashment | : ₹. | 7,89,75,257 |
| Pension | : ₹. | 1,54,29,96,693 |
| Total | : ₹. | 1,71,67,55,959 |

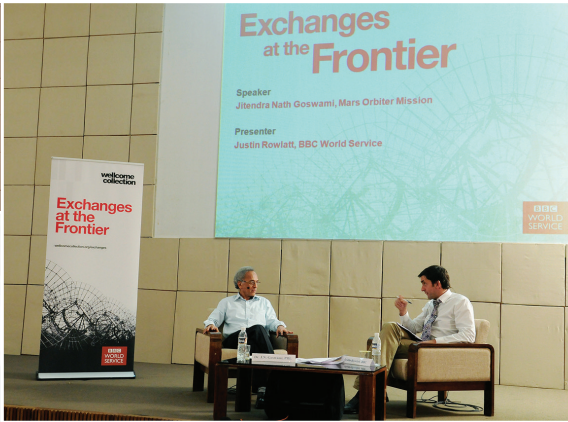
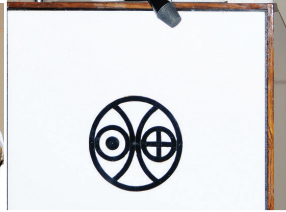
8. Foreign Transaction

Foreign currency transactions are recorded at the exchange rate prevailing as on the date of the payment. Foreign Exchange fluctuation gain or loss is not booked for the payments outstanding as on 31st March, 2014.





पी.आर.एल. में गतिविधियां Event at PRL





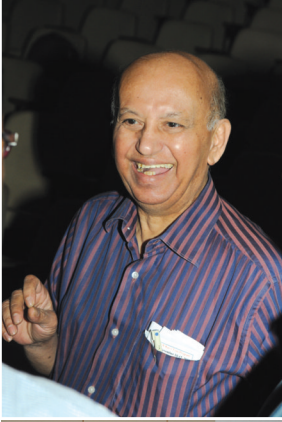
पी.आर.एल. में गतिविधियां Event at PRL

वार्ता रूपरेखा

- इसने दिन के विचारों पूर्व का संक्षिप्त परिचय
- गणित भाषा में पूर्व का मूल्य
- अध्यात्मिक भाषा में समावेश और तैरभौतिकी का विकास
- स्वच्छता पंचक विकास
- अनुभव की वेबसाइट - स्थापना से अब तक

भौतिक अनुसंधान प्रयोगशाला अहमदाबाद

PRL - SWC
Welcomes You
GITA CELEBRATION



पी.आर.एल. में गतिविधियां Event at PRL



